A Computational Tool for Seismic Collapse Assessment of Masonry Structures

Anjali Abhay Mehrotra

Department of Engineering
University of Cambridge

This dissertation is submitted for the degree of
Doctor of Philosophy

King's College December 2018

For Mom + Dad

Declaration

I hereby declare that except where specific reference is made to the work of others, the contents of this dissertation are original and have not been submitted in whole or in part for consideration for any other degree or qualification in this, or any other university. This dissertation is my own work and contains nothing which is the outcome of work done in collaboration with others, except as specified in the text and Acknowledgements. This dissertation contains fewer than 65,000 words including appendices, bibliography, footnotes, tables and equations and has fewer than 150 figures.

Anjali Abhay Mehrotra
December 2018

Acknowledgements

First and foremost I am extremely grateful to my supervisor, Dr Matthew DeJong, for his guidance, patience and unwavering support over the past four years. I would like to thank him for providing me with the most incredible opportunities, and for always looking out for my best interests. His passion and enthusiasm have been an inspiration to me.

I would also like to acknowledge the financial support provided for this research by the Jawaharlal Nehru Memorial Trust in conjunction with the Cambridge Commonwealth, European & International Trust. I am grateful to King's College, the Department of Engineering, and the Cambridge Philosophical Society for their generous grants over the past four years, which made it possible for me to attend a number of conferences.

I am grateful to Blerta Lipo for the fruitful discussions which inspired the research in Chapters 6 and 7, as well as Dr Alberto Mauro for taking the time to explain the derivations in his paper to me. I would also like to thank Professor Angelyn Bass, Professor Douglas Porter, and Professor John Ochsendorf for collaboration and data related to the assessment of the Casa Grande Ruins National Monument, and Professor Paulo Lourenco for data related to the LNEC shake table tests. I am also indebted to Professor Philippe Block, Dr Tom Van Mele, Dr Andrew Liew and Dr Noelle Paulson for their guidance regarding future directions of this work.

I am especially grateful to Karen Mitchell for all her help over the past few years, as well as my lab-mates - both current and former - who made coming into the office every day an infinitely better experience.

From old friends who have accompanied me on this journey from the start, to newer friends who I'm so very grateful to have met along the way- thank you all for making these past four years so wonderful. I am grateful to Anh Khoa for being a constant source of emotional support and always lending me a listening ear when I needed it, and to Amani, Adam and Fabio for their enduring friendship. Thank you to Priyanka, for the countless hours (and bottles of wine) spent discussing life, and Abhimanyu for always making me laugh. I am indebted to Krishna for going above and beyond the role of a grad-buddy and for always taking time out of his busy days to help me, and to Alessandra and Francesca for their warm and fierce friendship. I am especially grateful to Anna and Francesco for being the most wonderful of friends, for taking me on new adventures, and never letting me go hungry, and to Daniele for teaching me about life, masonry, and everything in between.

Finally, I would like to thank my parents for their love and ever-enduring support over the past four years - thank you for always encouraging me to pursue my dreams and for supporting me at every step along the way.

Abstract

Earthquakes represent a serious threat to the safety of masonry structures, with failure of these constructions under the influence of seismic action generally occurring via specific, well-documented collapse mechanisms. Analysis and assessment of these collapse mechanisms remains a challenge - while most analysis tools are time-consuming and computationally expensive, typical assessment methods are too simplified and often tend to underestimate the dynamic resistance of the structures. This dissertation aims to bridge the gap between the two through the development of a computational tool for the seismic collapse assessment of masonry structures, which uses rocking dynamics to accurately capture large displacement response, without compromising on computational efficiency. The tool could be used for rapid evaluation of critical mechanisms in a structure in order to prioritise retrofit solutions, as well as for code-based seismic assessment.

The framework of the tool is first presented, wherein the rocking equations of motion are derived for a range of different collapse mechanisms, for any user-defined structural geometry, using as a starting point a geometric model of the structure in Rhino (a 3D CAD software). These equations of motion are then exported for solution to MATLAB. As a number of collapse mechanisms take place above ground level, a methodology to account for ground motion amplification effects is also proposed, while in the case of comparison of multiple different mechanisms, an algorithm to automatically detect critical mechanisms is presented. These developments make it possible to rapidly conduct a seismic analysis of structures with complicated three-dimensional geometries.

However, the rocking equations of motion utilised thus far assume that the interfaces between the masonry macro-elements are rigid, which is not the case in reality. Thus, a flexible interface model is introduced, where the interfaces are characterised by a finite stiffness and compressive strength. This modelling strategy results in an inward shift of the rocking rotation points, and expressions are derived for these shifting rotation points for different interface geometries. The rocking equations of motion are also re-derived to account for the influence of the continuously moving hinges. However, the new equations tend to be highly non-linear - especially in the case of more complex collapse mechanisms. Thus to reduce computational burden, the semi-flexible interface model is proposed, which accounts for the shifting hinges in a more simplified manner than its fully-flexible counterpart. These new analytical models enable more accurate prediction of the seismic response of real-world structures, where interface flexibility tends to have a significant influence on dynamic response, while material damage in the form of crushing of the masonry also reduces dynamic resistance.

The ability of the tool to be used for both seismic analysis and assessment is finally demonstrated by using it to perform a rocking dynamics-based analysis as well as a code-based seismic assessment of the walls of a historic earthen structure.

Table of contents

List of figures

List of tables

Chapter 1

Introduction

1.1 Motivation

Masonry structures comprise a broad range of building materials and structural typologies - ranging from monumental structures such as Roman triumphal arches and Greek temples, which were usually constructed using materials such as stone and marble, to more modern constructions such as multi-story office buildings and apartment blocks, which are commonly built using brick and mortar, or even concrete blocks.

In the case of historic masonry structures in particular, their relatively large scale results in gravity being the predominant load acting on them. In fact, the effect of environmental loads such as wind and snow is usually small when compared to the structure's self-weight. Coupled with the durability of masonry as a building material as well as its high compressive strength, it is thus hardly surprising that masonry structures make up the majority of built cultural heritage still surviving today.

However, as the safety of these structures is usually governed by stability rather than material strength (Heyman, 1995), the large displacements induced by earthquakes have the potential to be extremely destructive to these constructions. In fact, failure of masonry structures under the influence of seismic action is frequently observed – most recently during the earthquakes in Central Mexico [2017], Amatrice, Italy [2016] and Nepal [2015]. The collapse of structures during earthquakes not only causes a catastrophic amount of damage in terms of human casualties and economic losses, but also results in the loss of a part of our shared cultural heritage through the destruction of monuments, churches and other historic masonry structures.

However, while failure of these structures during earthquakes is well-documented, the tools and methods currently used to assess their vulnerability to collapse (and consequently the need for intervention) leave room for improvement. This is particularly relevant in the case of historic masonry structures, where over-conservative predictions of seismic vulnerability can result in occasionally unnecessary retrofit solutions - which tend to disturb the original fabric/aesthetics of the structure. Furthermore, when applied incorrectly, such interventions can also further increase susceptibility to collapse - as was observed in the case of several cultural heritage buildings during the 2009 L'Aquila earthquake (Augenti and Parisi, 2010). These factors, combined with the formidable cost of seismic strengthening measures, make it impractical to retrofit all the potentially vulnerable elements in a structure, and thus emphasise the need for improved assessment tools which enable rapid comparison of the relative vulnerabilities of different elements within a structure, so that retrofit solutions can be prioritised and used as effectively as possible.

At present, the tools used for modelling collapse of these structures can be broadly divided into simplified code-based analytical methods and detailed numerical modelling programs. While code-based analytical methods provide rapid estimates of the response of the structure, they tend to ignore certain dynamic features of this response, and thus yield generally conservative predictions. Conversely, numerical modelling programs, while providing more realistic predictions, tend to be computationally-expensive and time-consuming, and are thus better suited for analysis of these structures, rather than assessment. There thus exists a need for the development a tool which bridges the gap between the two procedures - by better capturing large displacement response and thus more effectively modelling collapse than the current code-based methods, but by doing so in a manner that is more computationally-efficient than typical numerical modelling procedures.

Such a tool has the potential to be extremely useful not just in Europe, with its abundance of cultural heritage vulnerable to seismic action, but also in developing countries such as India, Pakistan and Nepal - which lie in highly seismic zones and tend to suffer from a disproportionately large number of casualties during earthquakes - with 8,790 people dying during the 2015 Gorkha earthquake in Nepal (National Planning Commission (NPC), 2015), 72,760 people being killed during the 2005 Kashmir earthquake in Pakistan (EEFIT, 2005), and more than 20,000 casualties being recorded during the 2001 Bhuj earthquake in India (Hough et al., 2002). A dearth of government funding for the protection of built heritage in these countries thus makes it even more critical to develop an open-source, easy to use, computationally-efficient tool, which is independent of specific commercial software and can thus be used by engineers and academics all over the world.

1.2 Background

Failure of masonry structures during earthquakes generally occurs via specific, well-documented collapse mechanisms (D'Ayala and Speranza (2002), D'Ayala and Speranza (2003), PCM-DPC MiBAC (2006)), which can broadly be divided into in-plane and out-of-plane mechanisms, with local or out-of-plane collapse tending to dominate failure.

Dynamic analysis of these collapse mechanisms can be conducted using either analytical tools or numerical methods. Typical assessment tools, commonly applied in practice, comprise both force-based and displacement-based procedures, and include code-based methods such as those outlined by ASCE 43-05 (2007) and the Italian Building Code (DMI, 2008), the FaMIVE procedure proposed by D'Ayala and Speranza (2002), as well as various commercial software (Aedes Software Snc (1997), STADATA (2012), Lagomarsino and Ottonelli (2012)). The dynamic resistance of the structure, which increases with its scale, is generally factored into these assessment methods by either using a multiple of the static acceleration required to activate the mechanism (e.g. through the use of a behaviour factor, typically equal to 2, as in the Italian Building Code), or by approximating the dynamic response using a single-degree-of-freedom linear-elastic oscillator. Such an approach tends to incorporate certain dynamic effects, but ignores others, and consequently yields results which are generally conservative (Shawa et al., 2012), which can lead to expensive and unnecessary retrofitting solutions.

At the other end of the spectrum, numerical methods such as Finite Element Modelling (FEM) and Discrete Element Methods (DEM) can be used for more detailed analysis of these collapse mechanisms. Using FEM, the masonry can either be modelled as a continuum (macro-modelling) or with each unit individually represented and the joints between them modelled as interfaces (micro-modelling). As an alternative, DEM can be used to model the masonry as rigid blocks separated by interfaces of a given stiffness, which enables the capture of large displacement response as well as the opening and closing of the joints. However such methods are sensitive to input parameters such as damping and joint properties, and can be both time-consuming and computationally expensive (de Felice et al., 2017), particularly when trying to model collapse.

Alternatively, non-linear dynamic analysis, which directly integrates the equations of motion of the local collapse mechanisms, can be used to analytically model collapse, based on the assumption of rigid body behaviour of the masonry macro-elements. Equations of motion derived in the literature thus far model these collapse mechanisms as single, two or multiple block mechanisms (Housner (1963), Mauro et al. (2015), Sorrentino et al. (2008b), Makris and Vassiliou (2013)), with formulations also being proposed for structures with more complicated geometries such as masonry spires and arches (DeJong (2012b), DeJong and Dimitrakopoulos (2014)). Such an approach has been found to better-reproduce experimental results, with considerably less scatter being observed with the experimental data - especially when compared to code-based predictions (Shawa et al., 2012). However, while such an approach enables faster assessment and depends on fewer variables than FEM and DEM, the solution of real geometries involving complicated 3D mechanisms has not been feasible up to this point.

Furthermore, while most of the rocking equations of motion found in the literature tend to model the kinematic chain as a set of rigid bodies with rigid interfaces, this is not realistic as real-world structures have non-rigid joints (generally due to the presence of mortar) with finite compressive strength. In fact, interface flexibility has been observed to have a substantial influence on dynamic response (ElGawady et al., 2011), while the assumption of infinite compressive strength also tends to be un-conservative - particularly for large-scale structures, or for vertically-spanning walls under large superimposed loadings.

1.3 Research objectives

While numerous formulations have been proposed in the literature for analytically modelling dynamic collapse of masonry structures, most of these formulations have been limited to simple structural geometries such as rectangular blocks and cones (DeJong (2012b), Mauro et al. (2015), Sorrentino et al. (2008b), Makris and Vassiliou (2013)). Conversely in the case of more complex structures, most analytical formulations have been restricted to kinematic limit analysis (de Luca et al. (2004), Block et al. (2006)) with the equivalent displacement demand being evaluated through the combination of this approach with the capacity spectrum method (DMI (2008), Lagomarsino (2015)). However, given that a number of real-world structures tend to have complicated geometries and thus cannot simply be idealised as simple rectangular blocks or cones, there is a need to integrate both aspects of this problem in a simplified manner that could also be implemented in codes of practice. Thus the first objective of this dissertation is to:

1. Develop a simple computational modelling tool to rapidly predict critical mechanisms and dynamic collapse of any user-defined structural geometry.

Furthermore, in the case of large-scale structures or structures with a low compressive strength, interface flexibility tends to influence dynamic response, with material damage in the form of crushing of the masonry leading to reduction in dynamic resistance. Thus to more realistically model the effects of non-rigid interfaces, the second objective of this dissertation is to:

2. Develop a new interface formulation to more realistically model the influence of interface stiffness and crushing (i.e. material damage) on the dynamic response of masonry structures - which can also be implemented within the framework of the tool.

More generally, the aim of this research is to develop an accurate but computationally-efficient modelling tool for the seismic assessment of masonry structures, which incorporates the dynamics of seismic collapse, while requiring only a 3D geometric model (i.e. CAD model) of the structure as input. Major benefits will include the circumvention of labour-intensive, manual generation of complicated structural analysis models, avoidance of time-intensive computation typical of many computational analysis methods, as well as the provision of more accurate results than typical assessment methods through the more direct incorporation of dynamic effects.

1.4 Outline of thesis

To meet the objectives outlined above, the following approach is adopted. Having introduced the problem in this chapter, Chapter 2 conducts a review of the numerical and analytical modelling tools currently being used for the seismic analysis of masonry structures.

The framework of the new tool is then presented in Chapter 3, which focusses on the derivation of the rocking equations of motion for user-defined structural geometries directly within the CAD environment, followed by their export to and eventual solution in MATLAB. Note that the equations presented here model the interfaces between blocks as rigid - which is an assumption that will be revisited in Chapter 6. Furthermore, as a number of collapse mechanisms tend to take place above ground level, a new methodology to account for ground motion amplification effects is also proposed. Additionally, as one of the objectives of the tool is to rapidly compare different mechanisms and identify the most vulnerable one(s), an algorithm to automatically detect critical mechanisms is also introduced here.

Chapter 4 conducts an evaluation of the rigid rocking tool through comparison of the predictions of the tool with the results of experimental shake table tests, numerical simulations, and field observations from a recent earthquake. A potential application of the tool is then demonstrated in Chapter 5, by using it for the seismic analysis of a typical Italian church geometry. Both these chapters demonstrate the tool's ability to provide realistic predictions, as well as the potential effectiveness of the methodology proposed to account for ground motion amplification. Furthermore, Chapter 5 highlights the tool's capacity for rapid comparison and detection of critical collapse mechanisms.

In Chapter 6, the rigid interface assumptions are revisited through the introduction of the flexible interface model, wherein the interfaces between block macroelements are characterised by a finite stiffness and compressive strength. Modelling interfaces as non-rigid results in an inward shift of the rocking rotation points, and expressions defining these shifting rotation points are derived for different interface geometries. These shifting rotation points also result in the rocking equations of motion needing to be re-derived for the single, two and multiple-block mechanisms. However, these new equations of motion are highly non-linear, and thus to reduce computational burden, a semi-flexible interface model is also introduced, which accounts for the inward shift of the rotation points in a more simplified manner than its fully-flexible counterpart. The new analytical models are then evaluated in Chapter 7 through comparison with field observations as well as validated against the results of numerical simulations.

Finally, the tool's ability to be used for both seismic analysis and assessment is illustrated in Chapter 8, by using it to conduct a rocking dynamics-based analysis as well as a code-based seismic assessment of the walls of a historic earthen structure.

Chapter 9 summarises this work, while also highlighting the scientific contributions as well as practical applications of the research. Furthermore, future research ideas, in the form of additional theoretical and computational developments required before the tool can be disseminated for practical use, are also presented.

Chapter 2

Literature Review

2.1 Introduction

Recent earthquakes have emphasised the need to better understand the behaviour of masonry structures, both unreinforced and reinforced, under dynamic loading, and the need for better assessment tools. Typical failure of these structures generally occurs via specific collapse mechanisms, which have been well documented (D'Ayala and Speranza, 2002, 2003; PCM-DPC MiBAC, 2006) (Figs. 2.1-2.2). These mechanisms can broadly be divided into in-plane and out-of-plane mechanisms, with local or out-of-plane collapse being particularly common modes of failure, as was observed during the recent earthquakes in Amatrice, Italy (2016) (Fiorentino et al., 2017) and Nepal (2015) (Rai et al., 2016).

Analysis of these collapse mechanisms can be conducted using a range of tools, which fall into two primary categories: (1) Detailed computational analysis and (2) Simplified analytical/code-based assessment methods.

Image of typical out-of-plane collapse mechanisms of masonry walls removed for copyright reasons. Copyright holder is Prof. Dina D'Ayala.

Fig. 2.1 Typical out-of-plane collapse mechanisms of masonry walls (D'Ayala and Speranza, 2002)

Figure illustrating abacus of typical church collapse mechanisms removed for copyright reasons. Copyright holder is the Italian Ministry for Cultural Assets and Activities (MiBAC).

Fig. 2.2 Abacus of typical church collapse mechanisms (PCM-DPC MiBAC, 2006)

The computational analysis of masonry is generally conducted using numerical modelling techniques such as finite element modelling programs (FEM), which have been well-developed and are commonly used by practising engineers. However, while extensive research into the seismic response of masonry structures has been conducted using FEM, they are better suited to problems of elasticity and plasticity such as global in-plane behaviour and pushover analysis, and not overturning stability, which is often the primary concern in the case of masonry structures (DeJong, 2009) as well as the focus of this dissertation. Discrete element modelling (DEM), on the other hand, inherently captures the interaction of discrete bodies, and allows for joint contact recognition in a more efficient manner than many finite-element modelling procedures, thereby enabling masonry collapse mechanisms to be modelled with a reasonable degree of accuracy. In this dissertation, DEM will be used for comparison with existing analytical formulations as well as for validation of new analytical models. Consequently Section 2.2 of this chapter reviews the various studies conducted using DEM to model masonry structures.

The dynamic behaviour of masonry can also be captured using simplified code-based assessment methods, in addition to analytical tools such as pushover analyses, macro-element modelling, and dynamic analysis comprising the direct integration of equations of motion. Thus Section 2.3 of this chapter reviews the various analytical tools and methods developed to describe the response of masonry structures to seismic loading.

2.2 Numerical tools

Masonry structures are made up of distinct blocks separated by dry or mortared joints and thus exhibit complex behaviour, including large displacements and the opening and closing of joints, in strong seismic events. This behaviour can be modelled using either macro or micro modelling. While macro-modelling represents the intrinsic structure of masonry by using appropriate constitutive relations, and is predominantly used in practice, micro-modelling explicitly represents the individual blocks and joints and is more commonly used for research purposes, although its applicability to real structures is also increasing (Lemos, 2007).

While finite element models are generally used for the macro-modelling of masonry, they can also be used for micro-modelling if they feature joint or interface elements. However, discrete element models are not only more computationally efficient than their finite element counterparts, but are also more applicable to problems of stability or in cases where structures fail by mechanisms, as they allow large displacements and full separation between blocks, as well as automatic contact detection and updates (Lemos, 2007).

The other features that distinguish discrete element models from finite element models include the assumption of rigid blocks with system deformability concentrated in the joints (although deformable blocks, where blocks are discretized into finite element meshes are also allowed), as well as the use of contacts to represent block interaction (Lemos, 2007). These contacts can be modelled as either rigid (no overlap between blocks) or deformable (small overlap between blocks in compression). In the case of deformable contacts, the permitted overlap size is defined in terms of the normal and shear contact stiffness (Lemos, 2007). The solution of the equations of motion of the system is carried out using an explicit time-stepping algorithm, and an example of the calculation cycle for one DEM program (3DEC (Itasca Consulting Group, 2007a)) is illustrated by Fig. 2.3.

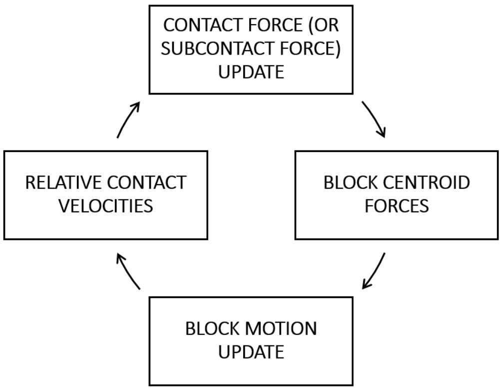

Fig. 2.3 Cycle of mechanical calculations in 3DEC (Itasca Consulting Group, 2007b)

Numerous discrete element formulations can be used in the analysis of masonry structures, and are broadly divided into the following categories: discrete/distinct element models, discrete-finite elements, discontinuous deformation analysis (DDA), and rigid block analysis and limit equilibrium methods. Discrete-finite elements are primarily used for problems of fracture mechanics, while the use of DDA is limited to cases where contacts are assumed to be rigid and blocks are assumed to be in a state of uniform strain and stress (Lemos, 2007). Similarly, the use of rigid block analysis and limit equilibrium methods is based on plasticity concepts developed by Heyman (1995) and is predominantly used to determine collapse loads and is, as the name suggests, limited to rigid blocks.

Discrete/distinct element models (DEM), on the other hand, allow blocks to be modelled as either rigid or deformable, and use deformable contacts. Furthermore, distinct element codes such as the Universal Distinct Element Code (UDEC, for 2D problems) and the 3 Dimensional Distinct Element Code (3DEC, for 3D problems) not only allow collapse conditions to be determined, but also enable the dynamic behaviour of the structure to observed until complete collapse (Cundall, 1988; Hart et al., 1988). These two programs also perform automatic contact detection and update, and enable structural reinforcement to be modelled in the form of cable and beam elements.

The suitability of DEM for modelling both the static and dynamic behaviour of masonry structures has been demonstrated through several studies, with the tested structures comprising both unreinforced (Bui and Limam, 2012; de Felice and Giannini, 2000; Mendes et al., 2017) and retrofitted (Alexandris et al., 2004; Zhuge, 2008) masonry walls, 3-wall assemblages (Lemos and Campos Costa, 2017), free-standing columns (Papantonopoulos et al., 2002; Papastamatiou and Psycharis, 1993) and column-lintel configurations (Psycharis et al., 2003), arches (Azevedo et al., 2000; De Lorenzis et al., 2007;

Dimitri et al., 2011; Lemos, 1998; Mehrotra et al., 2015; Mirabella-Roberti and Calvetti, 1998) and aqueducts (Azevedo et al., 2000; Drei and Oliveira, 2001). DEM was also used for the seismic assessment of structures such as bell towers (Azevedo and Sincraian, 2001; Azevedo et al., 2000), a lighthouse (Oliveira et al., 2002) and stone spires (DeJong and Vibert, 2012a), while its ability to realistically model irregular masonry walls was demonstrated by studies conducted by Mirabella-Roberti and Spina (2001) and de Felice (2011).

However numerical methods like DEM are sensitive to input parameters such as damping and joint properties, and can be both time-consuming and computationally expensive (de Felice et al., 2017), particularly when trying to model collapse. As an alternative, both non-linear static and dynamic analysis tools have been developed to analytically model these collapse mechanisms, which are based on the assumption of rigid body behaviour of the masonry macro-elements. While such an approach enables faster assessment and depends on fewer variables than its numerical counterpart, it also requires explicit definition of the collapse mechanisms, which depends in turn on user experience and engineering judgement (de Felice et al., 2017).

2.3 Analytical models and tools

Modern codes such as Eurocode 8 (EN 1998-1, 2004) and ASCE-FEMA (Applied Technology Council (ATC), 2000) consider the following four methods of structural analysis for the seismic assessment of buildings: linear static, linear dynamic, non-linear static and non-linear dynamic (Magenes, 2006). Although linear analysis tools and software are more commonly used by practising engineers, they are over-conservative in their solutions and cannot fully capture the non-linear behaviour of masonry (Magenes, 2006), and thus shall not be reviewed in this section. Furthermore, while detailed computational models used for the non-linear analysis of masonry (e.g. DEM as discussed in Section 2.2) could also be used for (non-linear) assessment, they can be computationally demanding and time-consuming and as such are not entirely feasible for day-to-day use by practising engineers. Thus the focus of this section shall be on simplified analytical/computational assessment/design methods which capture the non-linear behaviour of masonry in a computationally efficient and rapid manner.

These methods can be further divided into the following two aspects – local mechanisms, which generally comprise the out-of-plane response of the individual structural elements, and global mechanisms, which involve the in-plane response of walls (Magenes, 2006). However, during an earthquake, both local and global mechanisms are activated simultaneously, and it is upon the prevention of local out-of-plane collapse that global in-plane mechanisms are allowed to develop (Magenes, 2006). The main tools that currently exist for the non-linear analysis of masonry structures are summarized in Table 2.1, and shall be discussed in greater depth in this section.

Table 2.1 Non-linear analytical and computational assessment and design methods

	Static	Dynamic
Global	(a) POR method (b) Equivalent frame models: - Simplified Analysis of Masonry - SSWP, WSSP	(a) TREMURI (b) Macro-element models
Local	(a) Code-based methods: - Italian Building Code - ASCE 43-05 (b) FaMIVE procedure (c) MB_PERPETUATE (d) *MeBaSe* procedure	(a) Modified macro-element model (b) Classical rocking theory

2.3.1 Code-based assessment methods

Most damage to masonry buildings under seismic action is due to local mechanisms in the form of out-of-plane damage and collapse. Furthermore, as was previously mentioned, global mechanisms are only allowed to develop if out-of-plane or local collapse is prevented. Thus, the assessment of local mechanisms was made mandatory by the Italian Building Code (DMI, 2008), which proposed the use of rigid-body limit analysis to assess the behaviour of masonry structures, through the performance of either a strength-based or displacement-based safety check.

In the case of the strength-based check, a maximum allowable peak ground acceleration (PGA) to prevent collapse is determined, which is usually equal to the ground acceleration required to activate the mechanism, multiplied by a safety/behaviour factor q (typically equal to 2) (Shawa et al. (2012), DeJong (2014)). In the case of the displacement-based check, the displacement capacity d_u* is first defined, which is equal to 40% of the displacement which would cause the actual structure/mechanism to overturn. This displacement is then used to determine the effective secant period of the mechanism (calculated at 40% of d_u*), which in turn is used to evaluate the corresponding displacement demand Δ_d from the linear-elastic response spectrum (Shawa et al. (2012), DeJong (2014)).

Linear-elastic response spectra are also used in ASCE 43-05 (2007) to calculate a "best estimate" for the maximum rocking response of the structure/mechanism (DeJong, 2014). In this case, a maximum rocking rotation rather than displacement is specified, which is used to determine the spectral acceleration capacity $S_{a,CAP}$. The equivalent natural period T_n of the linear-elastic oscillator is then determined by equating the potential energy of the oscillator to that of the mechanism at the maximum rocking angle - which in turn is used to extract the spectral acceleration demand $S_{a,DEM}$ from the linear-elastic spectral design chart (scaled to a PGA = 1g) (DeJong, 2014).

However, due to their relative simplicity, code-based methods tend to disregard certain features of the motion of the structure, such as the evolution of the system over time and the energy dissipation (Giresini et al., 2015). Consequently, the results of the analysis, as found using the code-based approach, tend to be over-conservative - as was observed for the case-study of the altar of the Beata Vergine Annunziata church, where the predictions obtained using the Italian code were found to be more conservative than those obtained using classical rocking theory (Giresini et al., 2015).

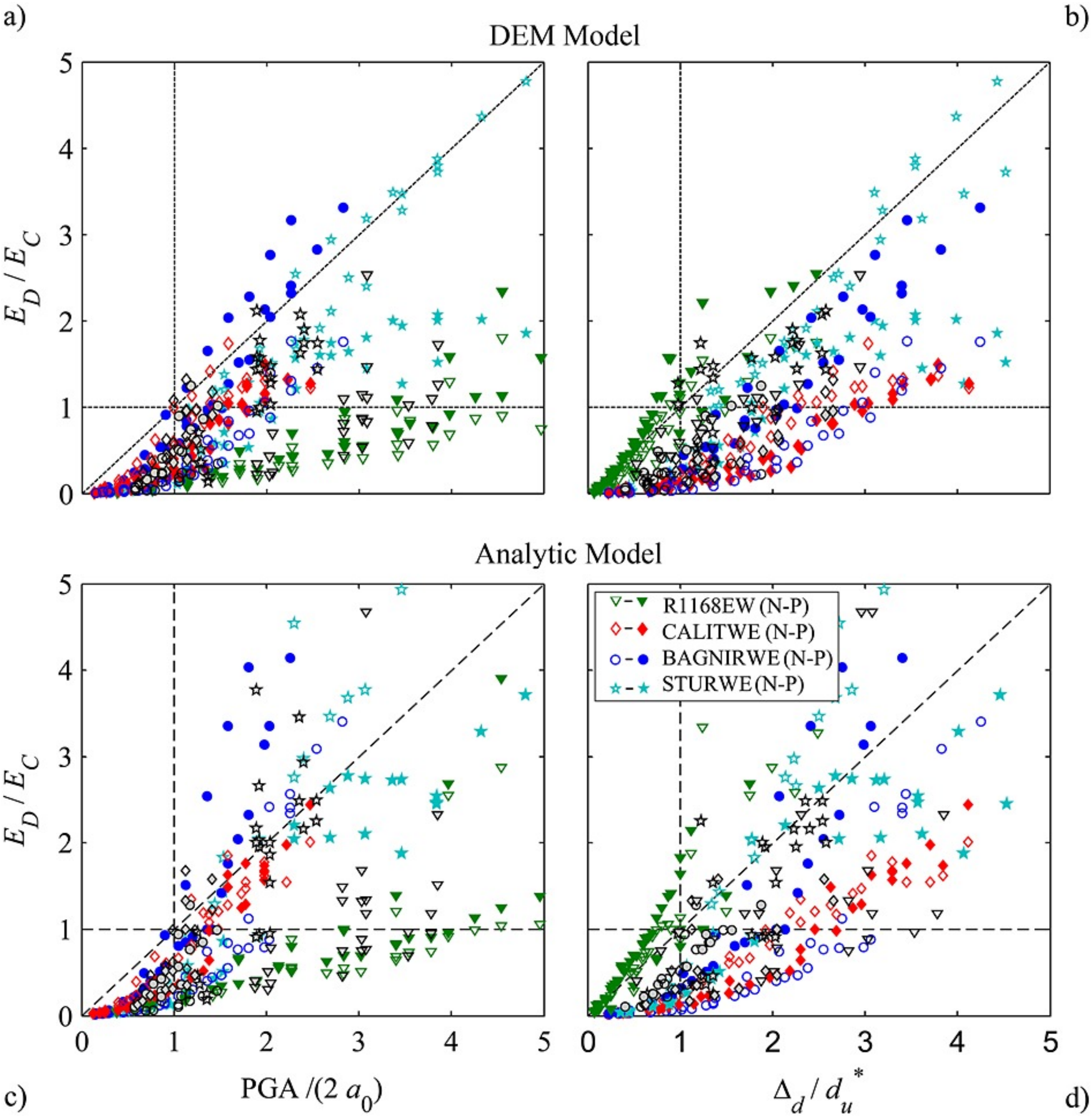

Fig. 2.4 Comparison of the predictions obtained using the strength-based (a, c) and displacement-based (b, d) procedures of the Italian Building Code with those obtained using DEM (a, b) and analytical (c, d) modelling, as found in Shawa et al. (2012)

Similar trends were also observed by Shawa et al. (2012), where a comparison of the predictions obtained using both Italian code-based procedures with those obtained using analytical modelling as well as DEM for a set of masonry walls with varying geometries revealed a significant scatter in the results (Fig. 2.4). The predictions of the analyses were compared in terms of demand/capacity ratios, which in the case of the Italian strength-based procedure was the ratio of the PGA to the ground acceleration a_0 required to activate the mechanism (multiplied by the safety/behaviour factor of 2), while in the case of the displacement-based procedure was the ratio of the spectral displacement Δ_d to the displacement capacity d_u*. In the case of the numerical (DEM) and analytical models, the demand/capacity ratios were evaluated in terms of the potential energy of the walls, with the capacity E_C being defined as the maximum potential energy of the wall - attained when the structure is at the unstable equilibrium configuration (i.e. at the point of overturning), while the demand E_D was the defined as the maximum potential energy recorded during the motion of the wall (in the case where the wall does not overturn) or the sum of the potential and kinetic energies evaluated at the point of overturning (when the wall does overturn). For all four methods, collapse occurs when the demand/capacity ratio exceeds 1. From this comparison, and as Fig. 2.4 illustrates, the code strength-based and displacement-based procedures were found to be conservative in 99% and 90% of the cases respectively.

One potential drawback of these over-conservative methods is that they could lead to expensive and sometimes unnecessary retrofitting solutions, which in the case of historical masonry structures could also detract from their cultural value (Giresini et al., 2015).

2.3.2 Non-linear static analysis tools

Local Mechanisms

In addition to code-based methods, static-equivalent pushover analysis of local collapse mechanisms can also be conducted using the FaMIVE procedure, which uses a failure mechanisms approach to analyse seismic vulnerability (D'Ayala, 2005). In the case of complex structures, where a number of possible collapse mechanisms could occur, the procedure first calculates the collapse load factor λ_i for each mechanism, before identifying the most vulnerable one, with a displacement-based vulnerability analysis ultimately being conducted of the critical mechanism. The reduction in vulnerability due to various strengthening interventions is also factored into this approach when predicting the most probable damage modes and vulnerability levels of the structure (D'Ayala, 2005; D'Ayala and Speranza, 2002).

Non-linear static-equivalent analysis of local collapse mechanisms can also be performed using software such as MB_PERPETUATE (Lagomarsino and Ottonelli, 2012), which makes use of incremental kinematic analysis to generate a pushover curve for a given mechanism (Lagomarsino, 2015). Similar to the FaMIVE procedure, a displacement-based vulnerability analysis is then conducted, with the corresponding seismic demand being defined through an over-damped Acceleration-Displacement Response Spectrum (ADRS), which also accounts for the filtering effect of the structure, and in the case of mechanisms taking place at a height above ground level - amplification of the ground motion (Lagomarsino, 2015).

Alternatively, the *MeBaSe* procedure proposed by Restrepo-Vélez (2004) could be used instead. Building on the work of D'Ayala and Speranza (2003), and based on the results of experimental static tests on dry stone masonry walls (Restrepo-Vélez et al., 2014), new equations for the collapse load multiplier λ_i are proposed, in order to better fit the experimental data (Restrepo-Vélez, 2004). Upon the identification of the most probable out-of-plane failure mechanism, a displacement-based assessment of seismic vulnerability is then conducted through the definition of limit state functions for the period T_{LS} and displacement (i.e. capacity) Δ_{LS}. However, unlike the FaMIVE procedure and MB_PERPETUATE, which use ADRS to determine seismic demand, the demand in this case is determined using elastic displacement response spectra, with the corresponding displacement demand being evaluated at the limit state period T_{LS} of the mechanism.

Global Mechanisms

A simplified non-linear static (pushover) assessment method (POR) that could be applied to global analysis of masonry buildings was first developed by Tomazevic (1978). This method was based on the storey-mechanism approach, whereby separate non-linear inter-storey shear-displacement analysis was conducted for each storey, with each connecting pier being characterized by an idealized non-linear (bilinear) shear-displacement curve (Magenes, 2006). Although this method is widely used due to its introduction into the Italian code, its application is restricted to certain classes and sizes of buildings (Magenes, 2006).

The storey-mechanism approach was extended by Magenes (2000) using an equivalent frame idealization, in which the resisting masonry walls were subdivided into macro-elements comprising deformable masonry panels - where the deformation and non-linear response were concentrated, and rigid portions which connected the deformable sections (Lagomarsino et al., 2013). The limited number of degrees of freedom and corresponding low computational burden make this method, also known as SAM or Simplified Analysis of Masonry, attractive to practitioners, and it can now be found in both Eurocode 8 and the Italian building code (DMI, 2008; EC (Eurocode) 8, 2004; Lagomarsino et al., 2013; Magenes, 2000).

In addition to the equivalent frame model, masonry walls can also be idealized using simplified models such as the strong spandrels-weak piers model (SSWP) which is based on the assumption that the piers crack first, and the weak spandrels-strong piers model (WSSP), which assumes that the spandrels have null strength and stiffness (Lagomarsino et al., 2013). SSWP and WSSP models are both recommended by FEMA guidelines (Applied Technology Council (ATC), 1998, 2000), while the SSWP model is also consistent with Tomazevic's POR method (Tomazevic, 1978). The Italian building code assumes the WSSP scheme for simple cantilever models, while the SSWP scheme (storey mechanism) is no longer allowed for multi-storey buildings (DMI, 2008).

2.3.3 Non-linear dynamic analysis tools

Macroelements

The equivalent-frame formulation was further developed by Lagomarsino et al. (2013) to allow for both the static and dynamic global analysis of entire buildings in the form of the following procedures: incremental static with force or displacement control, 3D pushover analysis with fixed and adaptive load pattern, and 3D time-history dynamic analysis (Newmark integration, Rayleigh viscous damping). However, this method, which is also implemented in the TREMURI program, is limited to the in-plane response of walls (Penna et al., 2015).

Penna et al. (2014) extended the non-linear macroelement modelling technique to represent two main in-plane masonry failure modes: bending-rocking and shear-sliding (Penna et al., 2015). This model also accounts for the effect of crushing, but like TREMURI is limited to in-plane action.

Consequently, macro-elements were further developed by Penna and Galasco (2013) and Penna et al. (2015) to account for second order effects, thereby allowing local/out-of-plane failure modes to also be simulated. The modified macro-element model was validated by comparing the dynamic solution for overturning of a rigid block to that obtained using classical rocking theory (Housner, 1963; Penna et al., 2015). Further analytical validation was carried out by comparing the model solution to that reported by Sahlin (1971) for an eccentrically loaded column.

The modified macro-element model was also validated against two sets of experimental results – the first being an evaluation of the out-of-plane response of stone masonry walls (Costa et al., 2014) and the second comprising a cyclic test on a triumphal arch with a steel tie-rod (Preti et al., 2013). In both cases the model was found to be capable of satisfactorily reproducing the response in terms of the force-displacement curves, and in the case of the arch, was even able to identify the formation of hinges (Penna et al., 2015).

However, this modified macro-element model is still fairly new, and as such is limited to simple rocking systems (Penna et al., 2015). Thus in order to study more complex systems, classical rocking theory as first developed by Housner and advanced by several others since, could also be used.

Classical rocking theory

Classical rocking theory provides the basis to assess collapse mechanisms and has been used to derive equations of motion for several structural typologies starting from the basic rocking block, which could be used to model façade overturning, to more complex structures such as arches and asymmetric rocking frames, which could be used to model the dynamic response of monumental masonry structures such as triumphal arches, aqueducts, and column and lintel configurations.

Single block mechanism

Early work on rocking (Housner, 1963) derived equations of motion for a single rigid block rocking on a horizontal rigid base. The relevant geometric properties of the block, which are included in the

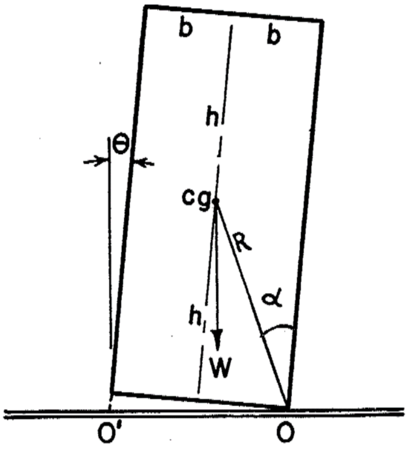

Fig. 2.5 Geometry of the rocking block as found in Housner (1963)

equation of motion, include the moment of inertia about the axis of rotation I_O, the weight of the block W, the distance R between the centre of gravity and the axis of rotation O, as well as α, which corresponds to the slenderness of the block (Fig. 2.5). Upon being subjected to a horizontal ground acceleration $\ddot{u}_g$, moment equilibrium about the axis of rotation O yields the following equation of motion:

$$I_O\ddot{\theta} + WR\sin(\alpha - \theta) = -WR\frac{\ddot{u}_g}{g}\cos(\alpha - \theta) \tag{2.1}$$

Assuming the block is tall and slender, that is, α is generally less than 20°, small angle approximation can be used to linearise Equation 2.1, resulting in it assuming the following form:

$$I_O\ddot{\theta} + WR(\alpha - \theta) = -WR\frac{\ddot{u}_g}{g} \tag{2.2}$$

Setting $WR/I_O = p^2$, Equation 2.2 can then be simplified and re-written as:

$$\ddot{\theta} = p^2\left(\theta - \alpha - \frac{\ddot{u}_g}{g}\right) \tag{2.3}$$

where p corresponds to the rocking frequency parameter. Energy dissipation at base impact is also accounted for by means of a coefficient of restitution η, which is derived by assuming inelastic impact (no bouncing) and conservation of angular momentum.

This model was then used to investigate the response of the block to rectangular and sinusoidal acceleration impulses, and to derive a relationship between block size, slenderness, impulse amplitude and duration required to cause overturning (Housner, 1963).

Building on Housner's work, Spanos and Koh (1984) and Zhang and Makris (2001) studied the rocking response of rigid blocks to harmonic motion. However, while Spanos and Koh (1984) examined long-duration motion, Zhang and Makris (2001) focussed instead on pulse-type excitations, which were found to better represent near-source ground motions (Campillo et al., 1989; Iwan and Chen, 1994; Makris and Roussos, 1998).

To investigate the response of typical unreinforced masonry façades to seismic action, Sorrentino et al. (2008a) developed a dynamic analytical model to describe one-sided rocking. Comparison of the analytical results to those from the code-based assessment procedures showed the latter to be overly conservative, thereby indicating that retrofitting of historical structures could occasionally be unnecessary (Sorrentino et al., 2008a). Furthermore, to account for the additional energy dissipated by the impact of the façade with the transverse walls (in addition to base impact), an analytical expression for the coefficient of restitution was also proposed (Sorrentino et al., 2011).

One-sided rocking was further studied by Shawa et al. (2012) through an experimental, numerical and analytical investigation into the seismic response of the façade of a U-shaped unreinforced masonry assemblage. Comparison of the numerical (UDEC) and analytical results with their experimental counterparts showed a reasonable agreement between both sets in terms of both entire time histories and maximum rotations.

DeJong (2012b) extended rocking theory to apply to other geometries such as stone spires in the form of rigid conical shells, and derived the rocking parameters and consequently equations of motion to describe the response of these structures to horizontal base motion. These equations were then used to predict the dynamic response in the form of collapse envelopes for both cracked and un-cracked spires subjected to impulse base motion. The model was also used to evaluate the observed damage to the spires of the Lion's Walk Congregational Church in the United Kingdom, as well as the Christchurch Cathedral in New Zealand.

Two block mechanism

In addition to cracked spires, rocking theory can also be used to model cracked wall sections. Doherty et al. (2002) demonstrated that a cracked unreinforced masonry (URM) wall that undergoes rocking with considerable horizontal displacements can be idealized as a single-degree-of-freedom (SDOF) system in the form of rigid blocks separated by fully cracked cross-sections. However, this idealization only holds true for cantilever (parapet) and simply-supported walls (Doherty et al., 2002).

The dynamic behaviour of simply-supported walls was further investigated by Sorrentino et al. (2008b), with analytical formulations being proposed for both the intermediate hinge height (which depends on the superimposed load applied to the wall as well as the tensile strength of the mortar) and the coefficient of restitution. From these investigations it was found that the addition of a top restraint has a beneficial influence on the dynamic behaviour of the wall as it not only increases the threshold acceleration required for rocking to occur, but also results in greater energy dissipation than in a cantilever (parapet) wall of equal shape and size (Sorrentino et al., 2008b).

The dynamic response of two block mechanisms was also investigated by Psycharis (1990) whereby equations of motion were derived for systems comprising two symmetrically stacked blocks of different sizes - which could represent a piece of machinery, a statue, or any object placed atop a rigid base. Four different patterns of response and impact were analysed, with the equation of motion and corresponding coefficient of restitution (assuming conservation of angular momentum) being derived separately for each mode of response. Based on this work, Spanos et al. (2001) developed a more generalized model whereby non-linear equations of motion were derived for the stacked two-block system.

Multiple block mechanisms

Allen and Bielaks (1986) analytically modelled multiple-block rigid body systems by using a relatively simple model of a displaced two-storey 2DOF frame structure. Generalized equations of motion were derived to predict the response of the system to specific ground motions, with several simplifications - crushing was ignored, and no sliding, a rigid foundation, and energy dissipation upon impact alone were assumed. The equations were also linearised by making use of the small angle assumption and neglecting higher order (Coriolis) effects.

Extending the work of Allen and Bielaks (1986), Oppenheim (1992) analytically modelled the dynamic response of a masonry arch under impulse base motion. The kinematics of the arch assumes the form of a four-link rigid body mechanism with one degree of freedom in the form of the rotation θ of the end segment of the arch, upon which the rotation of the other arch segments are dependent (Oppenheim, 1992).

The masonry arch studied by Oppenheim (1992) was also analysed analytically using rigid body dynamics and numerically using DEM in UDEC, by DeJong and Ochsendorf (2006). Using Oppenheim's assumptions of constant hinge locations, no sliding, and an impulse ground motion, the analytical and numerical results were found to compare extraordinarily well. However, upon extending the numerical analysis, it was observed that critical collapse occurs during the second half-cycle of oscillation and that the hinge locations change continuously. Still assuming no sliding, failure would actually occur in a much shorter time for the same acceleration impulse, thus indicating that Oppenheim's method is actually un-conservative (DeJong and Ochsendorf, 2006).

Furthermore, the mechanism studied by Oppenheim (1992) is just one of several existing mechanisms, each with their own set of hinge locations, thus Clemente (1998) proposed an iterative procedure to determine the mechanism for a given arch. However, Clemente's analysis is still an approximation of the dynamic response of the stone arch, as it neglects the effect of impacts between adjacent blocks, which causes energy dissipation and consequently changes in the response of the structure (Clemente, 1998).

This impact problem was addressed analytically by De Lorenzis et al. (2007), albeit with simplifying assumptions such as constant hinge locations, unvarying position of the system during impact, occurrence of impact at the hinge sections, and location of the impulsive force on the opposite side of the hinge across the arch thickness. The resulting impact model thus does not account for complex behaviour such as sliding, slide-rocking or bouncing, but it does allow the equivalent coefficient of restitution to be estimated using conservation of angular momentum. This coefficient allows the impact to be described and is dependent only on the initial geometry of the arch (De Lorenzis et al., 2007). The results of this analysis were also found to be in good agreement with their numerical counterparts obtained using DEM.

These analytical and numerical models were also confirmed by the experimental tests conducted by DeJong et al. (2008), in which five different earthquake time histories and harmonic base excitations were applied to two different arch geometries. The formation of alternating four-hinge mechanisms and governance of rocking-type failure during these tests indicated that the assumptions made in the analytical model were both reasonable and effective (DeJong and Dimitrakopoulos, 2012).

Unifying theory with practice

Despite being fairly well-developed, rocking theory is not often implemented in codes of practice, as it can be rather complex. In order to make rocking theory more applicable and thus unify it with the codes of practice, simplified methods need to be developed to quickly predict the dynamic (rocking) response of structures subjected to seismic action.

Building on Housner's work, closed-form solutions were derived by Dimitrakopoulos and DeJong (2012) for the equation of motion for the rocking block when subjected to cycloidal pulses, with analytical equations being provided for non-dimensional overturning plots so that the response of the block to any pulse-type excitation could be easily predicted, needing only to be scaled by the amplitude and frequency of the excitation.

In addition to overturning plots, rocking response spectra, comparable to linear elastic response spectra but derived from the SDOF rocking block, could also be used to predict the dynamic response of these structures to seismic excitation. The use of these spectra was first studied by Makris and Zhang (1999) and Makris and Konstantinidis (2001), who derived relationships between size, slenderness and overall stability. Further investigations by DeJong and Dimitrakopoulos (2012) into the use of rocking spectra to capture the response of complex structures found that different rocking systems could be defined by the same four parameters used for the single rocking block: the rocking frequency parameter p, the critical rotation α, the coefficient of restitution η, and the uplift parameter λ, all of which depend solely on the geometry of the structure. Examples of systems which exhibit direct dynamic equivalence with the single block include SDOF systems such as a point mass supported by a rigid strut, a masonry spire, as well as a symmetric rocking frame, with the latter exhibiting local dynamic equivalence with the single block, assuming that sliding or bouncing do not occur (DeJong and Dimitrakopoulos, 2014).

In the case of more complicated multiple block mechanisms such as two and three block structures as well as the masonry arch and asymmetric frame, local equivalence with the rocking block can be derived at the point of unstable equilibrium ($\phi = \phi_{cr}$), and the equation of motion can be linearised about this point (DeJong and Dimitrakopoulos, 2014). The errors introduced by this linearisation are found to be dependent on the geometry and kinematics of the mechanism, but are, for the most part, acceptable (DeJong and Dimitrakopoulos, 2014).

Nevertheless, this method only allows the approximate magnitude of global rocking response to be determined, and not the exact displacements (DeJong and Dimitrakopoulos, 2014). However, it is a useful means of rapidly predicting the seismic response of a complex structure as it circumvents the need for solving complicated equations of motion.

This method was extended by Mauro et al. (2015) to predict and directly compare the relative dynamic resilience of the various out-of-plane collapse mechanisms of masonry façades, specifically examining the cases of one-sided rocking mechanisms of walls bearing loads from floors and additional applied forces, and multiple block mechanisms in the form of a generalized two block mechanism. Using this method, comparisons can then be made between the various possible mechanisms by using a single equation of motion to derive the overturning envelopes for each mechanism. This method can also be used to compare the relative effectiveness of various retrofit solutions.

Beyond the rigid model

Most of the formulations considered in the literature thus far have been extensions of the Housner (1963) model, which assumes the blocks have infinite stiffness until the onset of rocking motion. In reality, masonry structures have been found to exhibit small deformations before rocking initiates, due in part to elastic deformability as well as the progressive formation of hinges (Lagomarsino, 2015). This behaviour has been observed both experimentally in static push tests conducted on unreinforced brick masonry walls (Doherty et al., 2000; Griffith et al., 2004), as well as numerically as a result of discrete element analyses conducted on a set of real masonry wall sections (de Felice, 2011). The force-displacement curves obtained from both the experimental and numerical campaigns (Fig. 2.6) have been found to exhibit an initial elastic branch (positive stiffness) before rocking initiates.

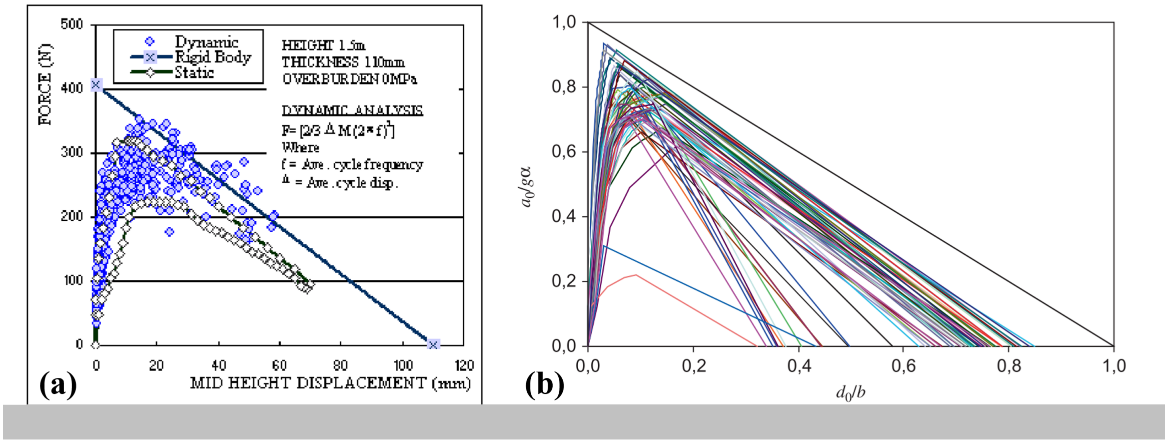

Fig. 2.6 (a) Experimentally (Doherty et al., 2000) and (b) numerically obtained (de Felice, 2011) force-displacement curves

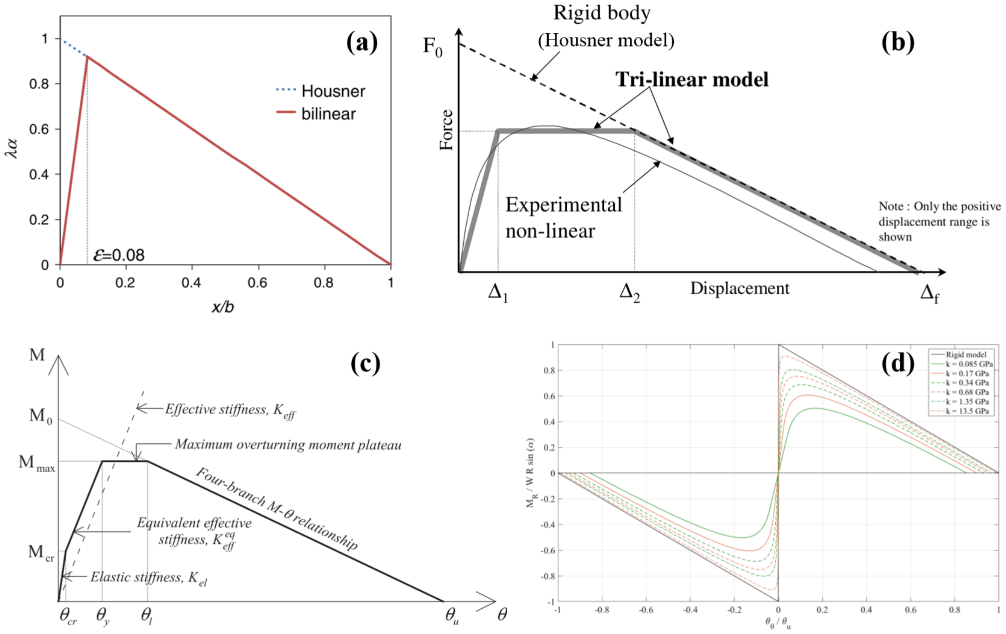

Fig. 2.7 (a) Bilinear (Lagomarsino, 2015) (Reprinted by permission from Springer Nature), (b) trilinear (Doherty et al., 2002), (c) four-branch (Ferreira et al., 2015) and (d) smooth (Lipo and de Felice, 2016) models

.

Furthermore, factors such as geometrical imperfections, non-rigid interfaces and disaggregation of multi-leaf wall sections due to poor transverse bonds between leaves have been found to contribute to the reduction in the strength and displacement capacity of the masonry sections (de Felice, 2011) - resulting in the structures having an overall lower dynamic capacity than the purely rigid (Housner) model. In fact, experimental tests conducted by ElGawady et al. (2011) using concrete, timber, rubber and steel joints demonstrated that the interface material tends to have a substantial influence on the free rocking response of rigid blocks. Similarly, numerical analyses conducted by de Felice (2011) on 30 real wall sections found the resulting capacity curves to always be lower than the Housner model, with an average reduction in both strength and displacement capacity of 25% and 35% respectively.

Several simplified analytical representations have been proposed for these more realistic force-displacement curves - including a bilinear (Lagomarsino, 2015) (Fig. 2.7a), trilinear (Doherty et al., 2002) (Fig. 2.7b) and four-branch (Ferreira et al., 2015) (Fig. 2.7c) model. Alternatively, a smooth force-displacement curve (Fig. 2.7d) can be obtained by modelling the structure as a rigid block resting on a flexible Winkler-type foundation (Lipo and de Felice, 2016, 2017), wherein the interface is modelled as a set of springs characterised by a normal stiffness k_n.

While most of the analytical studies previously conducted on these flexible interfaces assume pure elastic behaviour (Koh et al., 1986; Lipo and de Felice, 2016, 2017; Psycharis and Jennings, 1983; Shawa et al., 2012), recent work by Roh and Reinhorn (2009), Costa (2012); Costa et al. (2013) and

(Penna and Galasco, 2013) assume a bilinear elastic representation of the compressive behaviour of the interface, and thus also account for crushing effects. Nevertheless, in both cases the (non-linear) rocking equation of motion (Equation 2.1) now includes an additional term $a_f(\theta)$ which accounts for the moment due to the reaction from the elastic/elasto-plastic joint, and is a function of the rotation θ of the structure, as illustrated by Equation 2.4:

$$I_{O'}(\theta)\ddot{\theta} + WR\sin(\alpha - \theta) = -WR\frac{\ddot{u}_g}{g}\cos(\alpha - \theta) + Wa_f(\theta) \tag{2.4}$$

Note that the equation of motion now also depends on the moment of inertia $I_{O'}(\theta)$, which is no longer constant and is now determined relative to the inwardly-shifted rocking rotation point *O'*, which is also the point at which the reaction force from the interface acts. Note that the location of this point is given by $a_f(\theta)$, and that it varies based on the rotation of the structure (Costa, 2012).

2.4 Summary

In this chapter, the various numerical and analytical models and tools currently being used for the analysis of masonry collapse mechanisms are examined. The objective of this literature review is to identify what has been done, and to determine where progress still needs to be made. The main conclusions are as follows:

- The use of numerical models such as finite element analyses and discrete element methods (DEM) for the seismic assessment of masonry can be computationally-expensive and time-consuming, especially if the objective is to model collapse. However, DEM in particular has been proven to effectively capture the response of masonry structures to seismic action and could serve as a valuable tool for the validation of simpler analytical models. In Chapters 4 and 7, DEM simulations in 3DEC are thus used to evaluate simplifications made in the proposed analytical models and validate them for practical use.

- A substantial amount of progress has been made with respect to the analytical modelling of masonry collapse mechanisms using non-linear static and dynamic analysis methods. Moreover, efforts have also been made to simplify these models so that they can be easily implemented in practice. Currently, static limit analysis methods, combined with linear elastic dynamic response are the basis for assessment, while the non-linear dynamics of rocking are typically not considered. In the case of non-linear dynamic analysis, much progress has been made using classical rocking theory, with the resulting simplified models exhibiting a dependence on four rocking parameters which are all functions of the geometry of the structure. However, the work done so far is limited to simple structural geometries. Thus in Chapter 3, a new analytical modelling tool is presented whereby the rocking parameters defining the equation of motion can be derived for any user-defined structural geometry, using as a starting point a 3D CAD drawing (or laser scan) of the structure, thereby extending the application of this simplified method.

The predictions of this new tool are evaluated in Chapter 4, while potential applications are demonstrated in Chapters 5 and 8.

- Most of the equations of motion derived in the literature thus far have been based on classical rocking theory, which assumes that the blocks have an infinite stiffness before rocking initiates, and that the interfaces between blocks are entirely rigid. However, the results of experimental and numerical campaigns have demonstrated that masonry structures exhibit small deformations before rocking initiates, due in part to elastic deformability as well as the progressive formation of hinges, while factors such as geometrical imperfections, non-rigid interfaces and disaggregation of multi-leaf wall sections due to poor transverse bonds between leaves further contribute to reductions in their strength and displacement capacities. While equations of motion have been derived to account for the reduction in dynamic capacity due to the inward shift of the rocking rotation point, these formulations have been limited to single block mechanisms with solid rectangular interfaces. Thus in Chapter 6 the rocking equation of motion is re-derived for the single, two and multiple-block mechanisms to account for the inward shift of the rotation points for different interface geometries, and these modified equations of motion are implemented within the framework of the new analytical modelling tool. Studies validating the use of these new equations of motion are presented in Chapter 7.
- Finally, the potential of the tool to be used for both seismic analysis and assessment is demonstrated in Chapter 8.

The main contributions of this dissertation are summarised in Table 2.2, while the primary previous work upon which they build is also cited.

Table 2.2 Main contributions and primary previous work they build upon

Contribution	Primary Previous Work	Chapters
Rocking equations of motion for user-defined structural geometries	Housner (1963) DeJong and Dimitrakopoulos (2014) Mauro et al. (2015)	3, 4, 5
Ground motion amplification effects	Priestley (1985)	3, 4, 5
Critical mechanism detection	-	3, 4, 5
Flexible & semiflexible interface models	Costa (2012)	6, 7

Chapter 3

Framework of the new tool

3.1 Introduction

Much progress has been made with respect to the non-linear dynamic analysis of masonry collapse mechanisms. In addition to the rigid rocking block (Housner, 1963), equations of motion have also been derived for structures with more realistic geometries such as masonry spires (DeJong, 2012b), as well as for mechanisms involving multiple elements in the kinematic chain such as cracked wall sections (modelled as a two block mechanism) (Doherty et al., 2002; Mauro et al., 2015; Sorrentino et al., 2008b), arches (De Lorenzis et al., 2007), symmetric portal frames (Allen and Bielaks, 1986; Makris and Vassiliou, 2013), and asymmetric portal frames (DeJong and Dimitrakopoulos, 2014). In the case of simpler mechanisms such as the spire and symmetric portal frame, direct dynamic equivalence has been exhibited with the single rocking block, while the dynamic response of the more complicated multi-block mechanisms can be approximated by linearising the equations of motion about the point of unstable equilibrium (DeJong and Dimitrakopoulos, 2014). Furthermore, equations of motion have also been derived for structures such as façades, which are often subjected to external loads in the form of additional masses from floors/beams/roofs as well as thrusts from vaults and tie-bar reactions, which were approximated as static forces (Mauro et al., 2015).

However, derivation of these equations of motion can be fairly cumbersome and time-consuming, especially in the case of structures which have complicated geometries or mechanisms which involve multiple elements in the kinematic chain. To this end, a new tool has been developed which makes use of digital drawings of masonry structures in a typical CAD software (in this case Rhino (Robert McNeel & Associates, 2014)) to directly generate the relevant equations of motion for user-specified collapse mechanisms, which are defined based on factors such as quality and texture of the masonry, presence of openings, quality of connections at corners etc. The equations of motion are then exported to MATLAB where they can be solved for single sinusoidal pulse-type excitations, which in turn are used to generate overturning plots which predict whether or not the structure will overturn for pulses of varying frequencies and amplitudes. These plots are particularly useful for comparing the relative dynamic resilience of different collapse mechanisms, as well as the potential effectiveness of retrofitting solutions. Alternatively, a full time-history analysis can also be conducted, whereby the equations of motion are solved in order to predict the response of the structure to real earthquake ground motion records. A flowchart illustrating the functioning of the tool can be found in Fig. 3.1.

This chapter aims to outline the core essence of this tool, and will focus on the derivation of the equations of motion for the different mechanisms using Rhinoscript – which is one of the main contributions of the tool, as well as their solution in MATLAB. New developments including a methodology to account for amplification effects in the structure, as well as automatic detection of critical mechanisms, will also be discussed.

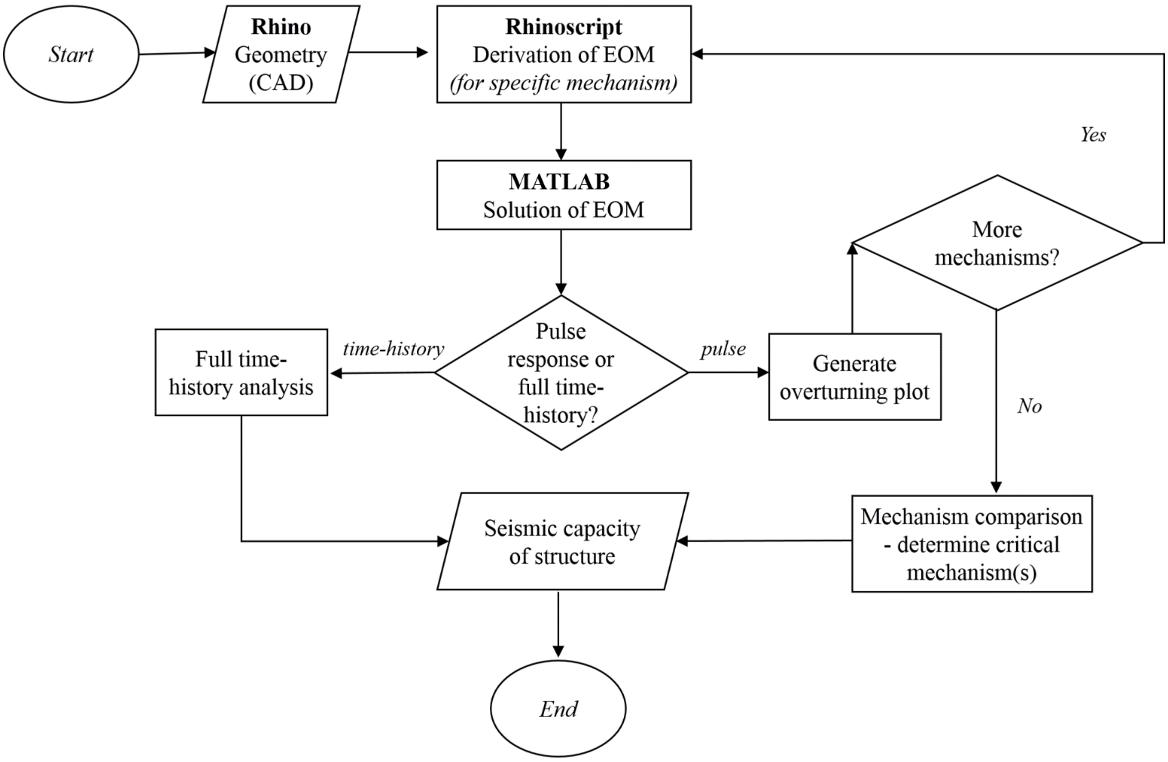

Fig. 3.1 Flowchart illustrating functioning of tool

3.2 Generation of the equation of motion in Rhino (rigid interfaces)

The mechanisms modelled by the tool can be broadly divided into four different typologies – namely a simple single block mechanism, a single block mechanism with added masses and forces, two block and multiple block mechanisms. Following the approach presented in Mauro et al. (2015), the equation of motion for any rocking mechanism can be derived using Lagrange's equation, which assumes the following form:

$$\frac{\partial}{\partial t}\left(\frac{\partial T\left(\phi,\dot{\phi}\right)}{\partial\dot{\phi}}\right)-\frac{\partial T\left(\phi,\dot{\phi}\right)}{\partial\phi}+\frac{\partial V\left(\phi\right)}{\partial\phi}=-B\left(\phi\right)\ddot{u}_g+M\left(\phi\right) \tag{3.1}$$

where ϕ is the rotation of the block and $\dot{\phi}$ the angular velocity. The term $T(\phi,\dot{\phi})$ represents the kinetic energy of the system, $V(\phi)$ the potential energy, $B(\phi)\ddot{u}_g$ the inertial force induced by the ground acceleration, and $M(\phi)$ the moment provided by the external static forces. However, in order to obtain local dynamic equivalence with the rocking block, Equation 3.1 can be linearised about the point of unstable equilibrium (ϕ=ϕ_{cr}), which corresponds to the configuration at which the potential energy of the system is maximum, and is thus the rotation at which:

$$\left.\frac{\partial V(\phi)}{\partial \phi}\right|_{\phi=\phi_{cr}} = 0 \tag{3.2}$$

This yields the following general linearised equation of motion:

$$\tilde{I}\ddot{\phi} - \tilde{K}(\phi - \phi_{cr}) = -\tilde{B}\ddot{u}_g + \tilde{M} \tag{3.3}$$

where $\tilde{I}$ is the moment of inertia of the portion of the structural system involved in the mechanism about the axis of rotation, and $\tilde{K}$ is the rotational stiffness:

$$\tilde{I} = \left.\frac{\partial^2 T(\phi,\dot{\phi})}{\partial \dot{\phi}^2}\right|_{\phi=\phi_{cr}} \tag{3.4}$$

$$\tilde{K} = \left.\frac{\partial M(\phi)}{\partial \phi}\right|_{\phi=\phi_{cr}} - \left.\frac{\partial^2 V(\phi)}{\partial \phi^2}\right|_{\phi=\phi_{cr}} \tag{3.5}$$

$$\tilde{B} = B(\phi)|_{\phi=\phi_{cr}} \tag{3.6}$$

$$\tilde{M} = M(\phi)|_{\phi=\phi_{cr}} \tag{3.7}$$

Using the following transformation of variables:

$$\theta = \phi\frac{\tilde{K}}{g\tilde{B}} \tag{3.8}$$

Equation 3.3 can be re-written as:

$$\ddot{\theta} = p_{eq}^2\left(\theta - \tilde{\lambda} - \frac{\ddot{u}_g}{g}\right) \tag{3.9}$$

where p_{eq} is the equivalent frequency parameter and is given by:

$$p_{eq} = \sqrt{\frac{\tilde{K}}{\tilde{I}}} \tag{3.10}$$

and $\tilde{\lambda}$ is an approximation of the static load multiplier which activates the mechanism:

$$\tilde{\lambda} = -\frac{\tilde{M} - \tilde{K}\phi_{cr}}{g\tilde{B}} \tag{3.11}$$

Thus p_{eq} and $\tilde{\lambda}$ are the equivalent rocking parameters defining the linearised equation of motion of the given mechanism, and depend primarily on the kinematic constants $\tilde{I}$, $\tilde{K}$, $\tilde{B}$ and ϕ_{cr}, which can be derived solely based on the geometry of the structure, as well as $\tilde{M}$ (where relevant), which depends on the external static forces applied to the system.

Furthermore, in the presence of external static forces (i.e. $\tilde{M} \neq 0$), the overturning rotation – that is, the rotation at which the restoring moment is zero, no longer corresponds to ϕ_{cr} and is instead defined as:

$$\tilde{\phi}_{ov} = \phi_{cr} - \frac{\tilde{M}}{\tilde{K}} \tag{3.12}$$

To this end, as part of the tool, scripts have been developed in Rhino to compute these kinematic constants (and consequently the equivalent rocking parameters) for the four aforementioned mechanism typologies, for any arbitrary or user-defined structural geometry, and which are described in further detail in the following sub-sections (3.2.1-3.2.4).

3.2.1 Single block mechanism

The simple single block mechanism can be used to capture the dynamic behaviour of many real-world masonry structures which rock monolithically - such as statues (Fig. 3.2), columns, pillars, and obelisks, as well as corner mechanisms and overturning of elements such as spires, apses and gables, which are commonly found in churches. The kinematic constants for this mechanism are:

$$\tilde{I} = I_O \tag{3.13}$$

$$\tilde{K} = gMR \tag{3.14}$$

$$\tilde{B} = MR \tag{3.15}$$

$$\phi_{cr} = \tilde{\phi}_{ov} = \alpha \tag{3.16}$$

where I_O is the moment of inertia of the portion of the structure involved in the mechanism about the axis of rotation, M is the mass, R is the distance between the center of mass and the axis of rotation and α is the slenderness (Fig. 3.2b).

In the case of structures with fairly regular geometries such as walls (which can be approximated as blocks) and spires (i.e. cones (DeJong, 2012b)), these geometric properties, and consequently the kinematic constants they define, can be easily derived analytically. However for structures with more complicated or irregular geometries, such as statues, derivation of these kinematic constants is far less straightforward. Thus a script was written in Rhino which makes use of the software's ability to

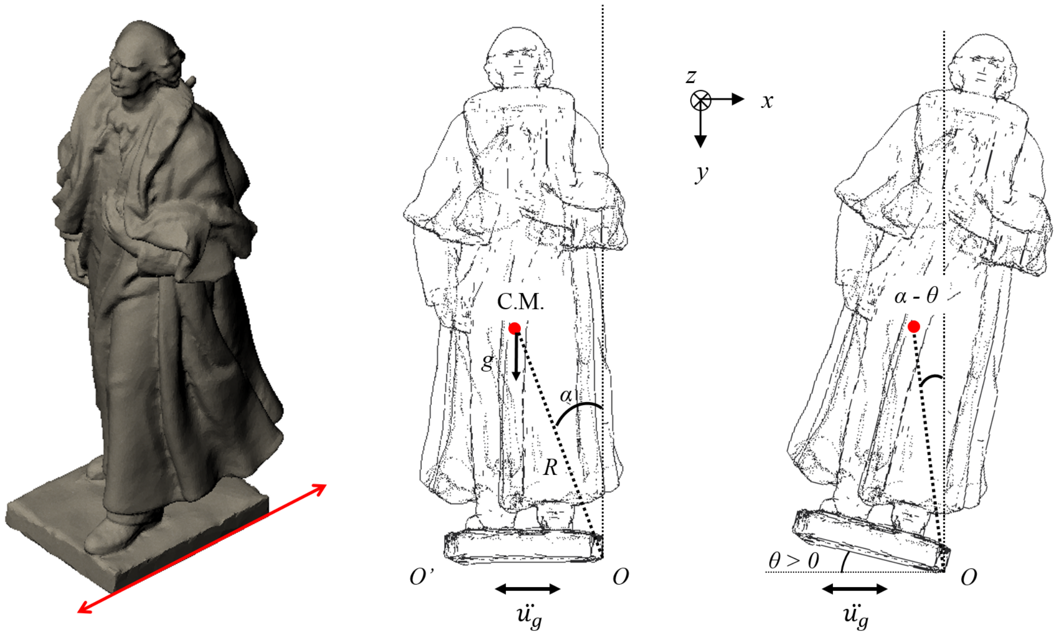

(a) **(b)** **(c)**

Fig. 3.2 Simple single block mechanism (Statue geometry and mesh from EPFL Computer Graphics and Geometry Laboratory). Note that the red line indicates the axis of rotation

quickly compute geometric quantities such as volumes, centroids, distances and moments of inertia, to determine the aforementioned geometric properties, and consequently the kinematic constants, for any user-defined structural geometry. For example, the geometry could be a meshed point cloud generated from photogrammetry or laser-scan data, as in Fig. 3.3.

However, Rhino can only compute the moment of inertia about the centroid of the object (for the volume moments of inertia) and about the global X, Y and Z axes (for the product moments of inertia). Furthermore, the moments of inertia output by Rhino are in terms of volume, which consequently need to be multiplied by the density of the object in order to get the corresponding mass moments of inertia. Thus in order to calculate the moment of inertia of the object about the user-defined axis of rotation, the script first has to compute the angles (β_x, β_y, β_z) between the axis of rotation and the global X, Y and Z axes. The product moments about the centroid are then obtained by applying the following set of transformations:

$$I_{xy} = I_{0xy} - (V_b \times x_c \times y_c) \tag{3.17}$$

$$I_{yz} = I_{0yz} - (V_b \times y_c \times z_c) \tag{3.18}$$

$$I_{zx} = I_{0zx} - (V_b \times z_c \times x_c) \tag{3.19}$$

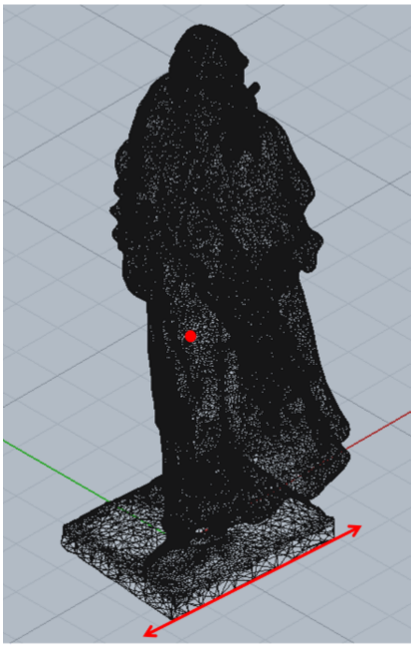

Fig. 3.3 Sample CAD geometry to illustrate functioning of script in Rhino, with the axis of rotation indicated by the red line and the centre of mass by the red dot

where I_{xy}, I_{yz} and I_{zx} are the product moments of inertia about the centroid, I_{0xy}, I_{0yz} and I_{0zx} are the product moments about the global axes, V_b is the volume of the object and x_c, y_c and z_c are the distances from the origin to the centroid of the object in the X, Y and Z directions respectively. The distance r_b between the centroid and the axis of rotation is also determined for each object. Using these quantities, the mass moment of inertia of the object about the user-defined axis of rotation (I_O) is then computed by means of the following equation:

$$I_O = \rho \left[\begin{array}{l} I_{xx}\cos^2\beta_x + I_{yy}\cos^2\beta_y + I_{zz}\cos^2\beta_z - 2I_{xy}\cos\beta_x\cos\beta_y \\ -2I_{yz}\cos\beta_y\cos\beta_z - 2I_{zx}\cos\beta_z\cos\beta_x + V_b r_b^2 \end{array} \right] \tag{3.20}$$

where I_{xx}, I_{yy} and I_{zz} are the volume moments of inertia about the centroid, and ρ is the density of the object.

As input, upon opening the relevant CAD file (e.g. Fig. 3.3) and calling the script, the user is first prompted to drag-select with the mouse all the objects involved in the mechanism and input the density of the selected objects. For mechanisms involving objects of different densities (for example, a stone column topped with a bronze statue), the user is prompted to first select objects of the first density, then select objects of the second density and so on, with the script then joining objects of the same density together. The user then defines (draws) the axis of rotation (indicated by the red line in Fig. 3.2 and Fig. 3.3) and any cracks which occur, and based upon this input alone the script computes the resultant kinematic constants for the mechanism. These kinematic constants are then used to calculate the rocking parameters, which are subsequently written to a text file for export to MATLAB, where they are used to generate and solve the corresponding equation of motion.

3.2.2 Single block mechanism with added masses and forces

Equations of motion have also been derived for the single block mechanism under the influence of additional masses and external static forces (Mauro et al., 2015). These equations can be used to model the behaviour of walls bearing loads from floors and roofs, which, depending upon which way they span, can transmit both their self-weight and inertial loads to the wall and can thus be modelled as either load-bearing (designated as M_i in Fig. 3.4) or non-load bearing (M_j in Fig. 3.4) concentrated masses (Mauro et al., 2015). The equations also account for the influence of external static forces in the form of thrusts from vaults and roofs (F_1 and F_3, Fig. 3.4), as well as the effect of tie-bars (F_2 in Fig. 3.4) (Mauro et al., 2015). The kinematic constants defining this type of mechanism are thus given by:

$$\tilde{I} = I_O + \sum_{ni} M_i R_i^2 \tag{3.21}$$

$$\tilde{K} = gM_cR_c + FR_f \sin(\alpha_f - \alpha_c) \tag{3.22}$$

$$\tilde{B} = M_c^* R_c^* \tag{3.23}$$

$$\tilde{M} = FR_f \cos(\alpha_f - \alpha_c) \tag{3.24}$$

$$\phi_{cr} = \alpha_c \tag{3.25}$$

$$\tilde{\phi}_{ov} = \alpha_c - \frac{FR_f \cos(\alpha_f - \alpha_c)}{gM_cR_c + FR_f \sin(\alpha_f - \alpha_c)} \tag{3.26}$$

where I_O is the moment of inertia of the portion of the structure involved in the mechanism about the axis of rotation and $\sum_{ni} M_i R_i^2$ is the sum of the moments of inertia of the load-bearing masses. M_c is the combined mass of the portion of the structure involved in the mechanism and the load-bearing masses, whose resulting center of mass is defined by R_c and α_c, while M_c* is the combined mass of the portion of the structure involved in the mechanism as well as the load-bearing and non-load bearing masses, the position of the center of mass of which is denoted by R_c* and α_c*. Similarly, F is the resultant force obtained by adding up all the external forces acting on the wall, which acts at a point defined by R_f and α_f so as to preserve the total moment about O (Mauro et al., 2015).

The script written in Rhino in this case is more complex. It first prompts the user to select the main wall (i.e. the wall to which the additional masses will be transmitted) as well as any adjacent walls involved in the mechanism, and define the density, axis of rotation (red line in Fig. 3.4), and any cracks which occur. The user is then provided with a check-box and asked to indicate which additional elements are acting on the structure, with the options including floors, the roof, vaults and tie-bars.

If floors are selected, the user is then prompted to select all the floor elements transmitting loads to the wall in the CAD file and enter their density. The script then cycles through each of the floors

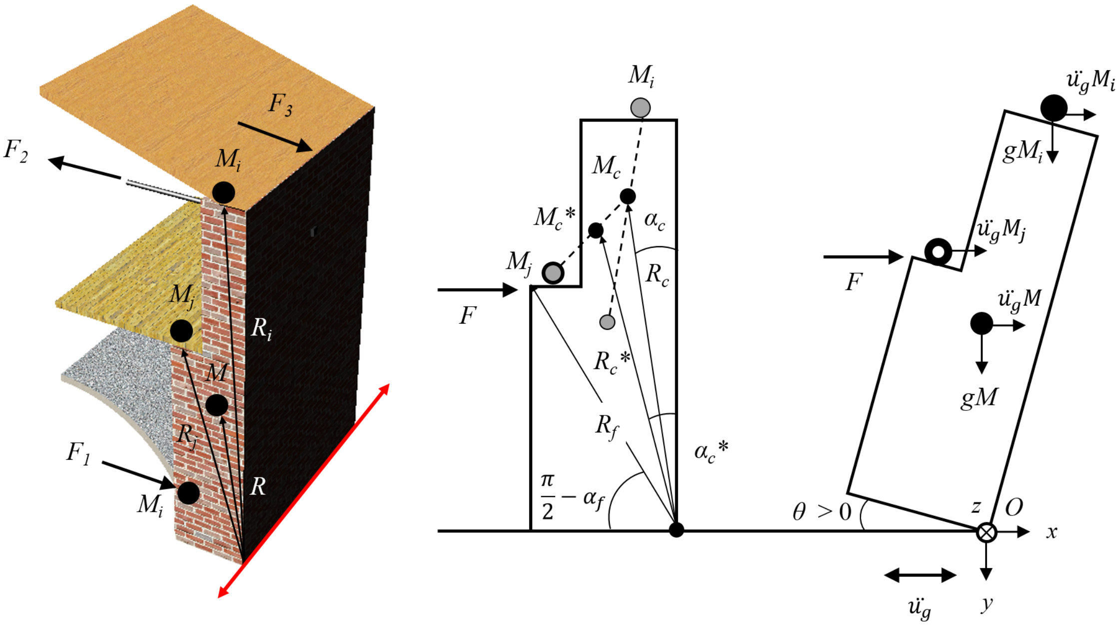

Fig. 3.4 Single block mechanism with added masses and forces, adapted from Mauro et al. (2015)

and determines how they intersect with the wall – based on the type of intersection, the corresponding concentrated mass is then classified as either load bearing or non-load bearing and is stored in the appropriate mass array. The resultant point of action of the mass, which is determined by finding the centroid of the area of intersection between the floor and the wall, is also stored in an analogous location array.

Similarly, if the roof option is selected, the user is asked to select the roof element and enter its density. The script then finds the intersection between the roof and the wall, and uses that to determine the orientation of the former relative to the latter. A bounding box is then created and used to calculate the span and height of the roof, which in turn is used to compute the corresponding thrust. This thrust is stored in the array of forces, with the point of application being stored in a separate location array. The mass of the roof is also calculated and, depending on the type of intersection with the walls, is classified as load or non-load bearing, with the corresponding point(s) of application being stored in the appropriate location array.

If the vault option has been selected, the user is prompted to select the relevant macro-element and, as in the case of the roof element, a bounding box is then used to calculate the height, span and length of the vault, as well as the height to span ratio, with the latter being used to determine the vertical and horizontal thrusts using Ungewitter's tables (assuming quadripartite vaults) (Ungewitter and Mohrmann, 1901). Since thrusts from the table also depend on the thickness of the vault and material used in its construction, the user is asked to select an option from a set of five cases, which are:

1. ½ lightweight brick (125 mm)
2. ½ strong brick (125 mm) or ¾ lightweight brick (190 mm)
3. ¾ strong brick (190 mm) or 1 lightweight brick (250 mm)
4. 1 strong brick (250 mm) or 200 mm sandstone
5. 300 mm rubble vault

Based on this input, the script then automatically determines the vertical thrust, which is converted into a load-bearing mass, and the horizontal thrust, which is treated as a static force, and which are stored in the appropriate arrays. The corresponding points of application of both the mass and force are also determined based on the intersection of the vault with the walls and are stored in their respective point cloud arrays.

Finally if the tie bar option is selected, the user is prompted to enter the number of tie bars and for each one is made to select the element and enter the magnitude of the force in the bar, which is stored in the force array. The point of application of each tie bar force is then determined based on the intersection of the bar element with the façade wall, and is stored in the location array.

The script then cycles through each of the mass, force and point cloud arrays to determine M_c, R_c, α_c, M_c*, R_c*, α_c*, F, R_f and α_f. These terms are used to calculate the corresponding kinematic constants as defined by Equations 3.21-3.26 - and by extension the equivalent rocking parameters, with the latter then being written to a text file for export to MATLAB.

3.2.3 Two block mechanism

The two block mechanism is used to capture the dynamic behaviour of structures such as façades which are well-restrained at both the top and bottom, resulting in the formation of two additional hinges – one at the top and another at an arbitrary location along the wall height (as indicated in Fig. 3.5). The height h_c at which the intermediate hinge occurs depends on the self-weight of the wall W, the external vertical force acting on it N, the base area (l x b) and full height of the wall h, as well as the tensile strength of the mortar f_{mt}. Following the approach presented in Sorrentino et al. (2008b), h_c can be determined analytically using the following equation:

$$h_c = h\left[1+\frac{\frac{N}{W}+\frac{f_{mt}(l\times b)}{W}-\sqrt{\left(2+\frac{f_{mt}(l\times b)}{W}+2\frac{N}{W}\right)\left(\frac{N}{W}+\frac{f_{mt}(l\times b)}{W}\right)}}{2+\frac{N}{W}}\right] \tag{3.27}$$

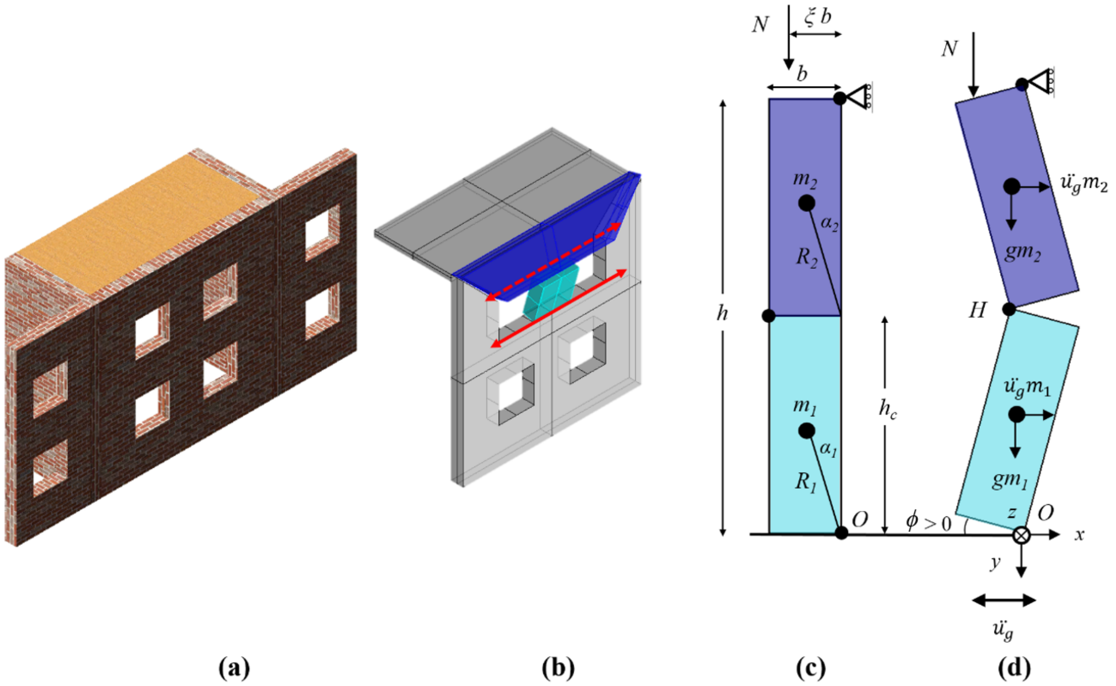

Fig. 3.5 Two block mechanism, image on right adapted from Mauro et al. (2015)

Once h_c has been determined, the wall can be divided into two blocks and the kinematic constants computed using Equations 3.28–3.33:

$$\tilde{I} = I_{O1} + I_{O2}\frac{\sin^2(\alpha_2)}{\sin^2(\alpha_1)} \tag{3.28}$$

$$\tilde{K} = R_2\frac{\sin(\alpha_2)}{\sin(\alpha_1)}\left[\begin{array}{l} g\left(m_1 + m_2\left(2 + \frac{\sin(\alpha_2)}{\sin(\alpha_1)}\right)\right) \\ +2N\frac{\sin(\alpha_2)}{\sin(\alpha_1)}\left(\cos^2(\alpha_2) + (1-\xi)\sin^2(\alpha_2) + \frac{\sin(\alpha_1)}{\sin(\alpha_2)}\right) \end{array}\right] \tag{3.29}$$

$$\tilde{B} = (m_1 + m_2)R_2\frac{\sin(\alpha_2)}{\sin(\alpha_1)} \tag{3.30}$$

$$\tilde{M} = \xi N\sin(2\alpha_2)R_2\frac{\sin(\alpha_2)}{\sin(\alpha_1)} \tag{3.31}$$

$$\phi_{cr} = \alpha_1 \tag{3.32}$$

$$\tilde{\phi}_{ov} = \alpha_1 - \frac{\xi N\sin(2\alpha_2)}{\left[2N + g(m_1 + 2m_2) + 2N\frac{\sin(\alpha_2)}{\sin(\alpha_1)}\left(\cos^2(\alpha_2) + (1-\xi)\sin^2(\alpha_2) + \frac{gm_2}{2N}\right)\right]} \tag{3.33}$$

where I_{O1} and I_{O2} are the moments of inertia of the bottom and top blocks about their respective axes of rotation, while α_1 and α_2 are the respective block slenderness values. R_2 is the distance between the center of mass of the top block and its axis of rotation, while m_1 and m_2 are the masses of the bottom and top blocks, and ξ represents the distance from the edge support at which the external vertical force N acts, normalized by the thickness of the wall b, as illustrated by Fig. 3.5c.

In this case, the script written in Rhino first prompts the user to select the main wall involved in the mechanism, and to draw the axis of rotation at its base (O in Fig. 3.5d). The user is then asked to select the structural component(s) transmitting external vertical forces N to the wall. Based on this input, the script determines the exact position at which this force acts, by finding the centroid of the area of intersection between the wall and the selected structural component(s). The user is then prompted to enter the relevant material properties – such as the densities of the wall ρ_w and the structural components ρ_{sc}, as well as the tensile strength of the mortar f_{mt}. The script then computes the volumes of the main wall and selected structural components, multiplying them by the input densities to get W and N respectively. Using a bounding box, the full height h and base area (l x b) of the main wall are determined, and Equation 3.27 is used to calculate the height h_c at which the intermediate hinge develops. A cutting plane is then generated at h_c and is used to split the wall into two blocks/segments, as well as create an additional axis of rotation at H (Fig. 3.5d). The relevant geometric properties and consequently kinematic constants are then computed, which are then used to calculate the equivalent rocking parameters for export to MATLAB.

3.2.4 Multiple block mechanism

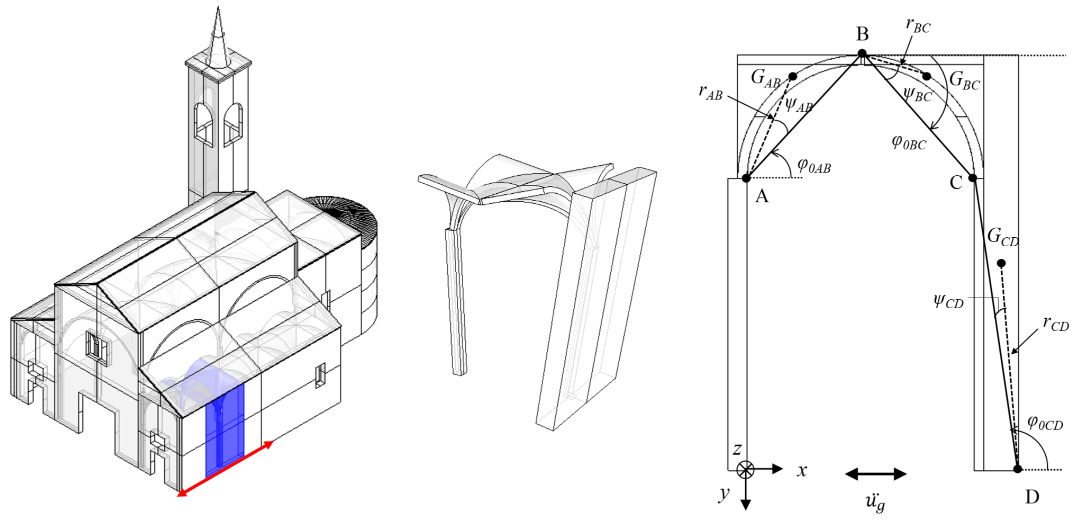

(a) **(b)** **(c)**

Fig. 3.6 Multiple block mechanism: (a) Location of side-aisle vault within church, (b) collapse mechanism of macroelement, (c) geometric properties of the blocks (adapted from DeJong and Dimitrakopoulos (2014))

Equations have also been derived for the multiple block mechanism (Fig. 3.6) (DeJong and Dimitrakopoulos, 2014), which can be used to model the dynamic response of structures such as arches, vaults, portal frames and belfries, which are commonly found in churches. This mechanism

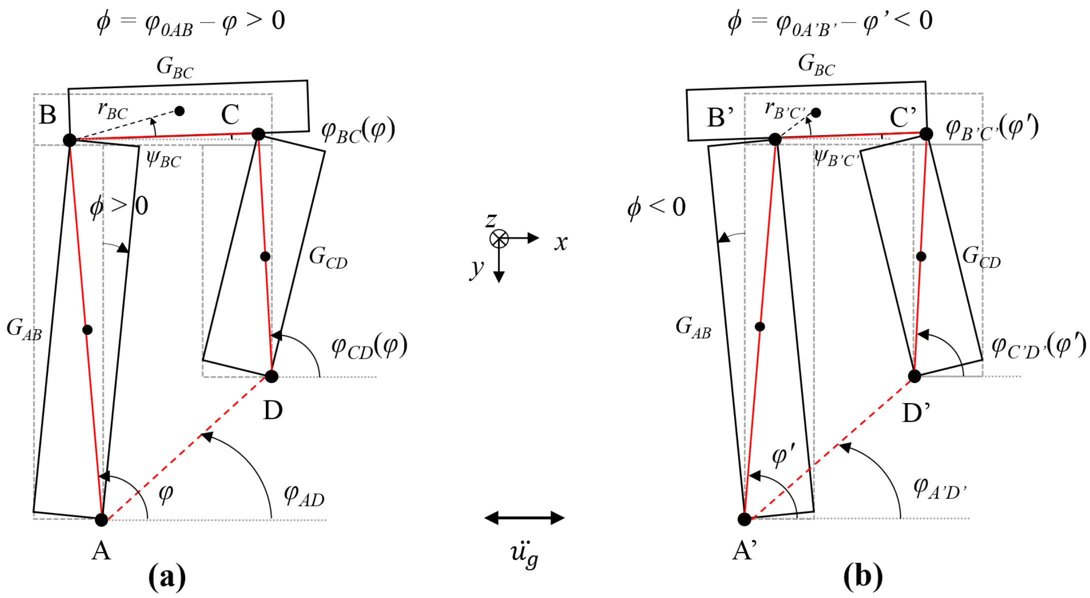

Fig. 3.7 Multiple block mechanism: (a) Hinge locations for positive rotations ($\phi > 0$), (b) hinge locations for negative rotations ($\phi < 0$), adapted from DeJong and Dimitrakopoulos (2014)

comprises three blocks with four hinges (labelled A-D as indicated in Fig. 3.6c), and it is assumed that once rocking motion initiates, the location of these hinges does not change – only reflecting to the opposite face of the block upon impact – thereby leading to one set of hinges for positive rotations (ABCD, Fig. 3.7a), and another for negative rotations (A'B'C'D', Fig. 3.7b) (DeJong and Dimitrakopoulos, 2014). The linearised equation of motion for this type of mechanism is fairly complex and the expressions defining the corresponding kinematic constants can be computed using Equations 3.34-3.37 (DeJong and Dimitrakopoulos, 2014):

$$\tilde{I} = \left\{ I_{AB} + I_{CD} f_{CD}(\varphi_{cr})^2 + I_{BC} f_{BC}(\varphi_{cr})^2 + m_{BC} AB \left[AB + 2 r_{BC} \cos\left(\varphi_{cr} - \varphi_{BC}\left(\varphi_{cr}\right) - \psi_{BC}\right) f_{BC}\left(\varphi_{cr}\right) \right] \right\} \tag{3.34}$$

$$\tilde{K} = -g \left\{ \begin{array}{l} m_{BC} r_{BC} \left[\cos\left(\varphi_{BC}\left(\varphi_{cr}\right) + \psi_{BC}\right) f'_{BC}\left(\varphi_{cr}\right) - \sin\left(\varphi_{BC}\left(\varphi_{cr}\right) + \psi_{BC}\right) f_{BC}(\varphi_{cr})^2 \right] \\ + m_{CD} r_{CD} \left[\cos\left(\varphi_{CD}\left(\varphi_{cr}\right) + \psi_{CD}\right) f'_{CD}\left(\varphi_{cr}\right) - \sin\left(\varphi_{CD}\left(\varphi_{cr}\right) + \psi_{CD}\right) f_{CD}(\varphi_{cr})^2 \right] \\ - m_{AB} r_{AB} \sin\left(\varphi_{cr} + \psi_{AB}\right) - m_{BC} AB \sin\varphi_{cr} \end{array} \right\} \tag{3.35}$$

$$\tilde{B} = \left\{ \begin{array}{l} m_{AB} r_{AB} \sin\left(\varphi_{cr} + \psi_{AB}\right) + m_{CD} r_{CD} \sin\left(\varphi_{CD}\left(\varphi_{cr}\right) + \psi_{CD}\right) f_{CD}\left(\varphi_{cr}\right) \\ + m_{BC} r_{BC} \sin\left(\varphi_{BC}\left(\varphi_{cr}\right) + \psi_{BC}\right) f_{BC}\left(\varphi_{cr}\right) + m_{BC} AB \sin\varphi_{cr} \end{array} \right\} \tag{3.36}$$

$$\phi_{cr} = \tilde{\phi}_{ov} = \varphi_{0AB} - \varphi_{cr} \tag{3.37}$$

Where:

$$BD(\varphi) = \sqrt{AB^2 + AD^2 - (2 \times AB \times AD \times \cos(\varphi - \varphi_{AD}))} \tag{3.38}$$

$$\varphi_{BC}(\varphi) = \arctan\left[\frac{-AB\sin\varphi + AD\sin\varphi_{AD} + CD\sin\varphi_{CD}(\varphi)}{-AB\cos\varphi + AD\cos\varphi_{AD} + CD\cos\varphi_{CD}(\varphi)}\right] \tag{3.39}$$

$$\varphi_{CD}(\varphi) = \arctan\left[\frac{AB\sin\varphi - AD\sin\varphi_{AD}}{AB\cos\varphi - AD\cos\varphi_{AD}}\right] - \arccos\left[\frac{BD^2(\varphi) + CD^2 - BC^2}{2 \cdot CD \cdot BD(\varphi)}\right] \tag{3.40}$$

$$f_{BC}(\varphi) = \frac{\partial \varphi_{BC}}{\partial \varphi}; \qquad f'_{BC}(\varphi) = \frac{\partial^2 \varphi_{BC}}{\partial \varphi^2} \tag{3.41}$$

$$f_{CD}(\varphi) = \frac{\partial \varphi_{CD}}{\partial \varphi}; \qquad f'_{CD}(\varphi) = \frac{\partial^2 \varphi_{CD}}{\partial \varphi^2} \tag{3.42}$$

The critical rotation of the system φ_{cr}, is obtained by iteratively solving the following equation for the first derivative of the potential energy of the system, for both the original and reflected hinge locations:

$$\left.\frac{\partial V}{\partial \varphi}\right|_{\varphi=\varphi_{cr}} = g\left[\begin{array}{l} m_{AB}r_{AB}\cos(\varphi_{cr} + \psi_{AB}) + m_{BC}AB\cos\varphi_{cr} \\ +m_{BC}r_{BC}\cos(\varphi_{BC}(\varphi_{cr}) + \psi_{BC})\,\frac{AB}{BC}\frac{\sin(\varphi_{cr} - \varphi_{CD}(\varphi_{cr}))}{\sin(\varphi_{CD}(\varphi_{cr}) - \varphi_{BC}(\varphi_{cr}))} \\ +m_{CD}r_{CD}\cos(\varphi_{CD}(\varphi_{cr}) + \psi_{CD})\,\frac{AB}{BC}\frac{\sin(\varphi_{cr} - \varphi_{CD}(\varphi_{cr}))}{\sin(\varphi_{CD}(\varphi_{cr}) - \varphi_{BC}(\varphi_{cr}))} \end{array}\right] = 0 \tag{3.43}$$

The script written in Rhino for this mechanism is far more complicated than those written for the other three mechanisms. As input, the user is first prompted to select the three sets of objects (segments *AB*, *BC* and *CD* in Fig. 3.6c and Fig. 3.7) and define two sets of four hinges (one set for positive, and one reflected set for negative rotations), as well as one axis of rotation (represented by the red line in Fig. 3.6a), which the script translates to the other hinges to create the other three/seven rotation axes. Based upon this input, the script then automatically determines the geometric properties such as mass, moment of inertia, distance between hinges etc., as well as φ, ψ and r for each of the three blocks, and iteratively solves Equation 3.43 to obtain the critical rotation of the system φ_{cr}. The other kinematic constants are then computed by plugging the values of the geometric properties as well as the critical rotation into Equations 3.34-3.37, which are then used to determine the equivalent rocking parameters for the system. A more detailed explanation about the functioning of this script can be found in Fig. 3.8.

3.3 Solution of the equation of motion in MATLAB

The rocking parameters p_{eq} (Equation 3.10) and $\tilde{\lambda}$ (Equation 3.11), upon being exported to MATLAB, are used to generate the linearised equation of motion as defined in Equation 3.9. The equation of motion as it currently stands can then be solved either for the pulse response or the full time-history, depending on the type of analysis being conducted. The pulse response in particular can be useful

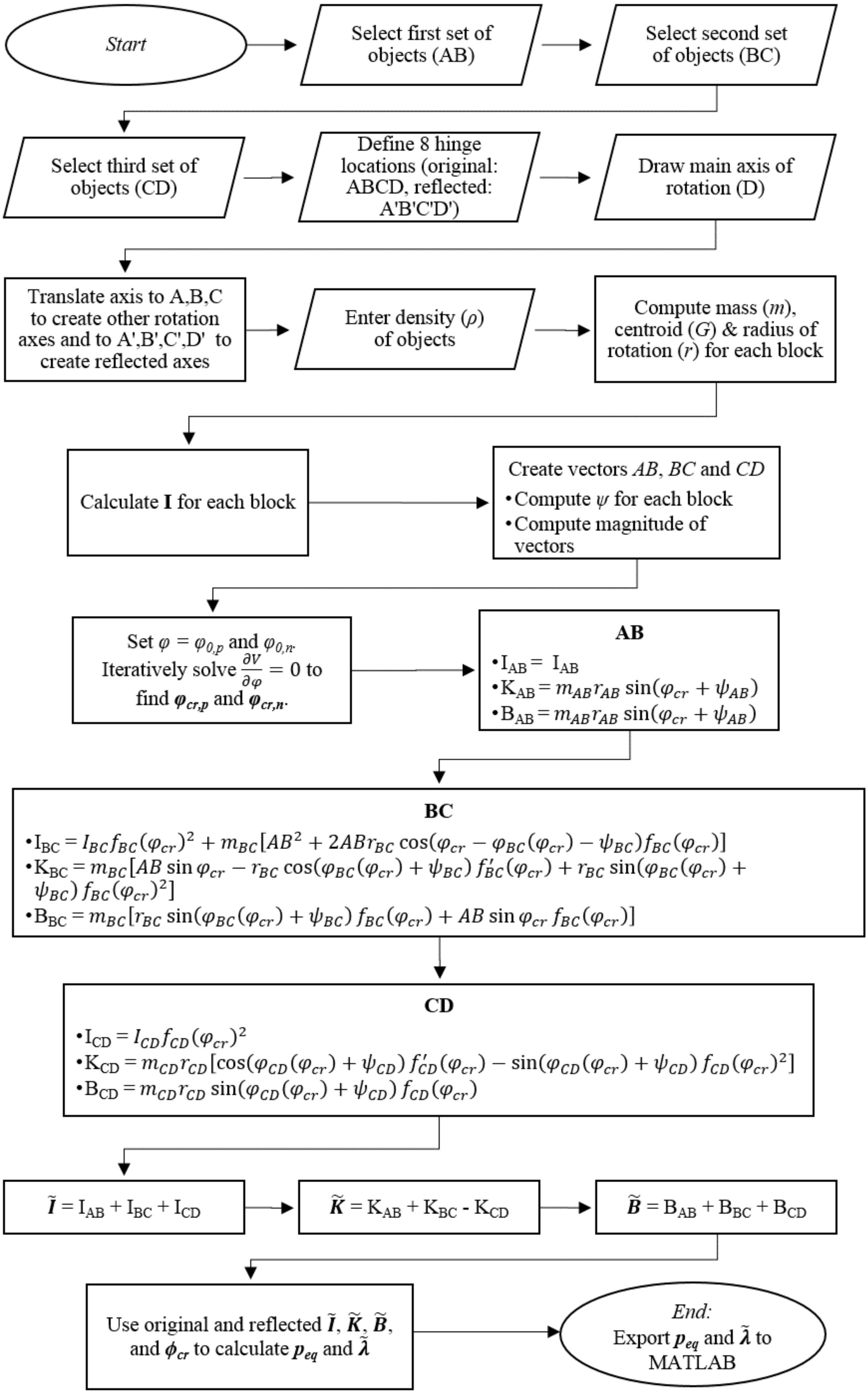

Fig. 3.8 Flowchart illustrating functioning of the Rhinoscript for the multiple block mechanisms

for comparing the relative dynamic resilience of different mechanisms (Mauro et al., 2015), and prioritizing retrofit solutions, as well as modelling known near-fault seismic scenarios.

Numerical integration of the equation of motion is conducted using the ode45 solver in MATLAB, which employs the Runge-Kutta algorithm with a variable time-step in order to provide a solution in a computationally-efficient manner. The solution procedure is iterative: starting from a given set of initial conditions, the algorithm computes the rotation and angular velocity at each time-step, which are subsequently used as input (i.e. the initial conditions) for the following time-step. Furthermore, in the case of impact, the energy dissipated by the block(s) - which results in a reduction in angular velocity - is accounted for in the form of the coefficient of restitution η, which is an additional rocking parameter to be considered when solving Equation 3.9 for both the pulse response and full time-history.

For the simple single block mechanism undergoing two-sided rocking, the following coefficient of restitution proposed by Housner (1963) is used:

$$\eta = 1 - 2\frac{MR^2}{I_O}\sin^2\alpha \tag{3.44}$$

For one-sided rocking (commonly observed in façades), the following coefficient of restitution proposed by Sorrentino et al. (2011) is used instead:

$$\eta = \left(1 - 2\frac{MR^2}{I_O}\sin^2\alpha\right)^2 \left(1 - 2\frac{MR^2}{I_O}\cos^2\alpha\right) \tag{3.45}$$

Similarly, for the two block mechanism, the coefficient of restitution as derived by Sorrentino et al. (2008b) can be applied:

$$\eta = \frac{I_{O1} - I_{O2}\frac{\tan\alpha_2}{\tan\alpha_1} - 2m_1R_1^2\sin^2\alpha_1 + m_2R_1^2\left[2 - 4\sin^2\alpha_1 + \sin\alpha_1\cos\alpha_1\left(\frac{1}{\sin\alpha_2\cos\alpha_2} + \frac{1}{\tan\alpha_2} - \tan\alpha_2\right)\right]}{I_{O1} - I_{O2}\frac{\tan\alpha_2}{\tan\alpha_1} + m_2R_1^2\left[2 + \sin\alpha_1\cos\alpha_1\left(\frac{1}{\sin\alpha_2\cos\alpha_2} + \frac{1}{\tan\alpha_2} + \tan\alpha_2\right)\right]} \tag{3.46}$$

As these coefficients depend entirely on the geometry of the structure, they are also calculated as part of the script in Rhino for the simple single block and two block mechanisms. However, it should be noted that these derivations assume inelastic impact between the blocks and the ground, providing the maximum amount of energy dissipated at impact – thus yielding a slightly un-conservative estimate for this parameter. Alternatively, a suitable coefficient of restitution can also be provided by the user based on the results of experimental tests (e.g. as in Sorrentino et al. (2011), Graziotti et al. (2016)).

In the case of the other mechanisms, derivation of the coefficient of restitution is not as straightforward. While analytical expressions/models can be used for the coefficient of restitution for the multiple block mechanisms (De Lorenzis et al., 2007), these tend to be quite complex. As an alternative, in keeping with the assumptions of Mauro et al. (2015), the coefficient of restitution can instead be treated as a parameter that is independently specified by the user, calibrated based on the results of either experimental campaigns (DeJong et al., 2008) and/or numerical simulations (De Lorenzis et al., 2007).

3.3.1 Pulse response (overturning plots)

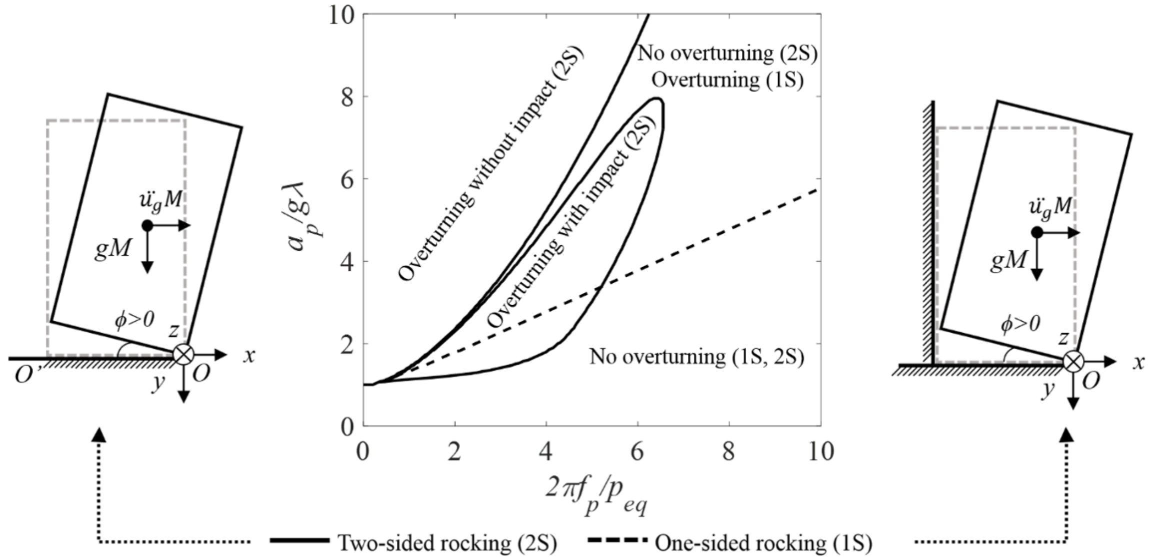

Fig. 3.9 Sample dimensionless overturning plot for both one and two-sided rocking

The equations of motion exported to MATLAB can be used to generate overturning plots, which predict the response of the structure to single sinusoidal acceleration pulses of varying frequency (f_p) and amplitude (a_p), and depend primarily on p_{eq}, $\tilde{\lambda}$, and the coefficient of restitution η. As the general linearised equations of motion derived for the different mechanisms have local dynamic equivalence with the single rocking block, the closed-form solutions for overturning plots obtained by Dimitrakopoulos and DeJong (2012) can be used. However, to avoid regenerating these plots for every prediction, a library of dimensionless plots (Fig. 3.9) for different coefficients of restitution was instead pre-generated and stored in the MATLAB directory. In the case of one-sided rocking, it was assumed that collapse of the structure is governed by positive pulse overturning without impact, which is true for the vast majority of practical one-sided mechanisms (Mauro et al., 2015), and is therefore independent of the coefficient of restitution. This assumption results in only a single dimensionless plot being needed.

Thus for each mechanism, depending on the coefficient of restitution either calculated or assumed, as well as the type of rocking (i.e. one or two-sided), the appropriate dimensionless plot is then selected by the tool and scaled by p_{eq} and $\tilde{\lambda}$ in order to get the actual overturning envelope for that particular mechanism.

3.3.2 Full time-history analysis

As an alternative to the overturning plots, full time-history analyses can also be conducted for the considered structures/mechanisms. The results in this case are presented in terms of the maximum rotation θ of the structure over time, with the rotation being expressed as a fraction of the overturning rotation $\tilde{\phi}_{ov}$ (as defined in Section 3.2 and equal to α, i.e. the slenderness of the block, in the case of the simple single block mechanisms in the absence of any external static forces). Overturning is herein assumed to occur when this ratio exceeds 1, though an appropriate safety factor such as that in the Italian Building Code (DMI, 2008), could also be applied. Furthermore, for assessment purposes, the tool could also be used to follow typical code-based procedures as specified for example in ASCE 43-05 (2007), where the code prescribes running full time-history analyses using a minimum of five different earthquake records to estimate the maximum rocking response of the structure.

3.4 New developments

3.4.1 Amplification effects

As a number of collapse mechanisms tend to take place above ground level, a methodology was also developed to account for dynamic amplification of the ground motion up the structure.

3.4.1.1 Pulse response (overturning plots)

In the case of pulse-response analysis, a method was developed to scale the overturning plots. Applying the approach originally proposed by Priestley (1985), elastic modal analysis is used to generate response spectra by solving the equation of motion for an equivalent single-degree-of-freedom system with 5% damping and a natural frequency f_n corresponding to that of the structure under consideration, under the influence of single acceleration sine pulses of varying frequency f_p. Only first-mode response is considered, without taking higher mode effects into account. The resulting pulse response spectrum (Fig. 3.10a) is obtained by plotting the variation of the maximum recorded response acceleration a_r (normalized by the input ground acceleration a_g) against the normalized pulse frequency f_p/f_n.

This response acceleration is assumed to act at the effective center (modal height) of seismic force h_e, and assuming a linear first-mode shape (Fig. 3.10b, (Priestley, 1985)), the response acceleration at heights h above and below h_e can then be determined through linear extrapolation. However, a_r is only the acceleration relative to the ground, and thus must be combined with the ground acceleration a_g in order to obtain the total acceleration of the structure a_{sc}. In order to do this, the square-root-sum-of-squares (SRSS) approach is used (Priestley, 1985), whereby:

$$a_{sc} = \sqrt{a_r^2\left(\frac{h}{h_e}\right)^2 + a_g^2} \tag{3.47}$$

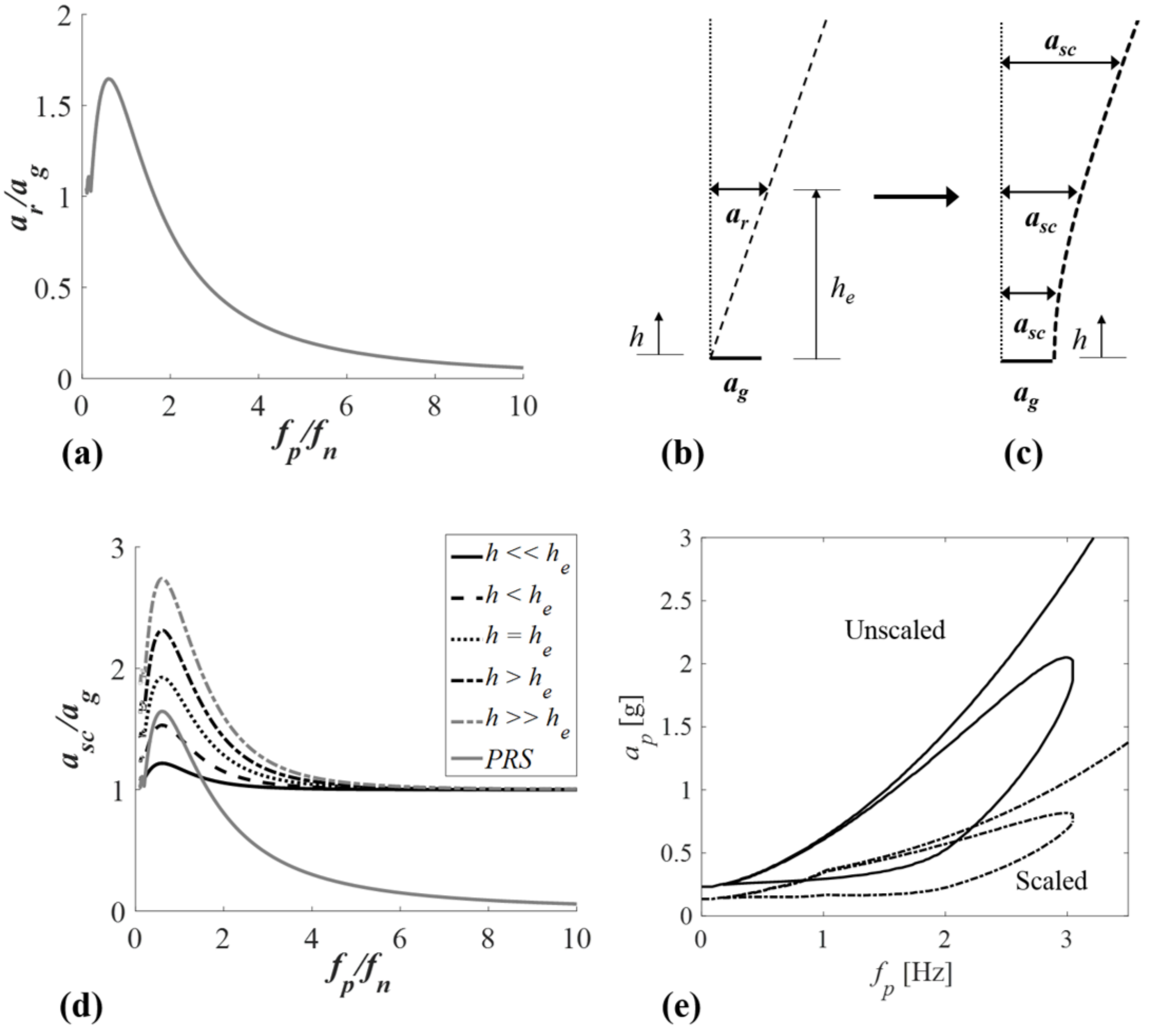

Fig. 3.10 Methodology for scaling the overturning plots: (a) Pulse response spectrum; (b) Linear mode shape assumed; (c) Scaled acceleration profile; (d) Scaled pulse response spectra and (e) Scaled overturning plots

Leading to the scaled acceleration profile as depicted in Fig. 3.10c.

This acceleration profile is then used to scale the pulse response spectrum (Fig. 3.10a) for different heights within the structure – as illustrated by Fig. 3.10d, with these modified linear-elastic pulse response spectra finally being used to scale the corresponding overturning plots in MATLAB (Fig. 3.10e).

3.4.1.2 Full time-history analysis

Similarly, in the case of full time-history analyses, an approach similar to that proposed in Section 3.4.1.1 can be employed - but by replacing the pulse response spectrum with the acceleration response spectrum generated for the recorded signal (assuming 5% damping). Using the acceleration response spectrum, the spectral acceleration S_a at the natural period of the structure T_n can then be determined, which is substituted into Equation 3.47 (in place of a_r) to get the scaled acceleration a_{sc}. The level of scaling to be applied to the ground motion is then found by dividing a_{sc} by the input ground acceleration a_g, leading to the following expression for the scale factor SF:

$$SF = \frac{a_{sc}}{a_g} = \sqrt{\left(\frac{S_a\left(T_n\right)}{a_g} \cdot \frac{h}{h_e}\right)^2 + 1} \tag{3.48}$$

Alternatively, simple code-based equations to account for amplification up the structure could be used instead. This includes the following expression as adapted from Eurocode 8 (EN 1998-1, 2004):

$$SF = S\left[3\left(1 + \frac{h}{H}\right) - 0.5\right] \tag{3.49}$$

where S is the soil factor and H is the full height of the structure; as well as smallest of the following three coefficients as defined in the New Zealand Standard, NZS 1170.5 (NZS, 2004):

$$SF = 1 + \frac{h}{6} \qquad h < 12\,m \tag{3.50}$$

$$SF = 1 + 10\frac{h}{H} \qquad h < 0.2\,H \tag{3.51}$$

$$SF = 3 \qquad h > 0.2\,H \tag{3.52}$$

In addition to the scale factor determined either using Equation 3.48 or code-based methods, other levels of scaling can also be applied to the earthquake ground motion in order to gauge their influence on the dynamic response of the structure.

3.4.2 Automatic detection of critical mechanisms

As the overturning plots enable comparison of the dynamic resilience of multiple different mechanisms (Fig. 3.11a), a methodology was also developed in MATLAB to automatically determine the most vulnerable mechanism for each pulse frequency. In order to do this, the lower bounds of each of

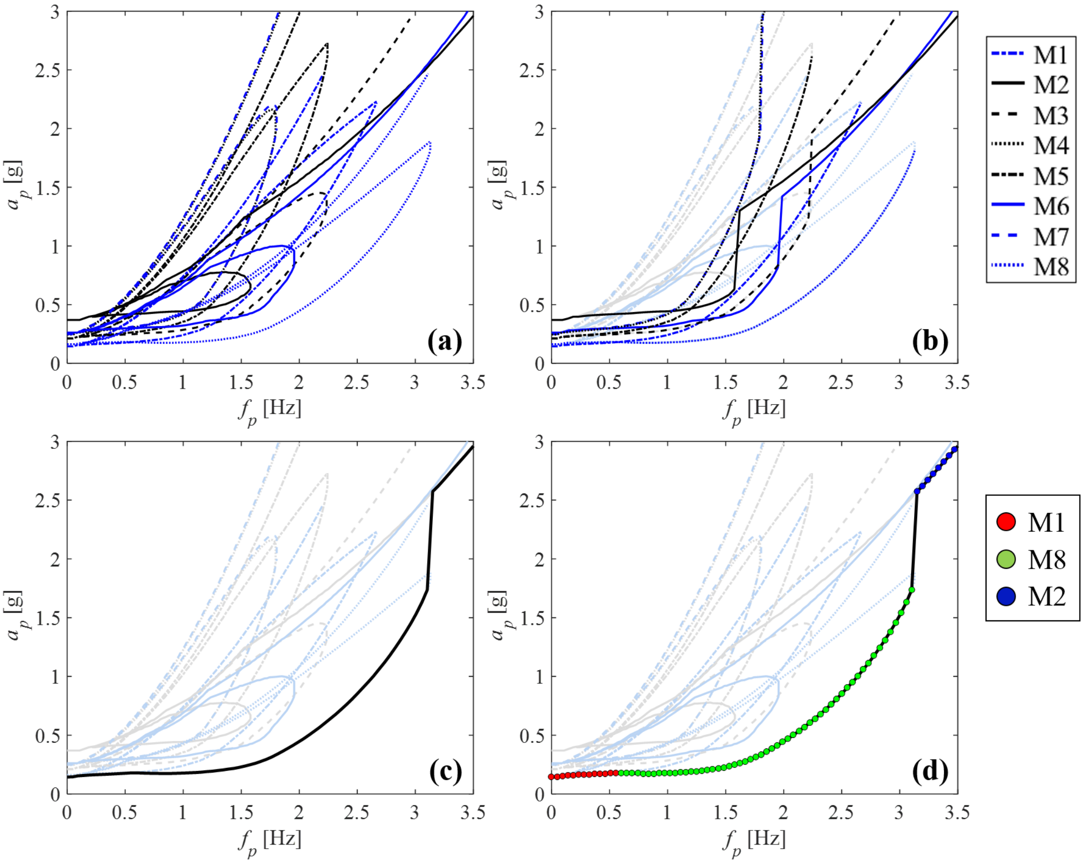

Fig. 3.11 Methodology for automatic detection of critical mechanisms: (a) Overturning plots for the different mechanisms; (b) Lower bound of each overturning plot; (c) Lower bound of all the overturning plots; (d) Most vulnerable mechanism for each pulse frequency

the overturning plots were first determined (Fig. 3.11b), which were stored in a master array. These lower bounds were then compared to get an overall lower bound for all the plots (Fig. 3.11c), with the mechanism that each lower bound corresponded to (i.e. the critical mechanism) being flagged and stored in a separate array. Different coloured markers were assigned to each of the considered mechanisms, with the script cycling through the flagged array and plotting the appropriate markers for each value of f_p - thus highlighting the most vulnerable mechanism for each pulse frequency (Fig. 3.11d).

3.5 Summary

In this chapter, a new tool is presented for the non-linear dynamic analysis of masonry collapse mechanisms. The tool makes use of rocking dynamics to derive and solve equations of motion for a range of different failure mechanisms, for any user-defined structural geometry, using as a starting point a digital drawing of the structure in a typical CAD software (in this case Rhino). Scripts have been written in Rhino which make use of the program's ability to quickly compute geometric properties for any arbitrary structural geometry, to derive the equivalent rocking parameters defining the equations of motion for the different mechanisms, which can broadly be classified as single block, single block with added masses and forces, two block and multiple block mechanisms. These rocking parameters are then exported to MATLAB, where they are used to generate the relevant equations of motion which can be solved for either the pulse response (for known near-fault seismic scenarios or to generate overturning plots to rapidly compare different mechanisms) or full time-history response. Furthermore, new developments such as a methodology to account for dynamic amplification of the ground motion up the structure, as well as a procedure to automatically detect the critical mechanisms, are also expounded upon.

The tool represents an improvement on typical code-based methods as well as analytical and numerical tools currently used in the field. Specific advantages include:

- The provision of a faster and less computationally-expensive alternative to typical numerical analysis procedures such as finite element analysis and discrete element methods, which allows for rapid comparison of different mechanisms, determination of the most vulnerable one(s), as well as prioritization of retrofit solutions.
- By making use of rocking dynamics, the tool accounts for the dynamic resistance of the structure in a more accurate manner than many current code-based assessment procedures.
- The tool's implementation in Rhino enables the equations of motion to be derived for any arbitrary geometry, and thus in contrast to most contemporary non-linear dynamic analytical methods it is not limited to simple structural geometries.
- The use of a pre-existing CAD file as input eliminates the need to generate a new model of the structure for analysis.

The ability of this new tool to provide realistic predictions for different structural geometries will be evaluated in Chapter 4, while a potential application of the tool for seismic analysis will be demonstrated in Chapter 5.

Chapter 4

Evaluation of the rigid rocking tool

4.1 Introduction

In order to assess the ability of the tool to realistically model the dynamic response of different structural geometries, a range of case studies are presented in this chapter, comprising masonry structures of varying scales and typologies such as regular buildings, monuments and temples. These case studies are experimental tests or structures which have experienced real earthquakes, and are used for evaluation of the predictions of the tool - which, depending on the type and purpose of the analysis, comprise either overturning plots or full time-histories (or both) - to actual observed behaviour.

4.2 LNEC 3-D Shaking Table Tests, Portugal

The tool's ability to provide realistic predictions was first evaluated by using it to simulate the experimental tests conducted on two masonry mock-ups in the LNEC-3D shaking table as part of a workshop on the out-of-plane assessment of existing masonry buildings (Candeias et al., 2017). The mock-ups used for the tests were U-shaped and comprised a façade with a central opening and a gable, as well as two transverse walls – one blind, and one with a window. While the first mock-up was constructed using slightly perforated clay bricks and cement-based mortar, in an English bond arrangement (Brick House, with density ρ_{br} = 1890 $\mathrm{kg\,m^{-3}}$, Fig. 4.1a), the other was made up of irregular granite stones and lime-based mortar, arranged in multiple leaves (Stone House, with density ρ_{st} = 2360 $\mathrm{kg\,m^{-3}}$, Fig. 4.1b) (Candeias et al., 2017). The Rhino models generated for each of these structures can also be found in Fig. 4.1.

Both mock-ups were subjected to unidirectional seismic loading of increasing intensity applied in a direction perpendicular to the façade. The accelerogram used for the testing was taken from the N64E strong ground motion component of the 2011 Christchurch (New Zealand) earthquake, and was filtered and cropped in such a manner so that only the most intense part of the motion remained (Candeias et al., 2017). The resulting seismic reference signal used as input in the tests is shown in Fig. 4.2. The response of both structures to this input ground motion was measured in terms of absolute

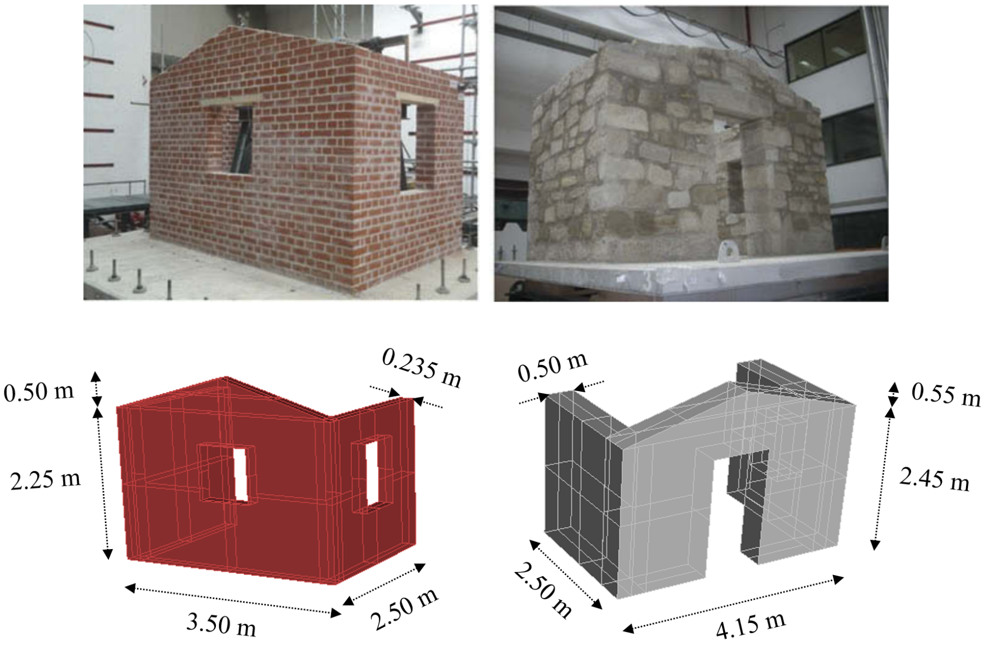

(a) **(b)**

Fig. 4.1 Shake table test mock-ups: (a) Brick House and (b) Stone House (Candeias et al., 2017)

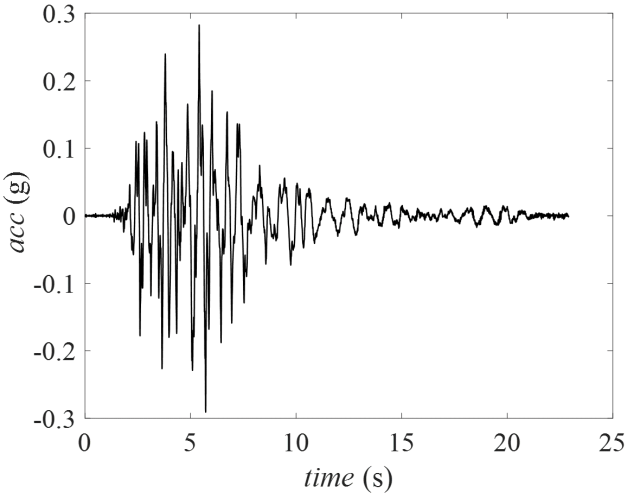

Fig. 4.2 Input ground motion (filtered and cropped) as used in the shake-table tests

accelerations (using 20 accelerometers distributed over the façade and the two transverse walls of the mock-ups) as well as relative out-of-plane displacements (using 6 linear variable displacement transducers distributed over the façade) (Candeias et al., 2017).

4.2.1 Analytical Modelling

A range of different collapse mechanisms were evaluated for both structures, as illustrated by Fig. 4.3, with the collapsed portion of the structure being highlighted in blue and the respective axes of rotation being indicated by the black lines. All the considered mechanisms are variations of the simple single block mechanism undergoing two-sided rocking, with the exception of Mechanisms 3 and 4 of the Stone House (SH_M3 and SH_M4), which undergo one-sided rocking. Note that Mechanisms 1 and 2 are identical for both structures, while Mechanisms 3 and 4 for the Stone House were selected based on the pattern of stonework within the structure, with a limit being imposed on the angle of the diagonal cracks. These mechanisms were not imposed for the brickwork due to the bonding pattern. The rocking parameters derived by the script in Rhino for these mechanisms can be found in Table 4.1. Note that the coefficients of restitution η derived for the one-sided rocking cases are negative due to the rebounding effect against the transverse walls (Sorrentino et al., 2011).

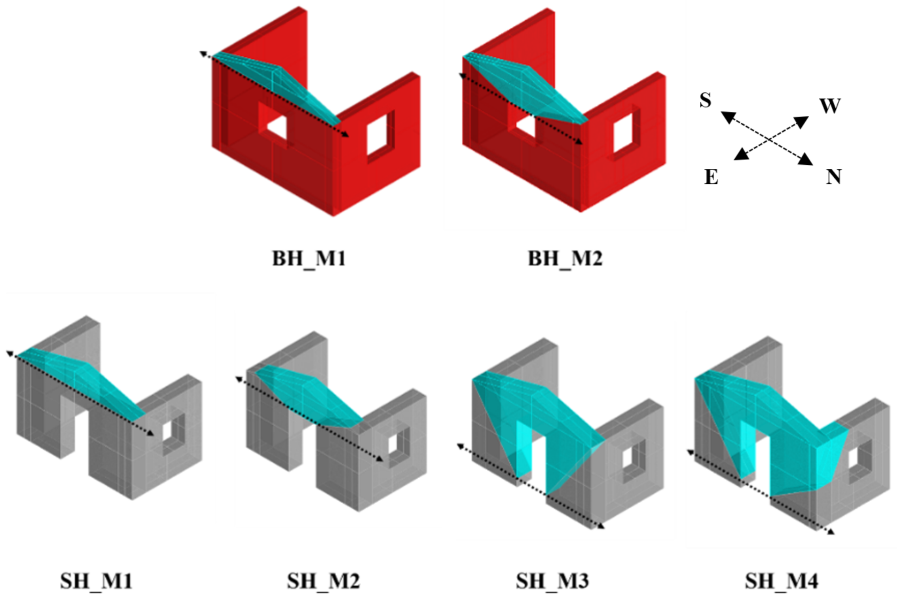

Fig. 4.3 Different mechanisms evaluated for the Brick House (BH) and Stone House (SH) mock-ups

These rocking parameters were then exported to MATLAB where the corresponding equations of motion were solved for the full time-history for different levels of scaling of the input ground motion. While most of the considered mechanisms were found to be fairly resistant to collapse, experiencing very small rotations with magnitudes in the order of 1×10^{-3} radians, Mechanism 2 of the Brick House (BH_M2, Fig. 4.4a) and Mechanism 3 of the Stone House (SH_M3, Fig. 4.4b) were observed

Table 4.1 Rocking parameters computed by the Rhinoscript for the different mechanisms

Mechanism	p_{eq} (s^{-1})	λ (rad)	η
BH_M1	5.77	0.61	0.54
BH_M2	4.16	0.26	0.89
SH_M1	4.77	0.94	0.07
SH_M2	3.84	0.49	0.65
SH_M3	2.24	0.14	-0.70
SH_M4	2.28	0.17	-0.63

to overturn for higher levels of scaling of the earthquake ground motion. To facilitate comparison with the results of the real tests (measured using the displacement transducer placed at the top center of the gable) (Mendes et al., 2017), the rotations predicted by the analytical model for both structures were converted into the corresponding displacements at the peak of the gable and are listed in Table 4.2 and Table 4.3 for the Brick House and Stone House respectively.

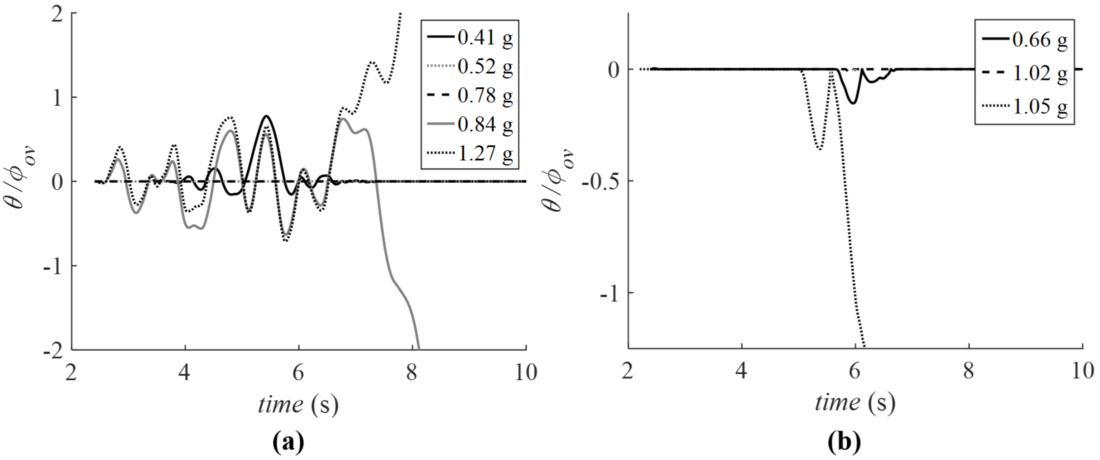

Fig. 4.4 Time-history responses for different levels of scaling (different PGAs) of the input ground motion for (a) Brick House Mechanism 2 (BH_M2) and (b) Stone House Mechanism 3 (SH_M3)

4.2.2 Comparison with experimental results

For the Brick House, the simulations of Mechanism 2 predicted relatively small response for smaller ground motions and then collapse for the 0.84g and 1.27g tests. Table 4.2 shows that for lower levels of scaling, the predictions and experimental results both indicate small displacements; the experimental results may be slightly higher due to elastic (non-rocking) displacements as well as damage accumulation due to progressive scaling of the input ground motion (de Felice et al., 2017). For the 0.41g test, rocking amplification (DeJong, 2012a) resulted in a significant over-prediction of the maximum displacement by the analytical model. This type of behaviour demonstrates the

Table 4.2 Analytical and experimental displacements obtained for the Brick House

Test	PGA (g)	Maximum relative displacement (mm)		
		BH_M1	BH_M2	Experimental
1	0.18	0.00	0.00	0.16
2	0.29	0.00	0.06	0.19
3	0.36	0.00	0.10	0.33
4	0.41	0.00	189.20	0.44
5	0.52	0.00	0.04	0.89
6	0.78	1.50	0.01	1.95
7	0.84	2.25	243.12 (c)	5.44
8	1.27	2.50	243.12 (c)	136.49 (c)

chaotic nature of the rocking response. For the 0.84g test, the analytical model predicted collapse (c) while a maximum displacement of 5.44 mm was recorded during the experiment, while the 1.27g test resulted in collapse of both the analytical model and the experimental test. Note that the displacement transducer at the top of the gable was disconnected during 1.27g test due to the partial collapse of the mock-up - resulting in truncation of this measurement and consequently a lower value for the experimentally-recorded displacement than was observed in reality (Candeias et al., 2017).

Furthermore, while the analytical model assumes that the collapse mechanism has already formed, in reality rocking is only activated after cracking of the structure - which depends in turn on factors such as the tensile strength of the mortar, as well as the degree to which the stones are interlocked. Thus in the case of the Brick House, the collapse mechanism only started to form after the 0.52g test, with rocking only initiating during the 0.84g test following the formation of a complete horizontal crack across the full length of the gable (Candeias et al., 2017). Moreover, the actual observed failure mechanism of the structure was also slightly more complex than the one predicted by the analytical model, with the asymmetry of the lateral walls inducing torsional movements in the mock-up. Thus during the final (1.27g) test, the northern part of the gable first collapsed out of plane, while the north-east pier rocked without falling and rotated around the vertical axis. At the same time, the north-west pier only rocked in-plane, and consequently due to lack of support from this pier, the lintel over the window opening on the north lateral wall collapsed vertically. Finally, the north-west pier fell towards the west, while the southern part of the gable eventually collapsed out-of-plane towards the east - that is, in the same direction as its northern counterpart (Candeias et al., 2017).

For the Stone House, the analytical simulations predicted Mechanism 3, but this was prevented from occurring in reality due to the good interlocking of the stones at the corner. Instead, interlocking of stones forced Mechanism 4 to occur. After the shaking table tests, the Stone House was found to have cracked in a pattern corresponding to this mechanism, though overturning did not occur. In fact, a comparison of the analytical predictions for SH_M4 and the experimental results (Table 4.3) reveals a reasonably good correlation between the two sets of displacements for the 0.41g and 0.66g tests.

Table 4.3 Analytical and experimental displacements obtained for the Stone House

Test	PGA (g)	Maximum relative displacement (mm)				
		SH_M1	SH_M2	SH_M3	SH_M4	Experimental
0	0.38	0.00	0.00	3.03	0.85	1.66
1	0.40	0.00	0.00	4.41	0.01	2.07
2	0.41	0.00	0.00	0.20	3.58	3.47
3	0.66	0.00	0.33	60.88	6.34	7.79
4	1.02	0.09	1.30	7.16	0.61	25.39
5	1.07	0.27	0.19	395.90 (c)	21.21	218.49

Qualitatively, for higher levels of scaling of the ground motion, it can also be observed that neither the analytical model nor the experimental test resulted in overturning of the structure. However, the maximum displacements for these last two tests were considerably underestimated by the analytical model - which could be due in part to the accumulation of damage during the shaking table tests, which the rigid rocking model was not able to fully reproduce or account for.

Furthermore, as in the case of the Brick House, the analytical model of the Stone House assumes a more simplified (monolithic) collapse mechanism than was observed in reality. Specifically, the presence of the door opening created a discontinuity in the façade, and resulted in its division into three separate elements - namely north, central and south (Candeias et al., 2017). Thus during the 1.07g test, two stones atop the north-west corner of the structure first detached and fell, while the pier they surmounted rocked in-plane. Simultaneously, the north-east corner rocked in the east-west direction - first in one piece, then split into two by diagonal cracks, while the north and south parts of the façade rocked out-of-plane around cracks which had developed on either side of the door opening. Finally, the central part of the gable also rocked out-of-plane, separated from the rest of the façade by the diagonal cracks formed on either side of the lintel stone above the door opening (Candeias et al., 2017).

Thus while this case study exemplifies the potential of this simplified method of analysis, it should be pointed out that the effectiveness of these predictions depend on realistic, feasible collapse mechanisms, which currently relies on engineering judgement and proper consideration of factors such as masonry texture, presence of openings, quality of connections at corners etc.

4.3 2015 Gorkha Earthquake

The ability of the tool to model the seismic response of real-world structures was also evaluated by using it for the analysis of a number of monuments damaged during the 2015 Gorkha earthquake. This earthquake caused a significant amount of damage in the Kathmandu Valley – leaving over 8,790 dead, 22,300 injured, and in total affecting 8 million people - almost a third of Nepal’s population (National Planning Commission (NPC), 2015). Economic losses were also catastrophic and were estimated to be approximately $7 billion – or a third of Nepal's GDP (National Planning Commission (NPC), 2015). Many buildings and other constructions in the Kathmandu Valley also sustained severe structural damage. However, unlike the 1934 Nepal-Bihar earthquake, which destroyed about 20% of the vernacular dwellings in Kathmandu, less than 1% of these structures were destroyed during the earthquake in 2015 (Galetzka et al., 2015). Nevertheless, most destruction was generally limited to low-strength stone and brick masonry structures, while many reinforced concrete buildings sustained little to no harm (Goda et al., 2015). Furthermore, taller masonry structures were observed to have been more adversely affected by the earthquake, with structures such as Kathmandu's iconic Dharahara Tower completely collapsing, despite partially surviving the earthquake in 1934 (Galetzka et al., 2015).

Photo of Basantapur Column removed for copyright reasons. Copyright holder is Alamy/AP.

(a)

(b)

Photo of Dharahara Tower removed for copyright reasons. Copyright holder is Ian Trower/JAI/Corbis & Narendra Shrestha/EPA.

(c)

(d)

Fig. 4.5 (a) Basantapur Column (Source: Alamy/AP), (b) Patan Column (Source: Jean-Francois Gornet/CC BY-SA 2.0), (c) Dharahara Tower (Source: Ian Trower/JAI/Corbis & Narendra Shrestha/EPA) before and after the 2015 earthquake and (d) Narayan Temple after the earthquake and corresponding cracking mechanism

The objective of this section is to use the tool to evaluate the behaviour of slender monuments during the 2015 Gorkha earthquake – in particular, to assess the effects of scale, slenderness and pulse duration on the dynamic response of these structures. The selected monuments comprise a column topped with a statue of the Hindu god Garuda in the Basantapur Durbar Square (referred to here as the

Basantapur Column (Fig. 4.5a)), Yogendra Malla's statue in the Patan Durbar Square (referred to here as the Patan Column (Fig. 4.5b)), the Dharahara Tower in Kathmandu (Fig. 4.5c), and the Narayan Temple in Bhaktapur (Fig. 4.5d). These particular monuments were chosen as they are relatively simple, symmetric, and of considerably varying size.

In addition to being modelled analytically by the tool, the Basantapur column and the Dharahara Tower were also modelled numerically using discrete element modelling (DEM) in 3DEC. The objective in this case was to not only evaluate simplifications made in the analytical models, but also to investigate the influence of certain parameters on the structures' dynamic response that cannot be captured analytically.

4.3.1 Analytical Modelling

Methodology

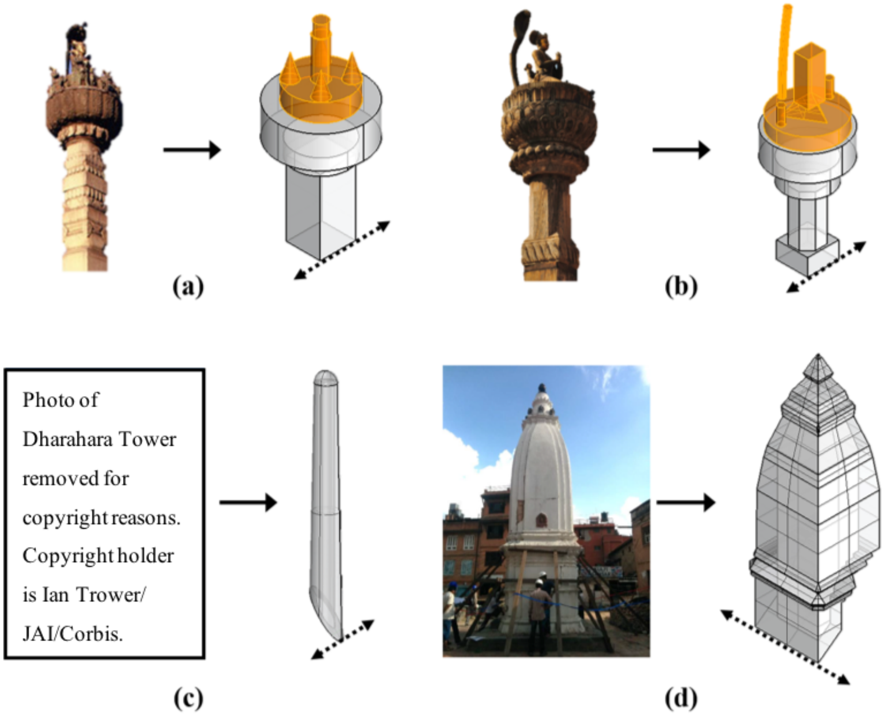

Photo of Dharahara Tower removed for copyright reasons. Copyright holder is Ian Trower/ JAI/Corbis.

Fig. 4.6 Rhino models of the collapsed portions of the (a) Basantapur Column, (b) Patan Column, (c) Dharahara Tower and (d) Narayan Temple

The Rhino models generated for each of the four monuments can be found in Fig. 4.6. Only the collapsed portions of the structures were modelled, and while the geometries of the stone segments of the Basantapur and Patan columns were recreated using survey data taken by hand, the entire

Table 4.4 Rocking parameters computed by the Rhinoscript for the different monuments

Structure	p_{eq} (s^{-1})	λ (rad)	η
Basantapur Column	2.06	0.16	0.96
Patan Column	1.84	0.15	0.96
Dharahara Tower	0.50	0.12	0.98
Narayan Temple	1.39	0.24	0.91

structural geometries of the Dharahara Tower and the Narayan Temple were reconstructed using point cloud data from the laser scanner, with this data also allowing the collapse mechanisms of the tower and temple to be easily determined. Moreover, as the bronze statues at the top of the Basantapur and Patan columns had been removed almost immediately after the earthquake, their dimensions had to be estimated using photographs and they were thus recreated using simple geometries in Rhino, as illustrated by Figs. 4.6a & b.

The collapse mechanisms of all four structures were assumed to take the form of the simple single block mechanism undergoing two-sided rocking, with the relevant axes of rotation defined by the dashed black lines in Fig. 4.6. Furthermore, as collapse of the Basantapur and Patan columns involved objects of two different densities (stone, as shown in grey in Fig. 4.6 with density ρ_{st} = 2300 $\mathrm{kg\,m^{-3}}$ and bronze, as depicted in orange in Fig. 4.6 with ρ_{br} = 8700 $\mathrm{kg\,m^{-3}}$), the script in Rhino first had the user separately select the two sets of objects, before cycling through and working out the relevant geometric properties and consequently rocking parameters, which are listed in Table 4.4 for each of the different monuments. These rocking parameters were then exported to MATLAB to generate and solve the equations of motion for the different mechanisms.

The equations of motion exported to MATLAB were solved for the full acceleration time-history of the Gorkha earthquake using the ground motion records from the USGS KATNP station in Kathmandu, as well as from the Bhaktapur (THM) and Patan (PTN) stations of Hokkaido University and Tribhuvan University (Takai et al., 2016), in both the east-west (EW) and north-south (NS) directions. The KATNP station was located approximately 1.2 km and 1.4 km away from the Basantapur Column and Dharahara Tower respectively, 4.6 km away from the Patan Column, and 12 km away from the Narayan Temple. As Fig. 4.7 illustrates, the ground motion recorded at this station was characterized by distinct high amplitude, low frequency pulses with periods of approximately 5 s and PGAs of 1.55 $\mathrm{m\,s^{-2}}$ and 1.61 $\mathrm{m\,s^{-2}}$, and was accompanied by relatively large ground displacements of 1.17 m and -1.39 m in the EW and NS directions respectively. The THM station, on the other hand, was located approximately 7.1 km and 6.5 km away from the Basantapur Column and Dharahara Tower respectively, 5.0 km away from the Patan Column, and 5.4 km away from the Narayan Temple. The ground motion recorded at this station had a number of distinct pulses, with periods of approximately 4 s and PGAs of 1.34 $\mathrm{m\,s^{-2}}$ and 1.42 $\mathrm{m\,s^{-2}}$ in the EW and NS directions respectively (Fig. 4.7). Similarly, the PTN station was found to be 1.3 km, 2.7 km, 2.1 km and 10.7 km away from the Patan Column, Basantapur Column, Dharahara Tower and Narayan Temple respectively. However the ground motion recorded at this station was characterized by higher frequency pulses and lower PGAs, with an average pulse period of approximately 3.5 s and PGAs of 1.28 $\mathrm{m\,s^{-2}}$ and 1.51 $\mathrm{m\,s^{-2}}$ in the EW and NS directions respectively (Fig. 4.7).

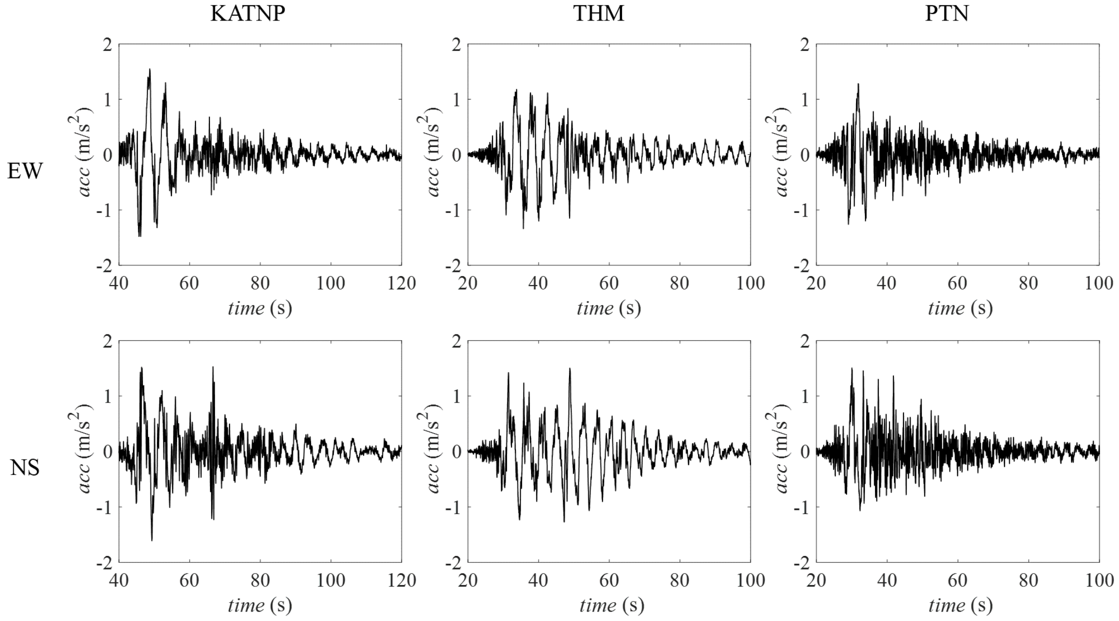

Fig. 4.7 Input ground motion as recorded at the USGS Kathmandu (KATNP), Bhaktapur (THM) and Patan (PTN) stations, in both the East-West (EW, top) and North-South (NS, bottom) directions (Takai et al., 2016)

Overturning envelopes (Section 3.3.1, Dimitrakopoulos and DeJong (2012)) were also generated for each of the structures and were used to predict the response of the monuments to the primary sine pulses isolated from the different ground motion records (Fig. 4.8). Each pulse is represented as a singular point on the overturning plot, and depending on which region of the plot it lies in, it is predicted to either cause no rocking, rocking but no overturning, overturning with impact, or overturning without impact. Furthermore, as the ground motion scaling (and consequently the isolated pulse amplitude a_p) increases, this point moves up in the plot – gradually migrating from the "safe" (no rocking/overturning) zone to the "unsafe" (overturning) zone. While this comparison does not account for the potential amplifying/de-amplifying effect of the remainder of the ground motion, it does however allow for rapid prediction of the proportion of the response that could be caused by the single maximum sine pulse alone.

Results

While all four structures were subjected to the six ground motion records depicted in Fig. 4.7, the results presented here are only for the ground motion recorded at the station closest to each site (in the dominant direction of collapse). In the case of the Basantapur Column and Dharahara Tower this

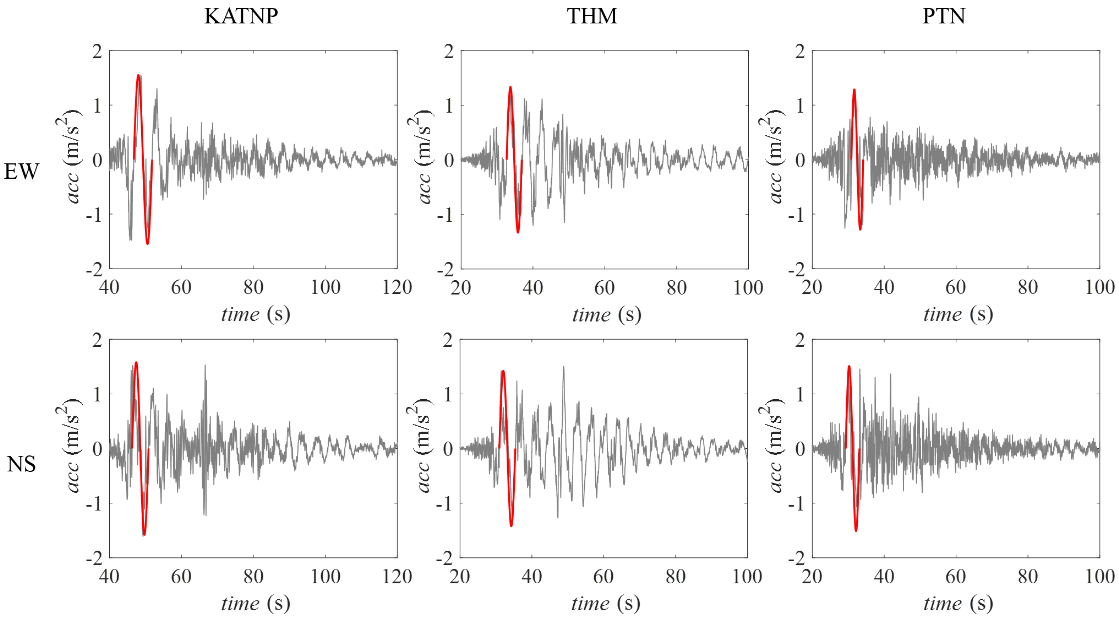

Fig. 4.8 Primary sine pulses (in red) extracted from the ground motion recorded at the USGS Kathmandu (KATNP), Bhaktapur (THM) and Patan (PTN) stations, in both the East-West (EW, top) and North-South (NS, bottom) directions (adapted from Takai et al. (2016))

was the USGS KATNP station in Kathmandu, while in the case of the Patan Column and Narayan Temple this was the Patan (PTN) station and the THM station in Bhaktapur respectively.

Basantapur Column

As collapse of the Basantapur Column occurred towards the east, the results presented here are for the EW component of the KATNP ground motion. In the case of this structure, the time-history results (Fig. 4.9a) predicted overturning of the column for scaling factors of 1.15 and higher, with overturning generally occurring when θ/ϕ_{ov} exceeded an absolute value of 1. For lower levels of scaling of the earthquake ground motion, the column was found to rock with multiple impacts before returning to equilibrium – indicating that the scaled acceleration was large enough to initiate rocking, but not large enough to cause collapse. For scaling factors of 1.15 to 1.25, the column rocked with multiple impacts before overturning, while for larger scaling factors the column overturned without impact. Moreover, while the time required for collapse generally decreased with an increase in ground motion scaling, overturning was actually observed to occur faster for the scaling factor of 1.15 than for the higher scaling factors of 1.20 and 1.25.

An overturning plot (Fig. 4.9b) was also generated, including the primary pulses isolated from the scaled acceleration records. To facilitate comparison with the time-history results, these pulses were plotted using filled circles (•) for cases where the time-history plots predicted collapse, and crosses (×) for cases where they did not. In general, good agreement was observed between both sets of results, with the overturning plot usually providing more conservative predictions – as was the case for the scaling factor of 1.10, where the overturning plot predicted collapse while the time-history indicated a return to equilibrium.

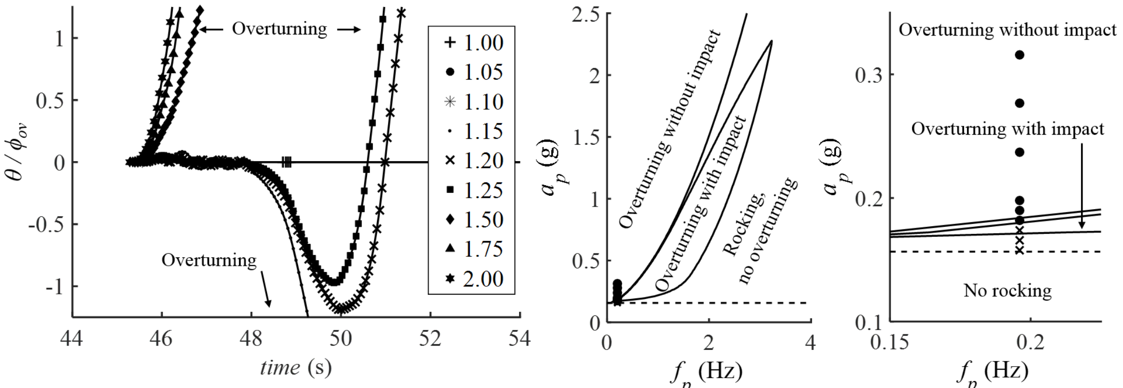

(a) (b)

Fig. 4.9 Basantapur Column: (a) time-history responses for ground motion scaling values shown, (b) overturning envelope (right figure is zoomed view of left) for same ground motion scaling values

Patan Column

As collapse of the Patan Column occurred towards the west, it was subjected to the EW component of the PTN ground motion. In the case of this structure, rocking only initiated for scaling factors of 1.15 and higher (although this is due in part to the slightly lower PGA of the PTN ground motion) with overturning of the structure taking place for scaling factors of 1.50 and above (Fig. 4.10a). For scaling factors between 1.15 and 1.25 (inclusive), the column was observed to rock with multiple low-amplitude impacts before returning to equilibrium. As in the case of the Basantapur Column, an overturning plot was also generated for the Patan Column, and the primary pulses isolated from the scaled PTN records were plotted on it. In this case, a very good correlation was observed between both sets of predictions, with the overturning plot once again yielding slightly more conservative estimates than its time-history counterpart - as exemplified by the scaling factor of 1.75, where the plot predicted overturning without impact, whereas the time-history indicated a single impact before the column overturned and collapsed.

Dharahara Tower

As collapse of the Dharahara Tower was observed to have occurred in a roughly south-western direction, the results presented here are for both the NS and EW components of the KATNP ground motion (Fig. 4.11a & b respectively). An overturning plot was also generated for the tower, which contains pulses isolated from both components of the ground motion. In the case of the time-history

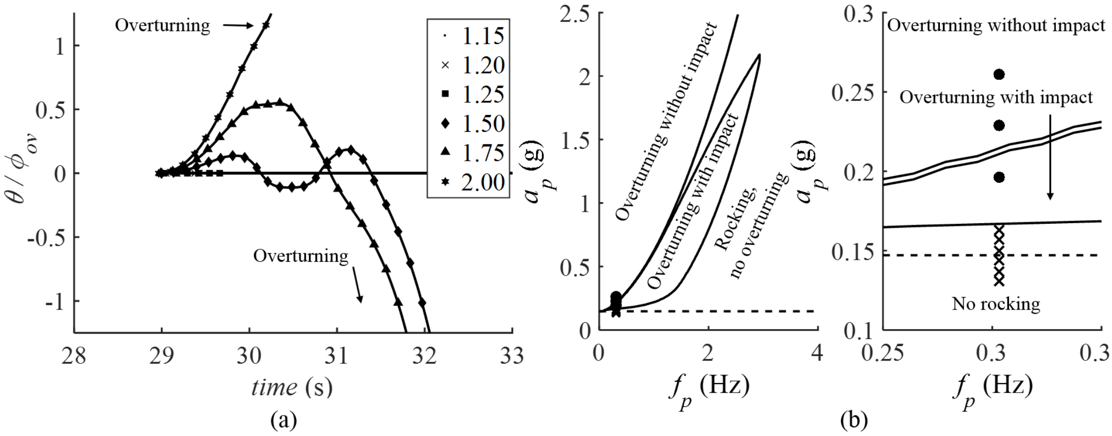

(a) (b)

Fig. 4.10 Patan Column: (a) time-history responses for ground motion scaling values shown, (b) overturning envelope (right figure is zoomed view of left) for same ground motion scaling values

results, collapse of the tower was generally found to occur for scaling factors of 1.50 and higher, with the exception of the scaling factor of 1.15, which was found to cause overturning in the NS direction as well.

For scaling factors of 1.50 and higher in both directions, the tower was found to rock with a single impact before collapsing – comparing quite well with the mode of failure predicted by the overturning plots (Fig. 4.11c). For the scaling factor of 1.15 in the NS direction, the tower was observed to rock with multiple (3) impacts before overturning indicating that more than a single sine pulse must be considered in order to predict the response. Similar behaviour was also observed in the case of the Patan Column for the ground motion scaling factor of 1.50. For ground motion scaling of 1.05 and 1.15 times and higher in the NS and EW directions respectively, the tower was found to experience rocking amplitudes greater than $\theta/\phi_{ov} = 0.4$, and rock with multiple impacts before returning to equilibrium. It is noteworthy, that although complete rigid body collapse is not predicted, the Italian building code (DMI, 2008) specifies a value of $\theta/\phi_{ov} = 0.4$ when predicting collapse of out-of-plane mechanisms in unreinforced masonry structures. Thus these very large rotation values indicate that if material failure and geometric imperfections were considered, collapse may well still occur.

Unlike the Basantapur and Patan Columns, the predictions of the overturning plots of Dharahara Tower had far more inconsistencies with their time-history counterparts, with the former once again yielding more conservative results. Moreover, dashed lines demarcating the threshold acceleration below which no rocking occurs were added to each of the overturning plots and it can be seen that in the case of the columns in particular, the region in which the structures go from no rocking at all to complete overturning is extremely small – highlighting the importance of the long pulse present in the Nepal earthquake ground motion.

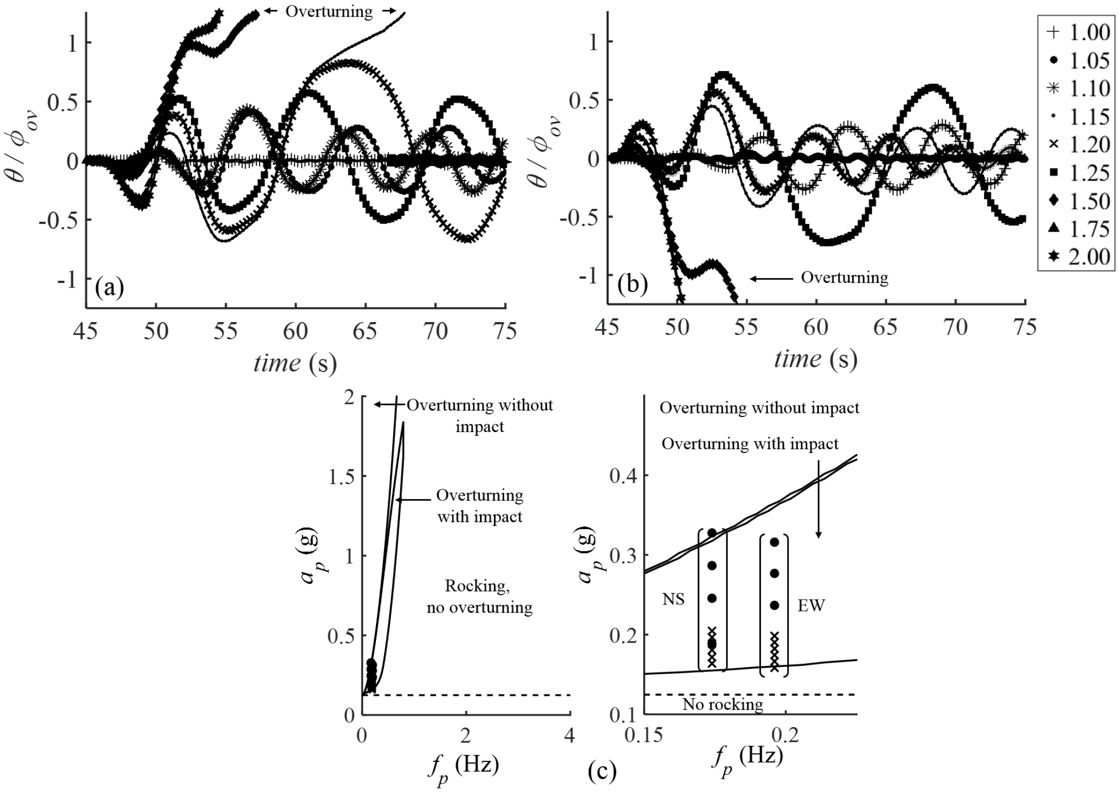

Fig. 4.11 Dharahara Tower: time-history responses for ground motion scaling values shown in both the (a) NS and (b) EW directions; (c) overturning envelope (right figure is zoomed view of left) for same ground motion scaling values

Narayan Temple

As the principal axis of the Narayan Temple is oriented along the NNE-SSW direction, and the main cracks were observed to occur on the south-eastern façade (Menon et al., 2017), the results presented here are for the NS component of the ground motion recorded at the THM station. From the time-history results (Fig. 4.12a) it can be seen that rocking of the structure only initiates for scaling factors of 1.75 and higher, while overturning of the structure does not occur for any of the considered scaling factors. For both the scaling factors of 1.75 and 2.00, the temple undergoes low-amplitude, high-frequency rocking before returning to equilibrium. In fact, the maximum rotation experienced by the temple is for the scaling factor of 1.75, and corresponds $\theta/\phi_{ov} \approx 0.004$. However, this small rotation is still most likely an overestimate, as the assumption of two-sided rocking for the temple is conservative – in fact, two-sided rocking would require formation of the identical mechanism in the opposite direction, which would result in far more energy dissipation than is assumed here.

An overturning plot was also generated for the temple and the primary pulses isolated from the scaled acceleration records were plotted on it (Fig. 4.12b). In general, a fairly good correlation was observed between the predictions of the overturning plot and the time-history results, with the exception of the scaling factor of 2 - for which the overturning plot predicted collapse while the time-history indicated a return to equilibrium.

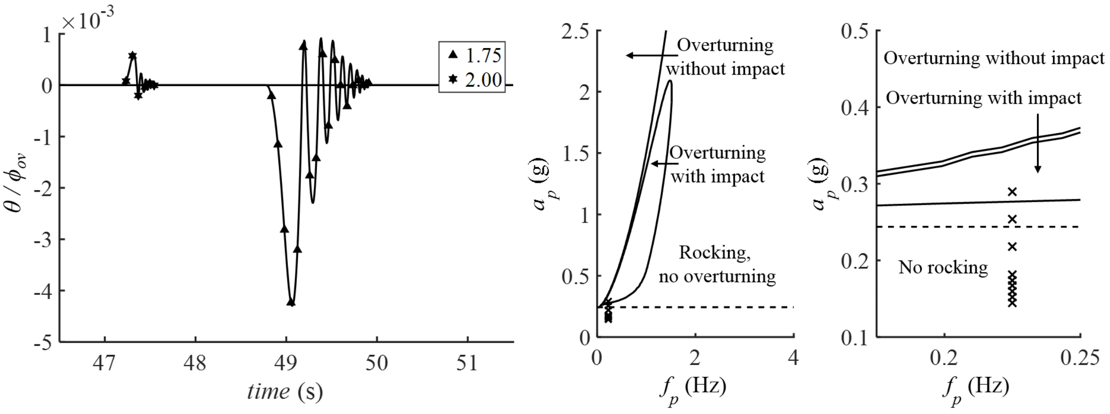

Fig. 4.12 Narayan Temple: (a) time-history responses for ground motion scaling values shown, (b) overturning envelope (right figure is zoomed view of left) for same ground motion scaling values

In order to compare the responses of the four structures to the ground motion recorded at each of the different stations, bar graphs were also generated showing the minimum scaling factors required for rocking to initiate (Fig. 4.13a) and overturning to occur (Fig. 4.13b) for each structure, for each of the acceleration records provided in Fig. 4.7. From Fig. 4.13a it can be seen that the Dharahara Tower (DT), being the most slender, starts rocking for lower scaling factors than the Narayan Temple (NT) or even the Basantapur and Patan Columns (BC, PC). Nevertheless once rocking initiates, the

Basantapur and Patan Columns, due to their smaller size, generally overturn for lower scaling factors than either the tower or the temple (Fig. 4.13b).

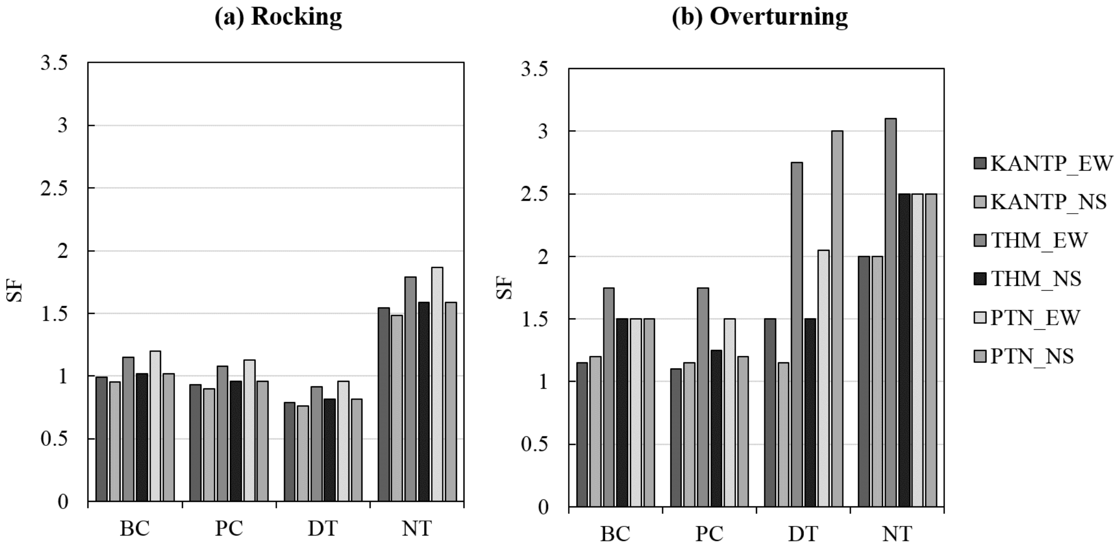

Fig. 4.13 Scaling factors required to (a) initiate rocking and (b) cause overturning of each of the four monuments, for the different ground motion records

4.3.2 Numerical Modelling using DEM

While the analytical models provide a very quick and computationally-inexpensive way of modelling the global seismic response of the selected monuments, they are not capable of predicting the more complicated features of dynamic collapse of multi-block structures, which can be influenced by block stereotomy and local block displacements (DeJong and Vibert, 2012b). Thus computational analyses were also conducted using discrete element modelling (DEM) in 3DEC to investigate certain aspects of the dynamic response not considered by the simplified analytical models. In addition to validating the analytical results, parametric studies are also conducted to assess the influence of factors such as the column embedment depth and joint stiffness, and in the case of the Dharahara Tower the effect of the pedestal and joint tensile strength, on the dynamic response.

Methodology

Basantapur Column

The 3DEC model of the Basantapur Column was directly generated from the CAD file created for the analytical modelling of the structure. Rigid blocks were used in the analysis, and their material properties were assumed to be those of stone for the column itself and bronze for the statue on top (see Table 4.5). The joint stiffnesses were calculated individually for each joint based on the Young's

Table 4.5 Block material properties

Property	Stone	Bronze	Brick
Density, ρ ($\mathrm{kg\,m^{-3}}$)	2300	8700	2000
Young's modulus, E (GPa)	45	108	4.75
Poisson's ratio, υ	0.25	0.34	0.25

modulus of the materials involved and the distance between the interfaces. A friction angle of 35° was specified for all joints, which falls within the range of values reported in Barton (1976) for rock joints, except at the base where a larger angle of 80° was adopted to account for the presence of the tenon and mortise joints observed on site. The joints were also assumed to have no tensile strength or cohesion, as the column was made of dry stone masonry with no mortar.

Stiffness-proportional Rayleigh damping was used for the dynamic simulations in order to damp out the influence of unrealistic high-frequency vibrations (DeJong, 2009), with a damping constant of 1.96×10^{-4} being specified, while mass damping was set to zero. For both the column and the Dharahara Tower, the earthquake loading was applied simultaneously in both cardinal directions using the acceleration data from the KATNP station in Kathmandu (Figure 4.7). The vertical component of the ground motion was not applied, as its influence is practically negligible for heavier blocks (Gazetas et al., 2012). Furthermore, as dynamic analyses can be computationally expensive and fairly time-intensive, the analyses in 3DEC were run for the most destructive 20 seconds of the record, beyond which the ground motion was so small that it was found to have a negligible effect on the results.

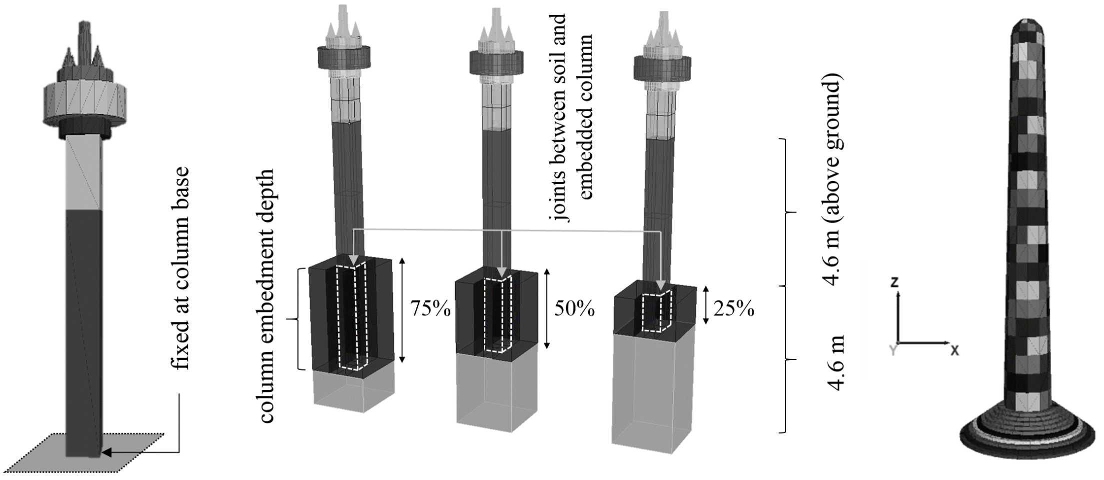

(a) **(b)** **(c)**

Fig. 4.14 (a) Fixed base column 3DEC model; (b) Embedded base column 3DEC models; (c) Dharahara Tower 3DEC model (final discretized geometry)

In the first set of analyses, the base column was assumed to be embedded deep enough into the ground that it could be treated as fixed (Figure 4.14a) – which was also the assumption made in the analytical model (see results in Figure 4.9). The results from these analyses were thus used to validate the predictions of the analytical model. The second set of analyses used the Basantapur Column to investigate the influence of the column embedment depth and joint stiffness at the embedment on the stability of the structure. In order to do this, the base column was no longer assumed to be fixed and the 4.6 m of the column visible above the ground was kept constant, while the length of the column below the ground was varied from 25% to 75% of the length above ground (Figure 4.14b). Furthermore, the joint stiffness calculated at the embedment was divided by factors of 1, 10 and 100 in order to simulate different soil conditions and gauge how the softening of the joints at the base affects the response of the structure. The ground motion in this case was not scaled as the objective was to evaluate the responses by comparing the maximum rocking rotation.

Dharahara Tower

The 3DEC model for the Dharahara Tower was also generated using the CAD file created for the analytical modelling. However, unlike the columns which were made up of a few individual large blocks which could directly be modelled in 3DEC, the brick masonry tower was discretized into relatively large blocks to decrease computation time. Thus the shaft of the tower was divided into twenty 3.0 m high layers, with each layer containing 12 blocks joined in pairs of two in such a manner as to ensure some degree of interlocking over the height of the structure. The widths and thicknesses of the individual blocks making up each layer gradually decreased in line with the tapering form of the tower. The final discretized geometry is illustrated in Figure 4.14c.

Rigid blocks were once again used in the analysis. Typical material properties of clay brick masonry with lime surkhi mortar were assumed for the tower (Table 4.5, Rai and Dhanapal (2013), Kaushik et al. (2007)), while typical properties of stone were assumed for the pedestal upon which the tower sits. The joint stiffnesses were calculated based on the Young's moduli of the interface materials and the distance between joints, while a minimal joint tensile strength of 1.00 kPa was assumed in order to account for the mortar as well as eliminate disintegration throughout the tower and thus more realistically model its collapse – although the magnitude of this tensile strength was later varied in order to gauge its effect on the response of the structure. A friction angle of 35°, which falls within the range of values determined experimentally by Atkinson et al. (1989), Drysdale et al. (1979), Stockl and Hofmann (1986), and Capozucca (2011) for clay brick masonry with mortar, was defined for all the joints. Parametric studies were also conducted to analyse the effect of ground motion scaling on the tower's dynamic response, as well as the influence of the pedestal. Stiffness-proportional damping was again used for the dynamic analysis, with a damping constant of 1.85×10^{-4} being specified for the structure.

Results

Basantapur Column

In the case of the Basantapur Column, the fixed base column model was used for comparison with the predictions of the analytical model. In general it was found that the collapsed portions of the column did not behave as multiple sliding and rocking surfaces, and instead rocked monolithically – thereby confirming the simplified assumptions of the analytical model. To better facilitate comparison with the analytical results, the time-history responses of the computational model were plotted in terms of the variation of the maximum rotation of the column over time, with the rotation being expressed as a fraction of the overturning rotation ϕ_{ov}. As Figure 4.15 illustrates, the analytical and computational results were observed to be in fairly good agreement for the ground motion scaling levels shown.

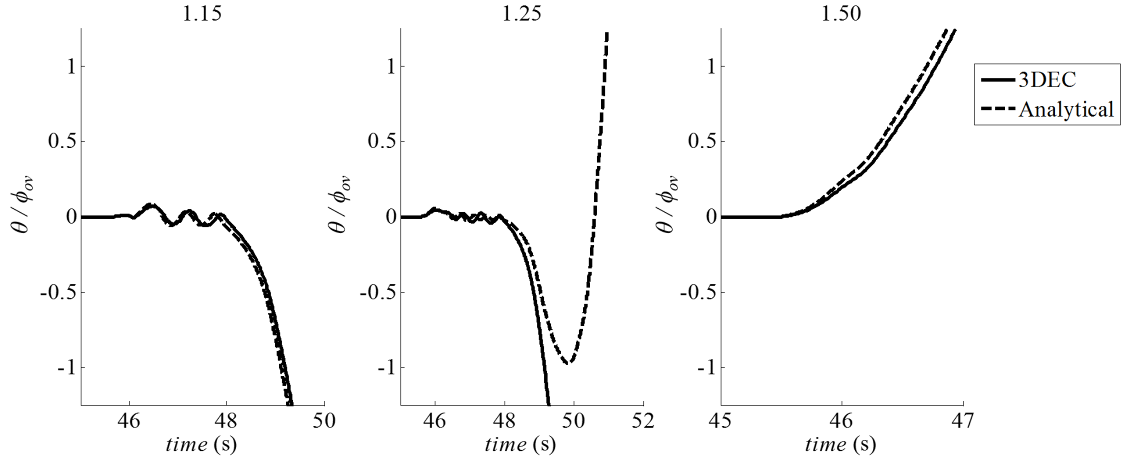

Fig. 4.15 Comparison between 3DEC and analytical time-history results for the fixed-base model of the Basantapur Column

The second set of analyses conducted on the model of the Basantapur Column evaluated the effect of column embedment depth and the related embedment joint stiffness (k_j) on the dynamic stability of the structure. Figure 4.16a shows that decreasing the embedment depth leads to an increase in the maximum rocking rotation of the column, while decreasing the joint stiffness at the embedment (in this case dividing it by factors of 10 and 100) also leads to a significant increase in the rocking response (Figure 4.16b). The extent to which these factors contributed to the response of the real structure cannot be conclusively determined without a more detailed geotechnical investigation, but it is clear that rotation of the column due to embedment could well have increased the rocking response of the upper part of the structure. During the field survey, a gap was noticed between the base of the column and surrounding paving stones, indicating that some rotation of the embedded column did occur. This provides an additional explanation as to why the simulation results for the actual ground motion predict a marginally smaller response than the collapse that occurred.

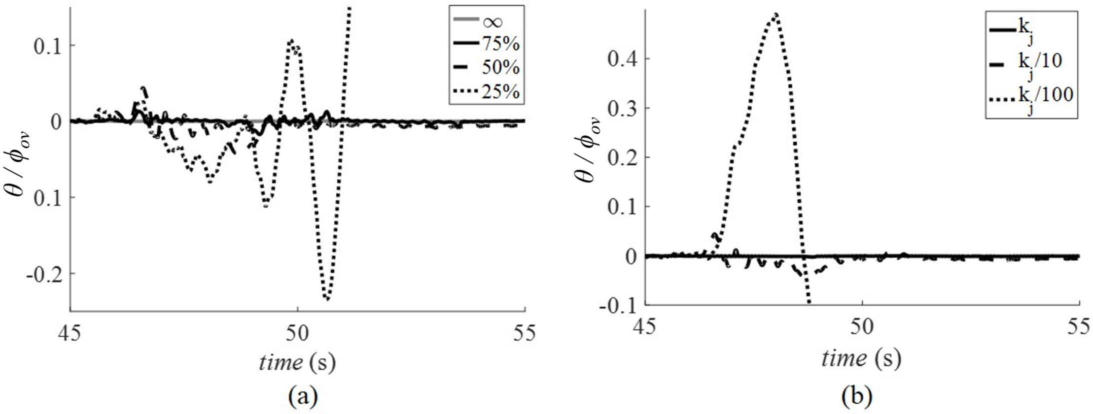

(a)

(b)

Fig. 4.16 (a) Effect of embed depth on response (for case where joint stiffness is reduced by factor of 10) (b) Effect of joint stiffness on response (for 50% embedment case)

Dharahara Tower

In the case of the Dharahara Tower, the results from the computational analyses were compared both to the predictions of the analytical model, as well as corroborated with field observations, according to which the tower first cracked diagonally and rotated towards the south east, before eventually collapsing in a south-western direction.

The first set of computational analyses evaluated the influence of ground motion scaling on the dynamic response of the tower. From this analysis it was found that when the acceleration data is scaled by a factor of 1.50, the computational model of the tower first rotates towards the north-east before a pulse in the opposite direction causes ground displacement towards the south-west, resulting in most of the debris falling in this direction (Figure 4.17) – which corresponds quite well with the final failure mode of the tower.

Varying the level of scaling of the earthquake ground motion was found to affect both the direction of collapse as well as the height at which the tower cracked – as illustrated by Figure 4.18. A decrease in ground motion scaling was observed to increase the height at which the crack occurred, and consequently decrease the size of the collapsed portion of the tower, while the direction of collapse appeared to follow a clockwise pattern – with the collapse direction progressively changing from south-east (for a scaling factor of 2) to north-west (scaling factor of 1).

As the Dharahara Tower experienced significant displacements in both cardinal directions, the time-history results are plotted in the form of displacement traces on a horizontal X-Y axis, as illustrated by Figure 4.19. The displacements are tracked at both the top center of the tower (T), as well as at the base (B) for the different levels of scaling of the earthquake ground motion. The diameter of the tower is also plotted in the form of a grey filled circle, which allows the magnitude of the displacements to easily be compared to the original diameter of the tower, while the grey arrow indicates the actual direction of collapse. From Figure 4.19 it can be seen that for all ground motion

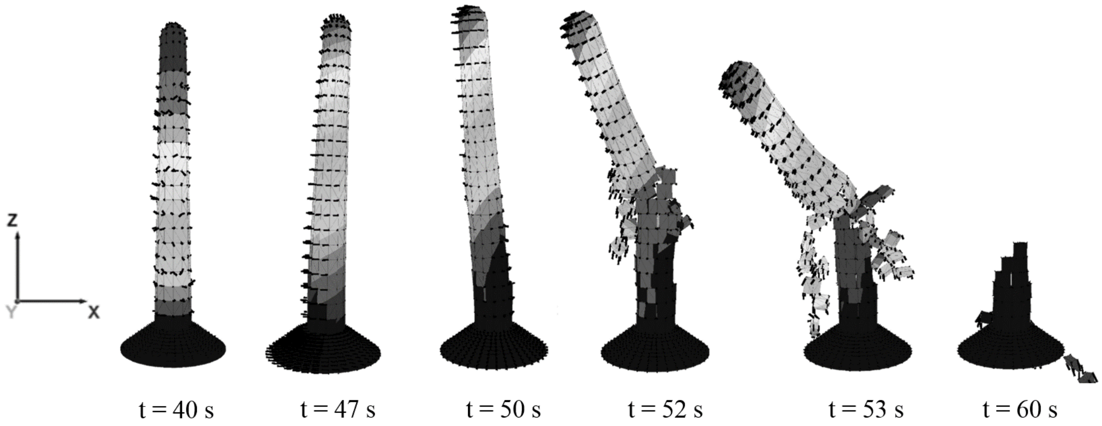

Fig. 4.17 Progressive collapse of Dharahara Tower for ground motion scaling of 1.50

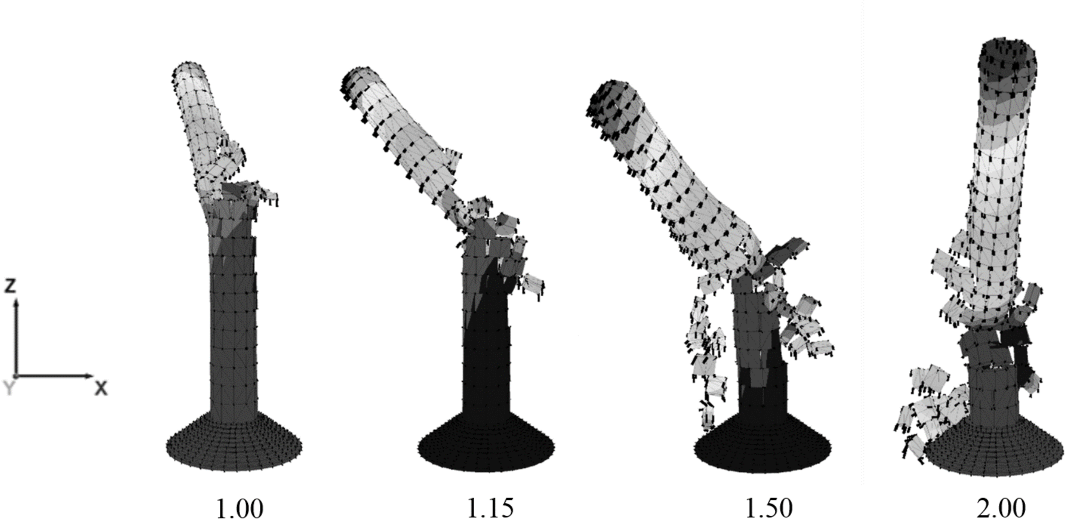

Fig. 4.18 Comparison of failure modes for different ground motion scaling levels

scaling levels both the base and the top of the tower appear to follow a similar swirling pattern, with the displacement magnitude generally increasing with an increase in scaling. Furthermore the magnitude of the displacement at the bottom of the tower starts off as fairly large at first (and in the case of the scaling factor of 2 is almost equal to the radius of the tower) before gradually decreasing, while the response at the top continuously increases in magnitude. The dominant collapse directions for the different scaling levels are also more clearly indicated by Figure 4.19 - reiterating the observations from Figure 4.18 about the different failure modes of the tower.

Parametric studies were also conducted to gauge the influence of joint tensile strength and the pedestal on the response of the tower. However, varying these parameters was found to have a relatively minor effect on the tower's dynamic behaviour, and thus the results have not been presented here.

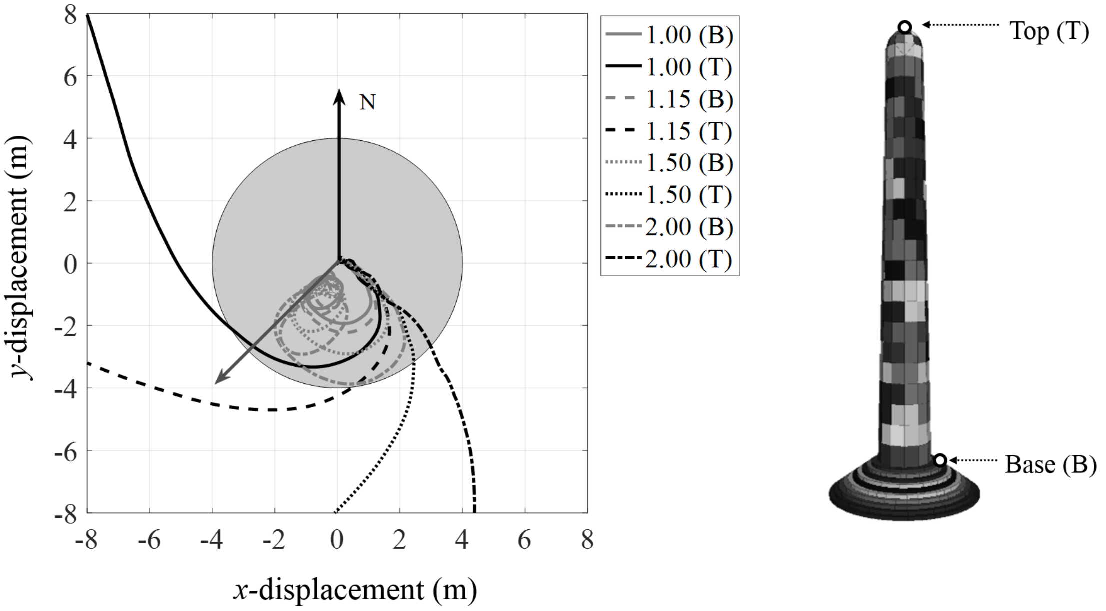

Fig. 4.19 Effect of ground motion scaling (joint tensile strength = 1 kPa, grey arrow indicates actual collapse direction)

4.3.3 Discussion

Importance of ground motion pulse

The resistance of objects to overturning is influenced by both their slenderness and size. While the slenderness of a structure determines when rocking initiates, the magnitude of rotation, and ultimately collapse, is governed by its size (as was illustrated in Fig. 4.13). Thus smaller objects can overturn without an obvious long duration pulse, while larger objects generally require a longer duration (lower frequency) pulse in order to generate enough rotational momentum to overturn and collapse – an observation which is also supported by the findings of this chapter. A comparison of the overturning plots for the selected structures reveals that the Dharahara Tower, with its considerably larger size, required a significantly longer pulse than any of the other monuments in order to overturn (Fig. 4.20). In the case of the Nepal earthquake ground motion, the primary pulse alone was large enough to cause overturning of both the tower and the Basantapur and Patan Columns, without taking into account any additional effects. Thus the large low-frequency content within the Nepal earthquake ground motion made slender unreinforced masonry structures particularly vulnerable to overturning, while structures of moderate size had their dynamic resistance almost completely eliminated by the long-duration pulse. In fact, any structure with a slenderness less than the amplitude of the dominant pulse extracted from the earthquake ground motion would have been in danger of collapse. Conversely, this could provide an explanation as to why the Narayan Temple, despite being of moderate size, did not overturn and collapse, as it was nearly twice as stocky as the tower, and 1.5 times as stocky as the columns (Table 4.4). Essentially, the additional dynamic resistance to overturning typically characteristic of rocking motion (Doherty et al., 2002) was essentially non-existent for this particular ground motion. In other words, the Italian building code (DMI, 2008) assessment method of predicting overturning to occur at ground accelerations equal to a multiple (typically 2) of the PGA, would have been extremely un-conservative here. The proper multiple would have been 1 for this earthquake, despite the fact that a value of 2 is usually conservative for typical ground motion recordings (particularly in Italy).

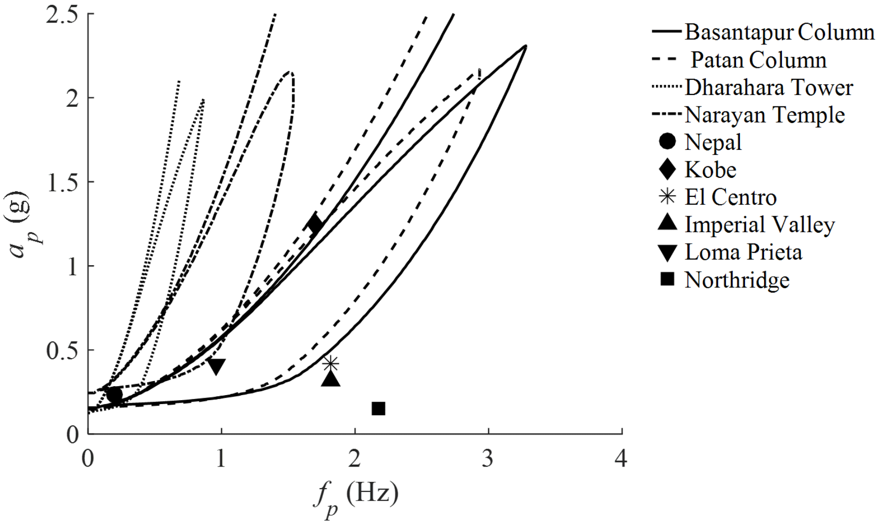

Fig. 4.20 Comparison of the overturning plots for the selected monuments, and their predicted response to pulses isolated from different major earthquakes

This detrimental effect of the long-duration pulse present within the Nepal earthquake ground motion is better illustrated by comparing the predicted response of the four structures to the primary pulses isolated from different major earthquakes. From Fig. 4.20 it can be seen that despite their large magnitudes, none of the other earthquakes have a pulse large enough or long enough to cause the overturning of the Dharahara Tower or the Narayan Temple, and only a few have pulses long enough to cause the Basantapur and Patan Columns to overturn. The scale effect becomes directly evident from this plot.

It should however be pointed out that this type of overturning failure is distinctly different from collapse caused by resonance, or by cumulative material failure causing excessive damage due to repeated cyclic loading. These types of failure are much more sensitive to the spectral acceleration at the natural frequencies of the structure. While elastic resonance can cause large base shears and subsequent damage, it cannot directly cause large rotations and overturning collapse. This provides some evidence as to the nature of the ground motion that caused only the top portion of the Dharahara Tower to collapse during the 1934 earthquake (as opposed to completely overturning around the base). Any distinct long-duration ground motion pulse, if present, would have had to have been of shorter period or lower amplitude than that observed in 2015. As a result, larger higher frequency excitation, accompanied by elastic amplification, might have played a larger role in the observed damage in 1934.

Comparison of analytical time-history and overturning plot results

A comparison between the analytical time-history responses and the predictions of the sine pulse overturning plots enables further discussion about the dominance of the long period pulse. For three out of four of the analysed monuments there were instances when the overturning plots predicted collapse when the time-history analyses did not. Possible reasons for this follow.

Firstly, to extract the pulse information from the Nepal earthquake ground motion, a single sine pulse was fit to the most destructive pulse in the acceleration data. However the actual earthquake time-history contains higher frequency content, as well as several cycles of long-period motion as opposed to just a single pulse. Thus the presence of high frequency content combined with the imperfect fitting of the sine pulse could be one reason for the discrepancy between the time-history responses and predictions of the overturning plots.

Furthermore, the multiple cycles of long period pulses present in the acceleration data could have had an amplifying or de-amplifying effect on the response of the structure – depending on the phase of rocking relative to the ground motion. This behaviour can be quantified in terms of the rate of energy input into the system (DeJong, 2012a), which for the linearised equation of motion presented earlier (Equation 3.9) is:

$$\frac{\partial E}{\partial \tau} = -MR\ddot{u}_g\theta' \tag{4.1}$$

where E is the total energy, τ is dimensionless time and θ’ is the rotational velocity of the structure. From Equation 4.1 it can be seen that the rate of energy input is positive only if the current rotational velocity and ground motion are opposite in sign (DeJong, 2012a). Thus maximum energy input (i.e. amplification resulting in overturning) is attained when the input ground motion (acceleration) is always opposite in sign to the rotational velocity, while removal of energy from the system (and subsequently de-amplification) takes place when the acceleration and rotational velocity are the same sign.

This de-amplifying effect is best illustrated by studying the response of the Dharahara Tower to the KATNP NS ground motion record scaled by a factor of 1.25. As Fig. 4.21a demonstrates, the rotational velocity and ground acceleration are initially perfectly out of phase, resulting in energy being input into the system thus causing an increase in the rocking amplitude of the tower. This is followed by a subsequent removal of energy from the system (de-amplification) by the pulse that followed, as a result of which the rocking amplitude of the tower never exceeded 0.5 α. Then, as the magnitude of the input acceleration decreased so did the rotation of the structure, resulting in a return to equilibrium despite the predictions of the overturning plot.

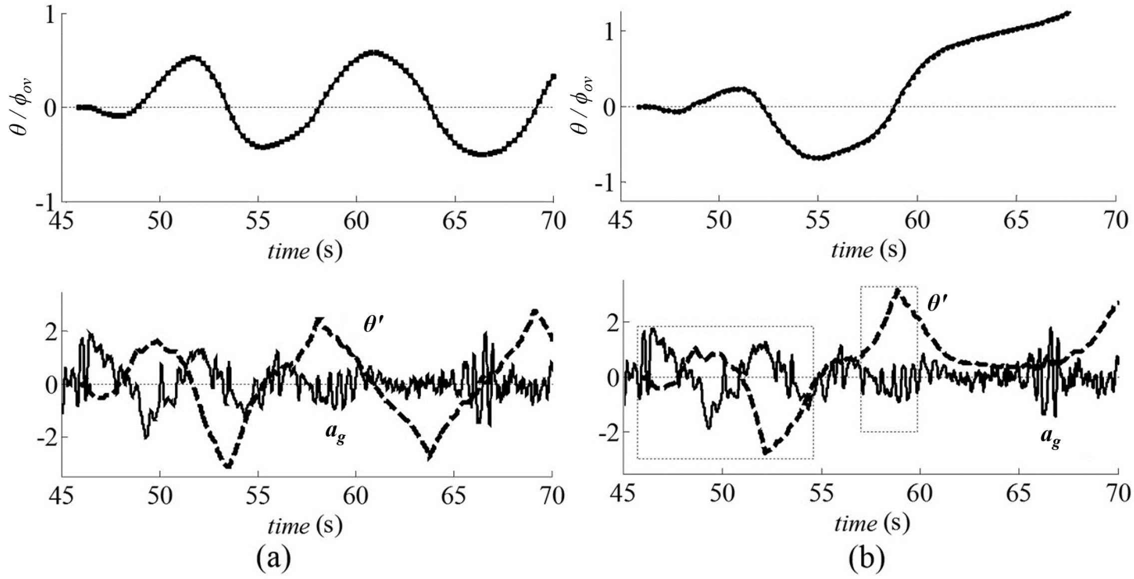

Fig. 4.21 Comparison of the rotation (top), acceleration and angular velocity (bottom) time-histories for the Dharahara Tower: (a) scaling factor of 1.25; (b) scaling factor of 1.15

While rocking de-amplification can explain why the overturning plots predicted collapse while the time-history analyses did not, rocking amplification could account for those cases where the structure overturned faster than expected – as was observed for the Basantapur Column for scaling factors of 1.15, as well as for the Dharahara Tower for a scaling factor of 1.15 in the north-south direction (Fig. 4.21b). As Fig. 4.21b illustrates, the tower experienced some initial amplification between 45-55 seconds, which initiated the large rotation of the structure. This was followed by a second amplification between 57-60 seconds, which added energy to the system thus leading to the overturning of the tower for lower ground motion scaling than in Fig. 4.21a.

The similarity between Figs. 4.21 a & b indicates that once the large rocking response of the structure commences the overturning collapse can be very sensitive to the ground motion, with minor differences in phase affecting the outcome. For the most part however, the sine-pulse overturning envelopes were found to be sufficient for predicting the collapse of the three monuments, with the rest of the ground motion generally de-amplifying the rotation of the structure rather than amplifying it.

Comparison of analytical and numerical (DEM) results

A comparison between the analytical time-history results and predictions of the computational (3DEC) model revealed a fairly good correlation between both sets of results for the Basantapur Column. For scaling factors of 1.15 and 1.50 the 3DEC and analytical results seemed to match almost exactly, while for the scaling factor of 1.25 the analytical model appeared to recover from a fairly large rotation before overturning about 2 seconds after the 3DEC model. This discrepancy could be due to the de-amplifying effect of the ground motion presented earlier, as well as the fact that both the NS and EW ground motion records were simultaneously applied to the computational model while the analytical model was subjected to the EW ground motion record only.

Comparison of analytical and numerical (DEM) results with field observations

From the analytical time-history results it was found that while rocking generally initiated for the Basantapur and Patan Columns and the Dharahara Tower for all levels of scaling of the input ground motion, overturning only occurred for scaling factors of 1.15, 1.10 and 1.50 and higher for the Basantapur Column, Patan Column and Dharahara Tower respectively (overturning of the tower for the scaling factor of 1.15 in the NS direction due to rocking amplification has already been discussed). Similarly, rocking of the Narayan Temple only initiated for scaling factors of 1.50 and higher, with overturning collapse only taking place when the ground motion was scaled by a factor of 2.00 or greater (Fig. 4.13).

However, collapse of the columns and tower (and initiation of rocking of the temple) obviously occurred for a scaling factor of 1, and the differences between the predictions of the time-history plots and what was observed in reality could be due to a number of factors. Firstly, the local ground motion at the site could have been different from what was recorded at the USGS KATNP, PTN and THM stations. All four monuments were situated in the Kathmandu Valley and would therefore have experienced similar long period effects, however they were separated by up to 12 km and could also have been subjected to local site effects. Furthermore, errors in estimating the mass and geometry of the structures when creating the Rhino models could have contributed to these discrepancies as well.

In the case of the Dharahara Tower, failure also involved some slipping of the tower off the pedestal which was not predicted in 3DEC due to the pre-defined block discretization which did not allow a true diagonal crack as observed in reality, while local crushing during rocking could have taken place as well.

Additionally, due to the tower's size and slenderness, elastic effects might not have been negligible. Thus an elastic analysis was also conducted wherein the possibility of elastic resonance due to modal amplification was investigated. Using Lord Rayleigh's principle, the natural frequency of the tower was calculated for the Young's modulus value specified in Table 4.5, as well as a range of density values, and was found to range between 0.64 – 0.83 Hz or 1.21 – 1.56 seconds, which is far from the 4 – 6 second dominant peak in the ground motion response spectra. Nevertheless, elastic resonance would have only initiated rocking earlier – it would not alone have caused complete overturning collapse about the base. This possibility of elastic resonance initiating rocking earlier, and consequently reducing the pulse amplitude required to cause collapse – especially in the region of the overturning plot where the Nepal earthquake pulse sits (Acikgoz and DeJong, 2012) - also supports the result that the (analytical) time-history results were un-conservative. The assumption of rigid blocks is less likely to be a source of error for the Basantapur and Patan Columns however, as the response of these solid stone monuments would probably be almost completely unaffected by elastic response.

Furthermore, due to the soft soil in the Kathmandu Valley basin, soil-structure interaction effects might not have been negligible. In the case of the Basantapur Column, the embedment of the column in the ground was also observed to cause some rotation at the base which in turn affected overturning at the height at which it occurred. While this behaviour was not reproduced analytically, the analyses conducted in 3DEC did corroborate these field observations.

Accounting for amplification effects

As the collapse mechanisms of the Basantapur and Patan Columns occurred at a height above ground level, amplification effects might not have been negligible and could also account for the discrepancies between the original predictions of the analytical model and what was observed in reality.

To this end, using the methodology outlined in Section 3.4.1, appropriate scale factors SF were determined for both columns. In order to do this, the natural frequencies f_n and modal heights h_e of the columns were first determined by treating the surviving 4.60 m of both structures as cantilevers, and the collapsed portions as point loads on top. Using Lord Rayleigh's principle as in DeJong (2012b) and assuming Young's modulus E_{st} = 45 GPa as specified in Table 4.5, the modal heights h_e were determined to be 4.54 m and 4.56 m for the Basantapur and Patan Columns respectively, while f_n was estimated to be 7.7 Hz and 6.5 Hz - leading to natural periods T_n of 0.13 s and 0.15 s respectively. As the input ground motion is applied at the base of the collapsed portion of the structure (and consequently the top surface of the surviving portion of the column), h is therefore 4.60 m for both columns.

The acceleration response spectra were then generated for both the KATNP and PTN ground motion records (assuming 5% damping), as illustrated by Fig. 4.22. From these graphs, the spectral accelerations S_a at T_n were determined to be 0.19 g for the Basantapur Column and 0.21 g for the Patan Column - as indicated by the red dots in Fig. 4.22. Using Equation 3.48, the scale factor was then calculated, and was found to be 1.6 and 1.9 for the Basantapur and Patan Columns respectively. Given that the Basantapur Column was found to overturn for ground motion scaling of 1.15 times and higher, a scale factor of 1.6 would almost certainly cause collapse of the structure. Similarly, the Patan Column was observed to overturn for ground motion scaling of 1.5 times and higher, thus applying a scale factor of 1.9 to the input ground motion would cause collapse as well. A comparison of these

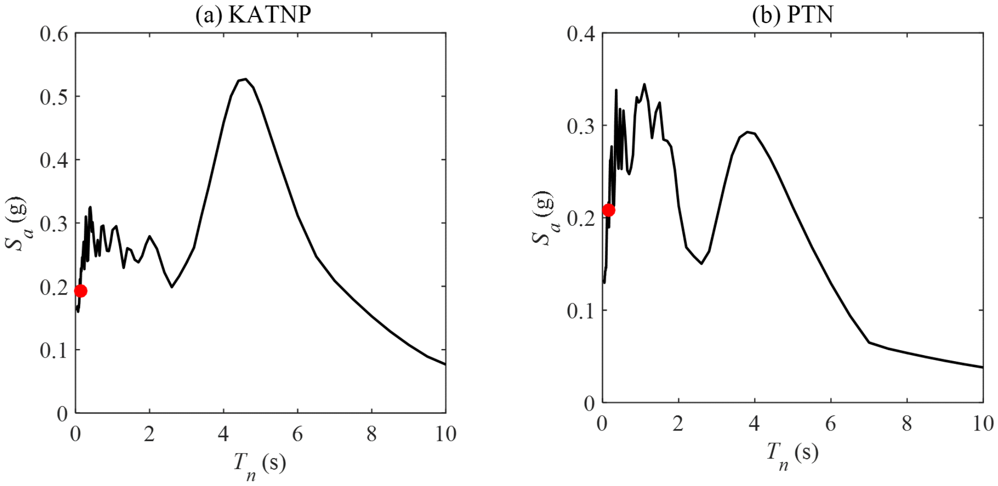

Fig. 4.22 Elastic acceleration response spectra generated (assuming 5% damping) for the (a) KATNP and (b) PTN ground motion

Table 4.6 Comparison of the scale factors computed by the different methods for the Basantapur and Patan Columns

Structure	Proposed Method (Equation 3.48)	Eurocode 8 (Equation 3.49)	NZS 1170.5 (Equation 3.50)
Basantapur Column	1.6	2.9	1.8
Patan Column	1.9	2.9	1.8

scale factors with those determined using code-based methods found them to be considerably lower than the scale factor of 2.9 calculated using the method presented in Eurocode 8 (EN 1998-1, 2004), and comparable to the scale factor of 1.8 determined using NZS 1170.5 (NZS, 2004) (Table 4.6).

Using the values of h_e, h and f_n determined above, the methodology presented in Section 3.4.1 was also used for scaling the overturning plots of both columns. A comparison of the scaled and unscaled plots (Fig. 4.23) demonstrates that accounting for amplification effects results in an overall reduction in the minimum pulse amplitude required for overturning to occur for all considered pulse frequencies, thus decreasing the dynamic resistance of the structures. This is better illustrated by once again comparing the response of these structures to the primary pulses isolated from the different major earthquakes. As Fig. 4.24 demonstrates, in addition to the pulses isolated from the Nepal, Kobe and Loma Prieta earthquakes, accounting for amplification effects now makes the Basantapur and Patan Columns vulnerable to collapse for the lower-amplitude, higher-frequency pulses isolated from the El Centro and Imperial Valley earthquakes as well.

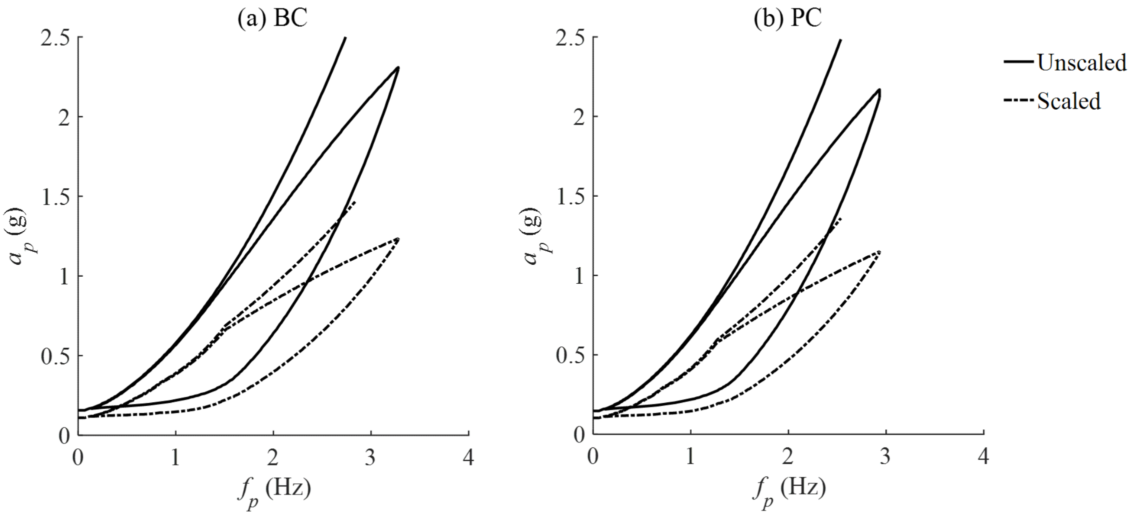

Fig. 4.23 Comparison of the scaled and unscaled overturning plots for the (a) Basantapur Column (BC) and (b) Patan Column (PC)

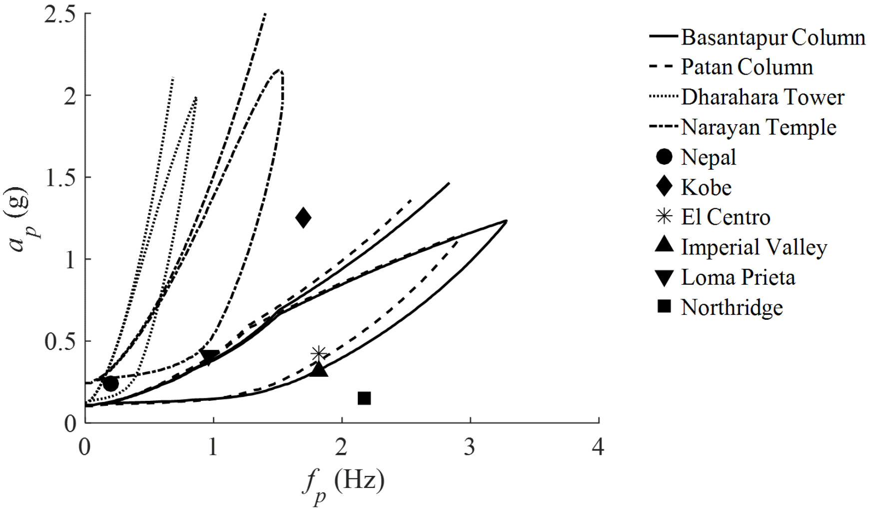

Fig. 4.24 Comparison of the overturning plots after the inclusion of amplification effects

4.4 Summary

The objective of this chapter was to evaluate the ability of the tool to realistically model the dynamic response of different structural geometries. To that end, a range of case-studies were investigated, which comprised masonry structures of varying scales and typologies. Detailed comparisons were conducted with the results of experimental tests, numerical simulations, and field observations from a recent earthquake, and in general, the tool was found to be capable of adequately capturing the dynamic response of the considered structures. These investigations allowed the following conclusions to be drawn:

- In the case of the LNEC Shaking Table Tests, while a fair correlation was observed between the predictions of the tool and the outcome of the laboratory tests, this correlation is influenced by the selection of appropriate mechanisms for analysis, which depends in turn upon user experience and engineering judgement.

- In the case of the Basantapur and Patan Columns (both of which overturned and collapsed during the Gorkha earthquake), some discrepancies were observed between the predictions of the tool and the field observations. However, using the methodology proposed in Section 3.4.1 to account for amplification effects eliminated these differences, and simultaneously illustrated the potential effectiveness of this model.

- The predictions of the tool and the results of the numerical (3DEC) simulations were in fairly good agreement for the Basantapur Column, thus illustrating the effectiveness of the analytical model currently implemented in the tool for the non-linear dynamic analysis of two-dimensional collapse mechanisms. However, this model cannot capture certain additional features of the response such as the rocking of the embedded portion of the column, the effect of joint stiffness on dynamic behaviour and in the case of the Dharahara Tower in particular - the three-dimensional nature of the rocking response.

- In the case of the Dharahara Tower, the discrepancies between the predictions of the tool and the field observations could be due in part to crushing of the masonry at the base of the tower, which the current analytical model, with its assumption of purely rigid interfaces, is not able to reproduce.

- The overturning plots generated by the tool for each of the structures damaged during the Gorkha earthquake illustrated the influence of size on stability, with smaller structures such as the Basantapur and Patan Columns being far more vulnerable to collapse. These plots also highlighted the importance of the large low frequency content within the Gorkha earthquake ground motion, as this is what caused larger structures such as the Dharahara Tower to overturn and fail.

- In general, a reasonably good correlation was observed between the predictions of the overturning plots and the results of the full time-histories, with discrepancies between the two generally being accounted for in terms of rocking amplification or de-amplification. From this particular investigation it was also found that once large rocking response of the structure begins, collapse can be fairly sensitive to the ground motion - thus highlighting the chaotic nature of the rocking response.

Chapter 5

Demonstration of the rigid rocking tool

5.1 Introduction

The rigid rocking tool presented in Chapter 3 can be applied in two main ways:

1. For seismic *analysis*, in order to rapidly evaluate critical mechanisms within a structure.
2. For seismic *assessment*, in order to evaluate the dynamic capacity of critical mechanisms.

While this chapter focusses on the first application, the second could be readily conducted for any given structure or mechanism using code-based methods as in (DeJong et al., 2015; Giresini et al., 2015; Shawa et al., 2012). Furthermore, application of the tool for seismic assessment of a real-world masonry structure will also be demonstrated in Chapter 8.

Thus, in order to demonstrate the ability of the rigid rocking tool to rapidly evaluate critical mechanisms, it was used for the seismic analysis of the Church of San Leonardo Limosino in the Italian municipality of Mirandola. Constructed in the 15th century, the church comprises a nave and side aisles (which are covered by cross-vaults), a roof supported by king-post trusses, a rounded apse, and a bell tower (Decanini et al., 2012). The church sustained a significant amount of damage during the 2012 Emilia earthquake sequence - during the first shock on May 20th, the tip of the bell tower's spire collapsed and a portion of the façade above the central window overturned out-of-plane (Fig. 5.1a). Vertical cracks below the spire and some corner spalling just above the roof level of the church were also observed in the bell tower (Decanini et al., 2012). Following the second shock on May 29th, the façade of the church suffered further damage, while the bell tower was partially destroyed (Fig. 5.1b).

In this chapter, the tool will be used to conduct a seismic analysis of the church, through the evaluation and comparison of a number of different collapse mechanisms, all of which are variations of typical church collapse mechanisms as presented in Chapter 2 (Fig. 2.2). The potential effectiveness of reinforcement, as well as the influence of accounting for ground motion amplification, will also be investigated. Finally, the tool's ability to identify critical mechanisms will be assessed through comparison with field observations.

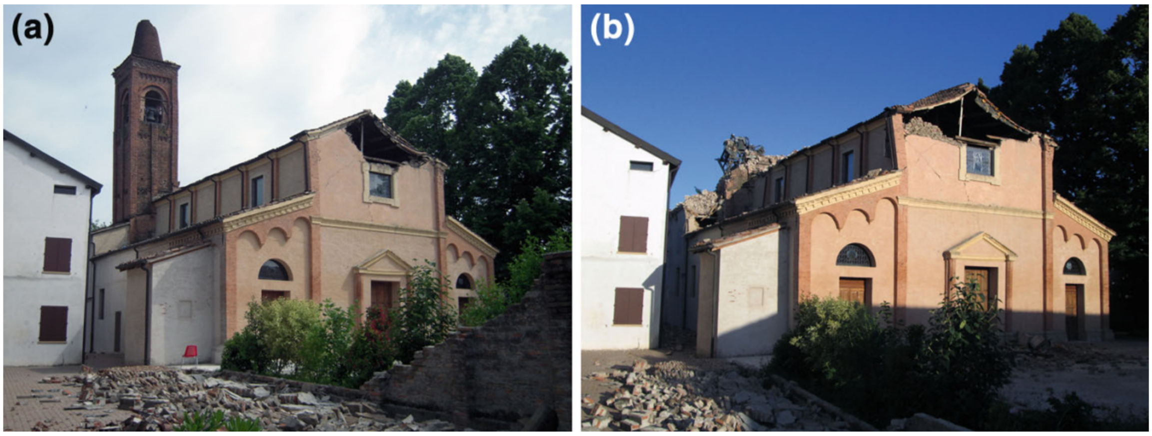

Fig. 5.1 Church of San Leonardo Limosino after the (a) 20th May 2012 shock; (b) 29th May 2012 shock (Sorrentino et al., 2014)(Reprinted by permission from Springer Nature)

5.2 Methodology

In order to analyse the church using the tool, a 3D CAD model of the structure was first generated in Rhino (Fig. 5.3) based on the dimensions and drawings presented in Decanini et al. (2012) and Sorrentino et al. (2014) (Fig. 5.2) - albeit with some simplifications. While the actual observed failure mechanisms – namely the overturning of the spire and façade, and collapse of the bell tower (Fig. 5.4a) - were all modelled by the tool, given that all three are simply variations of the simple single block mechanism, a number of other potential mechanisms were evaluated as well, which were selected based on the presence of certain macro-elements within the church (Fig. 5.4b). These included more complex mechanisms such as other possible overturning mechanisms for the façade, which accounted for additional loads in the form of the weight of the roof (ρ_r = 750 $\mathrm{kg\,m^{-3}}$, with a density ρ_m of 1800 $\mathrm{kg\,m^{-3}}$ assumed for the masonry), and thrust of the vault (F_v = 41 kN, from Ungewitter's table (Ungewitter and Mohrmann, 1901), assuming Case B, Section 3.2.2), as well as the restraining influence of tie-bars (F_t = 40 kN), and which were modelled as single block mechanisms with added masses and forces (Fig. 5.5a), as well as the collapse of the side-aisle vault, which was modelled as a multiple-block mechanism undergoing one-sided rocking (Fig. 5.5b). Parametric studies were also conducted through the modification of factors such as the location of the axis of rotation and variation of the crack angle. The equivalent rocking parameters derived by the scripts in Rhino for each of these different mechanisms were then exported to MATLAB, where they were used to generate the corresponding equations of motion.

As the objective in this case was to compare the relative dynamic resilience of the different collapse mechanisms and identify the most vulnerable one(s), the equations of motion generated in MATLAB were then solved for the pulse response in order to produce overturning plots. However as a number of these mechanisms (namely 1 – 6 in Fig. 5.4) take place at a height h above ground level, potential amplification of the ground motion up the structure was also accounted for through an

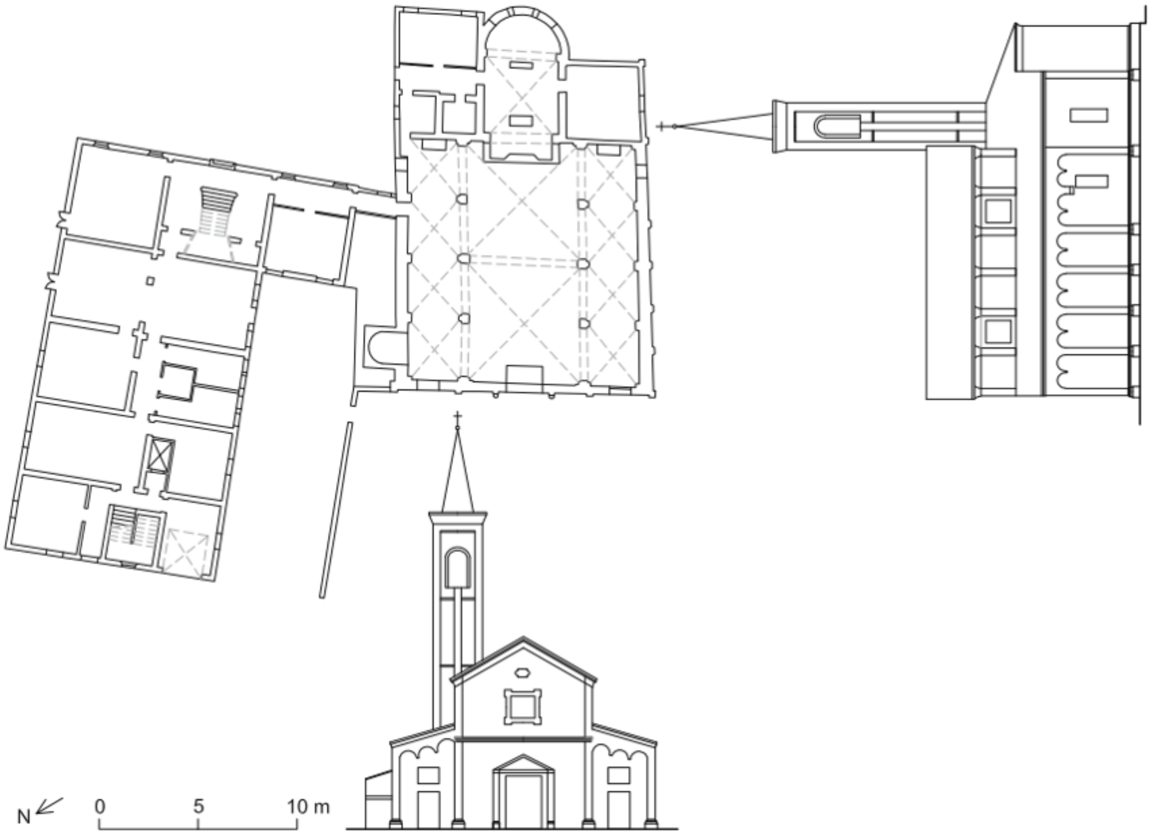

Fig. 5.2 Plan and elevation drawings of the Church of San Leonardo Limosino (reproduced from Sorrentino et al. (2014), reprinted by permission from Springer Nature)

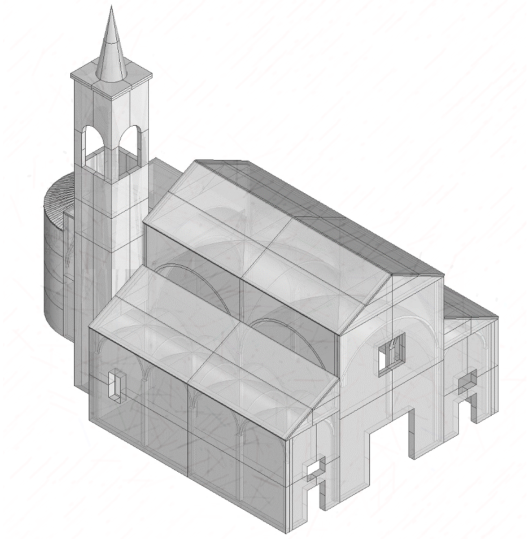

Fig. 5.3 Rhino model of the Church of San Leonardo Limosino

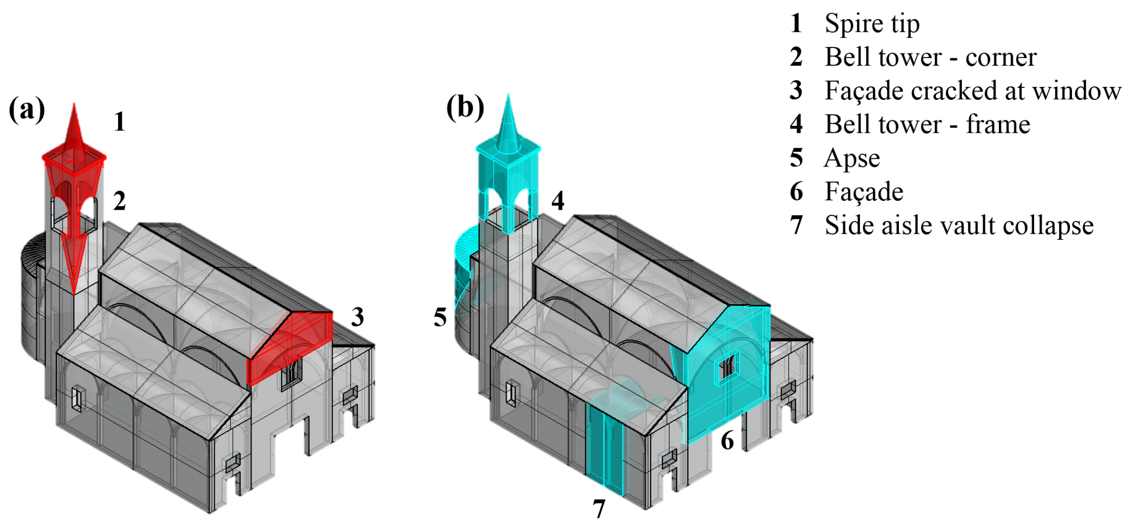

Fig. 5.4 Collapse mechanisms evaluated for Church of San Leonardo Limosino: (a) actual mechanisms and (b) potential mechanisms

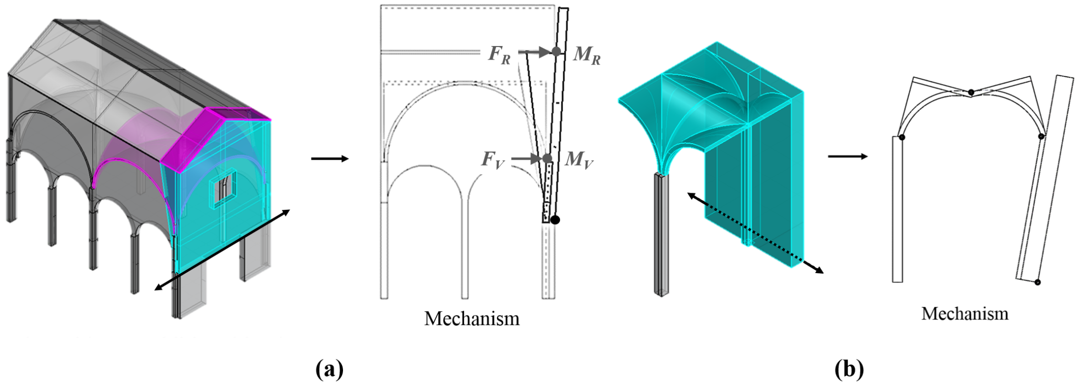

(a) (b)

Fig. 5.5 Complex mechanisms considered: (a) Overturning of the façade and (b) Side aisle vault collapse

extension of the method described by Priestley (1985) and outlined in Section 3.4.1. In order to do this, the natural frequency f_n of the church first needed to be determined. For mechanisms involving the bell tower (i.e. 1, 2 and 4), the structure was assumed to be free-standing (independent of the church) and its natural frequency was calculated using Lord Rayleigh's principle (assuming Young's modulus E = 2.4 GPa for the masonry), and was determined to be 1.8 Hz. For mechanisms involving the main church body (i.e. 3, 5 and 6) the natural frequency of the structure was estimated to be 2.9 Hz based on finite element analyses conducted on a number of churches of similar scale (Betti and Vignoli, 2008, 2011; Casarin and Modena, 2008; Castellazzi et al., 2013; Dal Cin and Russo, 2014; Mele et al., 2003). The modal heights h_e were also calculated, and were found to be 14.5 m and 6.5 m for the bell tower and church respectively. Using the computed natural frequencies and modal heights, the pulse response spectra and consequently the scaled overturning plots were then generated, with the latter being presented in the following section.

5.3 Results

In the case of the masonry spire of the bell tower (Mechanism 1, Fig. 5.4a and Mechanism 26, Fig. 2.2), two-sided rocking was assumed, and parametric studies were conducted for both varying crack angles β (with the angle being measured from the horizontal) and varying crack heights h_c (with the height being measured from the tip of the spire). Following the methodology outlined in Sections 3.3.1 and 3.4.1, overturning envelopes (Fig. 5.6) were then generated for each of these different mechanisms by using the rocking and scaling parameters listed in Table 5.1 to select and scale the appropriate dimensionless overturning plots in MATLAB. From Fig. 5.6a it can be seen that increasing the angle of the crack tends to decrease the stability of the spire, thus making it more vulnerable to overturning for all pulse frequencies, while Fig. 5.6b illustrates that increasing the height of the portion that separates and rocks tends to increase the stability of the spire, thus making it less vulnerable to overturning. In reality, the crack angle would be limited by the coursing of the masonry and thus appropriate limits on crack inclinations should be specified by the user.

Table 5.1 Rocking and scaling parameters used for generating the overturning plots for the different spire mechanisms

Mechanism		p_{eq} (s^{-1})	λ (rad)	η	f_n (Hz)	h_e (m)	h (m)
$h_c = H/2$	$\beta = 45°$	3.17	0.42	0.72	1.82	14.05	20.25
	$\beta = 60°$	3.04	0.34	0.81	1.82	14.05	20.25
	$\beta = 75°$	2.75	0.23	0.90	1.82	14.05	20.25
$\beta = 45°$	$h_c = H$	2.19	0.40	0.75	1.82	14.05	18.25
	$h_c = 2H/3$	2.73	0.41	0.73	1.82	14.05	19.58
	$h_c = H/2$	3.17	0.42	0.72	1.82	14.05	20.25
	$h_c = H/3$	3.88	0.43	0.72	1.82	14.05	20.92

In the case of the apse (Mechanism 5, Fig. 5.4b and Mechanism 16, Fig. 2.2), one-sided rocking was assumed, and parametric studies were conducted for varying crack angles β (once again measured from the horizontal), with the cracks occurring at both the base (B) of the apse as well as the window openings (W). Table 5.2 lists the rocking and scaling parameters used to generate the corresponding overturning plots (Fig. 5.7) for these different mechanisms. As Fig. 5.7 illustrates, the mechanisms originating at the window openings are, for the most part, more susceptible to overturning, and in general the overturning vulnerability increases with an increase in crack angle. However, in the case of the crack angle of 45°, the mechanism originating at the base is more likely to overturn for higher frequencies (> 3 Hz) as well as for frequencies less than 1 Hz.

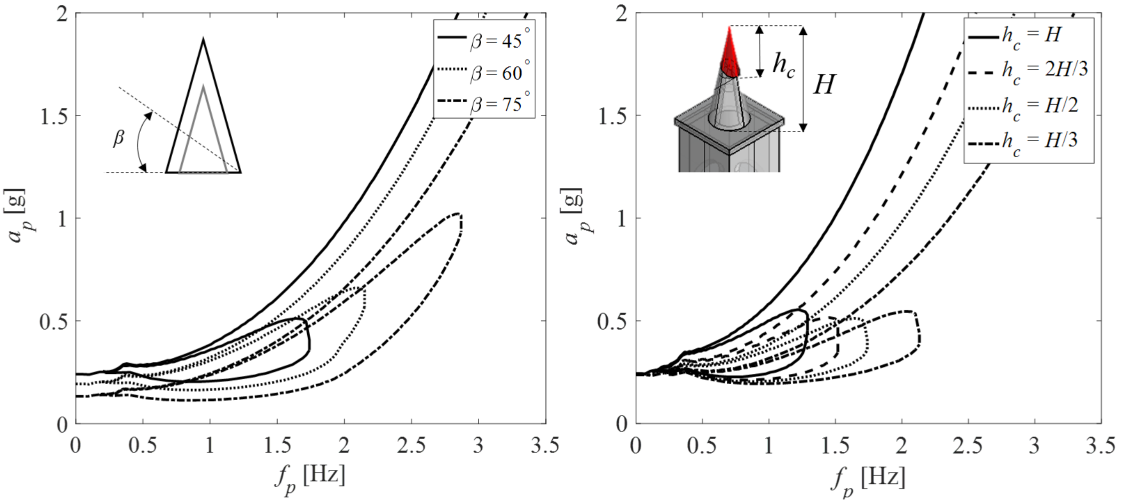

(a) (b)

Fig. 5.6 Overturning envelopes generated for the spire for: (a) varying crack angles at $h_c = H/2$; (b) varying heights for a constant crack angle $\beta = 45°$

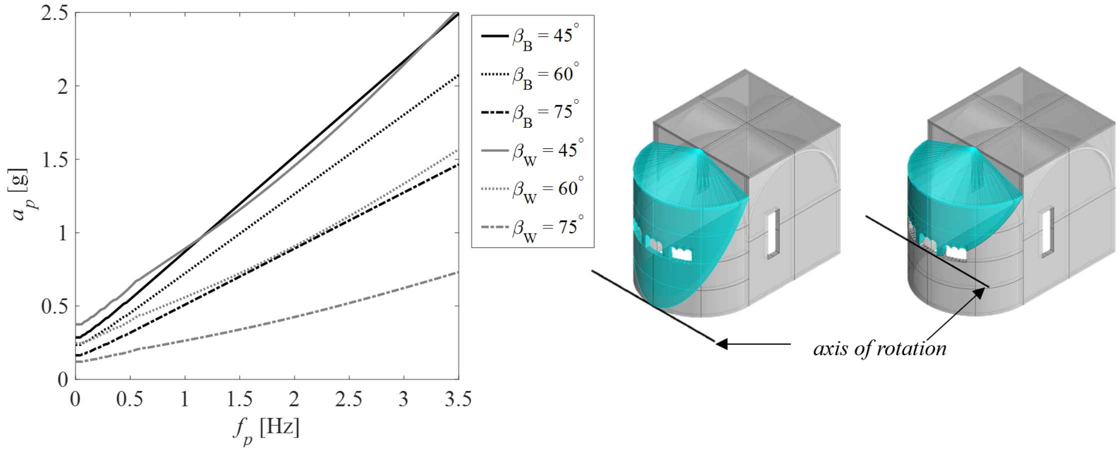

Fig. 5.7 Overturning plots generated for the apse for varying crack angles, with crack either starting from the base (B) or the window openings (W)

Table 5.2 Rocking and scaling parameters used for generating the overturning plots for the different apse mechanisms

Mechanism	p_{eq} (s^{-1})	λ (rad)	η	f_n (Hz)	h_e (m)	h (m)
$\beta_B = 45°$	1.39	0.29	N/A	2.89	6.64	0.00
$\beta_B = 60°$	1.37	0.24	N/A	2.89	6.64	0.00
$\beta_B = 75°$	1.35	0.16	N/A	2.89	6.64	0.00
$\beta_W = 45°$	1.74	0.41	N/A	2.89	6.64	3.00
$\beta_W = 60°$	1.85	0.27	N/A	2.89	6.64	3.00
$\beta_W = 75°$	1.96	0.13	N/A	2.89	6.64	3.00

In the case of the façade, five different mechanisms were evaluated, as illustrated by Fig. 5.8 (with the equivalent rocking and scaling parameters being listed in Table 5.3). Note that these five mechanisms are all variations of Mechanisms 3 and 6 as depicted in Fig. 5.4 and Mechanisms 1 and 2 as depicted in Fig. 2.2. One-sided rocking was assumed for all cases, and from the resulting overturning plots it was found that for all considered frequencies, Case 1 (gable only) was the least vulnerable to overturning, while Case 4 (façade + side walls (SW) + additional loads) was the most vulnerable.

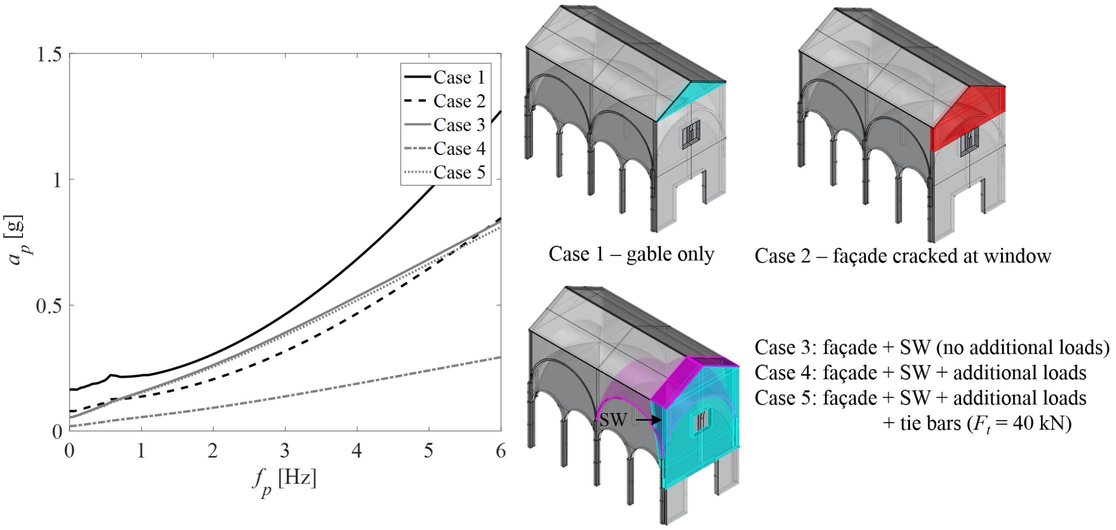

Case 1 – gable only

Case 2 – façade cracked at window

Case 3: façade + SW (no additional loads)
Case 4: façade + SW + additional loads
Case 5: façade + SW + additional loads
+ tie bars ($F_t = 40$ kN)

Fig. 5.8 Façade overturning plots for the different cases

Table 5.3 Equivalent rocking and scaling parameters used for generating the overturning plots for the different façade mechanisms

Mechanism	p_{eq} (s^{-1})	λ (rad)	η	f_n (Hz)	h_e (m)	h (m)
Case 1	3.25	0.29	N/A	2.89	6.64	9.70
Case 2	2.19	0.12	N/A	2.89	6.64	7.75
Case 3	1.38	0.06	N/A	2.89	6.64	3.00
Case 4	1.39	0.02	N/A	2.89	6.64	3.00
Case 5	1.39	0.06	N/A	2.89	6.64	3.00

In the case of the bell tower, corner mechanisms were evaluated at both the mid-height of the tower as well as at the belfry window (Mechanism 2, Fig. 5.4a and Mechanism 27, Fig. 2.2). The belfry was also evaluated as a portal frame (Mechanism 4, Fig. 5.4b and Mechanism 28, Fig. 2.2), as this mechanism is often observed during earthquakes, and takes the form as illustrated by Fig. 5.9. Two-sided (2S) rocking was assumed for all three mechanisms, while in the case of the corner mechanisms one-sided (1S) rocking was also investigated. The rocking and scaling parameters used to generate the overturning plots (Fig. 5.9) for these different mechanisms can be found in Table 5.4. From Fig. 5.9 it can be seen that for pulse frequencies between 0.5 - 2.5 Hz the portal frame mechanism appears to control collapse, while for frequencies greater than 2.5 Hz and less than 0.5 Hz the corner mechanism originating at the midpoint tends to dominate.

Table 5.4 Rocking and scaling parameters used for generating the overturning plots for the different bell tower mechanisms

Mechanism	p_{eq} (s^{-1})	λ (rad)	η	f_n (Hz)	h_e (m)	h (m)
Corner: Midpoint 2S	1.04	0.15	0.98	1.82	14.05	9.00
Corner: Midpoint 1S	1.04	0.15	N/A	1.82	14.05	9.00
Corner: Window 2S	1.32	0.27	0.93	1.82	14.05	13.00
Corner: Window 1S	1.32	0.27	N/A	1.82	14.05	13.00
Portal frame	2.21	0.21	0.92	1.82	14.05	13.00

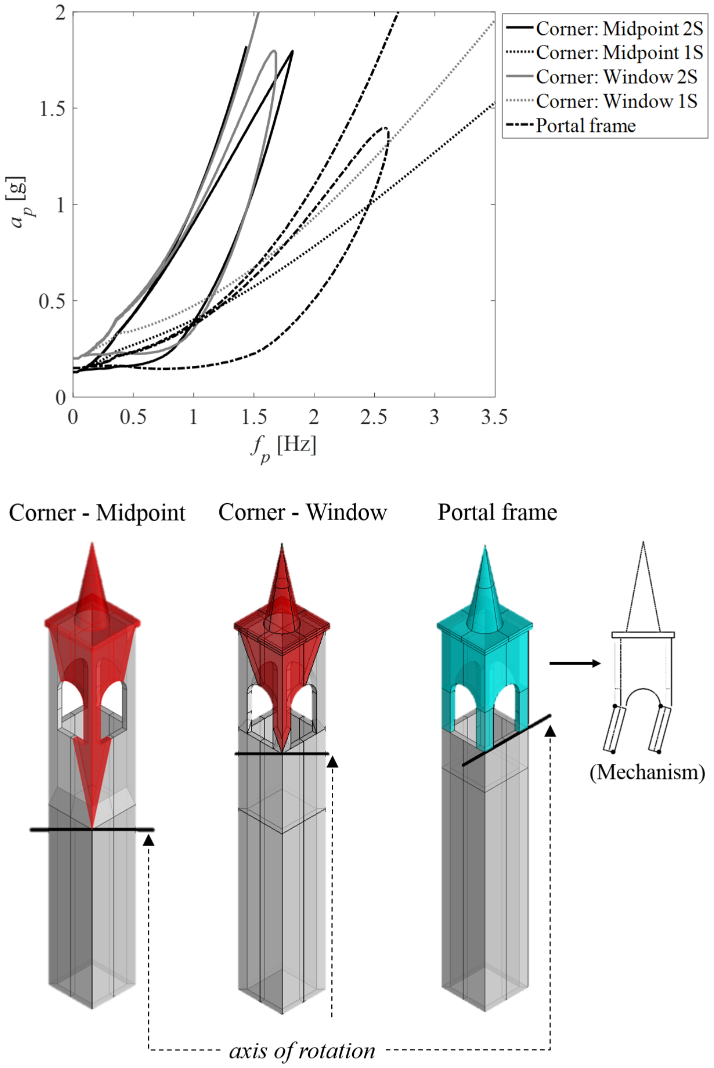

Fig. 5.9 Bell tower overturning envelopes for the different mechanisms. One-sided (1S) and two-sided (2S) envelopes are shown for the corner collapse mechanisms, while only the two-sided mechanism is shown for the portal frame.

Assuming one-sided rocking, overturning plots were also generated for the three-block mechanisms involving the vault of the side-aisle (Mechanism 7, Fig. 5.4b and and Mechanism 9, Fig. 2.2) as illustrated by Fig. 5.10, with the equivalent rocking and scaling parameters being listed in Table 5.5. The mechanisms were evaluated at both the base of the side wall and the mid-height, and the overturning envelopes in this case assume a relatively linear form - the resistance to collapse generally increases with an increase in pulse frequency, with the mechanism originating at the base displaying a larger vulnerability to overturning for all frequencies.

Table 5.5 Equivalent rocking and scaling parameters used for generating the overturning plots for the different side-aisle mechanisms

Mechanism	p_{eq} (s^{-1})	λ (rad)	η	f_n (Hz)	h_e (m)	h (m)
Base	1.85	1.11	N/A	2.89	6.64	0.00
Midpoint	2.21	4.82	N/A	2.89	6.64	2.70

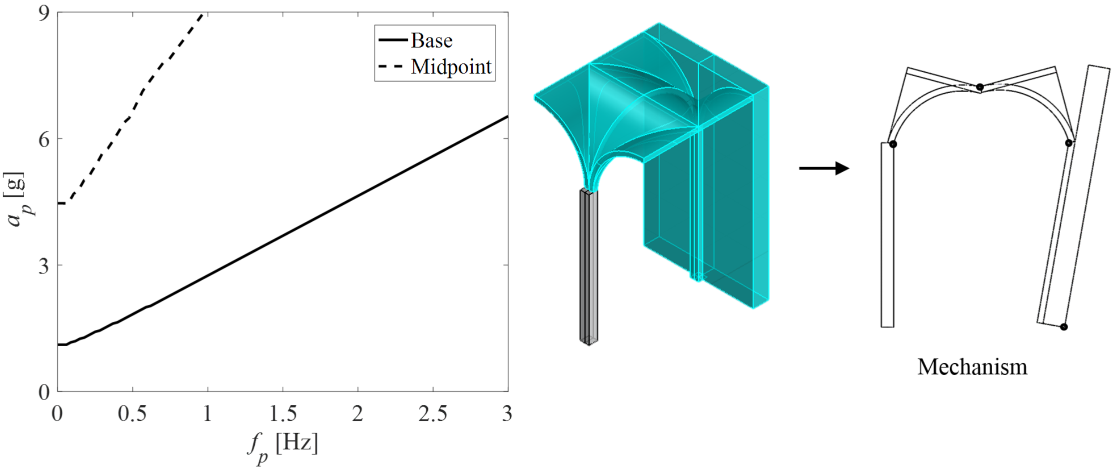

Fig. 5.10 Overturning plots for the side aisle vault (left), with an illustration of the corresponding (three-block) mechanism (right)

Finally, in order to compare the relative dynamic resilience of the different collapse mechanisms, the most vulnerable (controlling) mechanisms from each of the parametric studies were plotted in Fig. 5.11, with the only exception being the façade, where Case 2 (Mechanism 3, Fig. 5.4a) was plotted instead of Case 4 (Mechanism 6, Fig. 5.4b), as this was the mechanism which was actually observed to occur during the earthquake. Furthermore, the script written in MATLAB to automatically detect critical mechanisms (as described in Section 3.4.2) was also run in order to determine the most vulnerable mechanism for each pulse frequency.

Table 5.6 Rocking and scaling parameters used for generating the overturning plots for the controlling mechanisms from the different parametric studies

Mechanism	p_{eq} (s^{-1})	λ (rad)	η	f_n (Hz)	h_e (m)	h (m)
1. Spire	2.75	0.23	0.90	1.82	14.05	20.25
2. Bell tower (corner)	1.04	0.15	0.98	1.82	14.05	9.00
3. Façade (cracked at window)	2.19	0.12	N/A	2.89	6.64	7.75
4. Bell tower (frame)	2.21	0.21	0.92	1.82	14.05	13.00
5. Apse	1.96	0.13	N/A	2.89	6.64	3.00
6. Façade	1.39	0.02	N/A	2.89	6.64	3.00
7. Side aisle	1.85	1.11	N/A	2.89	6.64	0.00

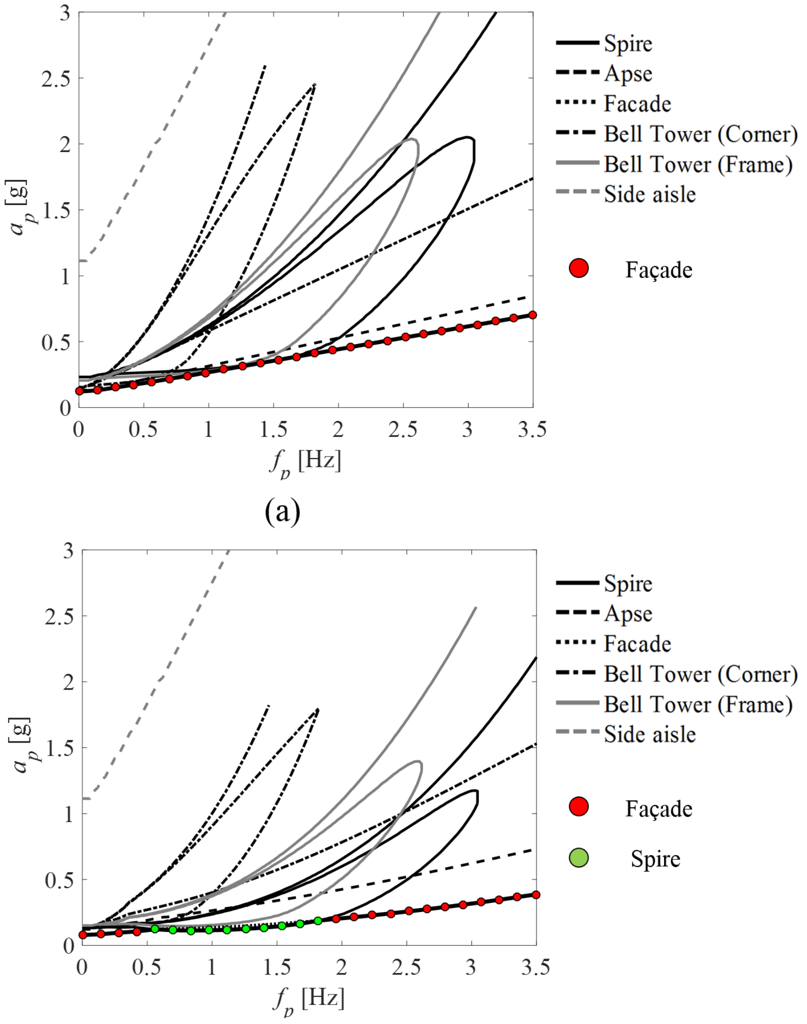

(a)

(b)

Fig. 5.11 Comparison of the overturning plots for the different mechanisms: (a) without and (b) with amplification

The rocking and scaling parameters for each of these controlling mechanisms are listed in Table 5.6. In order to highlight the effect of ground motion amplification, Fig. 5.11 includes both the unscaled and scaled overturning envelopes. From Fig. 5.11 it can be seen that for the unscaled case, the façade mechanism is the most vulnerable to overturning for all considered pulse frequencies, followed by the spire for frequencies less than 2 Hz and the apse for frequencies greater than 2 Hz. However, by accounting for amplification effects, the spire actually becomes most susceptible to collapse for pulse frequencies in the range of 0.5 - 2.0 Hz, while the façade remains the most vulnerable mechanism for frequencies less than 0.5 Hz and greater than 2 Hz. Fig. 5.11 also demonstrates that accounting for dynamic amplification generally reduces the minimum pulse amplitude required for overturning to occur, and in some cases even changes the relative vulnerabilities of the different collapse mechanisms.

5.4 Discussion

5.4.1 Effect of slenderness and scale

As expounded upon in Chapter 4, the resistance of objects to overturning is dependent on both their slenderness and scale. While the ratio of the acceleration amplitude of the ground motion to the slenderness of a structure determines when rocking initiates, the magnitude of rotation (and thus collapse) depends on the scale of the structure with respect to the period of large pulses within the ground motion.

This effect of slenderness and scale on the rocking stability of structures is illustrated by the overturning envelopes generated for the spire (Fig. 5.6). From Fig. 5.6a it can be seen that for a constant crack height, the resistance of the spire to overturning decreases with an increase in crack angle. An increase in crack angle results in an increased slenderness of the structure (Table 5.1), thus leading to rocking initiating earlier. Furthermore, these more slender structures are also of a relatively smaller scale than their stockier counterparts and are thus susceptible to overturning with impact for higher frequencies as well. This effect of scale on stability is reinforced by Fig. 5.6b, wherein for a constant crack angle and varying crack heights – that is, for a constant slenderness and varying scale - it can be seen that the overturning resistance again decreases with a decrease in scale.

For two-sided rocking mechanisms involving structures of similar scale but different slenderness, such as the two corner mechanisms (Fig. 5.9), it can be seen that for more slender structures (in this case the mechanism which originates at the tower midpoint) rocking not only initiates earlier, but for pulse frequencies less that 0.85 Hz overturning for both the case with and without impact occurs at a lower pulse amplitude. However, as the mechanisms involve structures of relatively similar scale, the range of pulse frequencies for which overturning with impact occurs remains unchanged.

For one-sided rocking mechanisms, such as those observed in the apse and façade walls (Fig. 5.7 and Fig. 5.8 respectively) only positive pulse overturning without impact is considered. In this case, the only variation observed is in the pulse amplitude at which overturning occurs. For the façade and its associated mechanisms, resistance to overturning was generally found to decrease with an increase in slenderness, with the gable (Case 1) being the stockiest and hence the most resistant to overturning. However, Case 2, despite being less slender than Case 3, was actually found to be more susceptible to collapse. This behaviour is due to amplification of the ground motion, which shall be discussed in greater detail in the following sub-section.

For the apse, the threshold pulse amplitudes at which overturning occurs were again found to decrease with an increase in slenderness. However, in the case of the 45° crack angle, the mechanism originating at the window, despite its smaller scale, was largely found to be more resistant to overturning than the corresponding base mechanism. This is due to the fact that the slenderness of the structure only controls the minimum acceleration (for an infinitely long pulse) required for overturning to occur, while the rate at which this increases for higher frequency pulses depends on the ratio between λ, which is linked to the slenderness, and p_{eq}, which is related to the scale. For the crack angle of 45°, the window mechanism was not only stockier than the base (0.41 vs 0.29 rad), but also had a higher ratio of λ to p_{eq} (0.24 vs 0.21), thus resulting in a generally higher resistance to overturning. However, the window mechanism also occurs at a height above the ground, and, like the façade, experiences amplification of the ground motion which reduces the overturning resistance, making it more vulnerable than the base mechanism for lower frequencies – especially in the range of 1 – 3 Hz.

5.4.2 Effect of ground motion amplification

As a number of the mechanisms considered in this study take place above ground level, amplification effects needed to be accounted for as they tend to increase the overturning vulnerability of the structure. This was done using pulse response spectra which were generated and scaled according to the height h at which the mechanisms occurred.

The effects of elastic amplification on one-sided mechanisms are best illustrated by the façade overturning envelopes (Fig. 5.8), where Case 2, despite being stockier than Case 3, was actually found to be more vulnerable to collapse for pulse frequencies between 1 - 3 Hz. As Case 2 occurs at a greater height than Case 3, it has greater amplification of the ground motion and consequently a greater increase in vulnerability to overturning. Correspondingly, the reduction of the overturning resistance of the 45° apse window mechanism can also be attributed to the effect of elastic amplification.

In the case of two-sided mechanisms, the effects of elastic amplification are illustrated by Fig. 5.11. If amplification effects are not considered (Fig. 5.11a), both the spire and the belfry (frame) have relatively similar vulnerabilities. However, accounting for elastic amplification (Fig. 5.11b) results in a greater increase in vulnerability of the spire than of the belfry, as this mechanism occurs at a greater height than the frame mechanism, and as such experiences a greater amplification of the ground motion.

5.4.3 Effect of reinforcement

The overturning envelopes generated in Fig. 5.8 also highlight the effect of reinforcement on the dynamic resilience of the façade. From Fig. 5.8 it can be seen that the addition of the tie bars to Case 4 effectively countered the influence of the additional loads from the roof and thrust from the vault, resulting in the structure having an overturning vulnerability comparable to the case in which there were no additional loads at all. In fact, it could very well be the case that such reinforcement, which ensures good connectivity between the façade and side walls, does actually exist (either directly or through good quality masonry with interlocking at the wall intersection) and prevented Case 4 from occurring in reality, thus making Case 2 the most vulnerable mechanism for the façade (as observed in the damage).

5.4.4 Comparison with field observations

Comparing the results from Fig. 5.11 to the findings of the post-earthquake damage surveys (Decanini et al., 2012; Sorrentino et al., 2014) it can be seen that there is a generally good correlation between the predictions of the overturning plots and results of the field inspections. Fig. 5.11 predicts that for frequencies less than 3.5 Hz, the most likely or vulnerable mechanisms are the out-of-plane collapse of the portion of the façade above the window, and the overturning of the bell tower spire. In reality, both these mechanisms took place during the first shock of the Emilia earthquake in 2012. After this first shock, some corner spalling of the bell tower had also been observed (Decanini et al., 2012), which could potentially have weakened the structure, thus making it more susceptible to corner failure during the second shock.

5.5 Summary

The objective of this chapter was to demonstrate a potential application of the rigid rocking tool, by using it to conduct a seismic analysis of a typical church geometry - based on the Church of San Leonardo Limosino, Italy. The tool was used to derive equations of motion for different collapse mechanisms (all of which are variations of the typical church collapse mechanisms presented in Fig. 2.2 of Chapter 2), and solve for their response to pulse-type excitations, while taking into account elastic amplification of the ground motion. The main conclusions to be drawn from this investigation are as follows:

- While the mechanisms modelled in Chapter 4 were variations of the simple single block mechanism, this study demonstrated the tool's ability to model more complex mechanisms such as the single block subjected to additional masses and forces (i.e. the façade mechanisms) as well as multiple block mechanisms such as the portal frame mechanism of the belfry and the collapse of the side aisle vault. Furthermore, the tool's potential for modelling the beneficial influence of reinforcement was also illustrated.

- The capacity of the tool to rapidly compare different mechanisms - either through parametric studies or through the juxtaposition of various types of mechanisms as in Fig. 5.11 - was also demonstrated. Moreover, ground motion amplification was also found to have a significant effect when comparing different mechanisms to evaluate which one is most critical.

- Through the parametric studies, the effect of slenderness and scale on the rocking stability of the church was evaluated. For both one and two-sided mechanisms, the slenderness was observed to control the point at which rocking initiates as well as the minimum acceleration required for very long-period pulses to cause overturning. For two-sided mechanisms, the scale of the macro-element involved in the rocking mechanism was found to govern the range of pulse frequencies for which single-impact overturning could occur, while for one-sided mechanisms the ratio of slenderness to scale determined the rate at which the structure's resistance to overturning increased with an increase in pulse frequency.

- Finally, the tool's ability to provide realistic predictions was evidenced by the generally good agreement observed between the analysis results and field observations, with the overturning plots correctly predicting the highest vulnerability for the portion of the façade above the window and the spire of the bell tower, both of which collapsed during the Emilia earthquake in 2012.

However, while this chapter focussed on the application of the tool for seismic analysis, the ability the new framework to be used for assessment will also be demonstrated in Chapter 8, by using it to conduct a code-based seismic assessment of a historic masonry structure.

Chapter 6

Extension of modelling to flexible interfaces

6.1 Introduction

The equations of motion presented in Chapter 3 assume that the structure can be modelled as a rigid body rocking on a rigid foundation, which is not necessarily true – especially since real structures have non-rigid interfaces, and typically rest on soil. In fact, experimental tests conducted by ElGawady et al. (2011) using concrete, timber, rubber and steel joints demonstrated that the interface material tends to have a substantial influence on the free rocking response of rigid blocks. Furthermore, the rigid model assumes that the blocks have an infinite stiffness (i.e. exhibit no deformations) until the initiation of rocking motion, which experimental tests and numerical simulations conducted on a set of unreinforced masonry walls by Doherty et al. (2000) and de Felice (2011) respectively, showed to be untrue (Fig. 2.6 in Chapter 2). In fact, factors such as non-rigid interfaces, geometrical imperfections, and disaggregation of multi-leaf wall sections due to poor transversal bonding tends to lead to a reduction in the dynamic capacity of these structures (de Felice, 2011).

In this case, it is perhaps more realistic to use a flexible Winkler-type foundation, which models the interface (and to some extent block deformability near the interface) using a set of springs with a stiffness k_n. While most of the analytical studies previously conducted on these flexible interfaces assume pure elastic behaviour with an infinite compressive strength for the masonry (Koh et al., 1986; Lipo and de Felice, 2016, 2017; Psycharis and Jennings, 1983; Shawa et al., 2012), they do not account for local material failure – which could potentially be both un-conservative and un-realistic, especially in the case of walls subjected to significant overburden forces. However, recent work by Roh and Reinhorn (2009), Costa (2012), Costa et al. (2013) and Penna and Galasco (2013) assumes a bilinear elastic representation of the compressive behaviour of the interface, and thus also accounts for crushing effects. Nonetheless, in both cases the rocking equation of motion now includes an additional term $a_f(\phi)$ which represents the inward shift of the rocking rotation point due to the reaction from the elastic/elasto-plastic joint, and is a function of the rotation ϕ of the structure, as illustrated by Equation 6.1:

$$\ddot{\phi} = -\frac{WR_0}{I_{O'}(\phi)}\left[\sin\left(\alpha_0 \operatorname{sgn}(\phi) - \phi\right) - \frac{a_f(\phi)}{R_0} + \frac{\ddot{u}_g}{g}\cos\left(\alpha_0 \operatorname{sgn}(\phi) - \phi\right)\right] \tag{6.1}$$

where $\ddot{\phi}$ is the angular acceleration, W is the weight, R_0 is the distance between the center of the mass and the axis of rotation, α_0 is the slenderness, $\ddot{u}_g$ is the input ground acceleration, g is the acceleration due to gravity, and ϕ is the corresponding rotation of the structure. The equation of motion also depends on the moment of inertia $I_{O'}(\phi)$, which in this case is determined relative to a shifting rotation point *O'*, which varies based on the rotation of the structure (Costa (2012)).

The analytical expressions derived for $a_f(\phi)$ thus far have been limited to interfaces which assume the form of solid rectangles as for the rocking block, whereas in reality this is not always the case – as demonstrated by structures such as bell towers, columns, domes etc., which tend to have non-rectangular and/or hollow cross-sections. For the analytical modelling tool described in this thesis to be practically useful, it needs to be able to automatically derive equations of motion for these more complicated geometries as well. Therefore, to incorporate the effects of interface flexibility and crushing into the tool, Section 6.2 of this chapter presents derivations for $a_f(\phi)$ for different interface geometries, including hollow rectangular bases, solid circular bases and hollow circular bases.

Furthermore, the equation of motion as derived by Costa (2012) is limited to the simple single block mechanism, whereas in reality failure of many masonry structures assumes the form of more complex collapse mechanisms. While recent work by Mordant et al. (2015) proposed a rocking model for the two block mechanism wherein a series of spring and dashpot elements were used to model the interfaces between the blocks as both flexible and viscous, such an approach results in the system having four degrees of freedom – namely the rotations and vertical displacements of the top and bottom blocks - which is more complex than the single degree-of-freedom (SDOF) formulation implemented in the analytical modelling tool. Thus in order to account for the presence of flexible interfaces and crushing effects in these more complicated collapse mechanisms without introducing additional degrees of freedom into the problem, Section 6.3 of this chapter uses Lagrange's equation to re-derive the equations of motion for the single, two and multiple block mechanisms.

6.2 Derivation of $a_f(\phi)$ for different interface geometries

In this section, expressions will be derived for $a_f(\phi)$ for different base geometries, which can then be substituted either into the equation of motion as defined in Costa (2012) (expressed in a different form in Equation 6.1) or into the modified equations of motion derived later in this chapter. The analytical tool allows the user to interactively select the 3D collapse mechanism in the CAD environment, and then exports the appropriate equations to MATLAB, where they can be solved for a variety of input ground motions.

6.2.1 Solid rectangular interface

Structures which can be modelled as having solid rectangular bases include walls, solid towers, rectangular columns, and statues or sculptures which rest on rectangular bases, as illustrated by Fig. 6.1. Due to the introduction of a flexible interface, the various terms in the equation of motion now depend on $a_f(\phi)$ which represents the position of the reaction force from the interface and consequently the new rotation point of the structure. This rotation point is a function of the rotation ϕ of the structure and can be calculated based on the relationship between the stiffness of the interface k_n ($=E/e$, where E is the Young's modulus and e is the thickness of the interface), curvature $\chi(=\phi/e)$, strain ε ($=\chi a$ where a is the width of the interface) and stress σ ($=E\varepsilon$), as presented in Costa et al. (2013).

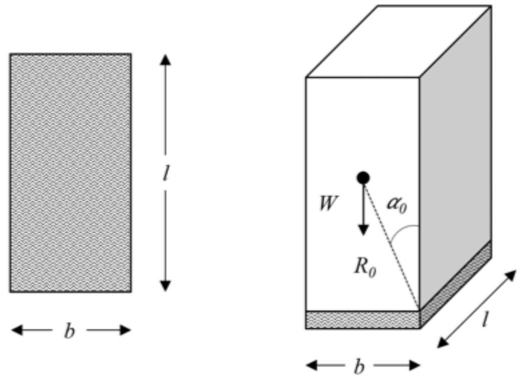

Photo of sculpture removed for copyright reasons. Copyright holder is Royal-Athena Galleries.

Fig. 6.1 Solid rectangular base geometry and example real-world application – sculpture of an Egyptian Royal Lady (Royal-Athena Galleries)

Following Costa's approach, the position of the reaction force is calculated for three different cases which depend primarily on the stress distribution at the base, which in turn is a function of the rotation of the structure ϕ as illustrated by Fig. 6.2, and includes: (1) full contact, (2) partial contact and (3) partial contact with crushing. Full contact is assumed for cases in which the rotation is less than the joint opening rotation ϕ_{jo}, which is determined analytically using the following expression:

$$\phi_{jo} = \frac{2W}{k_n b^2 l} \tag{6.2}$$

where W is the weight of the structure, b and l are the base dimensions as depicted in Fig. 6.1, and k_n is the normal stiffness of the interface. Upon exceeding ϕ_{jo}, the entire cross section is no longer in contact with the base and the stress distribution assumes a triangular form. The contact length a decreases with an increase in the rotation ϕ, until the point where the maximum stress σ equals the compressive strength f_m. At this point, the threshold contact length a_c is reached (indicated by the

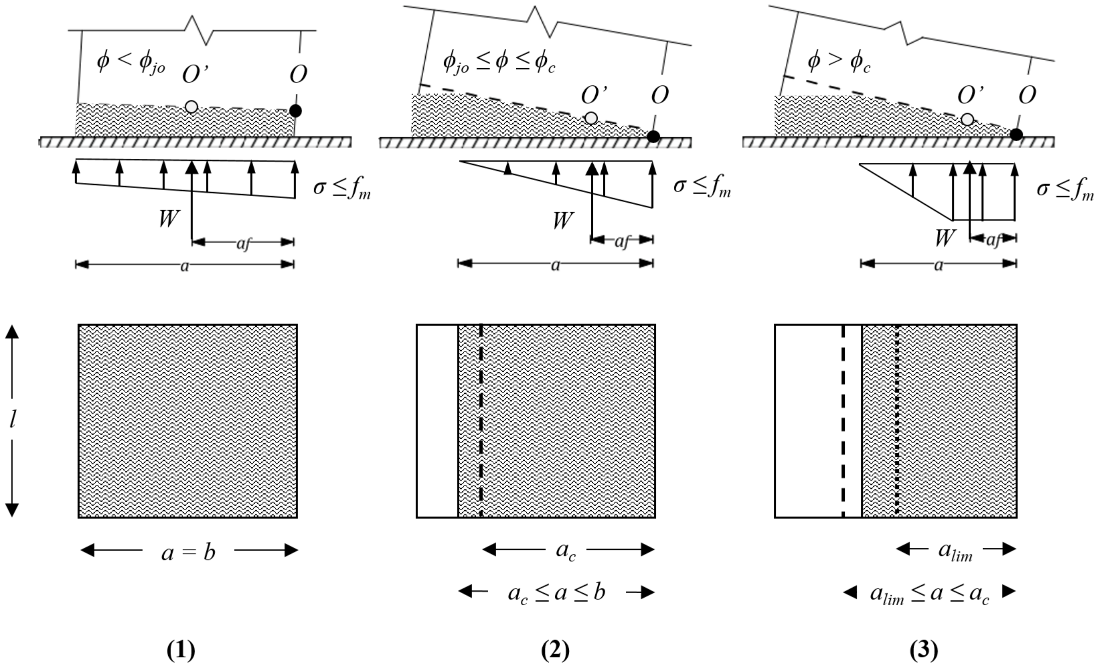

Fig. 6.2 Interface stress distributions and corresponding rotations (adapted from Costa et al. (2013))

dashed line in Fig. 6.2), which can be determined analytically using the following equation:

$$a_c = \frac{2W}{f_m l} \tag{6.3}$$

The corresponding threshold rotation at which crushing begins, ϕ_c, can then be obtained by substituting a_c into the following expression:

$$\phi_c = \frac{f_m}{k_n a_c} \tag{6.4}$$

Upon the exceedance of this threshold rotation, the behaviour of the interface switches from purely elastic to bilinear elasto-plastic, with the contact length continuing to decrease until the limiting length a_{lim} (depicted by the dotted line in Fig. 6.2) is reached at which point the behaviour is purely plastic across the entire area of joint contact.

Once the various threshold conditions (rotations and contact lengths) have been determined, expressions can then be derived for the position $a_f(\phi)$ of the reaction force for each of the different cases, as given by Equations 6.5-6.7. These expressions can then be used to determine $a_f(\phi)$ for a range of different rotations, which can then be substituted back into either Equation 6.1 or into the formulations presented in the second half of this chapter to generate and solve the modified rocking equation of motion.

$$a_f(\phi) = \operatorname{sgn}(\phi)\left[\frac{b}{2} - \frac{b^3 k_n l\,|\phi|}{12W}\right] \qquad 0 < |\phi| \le \phi_{jo} \tag{6.5}$$

$$a_f(\phi) = \operatorname{sgn}(\phi)\left[\frac{1}{3}\sqrt{\frac{2W}{k_n l\,|\phi|}}\right] \qquad \phi_{jo} \le |\phi| \le \phi_c \tag{6.6}$$

$$a_f(\phi) = \frac{\operatorname{sgn}(\phi)}{2}\left[\frac{W}{f_m l} + \frac{{f_m}^3 l}{12W{k_n}^2|\phi|^2}\right] \qquad \phi_c \le |\phi| \tag{6.7}$$

where sgn(ϕ) is the sign function and is equal to 1 for $\phi > 0$ and -1 for $\phi < 0$. Note that $a_f(0) = b/2$.

6.2.2 Hollow rectangular interface

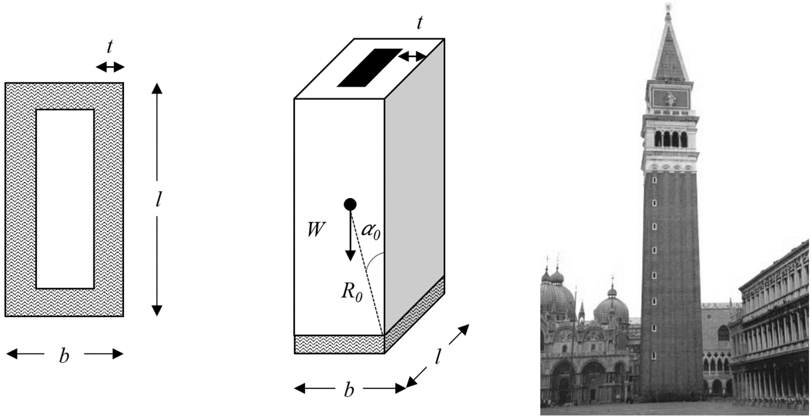

Fig. 6.3 Hollow rectangular base geometry and example structure - St Mark's Campanile (Wikimedia Commons)

While the analytical expressions determined for $a_f(\phi)$ for solid rectangular bases by Costa et al. (2013) can be used for a broad range of structures, there also exist cases in which they may not always be applicable – one such example being bell towers, which instead have hollow rectangular bases, as illustrated by Fig. 6.3. In the case of such bases, new expressions for $a_f(\phi)$, as well as the threshold rotations and contact lengths, need to be derived, which take into consideration the reduction in contact area due to the hollow base section.

However, complete overturning of these entire structures about their bases is unlikely - rather, failure in the form of partial collapse through the development of an inclined crack is more likely to occur. While expressions have been derived for $a_f(\phi)$ which factor in the crack inclination, for most realistic geometries this was not observed to have a substantial influence on the dynamic resistance of the structure - with the assumption of no inclination generally yielding more conservative predictions. Thus in this section (and those that follow), the derivations are presented assuming no inclination of the interfaces.

The threshold joint opening rotation ϕ_{jo} for the hollow rectangular base is consequently given by the following expression, where t corresponds to the thickness of the base as shown in Fig. 6.3:

$$\phi_{jo} = \frac{W}{k_n bt\,(l+b-2t)} \tag{6.8}$$

Similarly, in order to determine the threshold contact length a_c at which crushing occurs, i.e. the maximum stress at the base equals the compressive strength f_m, three possible cases need to be considered, as illustrated by Fig. 6.4. The corresponding analytical expressions for a_c for each of these different cases are provided by Equations 6.9-6.11:

$$\textit{Case I}: \quad a_c = \frac{1}{l}\left[\begin{array}{c} -\left(2bt+2tl-bl-4t^2-{}^{W}\!/_{f_m}\right) \\ +\sqrt{\left(2bt+2tl-bl-4t^2-{}^{W}\!/_{f_m}\right)^2-2l\left({}^{b^2l}\!/_{2}-b^2t-blt+2bt^2\right)} \end{array}\right] \tag{6.9}$$

$$\textit{Case II}: \quad a_c = \frac{-\left(2l-4t-{}^{2W}\!/_{f_m t}\right)+\sqrt{\left(2l-4t-{}^{2W}\!/_{f_m t}\right)^2-8t\,(2t-l)}}{4} \tag{6.10}$$

$$\textit{Case III}: \quad a_c = \frac{2W}{f_m l} \tag{6.11}$$

Once a_c has been determined, it can then be substituted into Equation 6.4 to obtain the resultant threshold rotation for crushing ϕ_c at which the behaviour of the interface switches from purely elastic to elasto-plastic. Expressions were then derived for $a_f(\phi)$ for the cases of full contact, partial contact and partial contact with crushing.

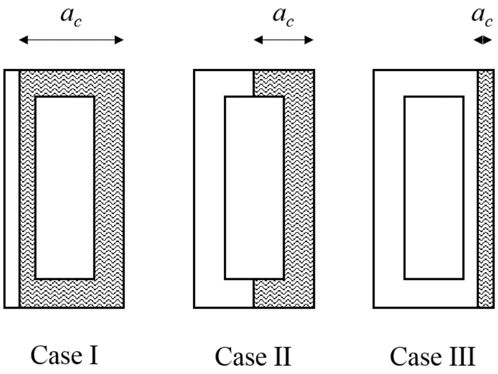

Fig. 6.4 Different cases considered for threshold contact length a_c for the hollow rectangular base

For full contact, the position of the reaction force can be determined using the following expression:

$$a_f(\phi) = \operatorname{sgn}(\phi)\left[\frac{b}{2} - \frac{k_n|\phi|}{6W}\left(8t^4 + 4t^3(3b-l) + 6bt^2(l-b) + b^2t(b+3l)\right)\right] \quad 0 < |\phi| \leq \phi_{jo} \tag{6.12}$$

For partial contact with pure elastic behaviour, three possible cases, analogous to those for a_c, need to be considered:

$$\textit{Case I}: \; a_f(\phi) = \operatorname{sgn}(\phi)\left[\frac{k_n|\phi|}{2W}\left(\frac{a^3t}{3} + \frac{(l-2t)}{6}\left(t^2(3a-2t) + 2(a+2b-2t)(a-b+t)^2\right)\right)\right] \tag{6.13}$$

$$\textit{Case II}: \quad a_f(\phi) = \operatorname{sgn}(\phi)\left[\frac{k_n|\phi|t}{W}\left(\frac{a^3}{3} + \frac{alt}{2} - t^2\left(a + \frac{l}{3}\right) + \frac{2t^3}{3}\right)\right] \tag{6.14}$$

$$\textit{Case III}: \quad a_f(\phi) = \operatorname{sgn}(\phi)\left[\frac{1}{3}\sqrt{\frac{2W}{k_n l|\phi|}}\right] \tag{6.15}$$

It is worth noting that the expression for $a_f(\phi)$ (as well as a_c) for Case III is the same as that for the solid rectangular base. Similarly for $\phi_c \leq |\phi|$ (partial contact with crushing), although theoretically the same three cases should be considered, it can be shown that for most reasonable values of compressive strength and density (and correspondingly W), the first two cases can be neglected and thus the same equation as is used for the solid rectangular base (Equation 6.7) can be applied here as well.

6.2.3 Solid circular interface

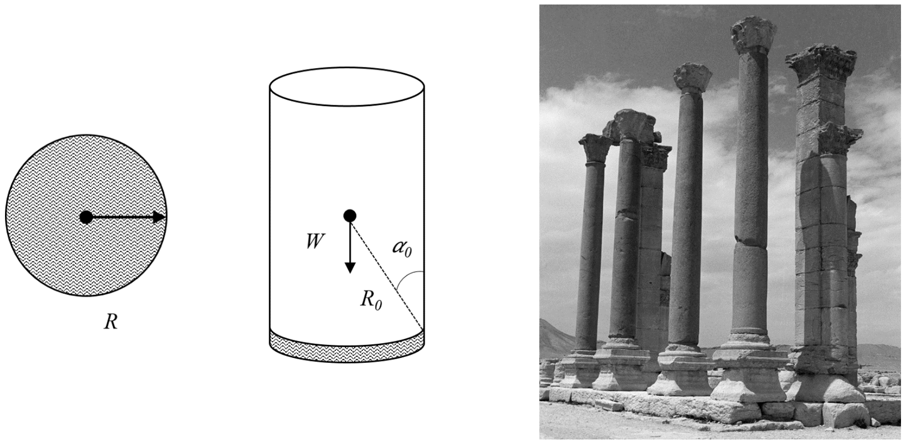

Fig. 6.5 Solid circular base geometry and example structure – Columns of the Baths of Diocletian (Jerzy Strzelecki CC BY-SA 3.0)

Expressions were also derived for solid circular bases, as are commonly found in structures such as monumental columns and pedestals, as illustrated by Fig. 6.5. The joint opening rotation ϕ_{jo} for such bases (which have a radius R) can be determined analytically using the following expression:

$$\phi_{jo} = \frac{W}{k_n \pi R^3} \tag{6.16}$$

However, unlike the rectangular base cases and due to the 3D nature of the stress distribution as illustrated by Fig. 6.6, a closed-form analytical solution does not exist for a_c. Instead, a_c needs to be determined by numerically solving the following expression, which is obtained by integrating the stress distribution and setting it equal to the weight of the structure W:

$$W = \frac{2 f_m R^2}{a_c}\left[\frac{\psi}{2}\left(a_c - R\right) + \frac{R}{3}\sin\psi\right] + \left|\frac{R^2\left|\sin\left(2\psi\right)\right| f_m \left(a_c - R\right)}{6a_c}\right| \quad where \quad \psi = \arccos\left(\frac{R - a_c}{R}\right) \tag{6.17}$$

Once computed, a_c can then be substituted into Equation 6.4 to obtain ϕ_c for the solid circular base.

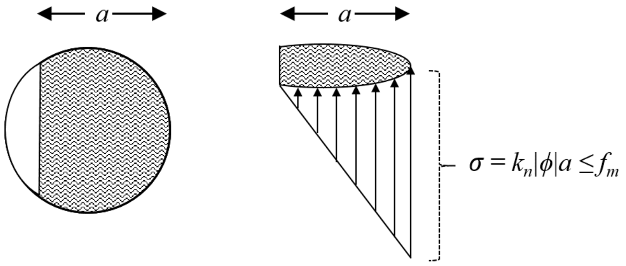

Fig. 6.6 Stress distribution for $\phi_{jo} \leq |\phi| \leq \phi_c$ for the solid circular base/interface

As in the case of the rectangular base, expressions were then derived for the position of the reaction force $a_f(\phi)$ for the cases of full contact, partial contact and partial contact with crushing.

In the case of full contact, i.e. for $0 < |\phi| \leq \phi_{jo}$, the following expression can be used for $a_f(\phi)$:

$$a_f\left(\phi\right) = \operatorname{sgn}\left(\phi\right)\left[R - \frac{\pi R^4 k_n \left|\phi\right|}{4W}\right] \tag{6.18}$$

Note that $a_f(0) = R$. For the case of partial contact with purely elastic behaviour, i.e. $\phi_{jo} \leq |\phi| \leq \phi_c$, the contact length a now varies with the rotation ϕ, and thus first needs to be determined by numerically solving the following expression for each value of ϕ:

$$W = 2k_n\left|\phi\right| R^2\left[\frac{\psi}{2}\left(a - R\right) + \frac{R}{3}\sin\psi\right] + \left|\frac{R^2\left|\sin\left(2\psi\right)\right| k_n \left|\phi\right| \left(a - R\right)}{6}\right| \quad where \quad \psi = \arccos\left(\frac{R - a}{R}\right) \tag{6.19}$$

The computed value of a is then substituted into Equation 6.20 to get $a_f(\phi)$:

$$a_f(\phi) = \operatorname{sgn}(\phi) R \left[1 - \left(\frac{2\left(\frac{R(\psi + \cos\psi \sin\psi)}{8} - \frac{\sin\psi (R-a)}{3} \right) + \frac{|R-a||\sin(2\psi)|\cos\psi}{12}}{\frac{|R-a||\sin(2\psi)|}{6} - 2\left(\frac{\psi(R-a)}{2} - \frac{R\sin\psi}{3} \right)} \right) \right] \tag{6.20}$$

For cases where the rotation ϕ exceeds the threshold rotation for crushing, i.e. for $\phi_c \leq |\phi|$, the derivation of $a_f(\phi)$ is not as straightforward. In this case, the elastic and plastic portions of the stress distribution (with lengths a_1 and a_2 as depicted in Fig. 6.7 respectively) need to be treated separately. In order to do this, the limiting contact length a_{lim} at which the interface exhibits pure plastic behaviour first needs to be determined by numerically solving Equation 6.21:

$$W = f_m R^2 \left(\psi_{\lim} - \frac{\sin(2\psi_{\lim})}{2} \right) \quad \textit{where} \quad \psi_{\lim} = \arccos\left(\frac{R - a_{\lim}}{R} \right) \tag{6.21}$$

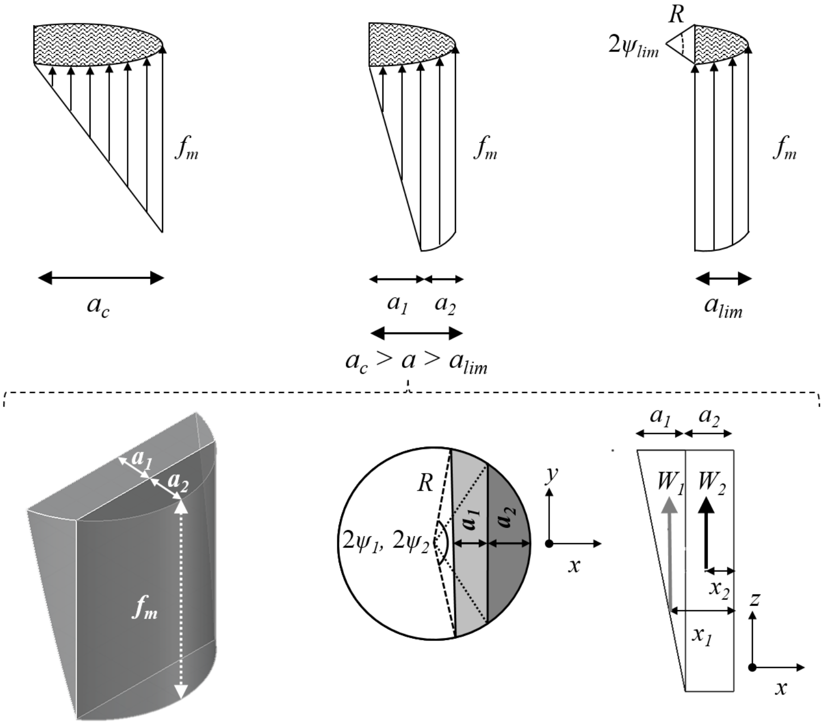

Fig. 6.7 Stress distribution for $\phi_c \leq |\phi|$ (solid circular base) – elastic portion shown in light grey, plastic in dark grey

The length a_2 of the plastic portion of the stress distribution, which depends on the rotation of the structure ϕ, can then be computed using the given expression:

$$a_2(\phi) = \left(\frac{|\phi| - \phi_c}{|\phi|} \right) a_{\lim} \tag{6.22}$$

Upon calculating a_2, the reaction force W_2 from the plastic portion of the stress distribution is then calculated as shown below:

$$W_2 = f_m R^2 \left(\psi_2 - \frac{\sin(2\psi_2)}{2} \right) \quad \textit{where} \quad \psi_2 = \arccos\left(\frac{R - a_2}{R} \right) \tag{6.23}$$

This reaction force W_2 can be assumed to act at a distance of x_2 from the edge of the base:

$$x_2 = \frac{4R\sin^3\psi_2}{3\left(2\psi_2 - \sin(2\psi_2)\right)} \tag{6.24}$$

Similarly, the reaction force W_1 from the elastic portion of the stress distribution can be determined by simply subtracting W_2 from the total weight of the structure W:

$$W_1 = W - W_2 \tag{6.25}$$

Consequently, the length a_1 of the elastic portion of the stress distribution can be obtained by numerically solving the following equation:

$$W_1 = f_m R \left[\begin{array}{l} R\left(\frac{\sin(2\psi_2)}{2} - \psi_2 + \pi\right) + \frac{2R^2}{3a_1}\left(\sqrt{1 - \left(\frac{a_1+a_2-R}{R}\right)^2} - \sqrt{1 - \left(\frac{R-a_2}{R}\right)^2}\right) \\ +\frac{1}{3a_1}\left((a_1 + a_2 - R)^2\sqrt{1 - \left(\frac{a_1+a_2-R}{R}\right)^2}\right) - \\ \frac{R}{a_1}\left(\arccos\left(\frac{a_1+a_2-R}{R}\right)(a_1 + a_2 - R) + (R - a_2)(\pi - \psi_2)\right) \end{array} \right] \tag{6.26}$$

The distance x_1 at which the resultant force W_1 acts is found by determining the x-coordinate of the centroid of the 3D stress distribution (using triple integrals), which is considered as 3 separate sections as illustrated by Fig. 6.8.

$$\begin{gathered} V_1 = \int_{0}^{f_m} \int_{-R\sin\psi_1(z)}^{-R\sin\psi_2} \int_{R\cos\psi_1(z)}^{\left|R^2-y^2\right|} x\partial x\partial y\partial z \\ V_2 = \int_{0}^{f_m} \int_{-R\sin\psi_2}^{R\sin\psi_2} \int_{R\cos\psi_1(z)}^{R\cos\psi_2} x\partial x\partial y\partial z \\ V_3 = \int_{0}^{f_m} \int_{R\sin\psi_2}^{R\sin\psi_1(z)} \int_{R\cos\psi_1(z)}^{\left|R^2-y^2\right|} x\partial x\partial y\partial z \end{gathered} \tag{6.27}$$

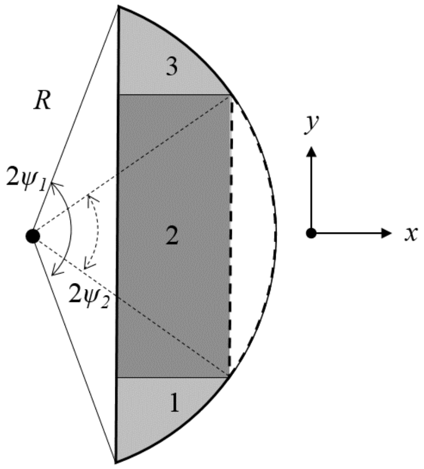

Fig. 6.8 3 separate sections of stress distribution considered for computation of x_1

Thus:

$$x_1 = \left(\frac{V_1 + V_2 + V_3}{W_1}\right) \quad where \quad \psi_1(z) = \arccos\left(\frac{R - a_2 - {}^{a_1 z}\!/_{f_m}}{R}\right) \tag{6.28}$$

Finally, the resultant point of application of the reaction force $a_f(\phi)$ for the elasto-plastic case is obtained by taking the weighted average of x_1 and x_2 as shown below:

$$a_f(\phi) = \operatorname{sgn}(\phi)\left(R - \frac{W_1 x_1 + W_2 x_2}{W}\right) \tag{6.29}$$

6.2.4 Hollow circular interface

The expressions derived in the previous section for solid circular bases were also modified to account for hollow circular bases, as are commonly found in structures such as minarets, spires and towers as illustrated by Fig. 6.9. The joint opening rotation ϕ_{jo} in this case is determined using the following expression:

$$\phi_{jo} = \frac{W}{k_n \pi R_O \left(R_O^2 - R_I^2\right)} \tag{6.30}$$

where R_O and R_I are the outer and inner radii of the base respectively.

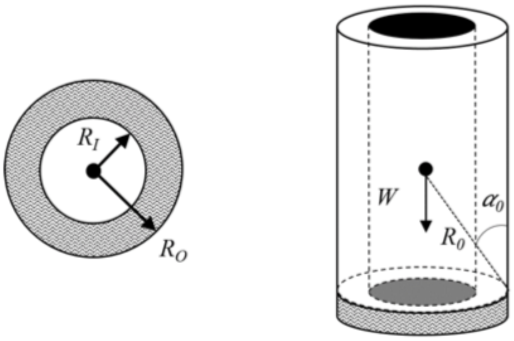

Photo of Dharahara Tower removed for copyright reasons. Copyright holder is Ian Trower/ JAI/Corbis.

Fig. 6.9 Hollow circular base geometry and example real-world application – Dharahara Tower (Ian Trower/JAI/Corbis)

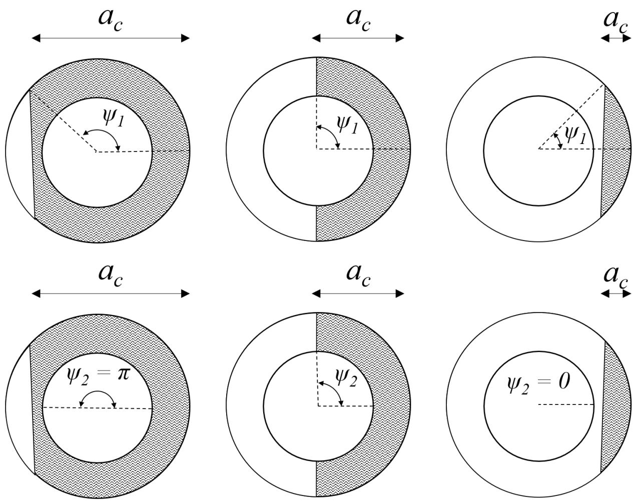

Case I Case II Case III

Fig. 6.10 Different cases considered for threshold contact length a_c for the hollow circular base

The threshold contact length a_c, at which the stress at the base is equal to the compressive strength f_m, is determined by numerically solving the following expression:

$$W = \begin{bmatrix} \frac{2 f_m R_O^2}{a_c}\left[\frac{\psi_1}{2}\left(a_c - R_O\right) + \frac{R_O}{3}\sin\psi_1\right] + \left|\frac{R_O^2 |\sin(2\psi_1)| f_m (a_c - R_O)}{6 a_c}\right| \\ -\frac{2 f_m R_I^2}{a_c}\left[\frac{\psi_2}{2}\left(a_c - R_O\right) + \frac{R_I}{3}\sin\psi_2\right] - \left|\frac{R_I^2 |\sin(2\psi_2)| f_m (a_c - R_O)}{6 a_c}\right| \end{bmatrix} \tag{6.31}$$

where:

$$\psi_1 = \arccos\left(\frac{R_O - a_c}{R_O}\right) \tag{6.32}$$

However, as in the case of the hollow rectangular base, three possible cases for a_c need to be considered, as illustrated by Fig. 6.10. Thus, depending on the case, the appropriate value/expression for ψ_2 needs to be selected, as shown below:

$$\begin{array}{ll} \textit{Case I}: & \psi_2 = \pi \\ \textit{Case II}: & \psi_2 = \arccos\left(\frac{R_O - a_c}{R_I}\right) \\ \textit{Case III}: & \psi_2 = 0 \end{array} \tag{6.33}$$

The computed value of a_c is then substituted into Equation 6.4 to obtain the threshold rotation for crushing ϕ_c for the hollow circular base.

Once the threshold rotations are computed, expressions can then be derived for the position of the reaction force. In the case of full contact, i.e. for $0 < |\phi| \leq \phi_{jo}$, the following analytical expression can be used for $a_f(\phi)$:

$$a_f(\phi) = \operatorname{sgn}(\phi)\left[R_O - \left(\frac{\pi\left(R_O^4 - R_I^4\right) k_n |\phi|}{4W}\right)\right] \tag{6.34}$$

Note that $a_f(0) = R_O$. In the case of partial contact with pure elastic behaviour, i.e. $\phi_{jo} \leq |\phi| \leq \phi_c$, the contact length a varies with ϕ and is determined by numerically solving the following expression in a manner similar to that for a_c for each value of ϕ, with ψ_1 and ψ_2 being defined as in Equations 6.32 and 6.33 respectively but in this case replacing a_c with a:

$$W = \begin{bmatrix} 2 k_n |\phi| R_O^2 \left[\frac{\psi_1}{2}\left(a - R_O\right) + \frac{R_O}{3}\sin\psi_1\right] + \left|\frac{R_O^2 |\sin(2\psi_1)| k_n |\phi| (a - R_O)}{6}\right| \\ -2 k_n |\phi| R_I^2 \left[\frac{\psi_2}{2}\left(a - R_O\right) + \frac{R_I}{3}\sin\psi_2\right] - \left|\frac{R_I^2 |\sin(2\psi_2)| k_n |\phi| (a - R_O)}{6}\right| \end{bmatrix} \tag{6.35}$$

The computed value of a is then substituted into the following equation to get $a_f(\phi)$:

$$a_f(\phi) = \operatorname{sgn}(\phi)\left[R_O - \frac{2k_n|\phi|}{W}\left(\begin{array}{l} R_O^3\left[\begin{array}{l}\frac{\sin\psi_1(a-R_O)}{3} + \frac{R_O(\psi_1+\sin\psi_1\cos\psi_1)}{8} \\ -\frac{|\sin(2\psi_1)(a-R_O)|\cos(\pi-\psi_1)}{24}\end{array}\right] \\ -R_I^3\left[\begin{array}{l}\frac{\sin\psi_2(a-R_O)}{3} + \frac{R_I(\psi_2+\sin\psi_2\cos\psi_2)}{8} \\ -\frac{|\sin(2\psi_2)(a-R_O)|\cos(\pi-\psi_2)}{24}\end{array}\right]\end{array}\right)\right] \tag{6.36}$$

As was observed for the solid circular base, in the case of partial contact with elasto-plastic behaviour, i.e. $\phi_c \leq |\phi|$, the derivation of $a_f(\phi)$ is more complicated. Once again a_{lim}, which is the limiting contact length at which the interface exhibits pure plastic behaviour, first needs to be determined, and this is done by numerically solving the following equation:

$$W = f_m\left[R_O^2\left(\psi_{\lim,O} - \frac{\sin(2\psi_{\lim,O})}{2}\right) - R_I^2\left(\psi_{\lim,I} - \frac{\sin(2\psi_{\lim,I})}{2}\right)\right] \tag{6.37}$$

where $\psi_{lim,O}$ and $\psi_{lim,I}$ are defined the same way as ψ_1 and ψ_2 respectively, but in this case substituting a_{lim} for a_c.

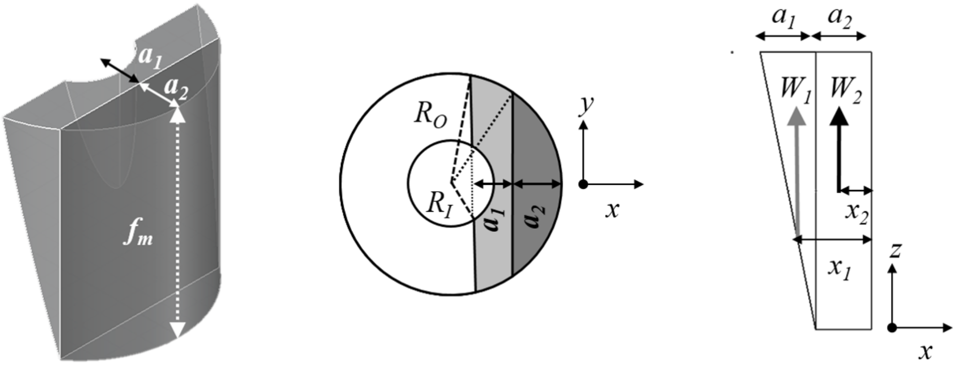

Fig. 6.11 Stress distribution for $\phi_c \leq |\phi|$ (hollow circular base) – elastic portion shown in light grey, plastic in dark grey

The length of the plastic portion of the stress distribution (a_2 in Fig. 6.11) is defined the same way as it was for the solid circular base (Equation 6.22) and once computed, it can be used to calculate W_2 using the following expression:

$$W_2 = f_m\left[R_O^2\left(\psi_{2,O} - \frac{\sin(2\psi_{2,O})}{2}\right) - R_I^2\left(\psi_{2,I} - \frac{\sin(2\psi_{2,I})}{2}\right)\right] \tag{6.38}$$

where $\psi_{2,O}$ and $\psi_{2,I}$ are defined the same way as ψ_1 and ψ_2 respectively, but in this case replacing a_c with a_2. This reaction from the plastic portion of the stress distribution can be assumed to act at a distance of x_2 from the edge of the base (Fig.6.11):

$$x_2 = \frac{2f_m}{3W_2}\left[R_O^3 \sin^3 \psi_{2,O} - R_I^3 \sin^3 \psi_{2,I}\right] \tag{6.39}$$

Similarly W_1, the reaction from the elastic portion of the stress distribution can be found by subtracting W_2 from the total weight of the structure W, as was done in the case of the solid circular base (Equation 6.25). The length a_1 of the elastic portion of the stress distribution is then found by numerically solving the following expression:

$$W_1 = \begin{bmatrix} R_O^2 \int\limits_0^{f_m} \left[\left(\psi_{1,O}(z) - \frac{\sin(2\psi_{1,O}(z))}{2}\right) - \left(\psi_{2,O} - \frac{\sin(2\psi_{2,O})}{2}\right)\right] \partial z \\ -R_I^2 \int\limits_0^{f_{mI}} \left[\left(\psi_{1,I}(z) - \frac{\sin(2\psi_{1,I}(z))}{2}\right) - \left(\psi_{2,I} - \frac{\sin(2\psi_{2,I})}{2}\right)\right] \partial z \end{bmatrix} \tag{6.40}$$

where:

$$\psi_{1,O}(z) = \arccos\left(\frac{R_O - a_2 - {}^{a_1 z}\!/_{f_m}}{R_O}\right) \tag{6.41}$$

and $\psi_{1,I}$(z) and f_{mI} depend on the magnitude of a_2 and are defined as follows:

$$\psi_{1,I}(z) = \arccos\left(\frac{R_I - {}^{a_1 z}\!/_{f_m}}{R_I}\right) \qquad f_{mI} = f_m\left(\frac{a_1 + a_2 - (R_O - R_I)}{a_1}\right) \qquad (if\ a_2 < R_O - R_I) \tag{6.42}$$

$$\psi_{1,I}(z) = \arccos\left(\frac{R_O - a_2 - {}^{a_1 z}\!/_{f_m}}{R_I}\right) \qquad f_{mI} = f_m \qquad (if\ a_2 > R_O - R_I) \tag{6.43}$$

The distance x_1 at which W_1 acts is found by determining the x-coordinate of the centroid of the 3D stress distribution (using triple integrals), but in this case by treating the inner and outer sections separately:

$$\begin{aligned}
V_{1,O} &= \int\limits_0^{f_m} \int\limits_{-R_O \sin\psi_{1,O}(z)}^{-R_O \sin\psi_{2,O}} \int\limits_{R_O \cos\psi_{1,O}(z)}^{\left|R_O^2 - y^2\right|} x \partial x \partial y \partial z & V_{1,I} &= \int\limits_0^{f_{mI}} \int\limits_{-R_I \sin\psi_{1,I}(z)}^{-R_I \sin\psi_{2,I}} \int\limits_{R_I \cos\psi_{1,I}(z)}^{\left|R_I^2 - y^2\right|} x \partial x \partial y \partial z \\
V_{2,O} &= \int\limits_0^{f_m} \int\limits_{-R_O \sin\psi_{2,O}}^{R_O \sin\psi_{2,O}} \int\limits_{R_O \cos\psi_{1,O}(z)}^{R_O \cos\psi_{2,O}} x \partial x \partial y \partial z & V_{2,I} &= \int\limits_0^{f_{mI}} \int\limits_{-R_I \sin\psi_{2,I}}^{R_I \sin\psi_{2,I}} \int\limits_{R_I \cos\psi_{1,I}(z)}^{R_I \cos\psi_{2,I}} x \partial x \partial y \partial z \\
V_{3,O} &= \int\limits_0^{f_m} \int\limits_{R_O \sin\psi_{2,O}}^{R_O \sin\psi_{1,O}(z)} \int\limits_{R_O \cos\psi_{1,O}(z)}^{\left|R_O^2 - y^2\right|} x \partial x \partial y \partial z & V_{3,I} &= \int\limits_0^{f_{mI}} \int\limits_{R_I \sin\psi_{2,I}}^{R_I \sin\psi_{1,I}(z)} \int\limits_{R_I \cos\psi_{1,I}(z)}^{\left|R_I^2 - y^2\right|} x \partial x \partial y \partial z
\end{aligned} \tag{6.44}$$

leading to:

$$x_1 = \left[\frac{(V_{1,O} + V_{2,O} + V_{3,O}) - (V_{1,I} + V_{2,I} + V_{3,I})}{W_1} \right] \tag{6.45}$$

Finally, the resultant point of application of the reaction force $a_f(\phi)$ for this elasto-plastic case is obtained by taking the weighted average of x_1 and x_2 as presented in Equation 6.29 for the solid circular base.

6.3 Derivation of the modified equations of motion

In this section, the equations of motion for the single, two and multiple block mechanisms will be re-derived in order to account for the presence of flexible interfaces and crushing effects. Starting from first principles, the equation of motion for any rocking mechanism (single/two/multiple block) can be derived using Lagrange's equation as shown below:

$$\frac{\partial}{\partial t}\left(\frac{\partial T\left(\phi,\dot{\phi}\right)}{\partial \dot{\phi}}\right) - \frac{\partial T\left(\phi,\dot{\phi}\right)}{\partial \phi} + \frac{\partial V\left(\phi\right)}{\partial \phi} = -B\left(\phi\right)\ddot{u}_g + M\left(\phi\right) \tag{6.46}$$

where ϕ is the rotation of the block and $\dot{\phi}$ the angular velocity. The term $T(\phi,\dot{\phi})$ represents the kinetic energy of the system, $V(\phi)$ the potential energy, $B(\phi)\ddot{u}_g$ the generalized inertial force induced by the ground acceleration, and $M(\phi)$ the generalized force due to the external static forces (where relevant). Note that in Lagrange's equation, $B(\phi)\ddot{u}_g$ and $M(\phi)$ are obtained by taking the derivative of the virtual work done by these non-conservative forces. While the equations of motion presented in Chapter 3 for the rigid interface case derived these terms relative to a fixed rotation point, in this section new formulations - relative now to a shifting rotation point - will be presented for each of these terms for the single, two and multiple block mechanisms - which in turn will be used to derive their corresponding equations of motion. Specifically, two new formulations for modelling the interface are presented – namely a fully-flexible and semi-flexible model, with the latter also being used to re-derive the relationship between the relative rotations of the blocks (in the case of the two and multiple block mechanisms) as well as the coefficient of restitution (in the case of the single and two block mechanisms).

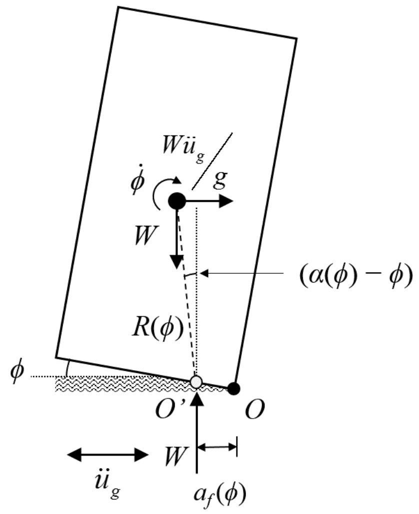

Fig. 6.12 Geometry of a rigid block rocking on a flexible interface

6.3.1 Single block mechanism

6.3.1.1 Fully-flexible model

In the case of the simple single block mechanism as depicted in Fig. 6.12, each of the aforementioned terms is defined as follows:

$$T\left(\phi,\dot{\phi}\right)=\frac{1}{2}I_{O'}\left(\phi\right)\dot{\phi}^2 \tag{6.47}$$

$$V\left(\phi\right)=WR\left(\phi\right)\cos\left(\alpha\left(\phi\right)-\phi\right) \tag{6.48}$$

$$B\left(\phi\right)=\frac{W}{g}R\left(\phi\right)\cos\left(\alpha\left(\phi\right)-\phi\right) \tag{6.49}$$

Note that the kinetic energy *$T(\phi,\dot{\phi})$* depends on *$I_{O'}(\phi)$*, which is the moment of inertia relative to the shifting rotation point *O'*, and is determined using the following equation:

$$I_{O'}\left(\phi\right)=I_C+\frac{W}{g}R(\phi)^2 \tag{6.50}$$

where I_C is the moment of inertia of the block about its centroid, and *$R(\phi)$* is the distance between the centroid of the block and the shifting rotation point *O'* (as indicated in Fig. 6.12). This distance *$R(\phi)$* is obtained from:

$$R(\phi)^2=R_0^2\cos^2\alpha_0+\left[R_0\sin\alpha_0-\mathrm{sgn}\left(\phi\right)a_f\left(\phi\right)\right]^2 \tag{6.51}$$

where *$a_f(\phi)$* is the “inward-shift” of the rotation point *O'* relative to original (rigid) rotation point *O*, as well as the location of the reaction force from the flexible interface. Similarly, $\alpha(\phi)$ is the slenderness of the block, and is obtained by making use of the following relationship between $R(\phi)$, R_0 and α_0:

$$\alpha(\phi) = \arccos\left(\frac{R_0 \cos\alpha_0}{R(\phi)}\right) \tag{6.52}$$

Substituting these terms into Lagrange's equation (Equation 6.46), results in the equation of motion assuming the following form:

$$\ddot{\phi} = -\frac{WR(\phi)}{I_{O'}(\phi)}\left[\begin{array}{l} -\frac{1}{g}\frac{\partial R}{\partial \phi}\dot{\phi}^2 + \frac{1}{R(\phi)}\frac{\partial R}{\partial \phi}\cos(\alpha(\phi)\,\mathrm{sgn}(\phi)-\phi) \\ -\sin(\alpha(\phi)\,\mathrm{sgn}(\phi)-\phi)\left(\frac{\partial \alpha}{\partial \phi}-1\right)+\frac{\ddot{u}_g}{g}\cos(\alpha(\phi)\,\mathrm{sgn}(\phi)-\phi) \end{array}\right] \tag{6.53}$$

where $\frac{\partial R}{\partial \phi}$ and $\frac{\partial \alpha}{\partial \phi}$ represent the rate of change of the radius of rotation $R(\phi)$ and the slenderness $\alpha(\phi)$ respectively, relative to the rotation of the block. However, for most considered values of interface stiffness and compressive strength, as well as block slenderness and scale, $\frac{\partial R}{\partial \phi}$ and $\frac{\partial \alpha}{\partial \phi}$ are only significant for extremely small rotations of the structure. While the maximum rotation for which these terms are significant tends to increase with a decrease in interface stiffness and increase in block slenderness, the influence of $\frac{\partial R}{\partial \phi}$ and $\frac{\partial \alpha}{\partial \phi}$ is generally minimal for $\phi/\alpha_0 \geq 0.05$, as illustrated by Fig. 6.13. Note that in the interest of brevity only the plots for varying joint stiffness and block slenderness are shown here as similar plots for joint compressive strength and block scale showed minimal variation in the results.

Thus, assuming $\frac{\partial R}{\partial \phi} = 0$ and $\frac{\partial \alpha}{\partial \phi} = 0$, Equation 6.53 can be simplified and re-written as:

$$\ddot{\phi} = -\frac{WR(\phi)}{I_{O'}(\phi)}\left[\sin(\alpha(\phi)\,\mathrm{sgn}(\phi)-\phi)+\frac{\ddot{u}_g}{g}\cos(\alpha(\phi)\,\mathrm{sgn}(\phi)-\phi)\right] \tag{6.54}$$

which is essentially similar in form to Equation 6.1, but now with the influence of the reaction due the flexible interface implicitly incorporated into the equation of motion through the derivation of the kinetic energy $T(\phi,\dot{\phi})$ and potential energy $V(\phi)$, as well as the generalized inertial force $B(\phi)\ddot{u}_g$, relative to the shifting rotation point *O'*.

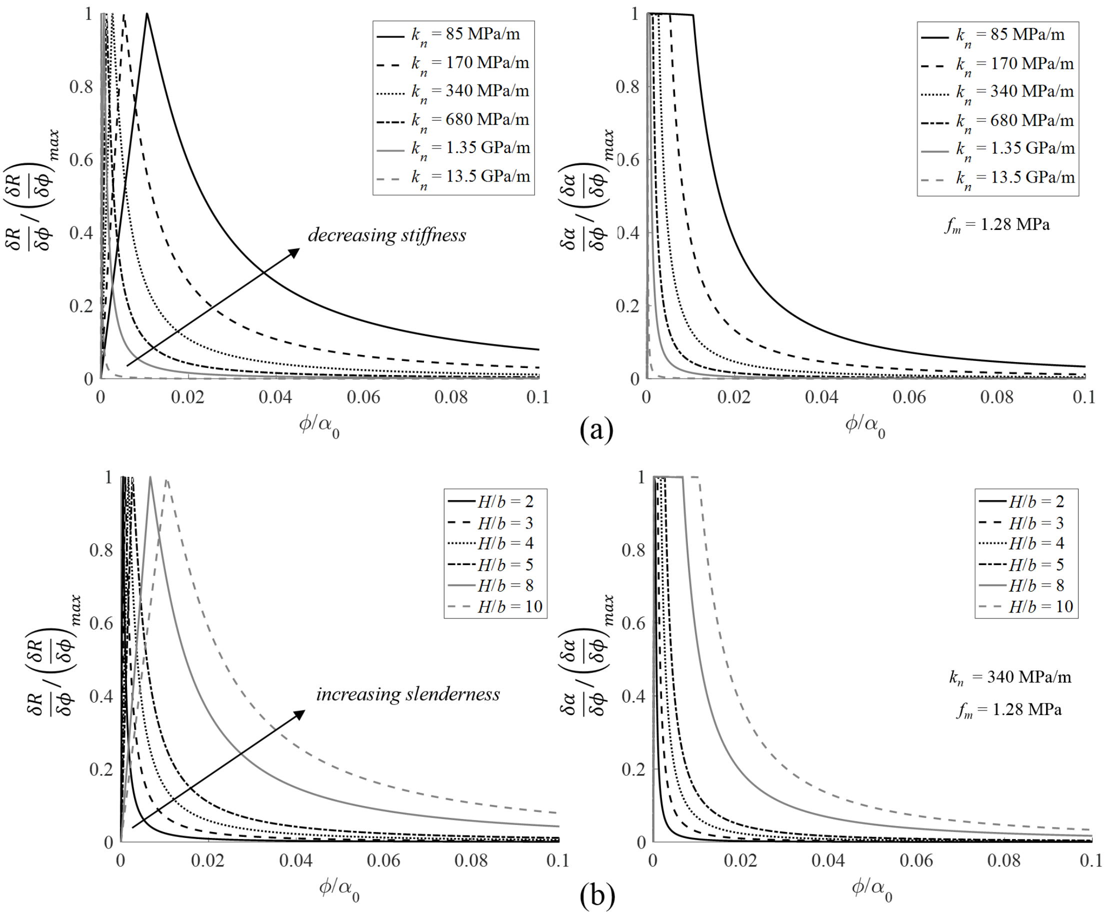

Fig. 6.13 Variation of $\frac{\partial R}{\partial \phi}$ (left) and $\frac{\partial \alpha}{\partial \phi}$ (right) (both normalized by their maximum values) with varying (a) interface stiffness k_n and (b) block slenderness

6.3.1.2 Semi-flexible model

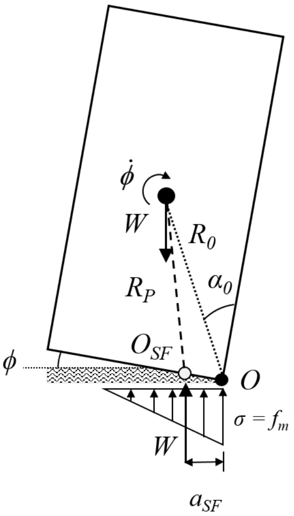

Fig. 6.14 Single block mechanism - semi-flexible interface model

Further simplifications to Equation 6.54 can be made through the introduction of the semi-flexible interface model. This model still accounts for the inward shift of the rotation point due to the introduction of the non-rigid joint, but in a more simplified/approximate manner than its fully-flexible counterpart. Unlike the fully-flexible formulation, which models the hinge as continuously moving, the semi-flexible model fixes the hinge in place at a distance a_{SF} from the original (rigid) hinge location, which is equal to the value of $a_f(\phi)$ for $\phi = \phi_c$, that is, the point at which the stress distribution at the base switches from elastic to elasto-plastic - as illustrated by Fig. 6.14.

The kinetic energy of the block $T_{SF}(\phi,\dot{\phi})$ in this case is determined relative to the inwardly-shifted (and now fixed) rotation point O_{SF}, and is defined as:

$$T_{SF}\left(\phi,\dot{\phi}\right) = \frac{1}{2} I_{SF}\dot{\phi}^2 \tag{6.55}$$

where I_{SF} is the moment of inertia of the block relative to O_{SF} and is determined using the following equation:

$$I_{SF} = I_C + \frac{W}{g} {R_P}^2 \tag{6.56}$$

where R_P is the semi-flexible radius of rotation and is given by:

$${R_P}^2 = (R_0 \cos\alpha_0)^2 + (R_0 \sin\alpha_0 - a_{SF})^2 \tag{6.57}$$

Similarly, the semi-flexible slenderness of the block α_P is calculated using the following equation:

$$\alpha_P = \arccos\left(\frac{R_0 \cos\alpha_0}{R_P}\right) \tag{6.58}$$

A comparison of the fully-flexible and semi-flexible models in terms of radius of rotation and moment of inertia (Fig. 6.15) revealed that for all considered values of interface stiffness k_n, the semi-flexible model is able to approximate the fully-flexible model fairly well (generally being accurate to within 2.5%). However, in the case of the block slenderness (Fig. 6.15c), the semi-flexible model's approximation is not as accurate - especially for smaller rotations of the structure. Similar trends were also observed for varying values of the compressive strength f_m, but in the interest of brevity only the plots for varying stiffness are included here.

Thus, while the semi-flexible model can be used to approximate the kinetic energy of the block, for the potential energy and generalized forces, it is recommended to use the fully-flexible derivations instead. Consequently, for the semi-flexible interface model, Equation 6.54 can be re-written as:

$$\ddot{\phi} = -\frac{WR(\phi)}{I_{SF}}\left[\sin\left(\alpha\left(\phi\right)\operatorname{sgn}\left(\phi\right)-\phi\right)+\frac{\ddot{u}_g}{g}\cos\left(\alpha\left(\phi\right)\operatorname{sgn}\left(\phi\right)-\phi\right)\right] \tag{6.59}$$

Using the assumption of conservation of angular momentum similar to Housner (1963), the semi-flexible model can also be used to re-derive the coefficient of restitution for the single rocking block, which now assumes the following form:

$$\eta_{SF} = 1 - 2\frac{MR_P^2}{I_{SF}}\sin^2\alpha_P \tag{6.60}$$

where M is the mass of the block. As evidenced by Fig. 6.16, for the range of compressive strengths, block scales and slendernesses considered, Equation 6.60 generally yields a slightly higher value for the coefficient of restitution than the purely rigid (η_R) formulation presented in Chapter 3, with the ratio between the two tending to increase with an increase in block scale and decrease in block slenderness (i.e. increase in α_0), as well as increase with a decrease in interface compressive strength f_m.

6.3.2 Two block mechanism

6.3.2.1 Fully-flexible model

The rocking equation of motion was also re-derived for the two block mechanism, which is used to represent cracked wall sections under the influence of varying overburden forces F. Following the approach outlined in Chapter 3 for the rigid interface case, the height h_c at which the wall segment cracks and develops an additional hinge is first determined using Equation 3.27, which in turn is used to determine W_1 and W_2, which are the weights of the bottom and top blocks respectively - as illustrated by Fig. 6.17a.

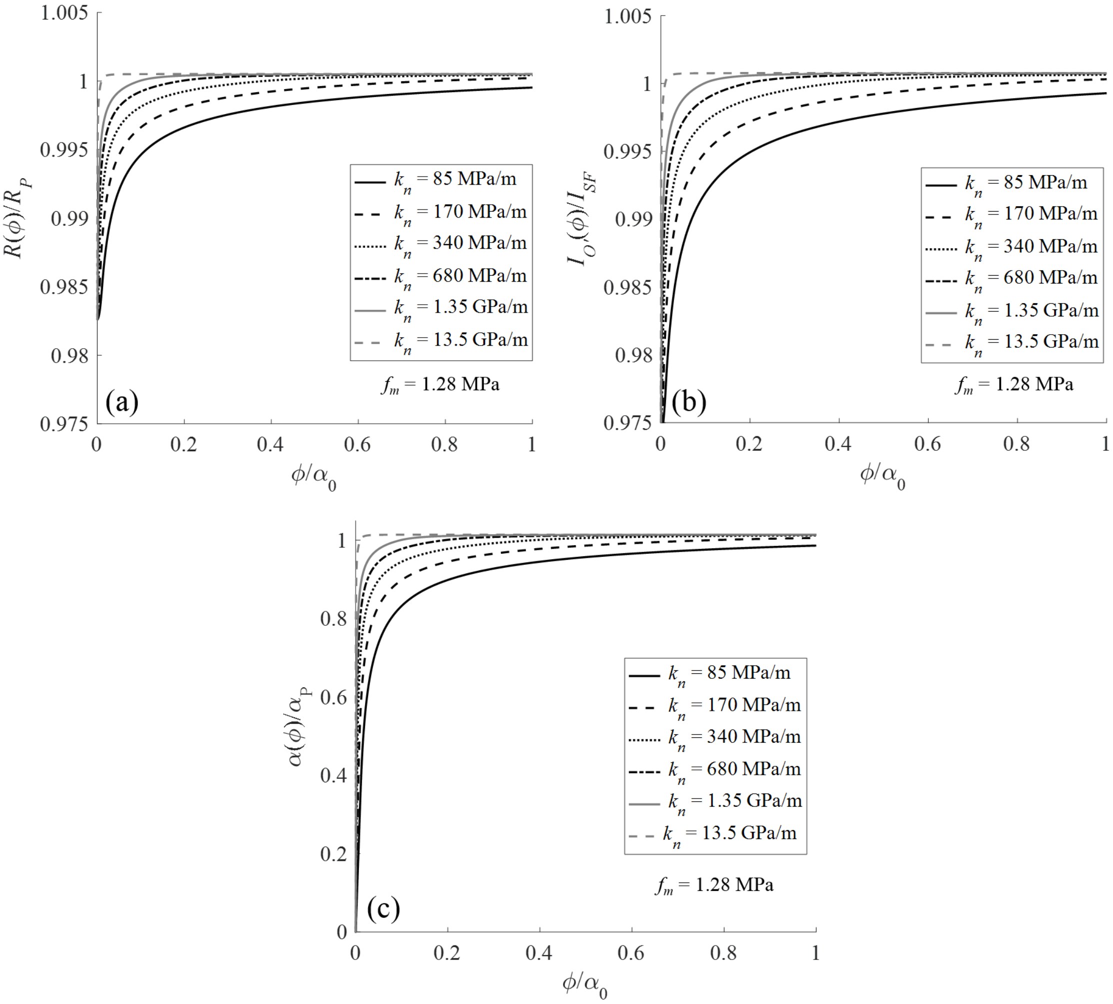

Fig. 6.15 Comparison of the fully-flexible and semi-flexible interface models in terms of (a) radius of rotation, (b) moment of inertia and (c) block slenderness, for varying values of the interface stiffness k_n

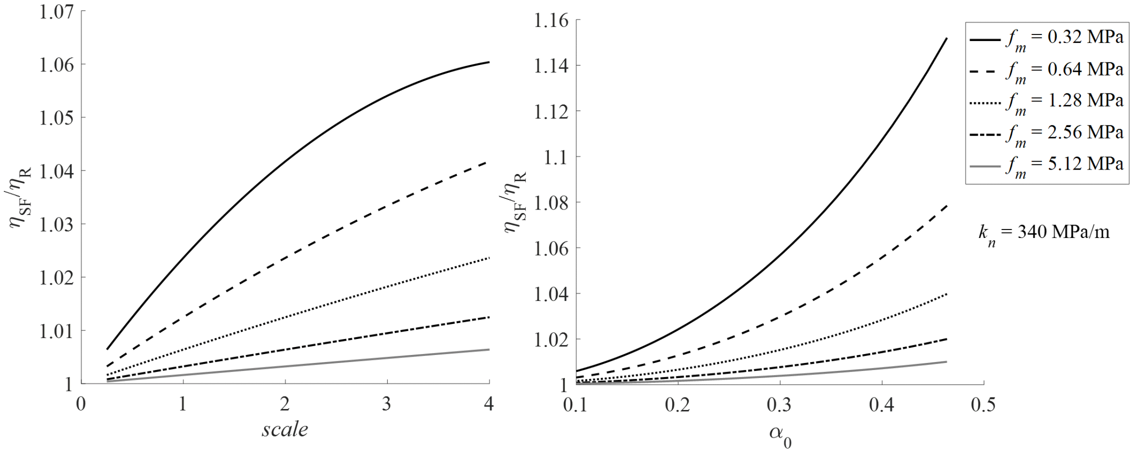

(a) (b)

Fig. 6.16 Comparison of the semi-flexible η_{SF} and rigid η_R coefficients of restitution for varying (a) block scale and (b) block slenderness, for varying values of the interface compressive strength f_m

The kinetic energy $T(\phi,\dot{\phi})$ and potential energy $V(\phi)$ of the blocks, as well as the generalized forces $B(\phi)\ddot{u}_g$ and $M(\phi)$, derived now relative to the shifting rotation points 1, 2 and 3 (Fig. 6.17(b-d)), can then be computed using Equations 6.61-6.64:

$$T(\phi,\dot{\phi}) = \frac{\dot{\phi}^2}{2}\left[\begin{array}{l} I_{G1}+I_{G2}\left(\frac{\partial\phi_2(\phi)}{\partial\phi}\right)^2+\frac{W_1}{g}R_1(\phi)^2+\frac{W_2}{g}R_2(\phi)^2\left(\frac{\partial\phi_2(\phi)}{\partial\phi}\right)^2+\frac{W_2}{g}R_{12}(\phi)^2 \\ -2\frac{W_2}{g}R_{12}(\phi)R_2(\phi)\cos(\alpha_{12}(\phi)-\phi+\alpha_2(\phi)-\phi_2(\phi))\frac{\partial\phi_2(\phi)}{\partial\phi} \end{array}\right] \tag{6.61}$$

$$V(\phi) = W_1R_1(\phi)\cos(\alpha_1(\phi)-\phi)+W_2\left[R_{12}(\phi)\cos(\alpha_{12}(\phi)-\phi)+R_2(\phi)\cos(\alpha_2(\phi)-\phi_2(\phi))\right] \tag{6.62}$$

$$B(\phi) = \frac{W_1}{g}R_1(\phi)\cos(\alpha_1(\phi)-\phi)+\frac{W_2}{g}\left[\begin{array}{l} R_{12}(\phi)\cos(\alpha_{12}(\phi)-\phi) \\ -R_2(\phi)\cos(\alpha_2(\phi)-\phi_2(\phi))\frac{\partial\phi_2(\phi)}{\partial\phi} \end{array}\right] \tag{6.63}$$

$$M(\phi) = -F\left[R_{12}(\phi)\sin(\alpha_{12}(\phi)-\phi)+R_{23}(\phi)\sin(\alpha_{23}(\phi)-\phi_2(\phi))\frac{\partial\phi_2(\phi)}{\partial\phi}\right] \tag{6.64}$$

where I_{G1} and I_{G2} represent the moments of inertia of the bottom and top blocks about their own centroids, while the other geometric properties are defined in Fig. 6.17. Note that the inward shift of each of the hinges varies based on both the magnitude of the reaction force F_x at the interface, as well as the rotation ϕ_x of the blocks relative to each other, as illustrated by Fig. 6.17. The values for F_x and ϕ_x for each hinge can be found in Table 6.1.

Furthermore, the relationship between the rotation $\phi_2(\phi)$ of the top and ϕ of the bottom block is determined by making use of the constraint that the wall is restrained in the horizontal direction, and that the two-block system can thus only translate vertically. However, unlike the approach presented in Mauro et al. (2015) and Sorrentino et al. (2008b), where the hinges are located at the outer extremity of the blocks, in this case the intermediate hinge is fixed at its semi-flexible location - that is, at a_{SF2}

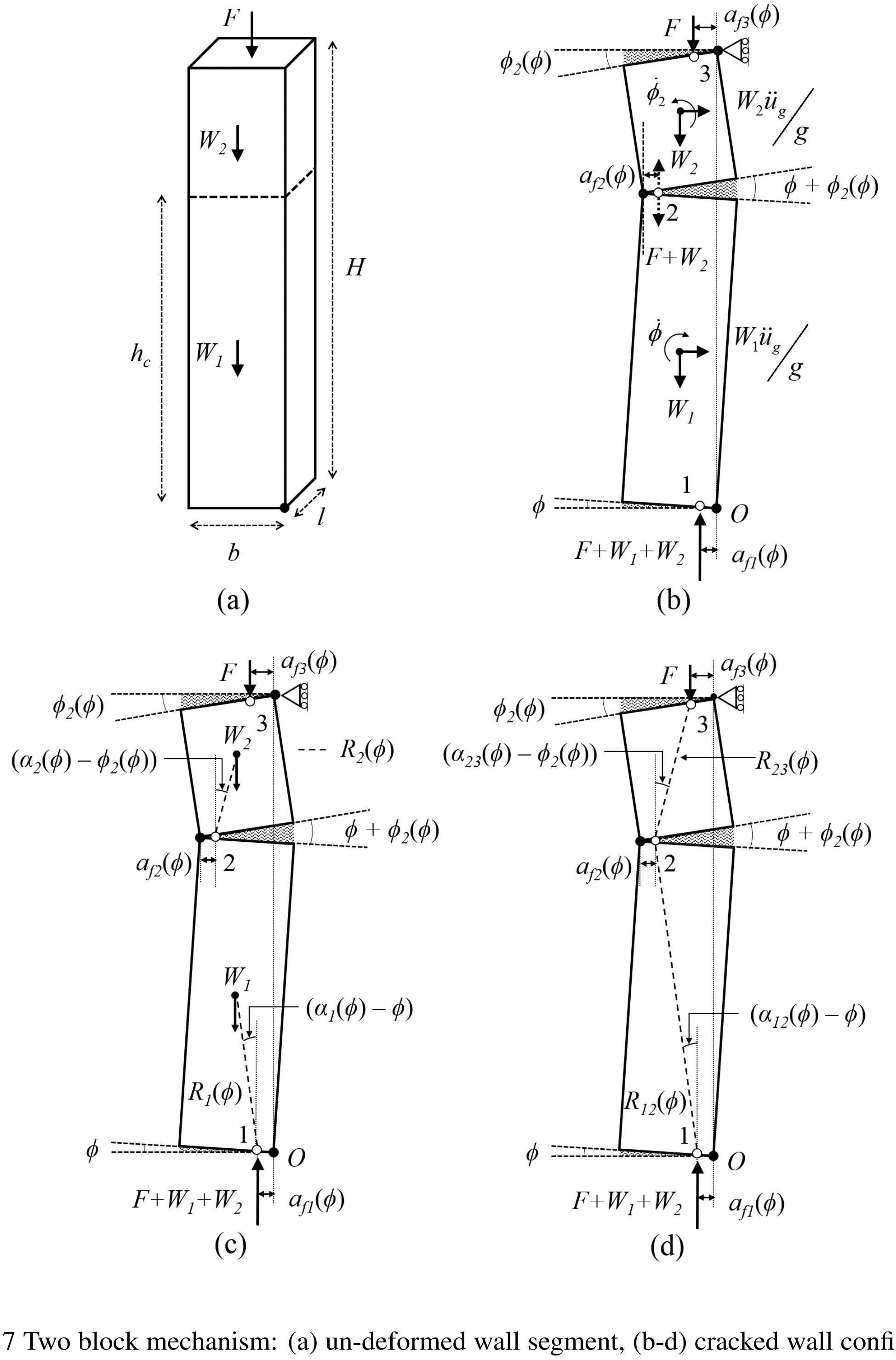

Fig. 6.17 Two block mechanism: (a) un-deformed wall segment, (b-d) cracked wall configuration showing the different geometric properties used in the equation of motion

Table 6.1 Two block mechanism: Reaction forces and rotations for each of the hinges

x	F_x	ϕ_x
1	F+W_1+W_2	ϕ
2	F+W_2	ϕ+ϕ_2
3	F	ϕ_2

= $a_{f2}(\phi = \phi_c)$, thus leading to the following expression for $\phi_2(\phi)$:

$$\phi_2(\phi) = \alpha_{2H} - \arcsin\left[\frac{R_{O2}}{R_{2H}}\sin(\alpha_{O2} - \phi)\right] \tag{6.65}$$

where α_{2H}, α_{O2}, R_{2H} and R_{O2} are defined in Fig. 6.18. Note that Equation 6.65 can then be used to determine $\frac{\partial \phi_2}{\partial \phi}$.

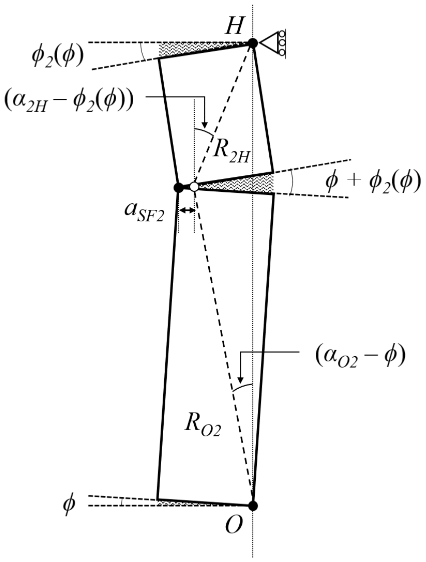

Fig. 6.18 Geometric parameters used to determine the relationship between the rotations of the top and bottom blocks

The expressions for $T(\phi,\dot{\phi})$, $V(\phi)$, $B(\phi)\ddot{u}_g$ and $M(\phi)$ are then substituted into Lagrange's equation (Equation 6.46) in order to generate the equation of motion for the system. As was the case for the single block mechanism, the influence of the terms $\frac{\partial R_x}{\partial \phi}$ and $\frac{\partial \alpha_x}{\partial \phi}$ (where x refers to the hinge number) is once again neglected as these were only found to be significant for small rotations of the structure (generally $\phi/\alpha_{01} \leq 0.05$, where α_{01} is the slenderness of the bottom block), as illustrated by Fig. 6.19 - both for the different blocks, as well as for varying values of the overburden force (normalized by the full weight of the un-cracked wall segment W_0, and shown here for the case of the bottom block).

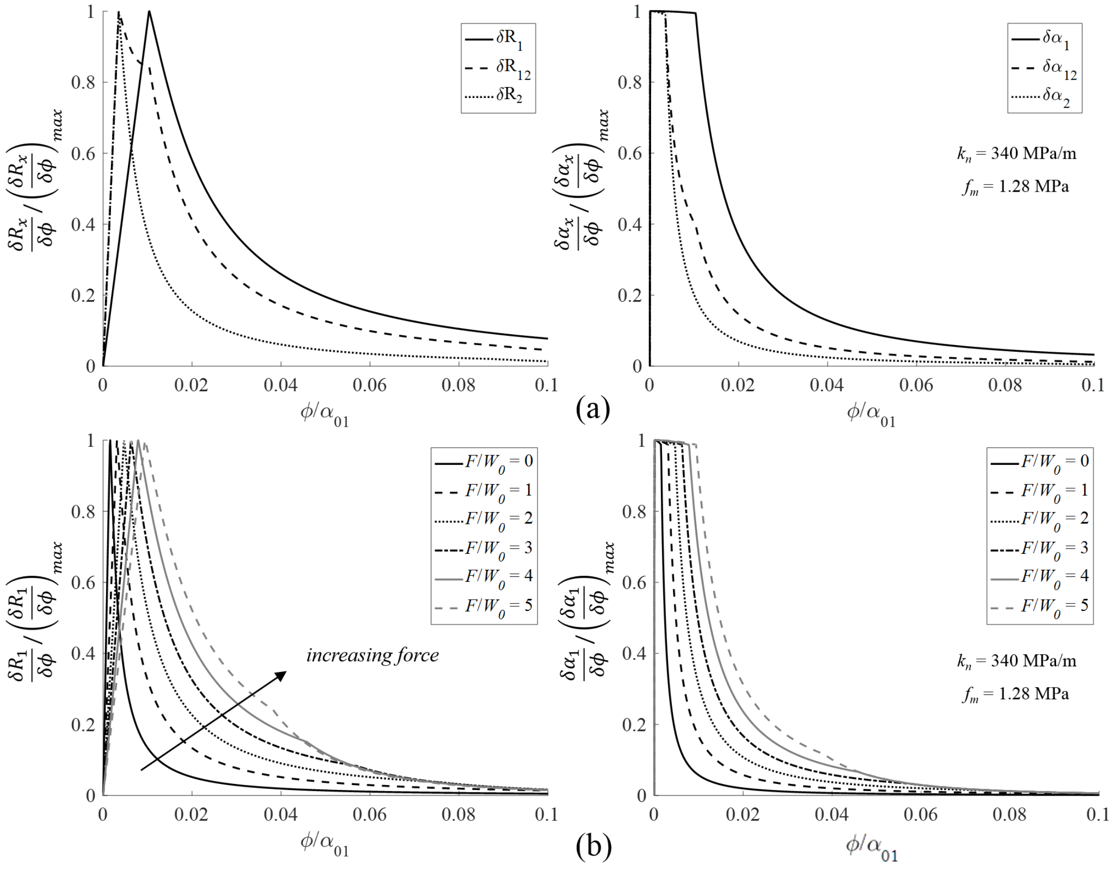

Fig. 6.19 Variation of $\frac{\partial R_x}{\partial \phi}$ (left) and $\frac{\partial \alpha_x}{\partial \phi}$ (right) (both normalized by their maximum values) for the two block mechanism for (a) the different blocks and (b) varying overburden forces

6.3.2.2 Semi-flexible model

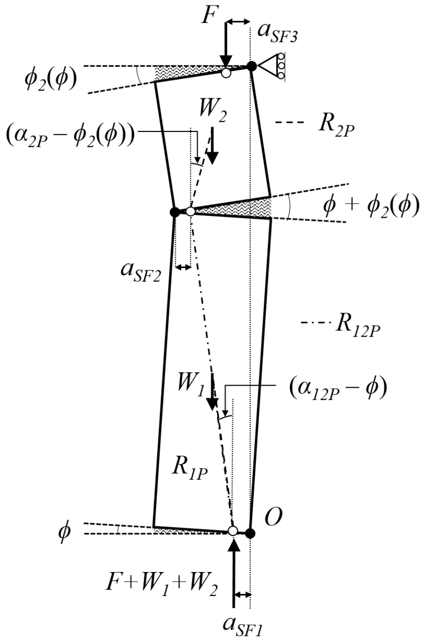

Fig. 6.20 Two block mechanism - semi-flexible interface model

In the case of the two block mechanism, the methodology to determine the semi-flexible hinge locations is the same as that used for the single block case, that is, at $a_{fx}(\phi_x = \phi_{cx})$, where x represents the hinge number and ϕ_{cx} the rotation at which the stress distribution at the interface switches from elastic to elasto-plastic. The kinetic energy of the system $T_{SF}(\phi,\dot{\phi})$ in this case is derived relative to the inwardly-shifted (but now fixed) rotation points, as given by Equation 6.66 below:

$$T_{SF}\left(\phi,\dot{\phi}\right) = \frac{\dot{\phi}^2}{2}\left[\begin{array}{l} I_{G1} + I_{G2}\left(\frac{\partial\phi_2(\phi)}{\partial\phi}\right)^2 + \frac{W_1}{g}R_{1P}{}^2 + \frac{W_2}{g}R_{2P}{}^2\left(\frac{\partial\phi_2(\phi)}{\partial\phi}\right)^2 + \frac{W_2}{g}R_{12P}{}^2 \\ -2\frac{W_2}{g}R_{12P}R_{2P}\cos\left(\alpha_{12P} - \phi + \alpha_{2P} - \phi_2\left(\phi\right)\right)\frac{\partial\phi_2(\phi)}{\partial\phi} \end{array}\right] \tag{6.66}$$

where I_{G1}, I_{G2}, $\phi_2(\phi)$ and $\frac{\partial\phi_2}{\partial\phi}$ are the same as for the fully-flexible interface model, while the other geometric properties are defined in Fig. 6.20. The coefficient of restitution is also re-derived for this mechanism by equating the angular momentum of the blocks before and after impact (similar to Sorrentino et al. (2008b), but determined now relative to the inwardly-shifted rotation points), leading to the following expression for η_{SF}:

$$\eta_{SF} = \frac{\left[\begin{array}{l} I_{G1} + m_1 (R_{1P} \cos \alpha_{1P})^2 - m_1 (R_{1P} \sin \alpha_{1P})^2 - I_{G2} \left.\frac{\partial \phi_2}{\partial \phi}\right|_{\phi=0} \\ +m_2 R_{2P} \cos \alpha_{2P} \left(R_{12P} \cos \alpha_{12P} + R_{2P} \cos \alpha_{2P}\right) \left.\frac{\partial \phi_2}{\partial \phi}\right|_{\phi=0} \\ -m_2 \left(R_{12P} \sin \alpha_{12P} + R_{2P} \sin \alpha_{2P} \left.\frac{\partial \phi_2}{\partial \phi}\right|_{\phi=0}\right) \left(R_{12P} \sin \alpha_{12P} - R_{2P} \sin \alpha_{2P}\right) \end{array}\right]}{\left[\begin{array}{l} I_{G1} + m_1 R_{1P}^2 - I_{G2} \left.\frac{\partial \phi_2}{\partial \phi}\right|_{\phi=0} \\ +m_2 R_{2P} \cos \alpha_{2P} \left(R_{12P} \cos \alpha_{12P} + R_{2P} \cos \alpha_{2P}\right) \left.\frac{\partial \phi_2}{\partial \phi}\right|_{\phi=0} \\ +m_2 \left(R_{12P} \sin \alpha_{12P} + R_{2P} \sin \alpha_{2P} \left.\frac{\partial \phi_2}{\partial \phi}\right|_{\phi=0}\right) \left(R_{12P} \sin \alpha_{12P} - R_{2P} \sin \alpha_{2P}\right) \end{array}\right]} \tag{6.67}$$

where m_1 and m_2 are the masses of the bottom and top blocks respectively. A comparison of η_{SF} to the coefficient of restitution obtained using the rigid formulation (η_R) presented in Chapter 3 revealed that, as in the case of the single block mechanism, Equation 6.67 generally yields a more conservative estimate for this parameter than its rigid counterpart. Furthermore, as Fig. 6.21 demonstrates, the difference between the two tends to increase with an increase in overburden force F as well as increase with a decrease in interface compressive strength f_m.

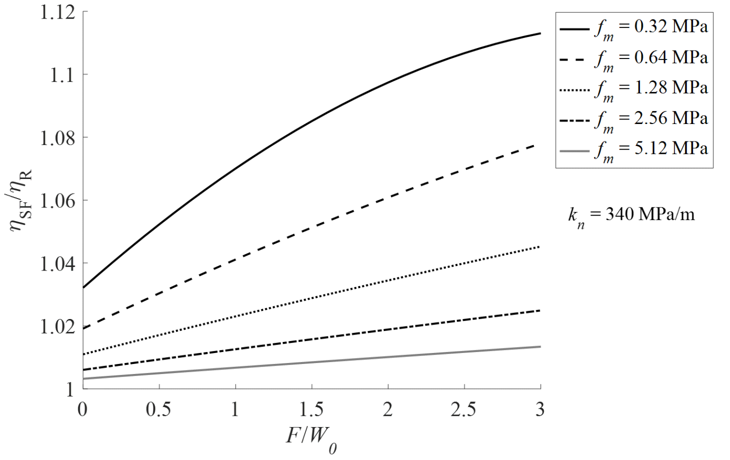

Fig. 6.21 Comparison of the semi-flexible η_{SF} and rigid η_R coefficients of restitution for varying overburden forces F (normalized by the full weight of the un-cracked wall segment W_0), for different values of the interface compressive strength f_m

6.3.3 Multiple block mechanism 1: Symmetric rocking frame

6.3.3.1 Fully-flexible model

The equation of motion was also re-derived for the symmetric rocking frame - which is used to capture the dynamic behaviour of structures such as portal frames as well as free-standing columns topped

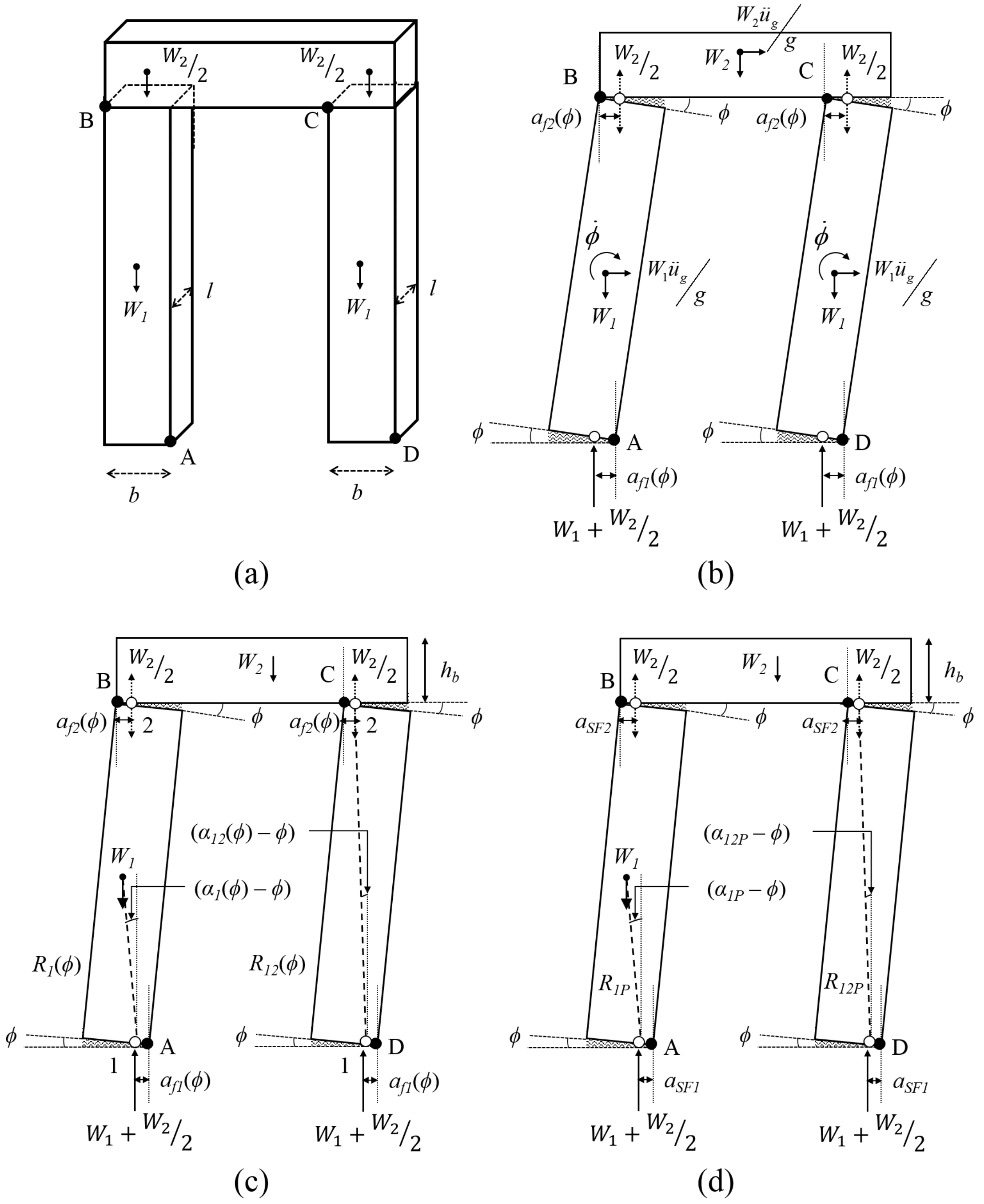

Fig. 6.22 Symmetric rocking frame: (a) un-deformed configuration, (b) forces acting on each of the blocks, (c) geometric properties used in the equation of motion and (d) semi-flexible interface model

Table 6.2 Symmetric rocking frame: Reaction forces and rotations for each of the hinges

x	F_x	ϕ_x
1	W_1+W_2/2	ϕ
2	W_2/2	ϕ

with rigid beams - as are commonly found in Greek temples (Makris and Vassiliou, 2013). Due to the symmetry of this structure, the columns exhibit identical rotations in this mechanism , while the beam only undergoes translation. The kinetic and potential energies, as well as the generalized inertial force for this mechanism - derived now relative to the shifting rotation points 1 and 2 (due to the symmetry of the mechanism and as indicated in Fig. 6.22c) - are defined as follows:

$$T\left(\phi,\dot{\phi}\right)=\dot{\phi}^2\left[I_{G1}+\frac{W_1}{g}R_1(\phi)^2+\frac{W_2}{2g}R_{12}(\phi)^2\right] \tag{6.68}$$

$$V\left(\phi\right)=2W_1R_1\left(\phi\right)\cos\left(\alpha_1\left(\phi\right)-\phi\right)+W_2\left[R_{12}\left(\phi\right)\cos\left(\alpha_{12}\left(\phi\right)-\phi\right)+\frac{h_b}{2}\right] \tag{6.69}$$

$$B\left(\phi\right)=\frac{2W_1}{g}R_1\left(\phi\right)\cos\left(\alpha_1\left(\phi\right)-\phi\right)+\frac{W_2}{g}R_{12}\left(\phi\right)\cos\left(\alpha_{12}\left(\phi\right)-\phi\right) \tag{6.70}$$

where I_{G1} is the moment of inertia of each column about its own centroid, while the other geometric properties are defined in Fig. 6.22. As in the case of the two block mechanism, the inward shift of each of the hinges depends on both the magnitude of the reaction force F_x at the interface, as well as the rotation ϕ_x of the blocks relative to each other (Table 6.2) - which as Fig. 6.22 illustrates in the case of the symmetric rocking frame is simply ϕ everywhere.

Furthermore, as in the case of the single and two block mechanisms, the influence of the terms $\frac{\partial R_x}{\partial \phi}$ and $\frac{\partial \alpha_x}{\partial \phi}$ is once again neglected, as they were found to be negligible for $\phi \geq 0.05\alpha_0$, where α_0 is the slenderness of the columns.

6.3.3.2 Semi-flexible model

Using the same methodology as employed for the single and two block mechanisms, the semi-flexible hinge locations a_{SFx} for the symmetric rocking frame are determined by setting a_{SFx} = $a_{fx}(\phi_x$ = $\phi_{cx})$, where x represents the hinge number. Similarly, the kinetic energy of the system $T_{SF}(\phi,\dot{\phi})$ is now determined relative to the inwardly-shifted rotation points, and can be computed using Equation 6.71 below:

$$T_{SF}\left(\phi,\dot{\phi}\right)=\dot{\phi}^2\left[I_{G1}+\frac{W_1}{g}{R_{1P}}^2+\frac{W_2}{2g}{R_{12P}}^2\right] \tag{6.71}$$

where I_{G1} is the moment of inertia of each column about its own centroid, while R_{1P} and R_{12P} are defined in Fig. 6.22d. Furthermore, as the symmetric rocking frame exhibits direct dynamic equivalence with the single rocking block (DeJong and Dimitrakopoulos, 2014; Makris and Vassiliou, 2013), an analytical coefficient of restitution can also be derived for this mechanism (assuming conservation of angular momentum once again), as given by Equation 6.72:

$$\eta_{SF} = \frac{I_{G1} + m_1 R_{1P}^2 \left(1 - 2\sin^2 \alpha_{1P}\right) + \frac{m_2 R_{12P}^2}{2} \left(1 - 2\sin^2 \alpha_{12P}\right)}{I_{G1} + m_1 R_{1P}^2 + \frac{m_2 R_{12P}^2}{2}} \tag{6.72}$$

where m_1 is the mass of each column and m_2 the mass of the beam, while α_{1P} and α_{12P} are defined in Fig. 6.22d. A comparison of the semi-flexible coefficient of restitution η_{SF} with the rigid formulation η_R as found in the literature (Fig. 6.23) (DeJong and Dimitrakopoulos, 2014; Makris and Vassiliou, 2013) demonstrated that, as in the case of the single and two block mechanisms, η_{SF} is generally more conservative than η_R - with the difference between the two tending to increase with in increase in mass ratio γ (which compares the mass of the beam to the combined mass of the columns) and decrease with an increase in compressive strength f_m.

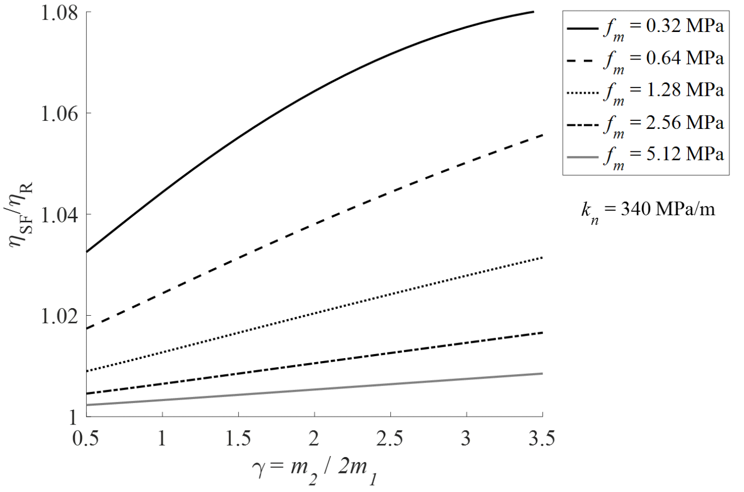

Fig. 6.23 Comparison of the semi-flexible η_{SF} and rigid η_R coefficients of restitution for varying mass ratios $\gamma = m_2/2m_1$ and varying values of the compressive strength f_m

6.3.4 Multiple block mechanism 2: Asymmetric rocking frame

6.3.4.1 Fully-flexible model

The equation of motion for the multiple block mechanism can be further generalized for the case of the asymmetric rocking frame. In this case, the two columns are no longer identical in size, and consequently exhibit different rotations, as a result of which the beam atop them undergoes both rotation and translation as demonstrated by Fig. 6.24b. Unlike the mechanisms considered thus far, different mechanisms exist for positive and negative rotations of this structure, and thus the sign of the rotation needs to be taken into account when deriving the kinetic and potential energies of the system, as well as the generalized inertial force, as indicated in Equations 6.73-6.78:

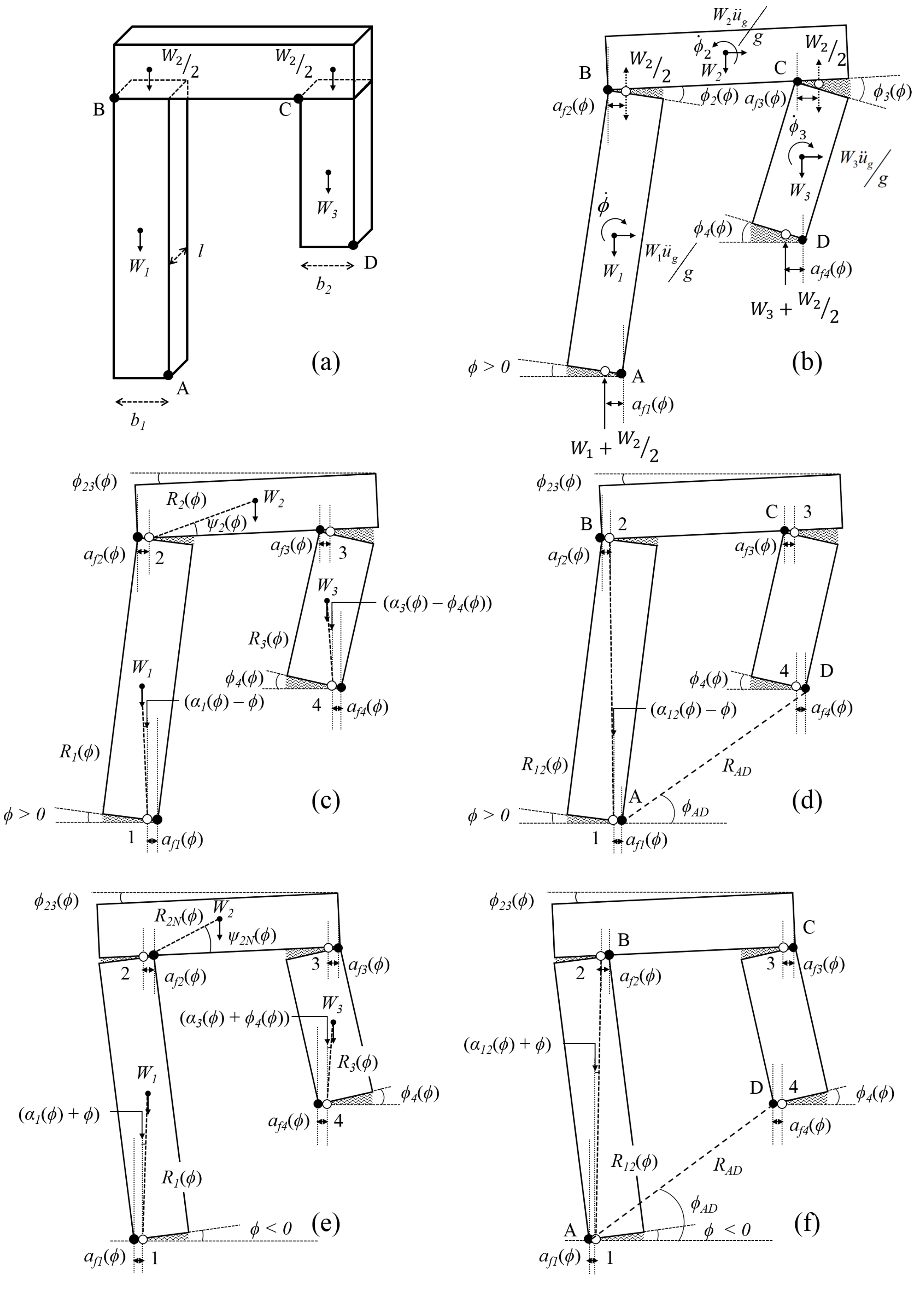

Fig. 6.24 Asymmetric rocking frame: (a) un-deformed configuration, (b) forces acting on each of the blocks, (c-d) geometric properties used in the equation of motion for positive rotations ($\phi > 0$) and (e-f) geometric properties used in the equation of motion for negative rotations ($\phi < 0$)

$$T\left(\phi,\dot{\phi}\right)=\frac{\dot{\phi}^{2}}{2}\left[\begin{array}{l} I_{G1}+\frac{W_1}{g}R_1(\phi)^2+I_{G2}\left(\frac{\partial\phi_{23}(\phi)}{\partial\phi}\right)^2+I_{G3}\left(\frac{\partial\phi_4(\phi)}{\partial\phi}\right)^2+\frac{W_3}{g}R_3(\phi)^2\left(\frac{\partial\phi_4(\phi)}{\partial\phi}\right)^2 \\ +\frac{W_2}{g}\left(\begin{array}{l} R_{12}(\phi)^2+R_2(\phi)^2\left(\frac{\partial\phi_{23}(\phi)}{\partial\phi}\right)^2 \\ -2R_{12}\left(\phi\right)R_2\left(\phi\right)\sin\left(\phi-\alpha_{12}\left(\phi\right)\operatorname{sgn}\left(\phi\right)+\phi_{23}\left(\phi\right)+\psi_2\left(\phi\right)\right)\frac{\partial\phi_{23}(\phi)}{\partial\phi} \end{array}\right) \end{array}\right] \tag{6.73}$$

$$V\left(\phi\right)=\left[\begin{array}{l} W_1R_1\left(\phi\right)\cos\left(\alpha_1\left(\phi\right)\operatorname{sgn}\left(\phi\right)-\phi\right) \\ +W_2\left(R_{12}\left(\phi\right)\cos\left(\alpha_{12}\left(\phi\right)\operatorname{sgn}\left(\phi\right)-\phi\right)+R_2\left(\phi\right)\sin\left(\phi_{23}\left(\phi\right)+\psi_2\left(\phi\right)\right)\right) \\ +W_3\left(\begin{array}{l} R_3\left(\phi\right)\cos\left(\alpha_3\left(\phi\right)\operatorname{sgn}\left(\phi\right)-\phi_4\left(\phi\right)\right)+R_{AD}\sin\phi_{AD} \\ +a_{f4}\left(\phi\right)\sin\phi_4\left(\phi\right)-a_{f1}\left(\phi\right)\sin\phi \end{array}\right) \end{array}\right] \tag{6.74}$$

$$B\left(\phi\right)=\frac{1}{g}\left[\begin{array}{l} W_1R_1\left(\phi\right)\cos\left(\alpha_1\left(\phi\right)\operatorname{sgn}\left(\phi\right)-\phi\right) \\ +W_2\left(R_{12}\left(\phi\right)\cos\left(\alpha_{12}\left(\phi\right)\operatorname{sgn}\left(\phi\right)-\phi\right)-R_2\left(\phi\right)\sin\left(\phi_{23}\left(\phi\right)+\psi_2\left(\phi\right)\right)\frac{\partial\phi_{23}(\phi)}{\partial\phi}\right) \\ +W_3R_3\left(\phi\right)\cos\left(\alpha_3\left(\phi\right)\operatorname{sgn}\left(\phi\right)-\phi_4\left(\phi\right)\right)\frac{\partial\phi_4(\phi)}{\partial\phi} \end{array}\right] \tag{6.75}$$

where I_{G1}, I_{G2} and I_{G3} represent the moments of inertia of the first column (AB), the beam (BC) and the second column (CD) about their own centroids, while the other geometric properties are derived relative to the shifting hinges (1, 2, 3 and 4) as defined in Fig. 6.24. The inward shift of each of these hinges depends on both the magnitude of the reaction force F_x at the interface, as well as the rotation ϕ_x of the blocks making up that interface, relative to each other, as illustrated by Fig. 6.24b and defined in Table 6.3. Note that at the different interfaces, the rotations ϕ_x of the blocks relative to each other are combinations of the rotation ϕ of the first column, as well as the rotation of the beam $\phi_{23}(\phi)$ and second column $\phi_4(\phi)$, which are defined as follows:

$$\phi_{23}\left(\phi\right)=\arctan\left[\frac{-R_{A2}\cos\left(\alpha_{A2}\operatorname{sgn}\left(\phi\right)-\phi\right)+R_{AD}\sin\phi_{AD}+R_{3D}\cos\left(\alpha_{3D}\operatorname{sgn}\left(\phi\right)-\phi_4\left(\phi\right)\right)}{R_{A2}\sin\left(\alpha_{A2}\operatorname{sgn}\left(\phi\right)-\phi\right)+R_{AD}\cos\phi_{AD}-R_{3D}\sin\left(\alpha_{3D}\operatorname{sgn}\left(\phi\right)-\phi_4\left(\phi\right)\right)}\right] \tag{6.76}$$

$$\phi_4\left(\phi\right)=\alpha_{3D}\operatorname{sgn}\left(\phi\right)-\arctan\left[\frac{R_{A2}\sin\left(\alpha_{A2}\operatorname{sgn}\left(\phi\right)-\phi\right)+R_{AD}\cos\phi_{AD}}{R_{A2}\cos\left(\alpha_{A2}\operatorname{sgn}\left(\phi\right)-\phi\right)-R_{AD}\sin\phi_{AD}}\right]+\arccos\left[\frac{R_{2D}(\phi)^2+R_{3D}^2-R_{23}^2}{2\cdot R_{3D}\cdot R_{2D}\left(\phi\right)}\right] \tag{6.77}$$

where:

$$R_{2D}\left(\phi\right)=\sqrt{R_{A2}^2+R_{AD}^2-\left(2\times R_{A2}\times R_{AD}\times\cos\left(\alpha_{A2}\operatorname{sgn}\left(\phi\right)+\frac{\pi}{2}-\phi-\phi_{AD}\right)\right)} \tag{6.78}$$

while the geometric parameters R_{A2}, α_{A2}, R_{AD}, ϕ_{AD}, R_{3D} and α_{3D} are defined in Fig. 6.25. Note that unlike the formulation presented in DeJong and Dimitrakopoulos (2014), where all the hinges in the kinematic chain are located at the outer edge of the blocks, in order to determine the relationship

Table 6.3 Asymmetric rocking frame: Reaction forces and rotations for each of the hinges

x	F_x	ϕ_x
1	W_1+W_2/2	ϕ
2	W_2/2	ϕ+ϕ_{23}
3	W_2/2	ϕ_{23}+ϕ_4
4	W_1+W_2/2	ϕ_4

between the rotations of the different blocks in this case, the hinges between the columns and the beam (B, C) are shifted inwards and fixed at their semi-flexible locations (2, 3) as illustrated by Fig. 6.25. However, these parameters are identical for both positive and negative rotations.

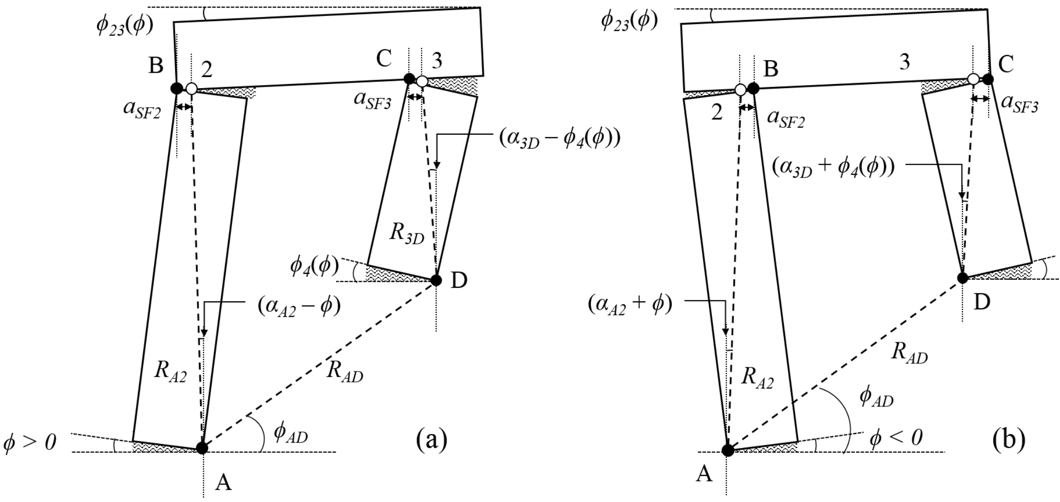

Fig. 6.25 Geometric parameters used to determine the relationship between the rotations of the different blocks for (a) positive rotations (ϕ > 0) and (b) negative rotations (ϕ < 0)

Furthermore, as in the case of all the previously considered mechanisms, the influence of the terms $\frac{\partial R_x}{\partial \phi}$ and $\frac{\partial \alpha_x}{\partial \phi}$ (where x refers to the hinge number) is once again neglected as they were only found to be significant for the different blocks for $\phi/\alpha_{01} \leq 0.05$ (Fig. 6.26), where α_{01} corresponds to the slenderness of the first column (AB).

6.3.4.2 Semi-flexible model

Adopting the same methodology as was used for the previous mechanisms, the semi-flexible hinge locations a_{SFx} (where x refers to the hinge number) for the asymmetric rocking frame were determined by setting $a_{SFx} = a_{fx}(\phi_x = \phi_{cx})$, where ϕ_{cx} is the rotation at which the interface stress distribution switches from purely elastic to elasto-plastic. Using these new hinge locations, the kinetic energy of the system $T_{SF}(\phi, \dot{\phi})$ was then calculated using Equation 6.79:

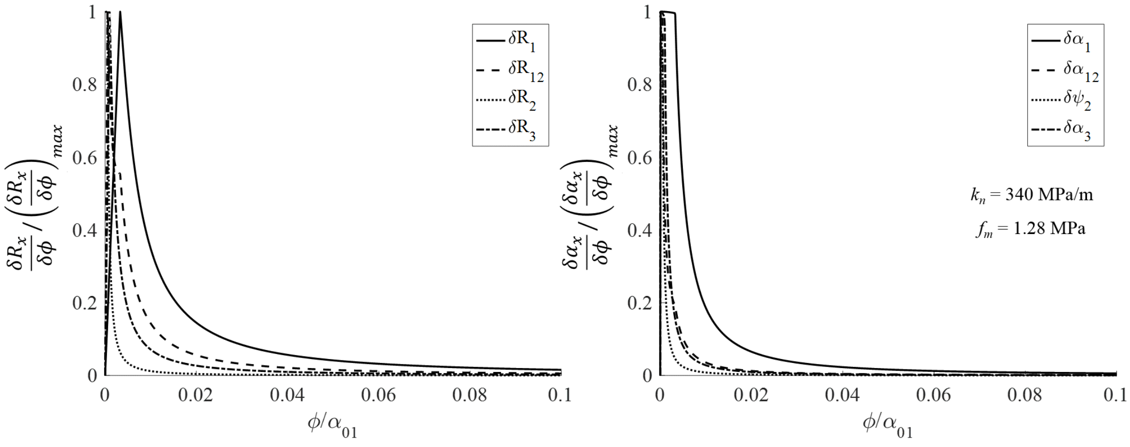

Fig. 6.26 Variation of $\frac{\partial R_x}{\partial \phi}$ (left) and $\frac{\partial \alpha_x}{\partial \phi}$ (right) (normalized by their maximum values) for the asymmetric rocking frame for each of the different blocks

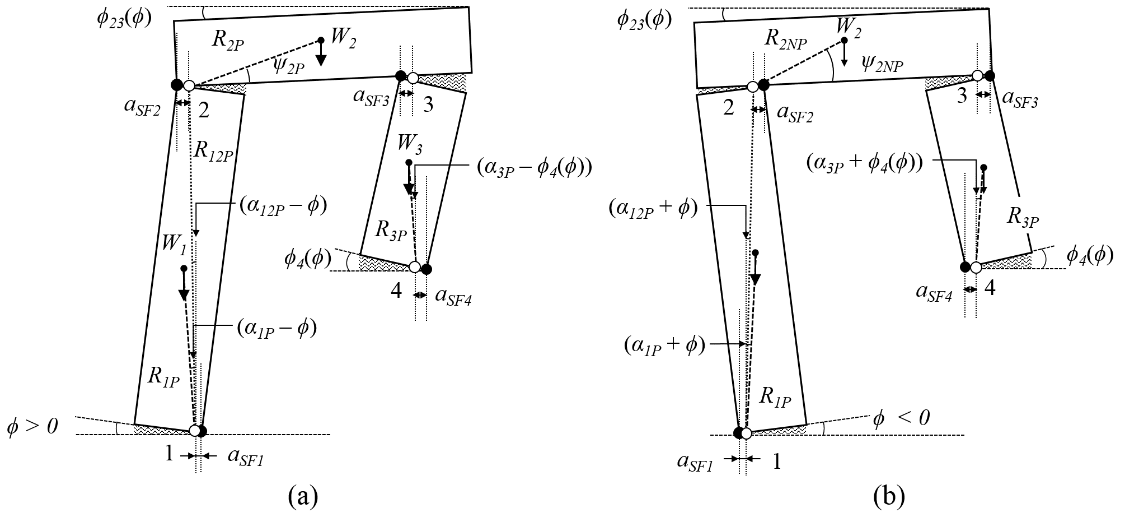

Fig. 6.27 Asymmetric rocking frame - semi-flexible interface model for (a) positive rotations ($\phi > 0$) and (b) negative rotations ($\phi < 0$)

$$T_{SF}\left(\phi,\dot{\phi}\right)=\frac{\dot{\phi}^2}{2}\left[\begin{array}{l} I_{G1}+\frac{W_1}{g}{R_{1P}}^2+I_{G2}\left(\frac{\partial\phi_{23}(\phi)}{\partial\phi}\right)^2+I_{G3}\left(\frac{\partial\phi_4(\phi)}{\partial\phi}\right)^2+\frac{W_3}{g}{R_{3P}}^2\left(\frac{\partial\phi_4(\phi)}{\partial\phi}\right)^2 \\ +\frac{W_2}{g}\left(\begin{array}{l} {R_{12P}}^2+{R_{2P}}^2\left(\frac{\partial\phi_{23}(\phi)}{\partial\phi}\right)^2 \\ -2R_{12P}R_{2P}\sin\left(\phi-\alpha_{12P}\operatorname{sgn}(\phi)+\phi_{23}(\phi)+\psi_{2P}\right)\frac{\partial\phi_{23}(\phi)}{\partial\phi}\end{array}\right)\end{array}\right] \tag{6.79}$$

where I_{G1}, I_{G2}, I_{G3}, $\phi_{23}(\phi)$, $\frac{\partial\phi_{23}}{\partial\phi}$ and $\frac{\partial\phi_4}{\partial\phi}$ are the same as for the fully-flexible interface model, while the other geometric parameters are defined in Fig. 6.27 for both positive ($\phi > 0$) and negative ($\phi < 0$) rotations. Note that in the case of the columns, the geometric properties are identical for both sets of rotations, while in the case of the beam, R_{2P} and ψ_{2P} change magnitude based on the sign of rotation and thus need to be substituted into Equation 6.79 accordingly.

6.3.5 Multiple block mechanism 3: Side-aisle vault collapse

6.3.5.1 Fully-flexible model

The multiple block mechanism can also be used to model the collapse of side aisle vaults, as are commonly found in churches. A simplification of this collapse mechanism involves the vault cracking and consequently developing a hinge (B) at the apex, as well as hinges at both the base of the vault (A, C) as well as the base of the wall supporting it (D, Fig. 6.28a). In the case of this mechanism, only one-sided rocking ($\phi > 0$) is considered, as it is assumed that the rest of the church restrains movement of the vault in the opposite direction. The kinetic and potential energies of this system, as well as the generalized inertial force, are derived relative to the shifting rotation points 1, 2, 3 and 4 as indicated in Fig. 6.28c, and can be computed using Equations 6.80-6.82:

$$T\left(\phi,\dot{\phi}\right)=\frac{\dot{\phi}^2}{2}\left[\begin{array}{l} I_{G1}+\frac{W_1}{g}R_1(\phi)^2+I_{G2}\left(\frac{\partial\phi_{23}(\phi)}{\partial\phi}\right)^2+I_{G3}\left(\frac{\partial\phi_4(\phi)}{\partial\phi}\right)^2+\frac{W_3}{g}R_3(\phi)^2\left(\frac{\partial\phi_4(\phi)}{\partial\phi}\right)^2 \\ +\frac{W_2}{g}\left(\begin{array}{l} R_{12}(\phi)^2+R_2(\phi)^2\left(\frac{\partial\phi_{23}(\phi)}{\partial\phi}\right)^2 \\ +2R_{12}(\phi)R_2(\phi)\cos\left(\phi+\alpha_{12}(\phi)+\phi_{23}(\phi)+\alpha_2(\phi)\right)\frac{\partial\phi_{23}(\phi)}{\partial\phi}\end{array}\right)\end{array}\right] \tag{6.80}$$

$$V(\phi)=\left[\begin{array}{l} W_1R_1(\phi)\cos\left(\alpha_1(\phi)+\phi\right) \\ +W_2\left(R_{12}(\phi)\cos\left(\alpha_{12}(\phi)+\phi\right)-R_2(\phi)\cos\left(\alpha_2(\phi)+\phi_{23}(\phi)\right)\right) \\ +W_3\left(R_3(\phi)\cos\left(\alpha_3(\phi)-\phi_4(\phi)\right)+R_{AD}\sin\phi_{AD}+a_{f4}(\phi)\sin\phi_4(\phi)-a_{f1}(\phi)\sin\phi\right)\end{array}\right] \tag{6.81}$$

$$B(\phi)=\frac{1}{g}\left[\begin{array}{l} W_1R_1(\phi)\cos\left(\alpha_1(\phi)+\phi\right) \\ +W_2\left(R_{12}(\phi)\cos\left(\alpha_{12}(\phi)+\phi\right)+R_2(\phi)\cos\left(\alpha_2(\phi)+\phi_{23}(\phi)\right)\dfrac{\partial\phi_{23}(\phi)}{\partial\phi}\right) \\ +W_3R_3(\phi)\cos\left(\alpha_3(\phi)-\phi_4(\phi)\right)\dfrac{\partial\phi_4(\phi)}{\partial\phi}\end{array}\right] \tag{6.82}$$

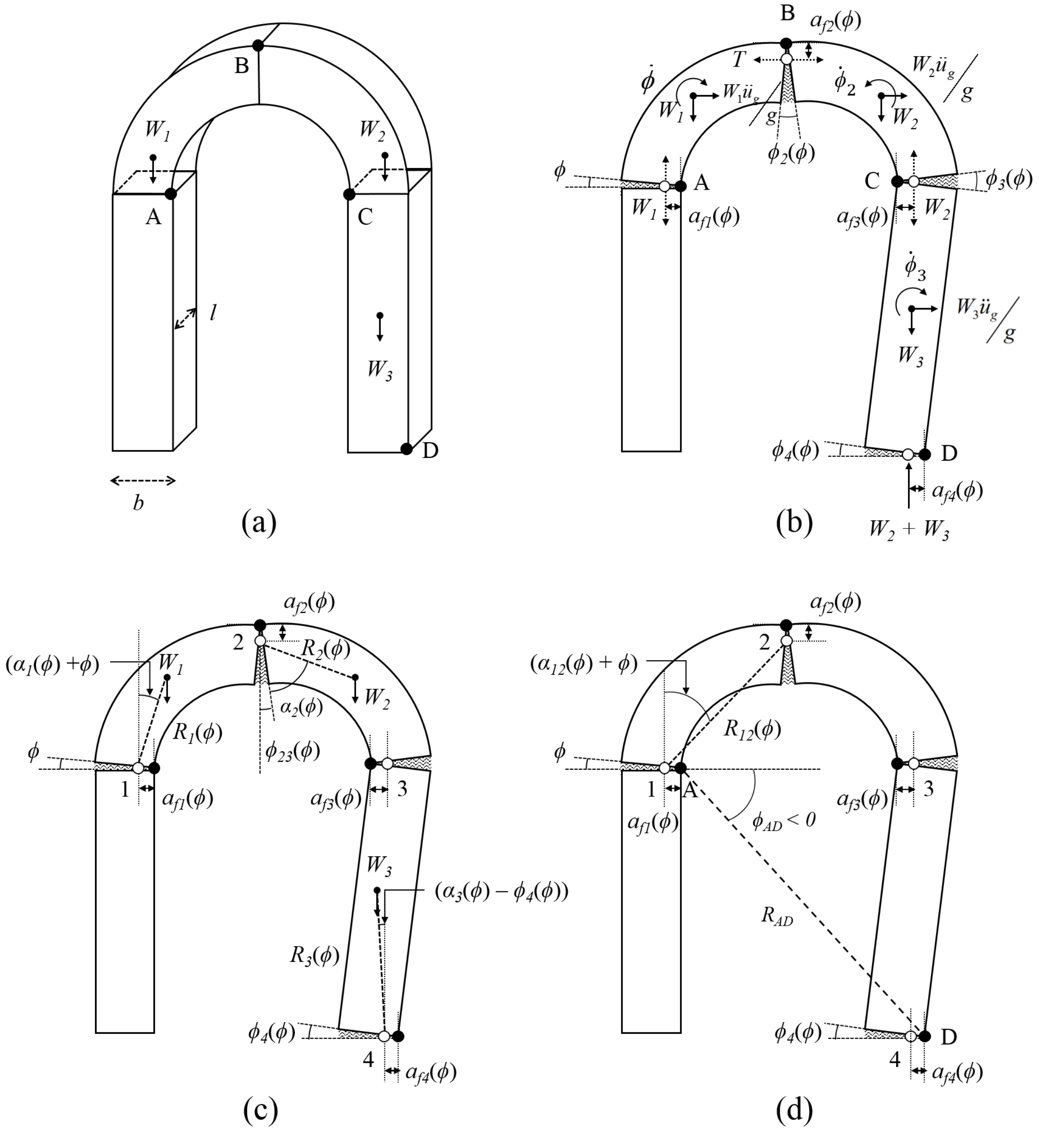

Fig. 6.28 Vault supported on a side wall: (a) un-deformed configuration, (b) forces acting on each of the segments and (c-d) geometric properties used in the equation of motion

Table 6.4 Side-aisle vault collapse: Reaction forces and rotations for each of the hinges

x	F_x	ϕ_x
1	W_1	ϕ
2	T	ϕ+ϕ_{23}
3	W_2	ϕ_{23}+ϕ_4
4	W_2+W_3	ϕ_4

where I_{G1}, I_{G2} and I_{G3} represent the moments of inertia of the two halves of the vault and the wall respectively, about their centroids, while the other geometric properties, computed relative to the shifting rotation points, are defined in Fig. 6.28. As in the case of all the mechanisms considered thus far, the inward shift of each of these rotation points depends on both the magnitude of the reaction force at the interface F_x, as well as the relative rotation ϕ_x of the segments making up the interface as illustrated by Fig. 6.28b, with the specific values for F_x and ϕ_x for each of the hinges being listed in Table 6.4. Note that for hinge 2, the force F_2 at the interface is equal to the thrust of the vault T.

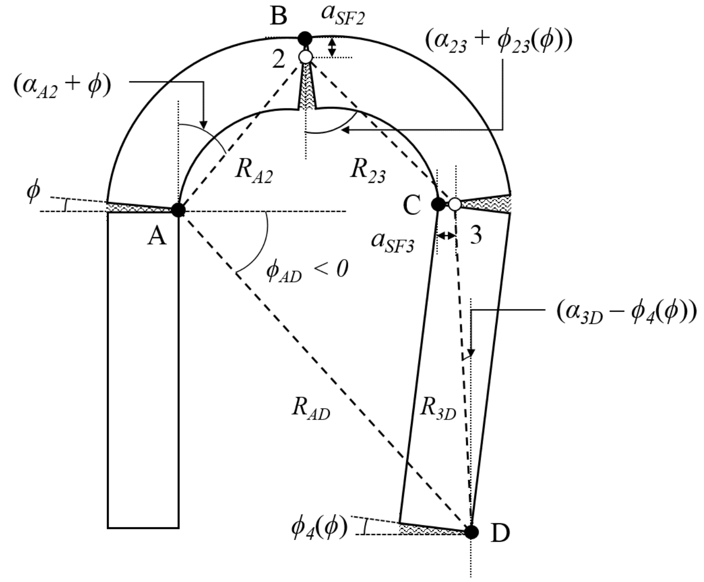

Fig. 6.29 Geometric parameters used to determine the relationship between the rotations of the different segments for the side-aisle vault collapse mechanism

Furthermore, as indicated in Table 6.4, the relative rotations ϕ_x of the blocks at the different interfaces are combinations of the rotation of the first half of the vault ϕ, the rotation of the second half of the vault $\phi_{23}(\phi)$ (determined relative to the vertical, Fig. 6.28c), as well as the rotation of the wall $\phi_4(\phi)$, with the latter two rotations being defined as follows:

$$\phi_{23}(\phi) = -\alpha_{23} + \arctan\left[\frac{-R_{A2}\sin(\alpha_{A2}+\phi) + R_{AD}\cos\phi_{AD} - R_{3D}\sin(\alpha_{3D}-\phi_4(\phi))}{R_{A2}\cos(\alpha_{A2}+\phi) - R_{AD}\sin\phi_{AD} - R_{3D}\cos(\alpha_{3D}-\phi_4(\phi))}\right] \tag{6.83}$$

$$\phi_4(\phi) = \alpha_{3D} - \arctan\left[\frac{-R_{A2}\sin(\alpha_{A2}+\phi) + R_{AD}\cos\phi_{AD}}{R_{A2}\cos(\alpha_{A2}+\phi) - R_{AD}\sin\phi_{AD}}\right] + \arccos\left[\frac{R_{2D}(\phi)^2 + R_{3D}^2 - R_{23}^2}{2\cdot R_{3D}\cdot R_{2D}(\phi)}\right] \tag{6.84}$$

where:

$$R_{2D}(\phi) = \sqrt{R_{A2}^2 + R_{AD}^2 - \left(2\times R_{A2}\times R_{AD}\times\cos\left(\frac{\pi}{2} - \alpha_{A2} - \phi - \phi_{AD}\right)\right)} \tag{6.85}$$

while the geometric parameters R_{A2}, α_{A2}, α_{23}, R_{AD}, ϕ_{AD}, R_{3D} and α_{3D} are defined in Fig. 6.29. Note that in order to determine the relationship between the rotations of the different segments, the intermediate hinges of the kinematic chain (i.e. hinges 2 and 3) are shifted inwards and fixed at their semi-flexible locations. Furthermore, as in the case of the asymmetric rocking frame, the influence of the terms $\frac{\partial R_x}{\partial \phi}$ and $\frac{\partial \alpha_x}{\partial \phi}$ (where x refers to the hinge number) is neglected here as well, as they were only found to be significant for extremely small rotations of the structure.

6.3.5.2 Semi-flexible model

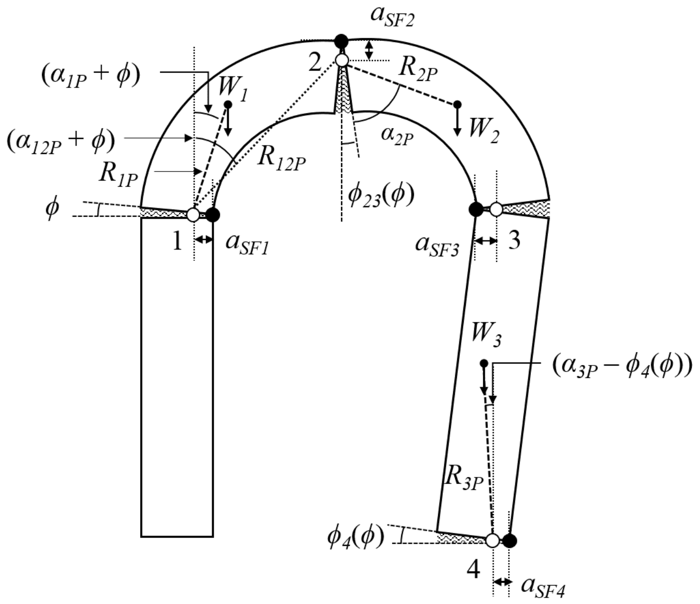

Fig. 6.30 Side-aisle vault collapse - semi-flexible interface model

The semi-flexible hinge locations a_{SFx} for the vault collapse mechanism were determined in a manner similar to that used for the other mechanisms considered thus far - that is, by setting a_{SFx}

$= a_{fx}(\phi_x = \phi_{cx})$. The kinetic energy of the system $T_{SF}(\phi,\dot{\phi})$, is then calculated relative to these new (fixed) rotation points, as given by Equation 6.86:

$$T\left(\phi,\dot{\phi}\right) = \frac{\dot{\phi}^2}{2}\left[\begin{array}{l} I_{G1} + \frac{W_1}{g}{R_{1P}}^2 + I_{G2}\left(\frac{\partial\phi_{23}(\phi)}{\partial\phi}\right)^2 + I_{G3}\left(\frac{\partial\phi_4(\phi)}{\partial\phi}\right)^2 + \frac{W_3}{g}{R_{3P}}^2\left(\frac{\partial\phi_4(\phi)}{\partial\phi}\right)^2 \\ +\frac{W_2}{g}\left(\begin{array}{l} {R_{12P}}^2 + {R_{2P}}^2\left(\frac{\partial\phi_{23}(\phi)}{\partial\phi}\right)^2 \\ +2R_{12P}R_{2P}\cos\left(\phi + \alpha_{12P} + \phi_{23}\left(\phi\right) + \alpha_{2P}\right)\frac{\partial\phi_{23}(\phi)}{\partial\phi} \end{array}\right) \end{array}\right] \tag{6.86}$$

where I_{G1}, I_{G2}, I_{G3}, $\phi_{23}(\phi)$, $\frac{\partial\phi_{23}}{\partial\phi}$ and $\frac{\partial\phi_4}{\partial\phi}$ are the same as for the fully-flexible interface model, while definitions for the other geometric properties can be found in Fig. 6.30.

6.4 Summary

In this chapter, the equations of motion presented in Chapter 3 for different masonry collapse mechanisms were re-derived in order to account for the presence of flexible interfaces and crushing effects. These modified equations of motion now account for the inward shift of the rocking rotation points due to the presence of flexible interfaces with finite compressive strengths, and fit within the broader framework of the CAD-interfaced computational tool described in this thesis for the seismic collapse assessment of masonry structures. Specifically, the new contributions of this work include:

- Derivation of expressions for the inward shift of the rocking rotation points for different interface geometries as are commonly found in real-world structures - including solid rectangular, hollow rectangular, solid circular and hollow circular interfaces.
- Re-derivation of the equations of motion for the single and two block mechanisms, as well as multiple block mechanisms such as the symmetric rocking frame, the asymmetric rocking frame, and collapse of a side-aisle vault that is supported on a wall.
- Development of a semi-flexible interface model which accounts for the inward shift of the rocking rotation points in a more simplified manner than the fully-flexible formulation, which in turn is used to re-derive the coefficient of restitution for the single, two and simplified multiple block mechanisms.

In Chapter 7, the modified equations of motion derived in this chapter will be used to investigate the influence of interface geometry, flexibility and crushing on the seismic resilience of a few simple masonry structures, while a potential application of this new methodology to real-world structures will be presented in Chapter 8.

Chapter 7

Evaluation of the new analytical models

7.1 Introduction

In this chapter, a series of analyses are conducted in order to evaluate the ability of the expressions and equations derived in Chapter 6 to model the dynamic response of masonry structures with non-rigid interfaces. The effect of interface geometry, stiffness and crushing on the dynamic response of different collapse mechanisms will be evaluated, while the ability of the relatively simple semi-flexible interface model to approximate its fully-flexible counterpart will also be assessed. Furthermore, the equations of motion derived for the complicated multi-block mechanisms will be validated through comparison of the analytical results to those obtained using numerical modelling in 3DEC.

7.2 Single block mechanism

In this section, the equation of motion derived for the single block mechanism (Equation 6.54) will be used to generate moment-rotation curves in order to investigate the influence of geometry, interface stiffness and compressive strength on the rocking response of a few simple structures. Free-rocking response analyses will also be conducted in order to compare the fully-flexible, semi-flexible and rigid interface models for interfaces of varying stiffness, as well as blocks with varying slenderness. Finally, a real-world application of the equations will be demonstrated by conducting a full time-history analysis of a monumental masonry tower which was completely destroyed during the 2015 Gorkha earthquake.

7.2.1 Moment-rotation curves

In the first set of analyses, the expressions derived for the shifting hinge location $a_f(\phi)$ for the different base geometries were used to generate moment-rotation curves, making use of the following

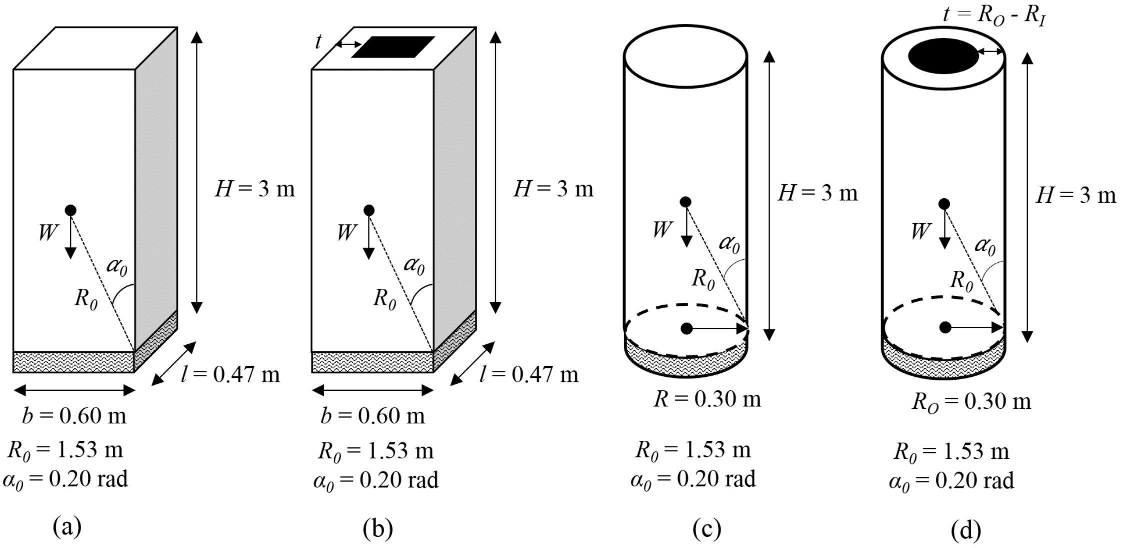

Fig. 7.1 Structural geometries used for the parametric study

generalized formula for the restoring moment $M_R(\phi)$:

$$M_R(\phi) = \frac{\partial V(\phi)}{\partial \phi} - M(\phi) \tag{7.1}$$

where $V(\phi)$ is the potential energy of the system, while $M(\phi)$ is the generalized force due to external static forces (where relevant).

These curves were used to evaluate the influence of cross-sectional geometry, as well as material properties (i.e. compressive strength and interface stiffness) on the dynamic response of the four structural geometries depicted in Fig. 7.1 (all with a density ρ of 1800 $\mathrm{kg\,m^{-3}}$).

In order to gauge the effect of interface geometry on the seismic resistance of the structures, moment-rotation curves (Fig. 7.2a) were first generated for the four structures depicted in Fig. 7.1. Note that all four structures have the same size (R_0) and slenderness (α_0). From Fig. 7.2a it can be observed that for structures of comparable scale and slenderness, the introduction of a flexible interface with a finite compressive strength leads to a greater reduction in the dynamic capacity of structures with circular bases than those with rectangular ones, with the former generally overturning for lower rotations (with the overturning rotation being defined as the rotation at which the restoring moment $M_R(\phi) = 0$). Moreover, structures with hollow bases appear to have a higher seismic resistance than their solid counterparts.

Examining more closely the behaviour of structures with hollow bases, moment-rotation curves were also generated for the hollow rectangular base (Fig. 7.1b) for varying base thicknesses (t) as illustrated by Fig. 7.2b. From this plot it was found that the inclusion of an elasto-plastic interface caused less of a reduction in the dynamic capacity of thinner–walled structures.

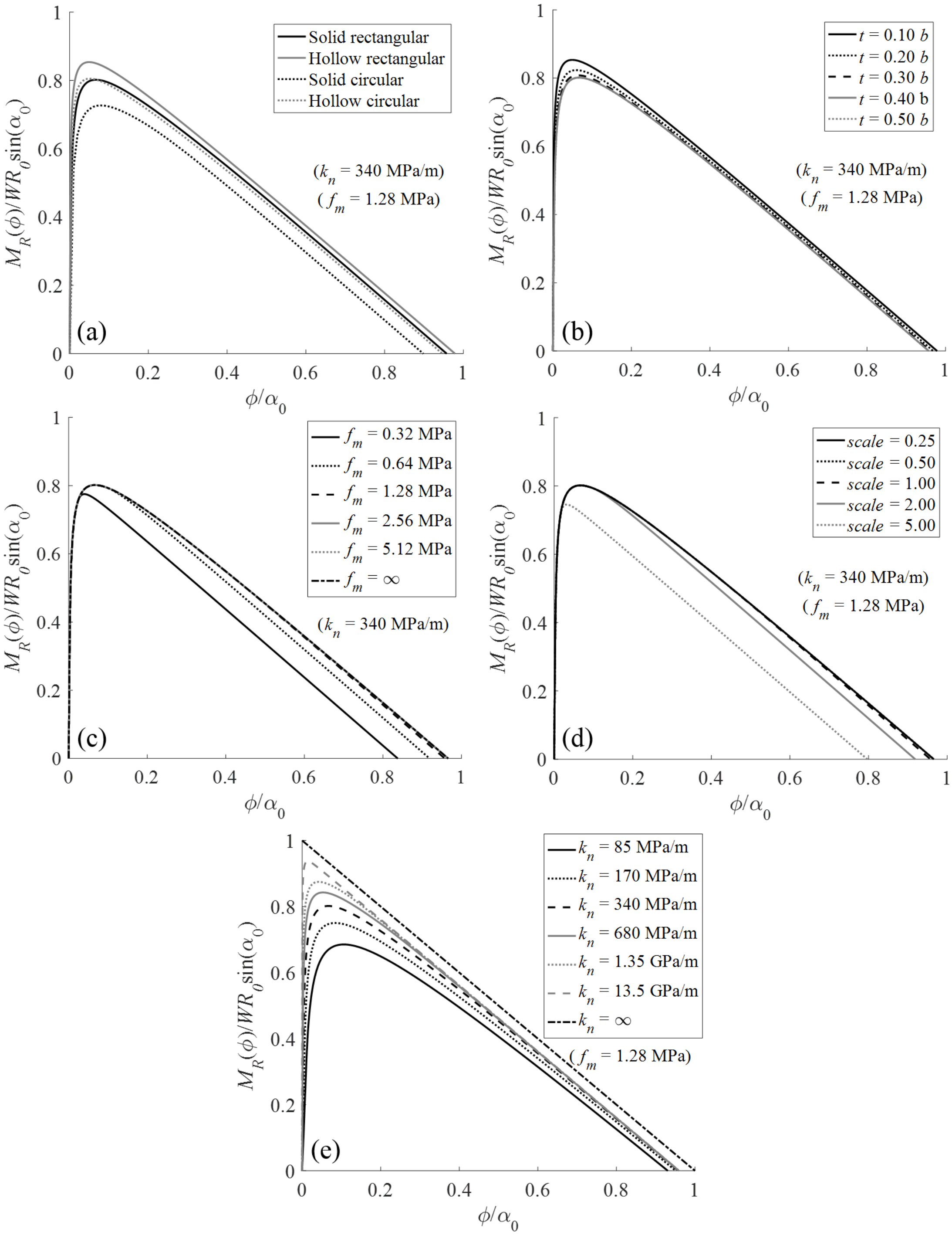

Fig. 7.2 Moment-rotation curves generated for: (a) varying base geometry; (b) varying thickness t (for hollow bases); (c) varying compressive strength f_m; (d) varying scale and (e) varying joint stiffness k_n

The effect of varying the compressive strength f_m of the interface was also investigated, using as a reference case the structure with a solid rectangular base (Fig. 7.1a). Assuming a constant normal stiffness k_n of 340 MPa/m, moment-rotation curves were generated for different compressive strengths as illustrated by Fig. 7.2c. As expected, decreasing the compressive strength was observed to decrease the dynamic resistance of the structure, with the block experiencing crushing (and ultimately overturning) for lower rotations when the compressive strength is reduced. Moreover, for compressive strengths higher than 1.28 MPa, the behaviour of the interface remained entirely elastic, and no crushing was observed to occur – with the curves for f_m = 2.56 and 5.12 MPa almost exactly matching the curve generated assuming an infinite compressive strength ($f_m = \infty$). Keeping the compressive strength and normal stiffness constant while varying the scale of the structure (Fig. 7.2d) yielded similar results - larger scale structures (scale = 2 and 5) experience crushing more rapidly (and consequently overturning more quickly) than their smaller counterparts (scale = 0.25, 0.50 and 1) - with the latter actually having near-identical moment-rotation curves.

Finally, keeping the compressive strength constant and increasing the normal stiffness k_n (Fig. 7.2e) was also found to increase the block's dynamic capacity. However, in this case, an increase in normal stiffness resulted in crushing occurring for smaller rotations, whereas purely elastic ("smooth") behaviour was observed for the lowest stiffness considered (85 MPa/m). Furthermore, to facilitate comparison with Housner's original assumption of an entirely rigid interface, the moment-rotation curve for the infinitely stiff case ($k_n = \infty$) is also shown, which predictably has a much higher capacity than the curves generated for the flexible interfaces – thus highlighting just how un-conservative this assumption can be.

7.2.2 Free-rocking response

In order to compare the performance of the fully-flexible, semi-flexible, and rigid interface models, a free-rocking response analysis was also conducted for varying values of the interface stiffness k_n (Fig. 7.3) and block slenderness α_0 (Fig. 7.4). From Fig. 7.3 it can be seen that for all considered values of interface stiffness, the fully-flexible and semi-flexible models appear to be in generally good agreement, and consistently yield more conservative predictions than the rigid model. However, the difference between the predictions of the fully-flexible/semi-flexible and rigid models tends to decrease with an increase in interface stiffness (that is, as the joint becomes more rigid).

Similarly, in the case of varying block slendernesses, the fully-flexible and semi-flexible models once again compare fairly well for all considered values of α_0 (Fig. 7.4), while the rigid model displays less conservative behaviour - going out of phase with the flexible solutions in relatively few cycles of rocking motion, as well as damping out earlier - particularly in the case of stockier blocks ($\alpha_0 \geq 0.24$ rad).

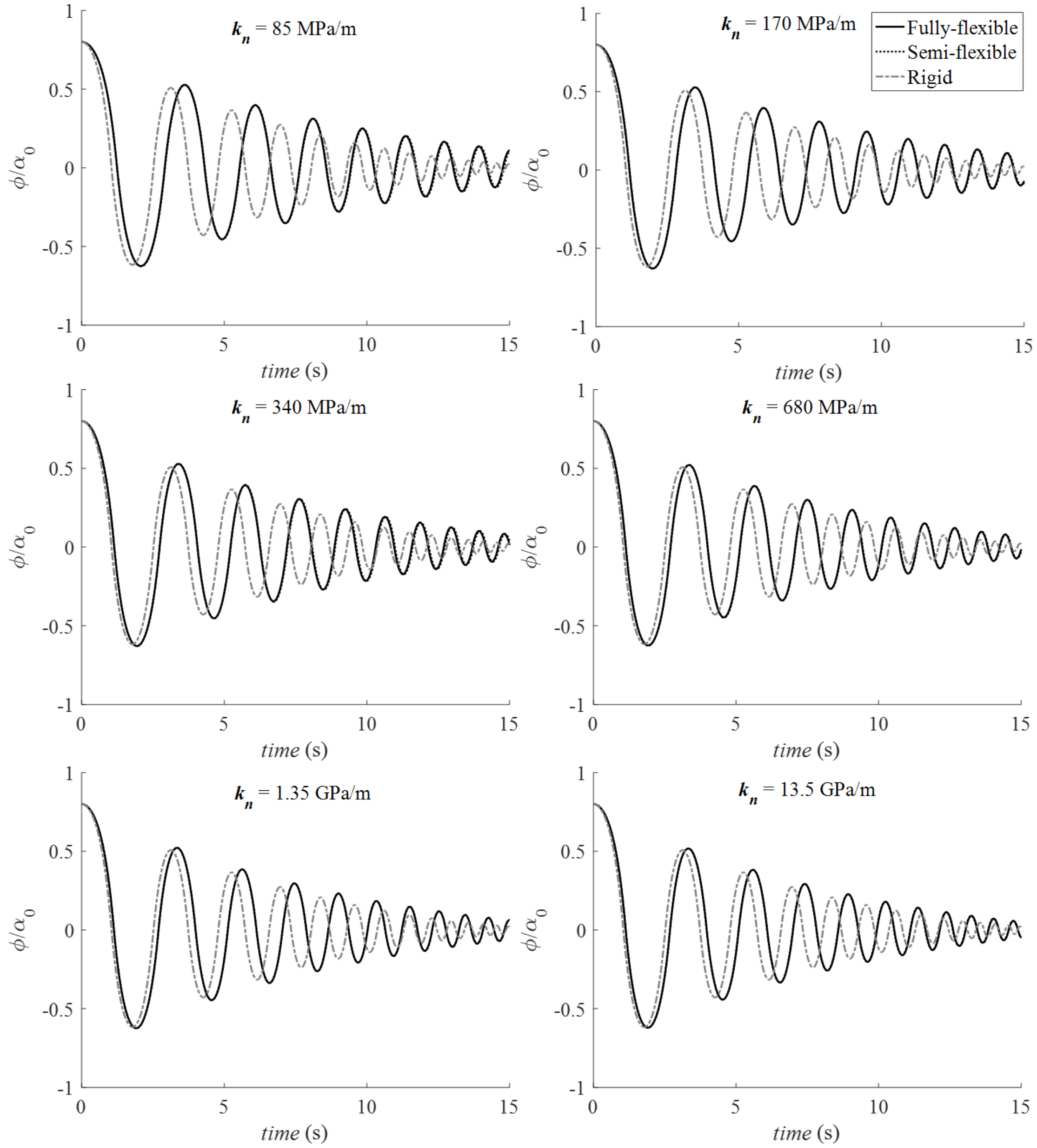

Fig. 7.3 Comparison of the fully-flexible, semi-flexible and rigid free-rocking response (ϕ_0/α_0 = 0.8) of interfaces of varying stiffness k_n (f_m = 1.28 MPa)

7.2.3 Case Study: Dharahara Tower

To evaluate the ability of the expressions and equations derived in Chapter 6 to realistically capture the dynamic behaviour of real-world structures, the Dharahara Tower in Kathmandu, Nepal (Fig. 7.5), which was almost completely destroyed during the 2015 Gorkha earthquake, was chosen as a case-study. The tower was also analysed in Chapter 4 using the rigid interface model. In this section,

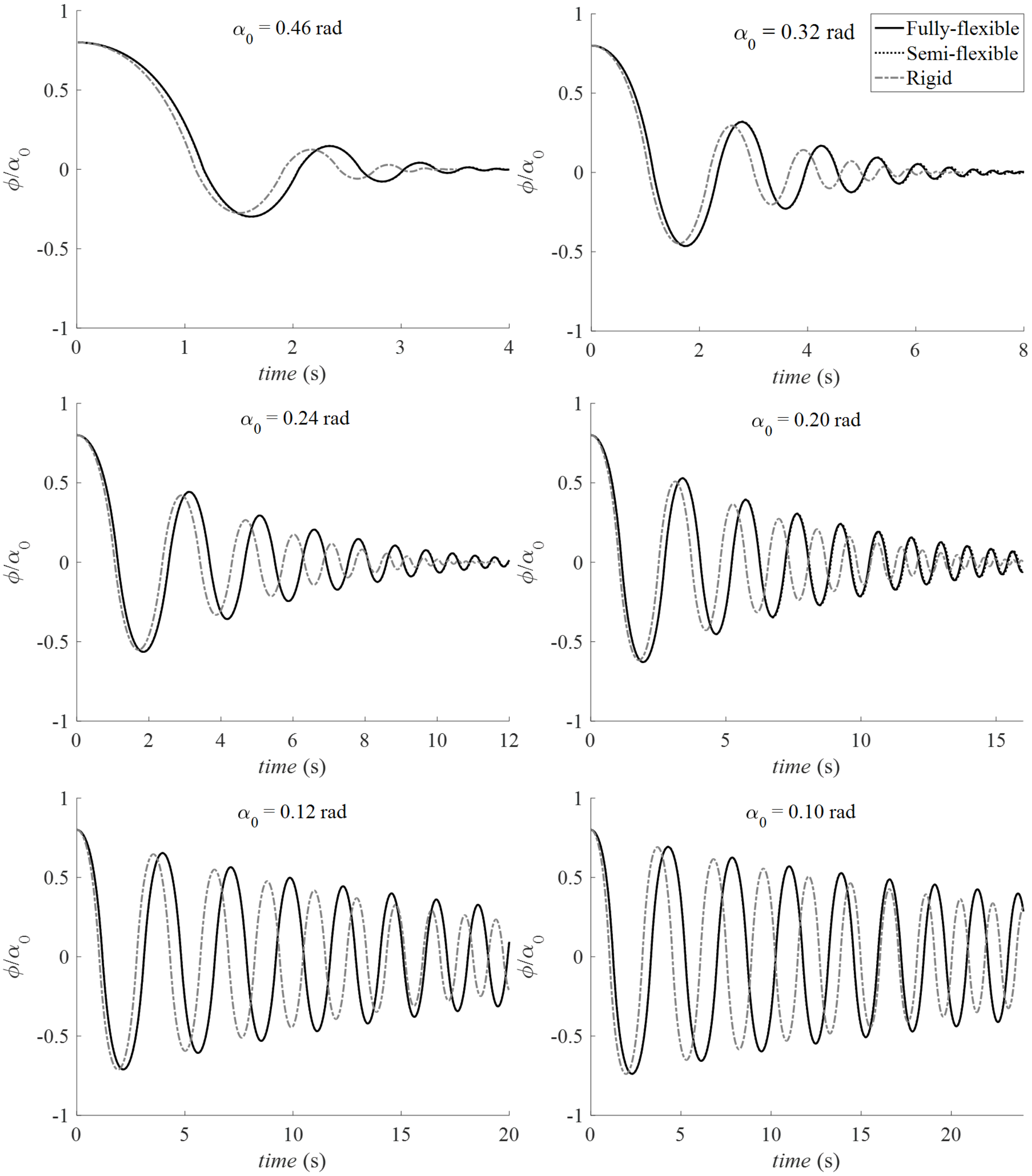

Fig. 7.4 Comparison of the fully-flexible, semi-flexible and rigid free-rocking response (ϕ_0/α_0 = 0.8) of blocks of varying slenderness α_0 (k_n = 340 MPa/m, f_m = 1.28 MPa)

the tower will be re-analysed using the flexible interface model in order to demonstrate the importance of accounting for crushing effects in the masonry.

The tower was constructed using brick masonry with lime and mud mortar (Bhagat et al., 2017) and the geometry of the structure, including that of its base, is shown in Fig. 7.5. The geometric properties were automatically extracted by the analytical tool, using as a starting point the 3D model

Photos of the Dharahara Tower removed for copyright reasons. Copyright holders are Ian Trower/JAI/Corbis and Turjoy Chowdhury/NurPhoto/Corbis.

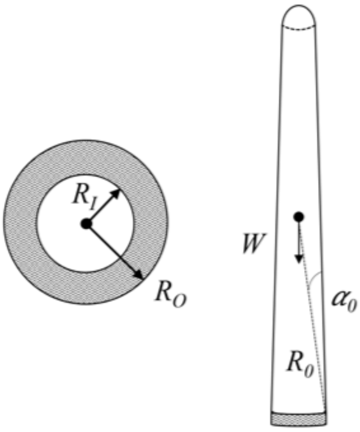

Fig. 7.5 Dharahara Tower before and after the 2015 Gorkha earthquake (L) (Ian Tower/JAI/Corbis, Turjoy Chowdhury/NurPhoto/Corbis) and structural geometry (R)

of the structure in Rhino, and are listed in Table 7.1, while the material properties adopted for the hollow circular interface can be found in Table 7.2. To illustrate different possible applications of the model, two different sets of joint stiffnesses and a range of compressive strengths were considered in the analysis. The compressive strengths were chosen based on the range of values provided in the Italian Building Code for brick masonry with lime mortar (DMI, 2008), as well as the results of both in-situ and experimental tests conducted on brick masonry structures in Nepal (Parajuli et al., 2011; Parajuli and Kiyono, 2015). Similarly, the first set of joint stiffnesses - varying from flexible (k_n = 85 MPa/m) to very stiff (k_n = 13.5 GPa/m), were chosen with the objective of exemplifying how foundation stiffness could be taken into account in the model, and were selected based on similar analyses conducted in Shawa et al. (2012), Lipo and de Felice (2016) and Lipo and de Felice (2017). The second set of stiffnesses is representative of interfaces within the structure - modelling both the stiffness of a single interface (k_n = 200, 500, 1500 GPa/m) as well as the deformation associated with of a larger portion of the structure in the vicinity of the interface (k_n = 2, 5, 15 GPa/m), with the latter having been found to lead to an overall reduction in dynamic capacity de Felice (2011). Note that to model the interface stiffness, the values of k_n were obtained by assuming a Young's modulus of 1000 $\times f_m$, and estimating the thickness of a single interface to be 0.01 m and the approximate portion of the structure involved in local deformation near the rotation point to be 1 m.

The expressions derived in Section 6.2 were then used calculate $a_f(\phi)$ for the specified range of joint stiffnesses and compressive strengths, which in turn were used to generate moment-rotation curves (both with and without crushing) for the structure, as illustrated by Fig. 7.6 and Fig. 7.7.

Table 7.1 Dimensions of the Dharahara Tower

R_O (m)	3.99
R_I (m)	2.12
W (kN)	24003.94
R_0 (m)	30.44
α_0 (rad)	0.125

Table 7.2 Material properties considered for the interface of the Dharahara Tower

Joint stiffness (foundation) k_n (MPa/m)	85, 170, 340, 680, 1350, 13500
Joint stiffness (interface) k_n (GPa/m)	2, 5, 15, 200, 500, 1500
Compressive strength f_m (MPa)	2, 5, 15

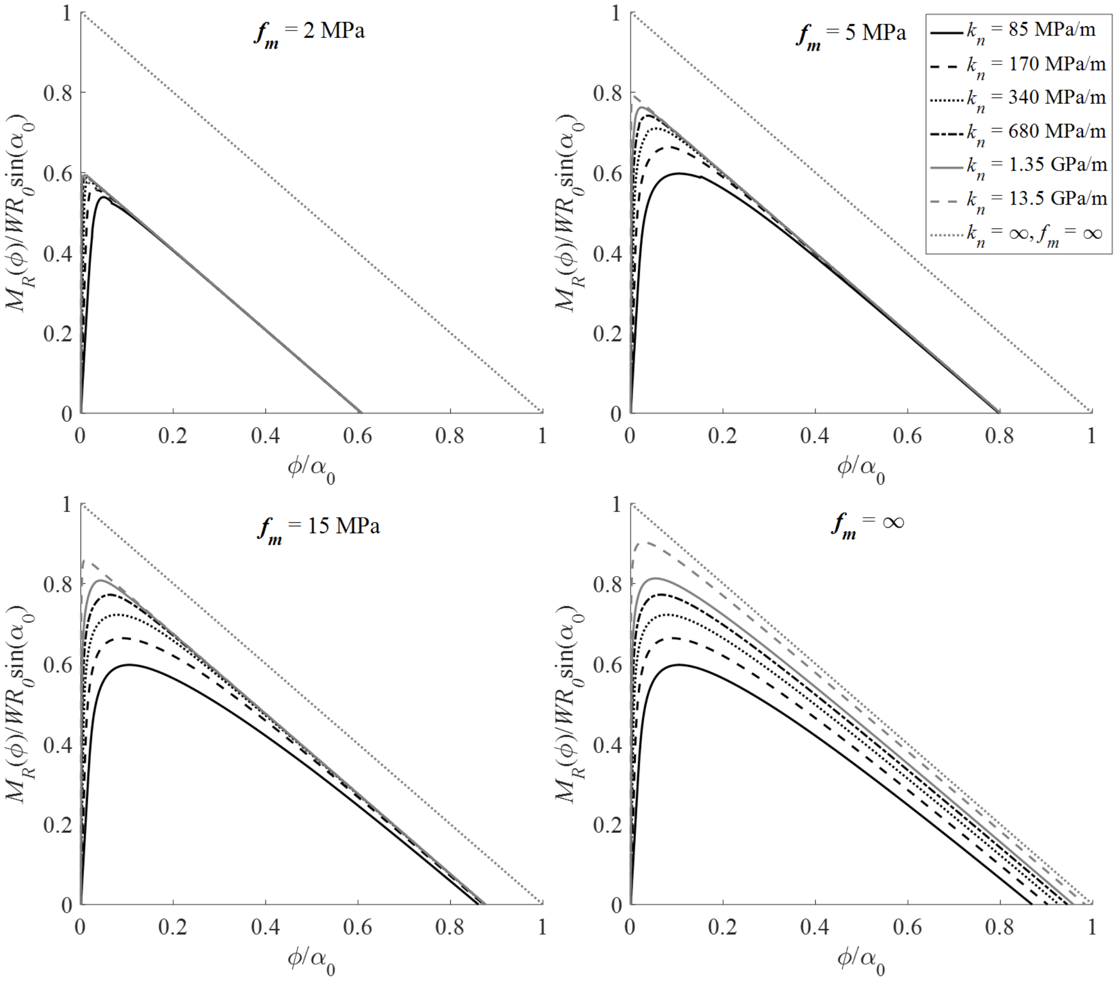

Fig. 7.6 Moment-rotation curves generated for the Dharahara Tower for different foundation stiffnesses, both with crushing (f_m = 2, 5 and 15 MPa) and without crushing ($f_m = \infty$)

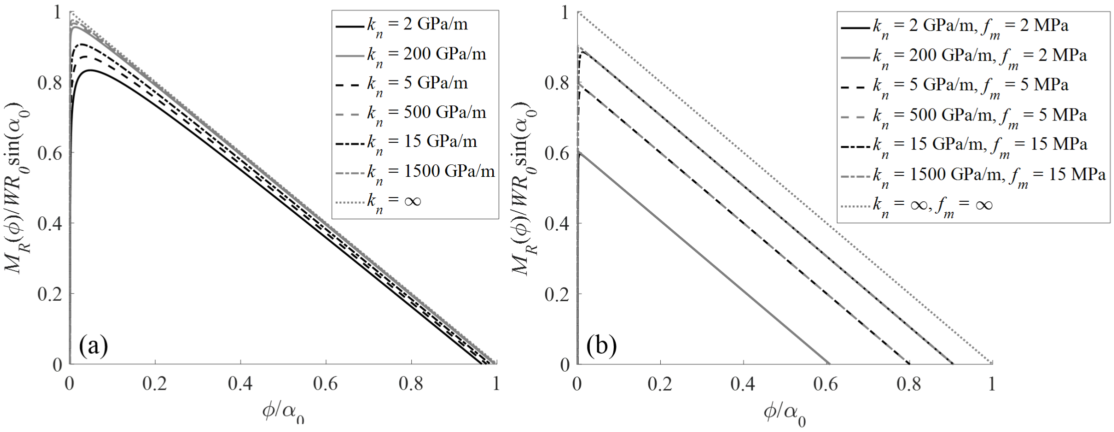

Fig. 7.7 Moment-rotation curves for the Dharahara Tower for different interface stiffnesses and compressive strengths: (a) without crushing and (b) with crushing

For the purpose of comparison with Housner's model, the curve for the pure rigid interface (infinite stiffness, infinite compressive strength) is also included in these plots.

Fig. 7.6 shows that for low values of compressive strength (f_m = 2 MPa), the structure experiences crushing at relatively small rotations for all considered levels of joint stiffness, which leads to an overall reduction of 40% in the dynamic capacity of the structure as compared to the rigid interface model. For higher compressive strengths (f_m = 15 MPa), the more flexible models (k_n = 85 MPa/m and 170 MPa/m) remain entirely in the elastic zone (compare with the curves for $f_m = \infty$), while the stiffer models still experience crushing, with the threshold rotation for crushing ϕ_c generally decreasing with an increase in foundation stiffness.

Similarly, in the case of varying interface stiffness, it was observed that including crushing effects resulted in a significant reduction in the dynamic capacity of the structure (Fig. 7.7a vs Fig. 7.7b). In fact, crushing occurred almost instantly for all levels of compressive strength, for both considered stiffness values – thus resulting in nearly-overlapping curves for each value of f_m (Fig. 7.7b). Furthermore, as rocking of the Dharahara Tower was observed to occur at the masonry-masonry interface during the earthquake, the values derived for $a_f(\phi)$ for the different interface stiffnesses were then substituted into Equation 6.54, to be used for the non-linear time-history analysis of the tower. The input ground motion used in the analysis was the north-south component of the 2015 Gorkha earthquake recorded at the USGS KANTP station, as illustrated by Fig. 7.8. No scaling was applied to the ground motion.

The results of the time-history analyses are presented in Fig. 7.9, both for the case without crushing (Fig. 7.9a) and with crushing (Fig. 7.9b). Furthermore, to facilitate comparison with Housner's model, the time-history response of an interface with infinite stiffness and compressive strength (i.e. a rigid interface) is also presented here. To better compare the relative magnitudes of the rotations predicted by the different interface models, the rotation of the structure ϕ was normalized

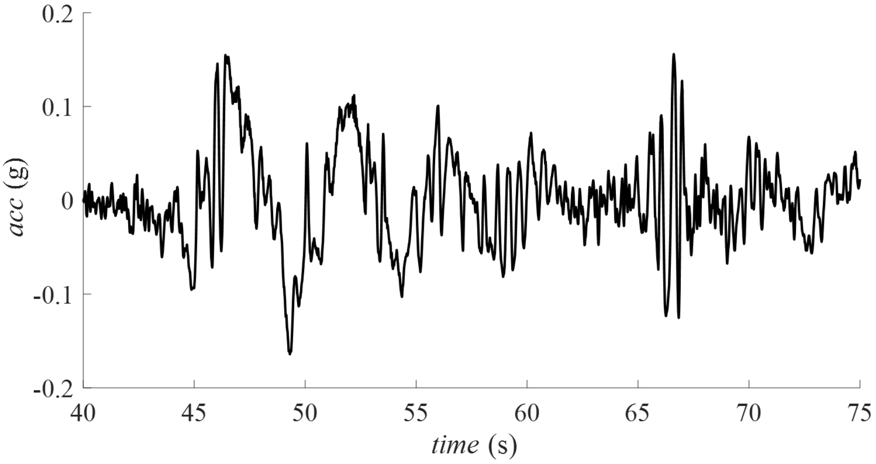

Fig. 7.8 North-south component of the 2015 Gorkha earthquake ground motion as recorded at the USGS KATNP station (unscaled)

by the slenderness of the tower α_0. Note that unlike Chapter 4, α_0 (or variations of it) is generally used in this chapter instead of the overturning rotation ϕ_{ov}, as this remains constant for the same mechanism regardless of the interface material properties, while ϕ_{ov} varies with the interface stiffness and compressive strength and is thus also different for the rigid model. As the objective here is to compare the magnitude of the rotations predicted by the different interface models, it is therefore more reasonable to normalize the rotations by α_0 instead. However, as overturning of the structure in this case no longer occurs when $\phi\ /\alpha_0$ exceeds 1 (as is the case for the rigid interface model) – and instead takes place when the restoring moment $M_R(\phi) = 0$, ϕ_{ov} for each of the models was extracted from Fig. 7.7, and the time-history analyses stopped when this rotation was exceeded.

In the case of the models with infinite compressive strength (no crushing, Fig. 7.9a), overturning of the tower was found to occur fairly quickly for lower levels of the joint stiffness ($k_n \leq 15$ GPa/m), while higher levels of the stiffness also caused overturning of the tower, albeit after the first big pulse in the ground motion (with the exception of $k_n = 500$ GPa/m, which exhibited low-amplitude high-frequency rocking before returning to equilibrium). On the other hand, including crushing effects at the interface results in the tower overturning for all considered levels of interface compressive strength and stiffness in a comparable amount of time, with lower levels of the compressive strength generally resulting in larger rotations and faster overturning of the structure (Fig. 7.9b). For the compressive strength of 2 MPa, the stiffer model was actually found to overturn faster than its more flexible counterpart, while for $f_m = 15$ MPa, the more flexible interface model results in collapse before the stiffer one. However, in both cases the difference between collapse times of the two models is generally less than 0.5 seconds, thus indicating that compressive strength more than stiffness tends to control dynamic response. This behaviour compares fairly well what was observed in reality – the Dharahara Tower did in fact overturn and collapse during the earthquake in 2015. Due to the scale of

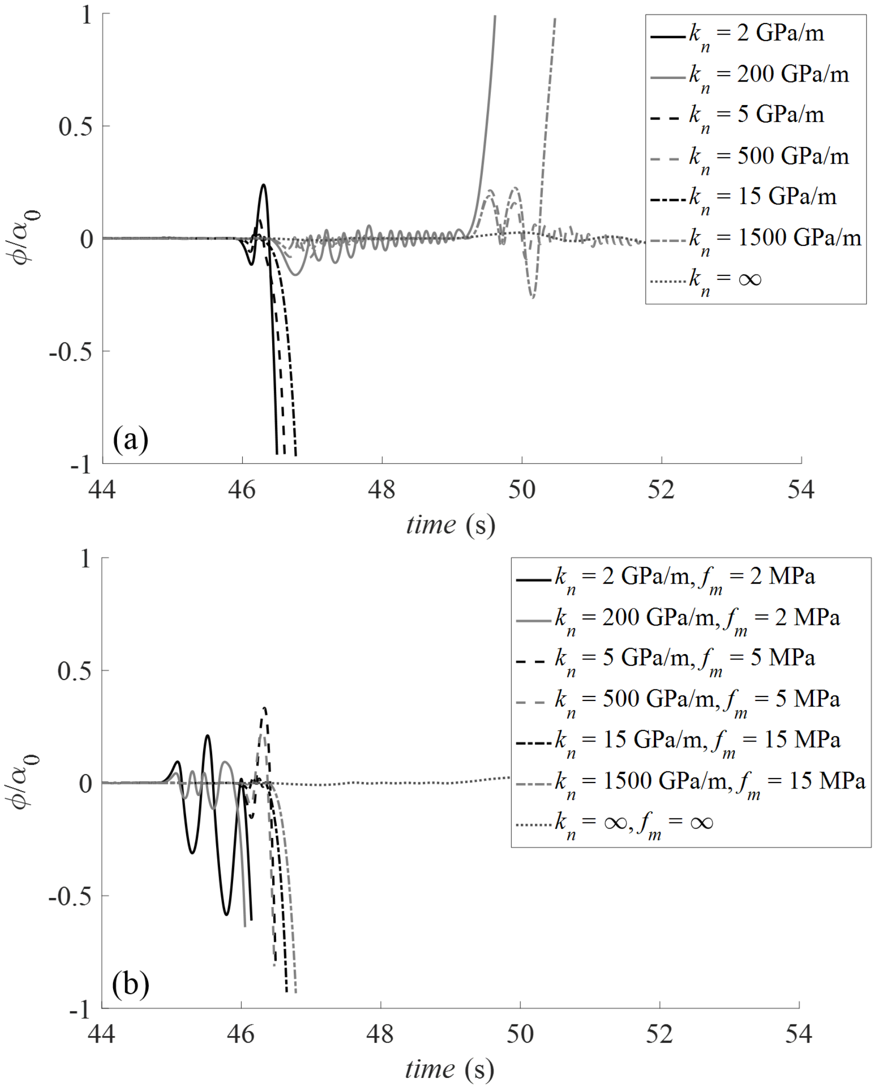

Fig. 7.9 Time-history responses of the Dharahara Tower for different interface stiffnesses and compressive strengths: (a) without crushing and (b) with crushing

the structure, it is quite possible that some crushing could have occurred at the base, which would have decreased its resistance to overturning. This behaviour failed to be captured by the purely rigid model, which instead predicted very small rotations for the tower (Fig. 7.9). Note that this study has focused on the effects of stiffness and strength at or near the rocking interface; the elastic deformation of the tower itself, being large and slender, was not considered here, though it could play a significant role in the response.

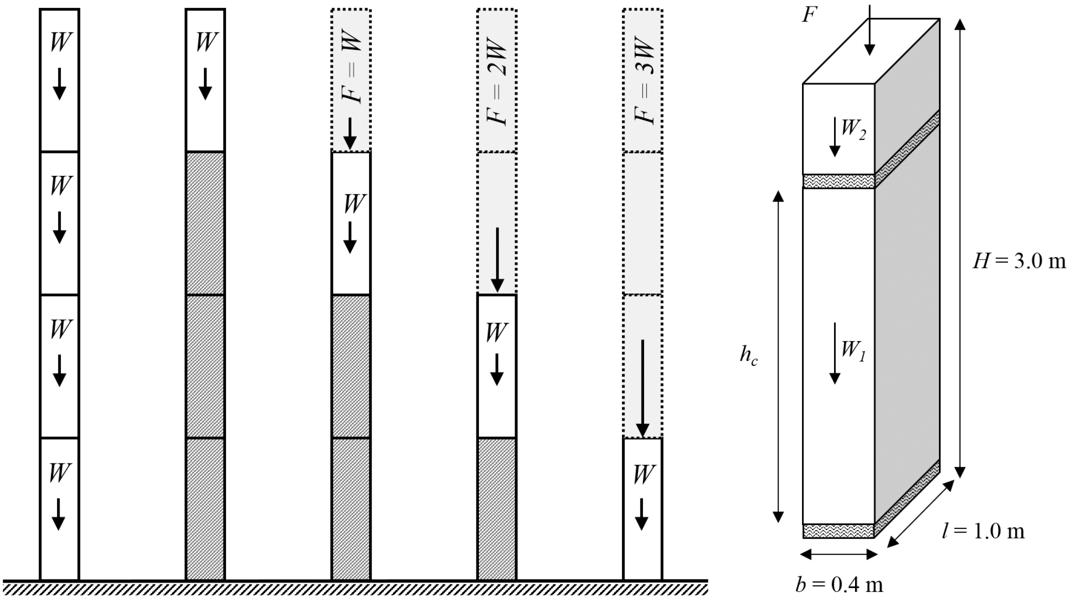

Fig. 7.10 Typical multi-story spanning masonry wall, with corresponding overburden forces for each wall segment (left); geometry of a single wall segment with an intermediate crack at height h_c (right)

7.3 Two block mechanism

In this section, the equations of motion derived for the two-block mechanism will be evaluated - using as a case-study a typical multi-story spanning masonry wall as depicted in Fig. 7.10. This load-bearing wall spans 4 floors, with each portion of the wall between floors having a constant width b of 0.4 m, length l of 1.0 m, height H of 3.0 m and density ρ of 1800 $\mathrm{kg\,m^{-3}}$ (Fig. 7.10). Each wall segment is subjected to a vertical overburden force F, the magnitude of which depends on the weight of the floors and walls above the segment in question, as illustrated by Fig. 7.10. Following the approach presented in Chapter 3, this overburden force, together with the tensile strength assumed for the mortar joints f_{mt}, can then be substituted into Equation 3.27 in order to calculate the height h_c at which the wall segment cracks and forms an additional hinge, which in turn can be used to determine W_1 and W_2 – the weights of the bottom and top blocks respectively. The corresponding equation of motion is then derived using Lagrange's principle as outlined in Section 6.3.2, and is used to evaluate the influence of interface stiffness, compressive strength and overburden force on the dynamic resilience of the wall - through the use of moment-rotation curves, free-rocking response, as well as full time-history analyses.

7.3.1 Moment-rotation curves

In the first set of analyses conducted on the cracked wall segment, moment-rotation curves were generated using Equation 7.1 for varying values of the joint stiffness k_n, compressive strength f_m and overburden force F (Fig. 7.11).

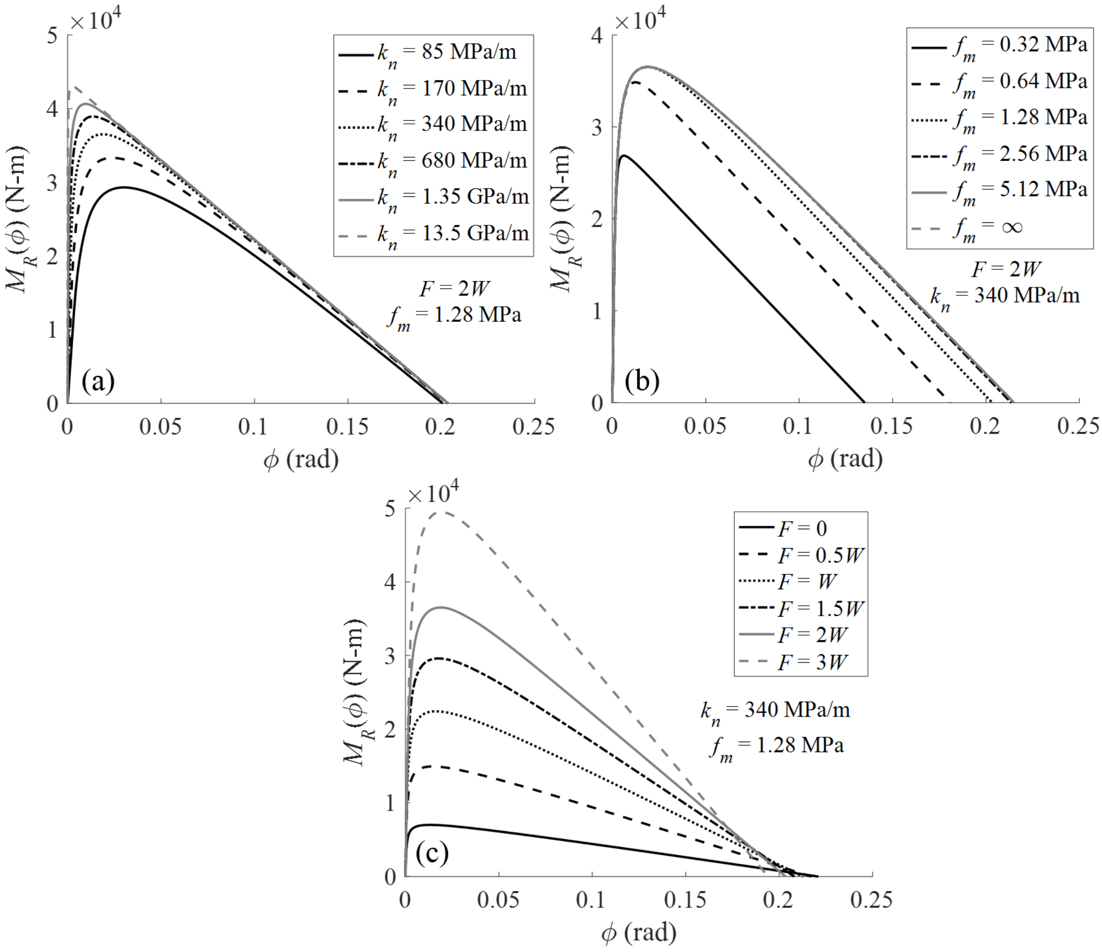

Fig. 7.11 Moment-rotation curves for: (a) varying interface stiffness k_n, (b) varying compressive strength f_m and (c) varying overburden force F

From Fig. 7.11a, it can be seen that for the same compressive strength and overburden force, an increase in joint stiffness k_n results in an increase in the dynamic capacity of the mechanism, as well as an increase in the overturning rotation (that is, the rotation at which the restoring moment $M_R(\phi)$ equals 0).

In the case of varying values of the compressive strength f_m (Fig. 7.11b), it was found that, as in the case of increasing joint stiffness, an increase in compressive strength results in a considerable increase in the maximum restoring moment of the structure as well as the overturning rotation. However, for the two highest compressive strengths (f_m = 2.56 and 5.12 MPa), the behaviour of the joints remains entirely elastic and no crushing is observed to occur – resulting in near-identical curves for these two values of f_m, which also correspond to the curve generated for the case of an infinite compressive strength ($f_m = \infty$).

Similarly, keeping k_n and f_m constant while increasing the overburden force F (Fig. 7.11c) was found to considerably increase the maximum restoring moment (and consequently the dynamic capacity) of the mechanism. However, this was generally accompanied by a decrease in the overturning rotation of the wall segment, thus making the structure more vulnerable to collapse at larger rotations.

7.3.2 Free-rocking response

To further investigate the effect of the overburden force, the free-rocking response of the cracked wall was also assessed, starting with an initial rotation of the bottom block $\phi_0 = 0.8\alpha_{01}$. As demonstrated by Fig. 7.12, an increase in the vertical loading was generally found to have a stabilizing effect on the wall – while the relative amplitude of rocking remained similar, the response damped out faster under the influence of overburden forces, than in the case of no force at all – with larger forces causing the blocks to return to equilibrium more quickly.

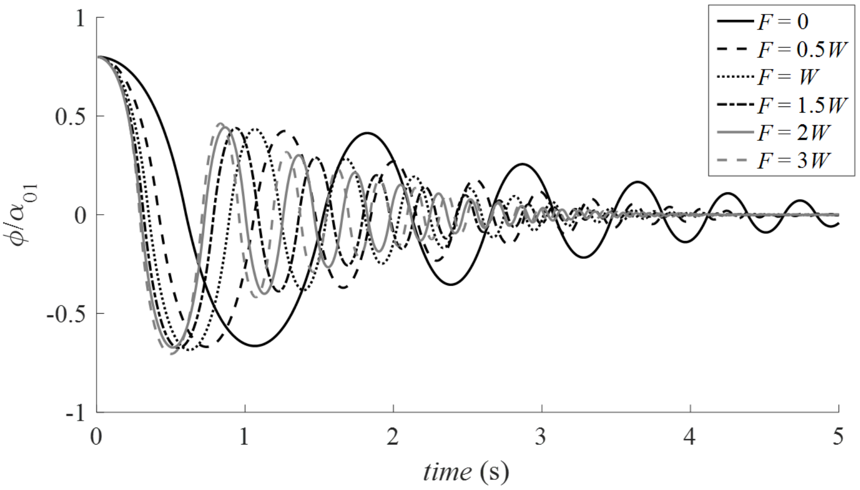

Fig. 7.12 Free-rocking response comparison for varying magnitudes of the overburden force F (k_n = 340 MPa/m, f_m = 1.28 MPa)

The free-rocking response was also used to compare the performance of the fully-flexible, semi-flexible and rigid interface models for a constant overburden force $F = 2W$. As Fig. 7.13 illustrates, the rigid model predicted smaller rotation amplitudes and damped out more quickly than the other two models – thus emphasizing just how un-conservative this approach can be. The fully-flexible and semi-flexible models, on the other hand, had a very similar response – indicating that the simpler semi-flexible model could well be used to model dynamic response in cases where absolute precision is not required and there is a need to reduce computational burden/solve time.

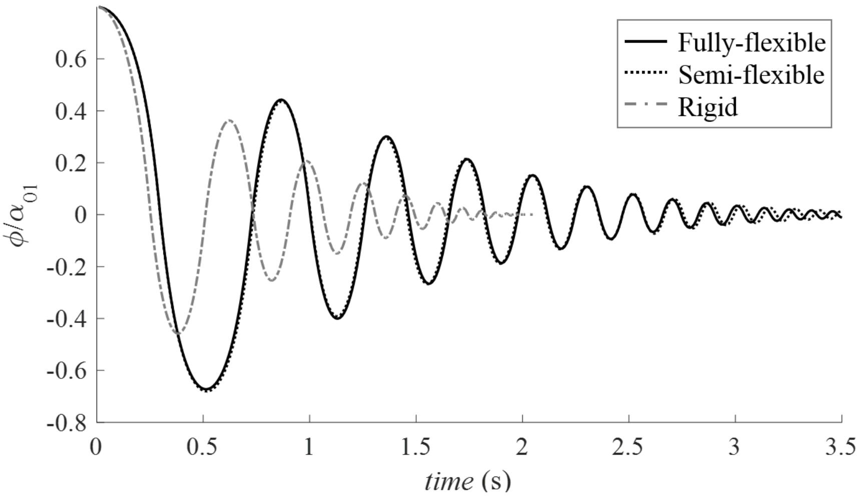

Fig. 7.13 Free-rocking response comparison for the flexible, semi-flexible and rigid interface models (k_n = 340 MPa/m, f_m = 1.28 MPa)

7.3.3 Full time-history analyses

In addition to the free-rocking response, the performance of the three interface models when subjected to forced excitations – in this case, the ground motion recorded during the 1999 Chi Chi (Taiwan) earthquake (Fig. 7.14) - was also investigated. All three models were also subjected to a constant overburden force $F = 2W$. In order for rocking to initiate in the rigid model, the input ground motion had to be scaled by at least a factor of 2.75, which was determined using the formulation for the static load multiplier λ presented in Chapter 3. However, this level of scaling of the ground motion caused a very small (almost imperceptible) response of the structure. Thus the scaling was increased to 4.50, which resulted in a larger rocking response and consequently collapse. To facilitate comparison between the three models, this scaling factor had to be applied to the input ground motion for the fully-flexible and semi-flexible models as well. The response predicted by each of these three models is found in Fig. 7.15. From this figure it can be seen that the rigid model is once again fairly un-conservative – initiating motion only after the other two models have already collapsed, while the predictions of the semi-flexible and fully-flexible interface models are, as in the case of the free-rocking response, in generally good agreement.

Further examination of the response of the fully-flexible interface model was conducted by varying the joint stiffness k_n and overburden force F. In this case three different levels of scaling SF of the input ground motion were used, as shown in Fig. 7.16. Note that the maximum response of the structure ϕ_{max} in each case was normalized by the overturning rotation ϕ_{ov} as extracted from the moment-rotation plots (Fig. 7.11) for each value of k_n and F. As Fig. 7.16a illustrates, for all considered levels of scaling of the ground motion, an increase in joint stiffness generally leads to a decrease in the maximum rotation of the cracked wall. A similar trend can also be observed in the case

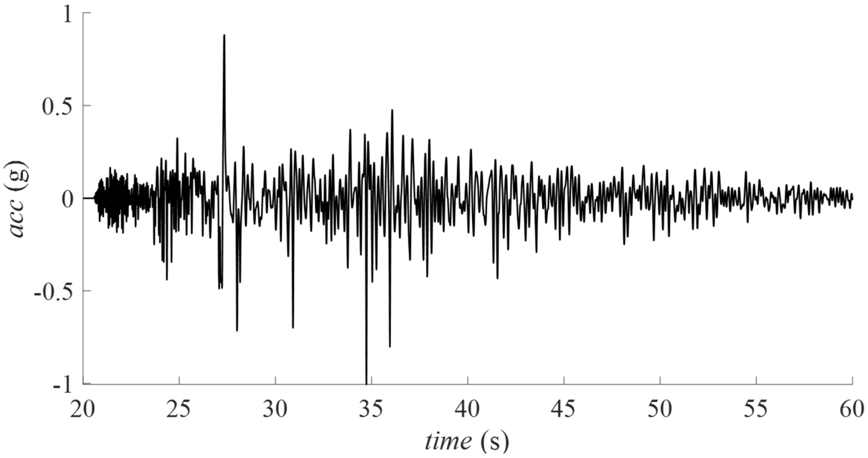

Fig. 7.14 Input ground motion (unscaled): 1999 Chi-Chi (Taiwan) earthquake

of varying overburden force (Fig. 7.16b), however for higher levels of F/W, the response eventually levels off – indicating that the benefit of the applied force is being counteracted by crushing effects. In fact, had a rigid interface model been used instead, more linear behaviour would most likely have been observed under the influence of increased vertical loading.

7.4 Multiple block mechanism

The equations of motion derived for the multiple block mechanisms - specifically the symmetric and asymmetric rocking frames - were also evaluated, using as case studies the two structural geometries depicted in Fig. 7.17, both with an assumed density ρ of $1800\,\mathrm{kg\,m^{-3}}$. Full time-history analyses were carried out in order to compare the responses of the fully-flexible, semi-flexible and rigid interface models, while validation of the new equations of motion was conducted through comparison of the analytical predictions to those obtained using discrete element modelling (DEM) in 3DEC. However, unlike the symmetric rocking frame, the coefficient of restitution for the asymmetric frame could not be easily calculated analytically and was instead specified to be 0.90 - which was calibrated based on the results of numerical simulations, as explained in greater detail in Section 7.4.3.

7.4.1 Full time-history analyses

In order to conduct a full time-history analysis, the symmetric and asymmetric rocking frames were subjected to the ground motion recorded during the 1989 Loma Prieta earthquake (Fig. 7.18). A scaling factor of 1.25 was applied to the acceleration record, as lower levels of scaling resulted in very small rotations of the structures. The results are presented here in terms of the variation of the rotation ϕ of the structure over time, normalized by the slenderness of the first column α_{01}.

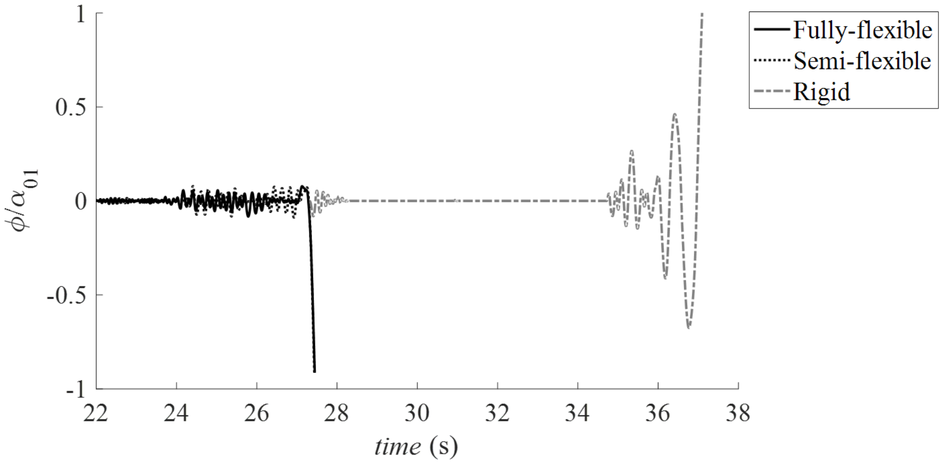

Fig. 7.15 Full time-history response comparison for the fully-flexible, semi-flexible and rigid interface models ($F = 2W$, $k_n = 340$ MPa/m, $f_m = 1.28$ MPa)

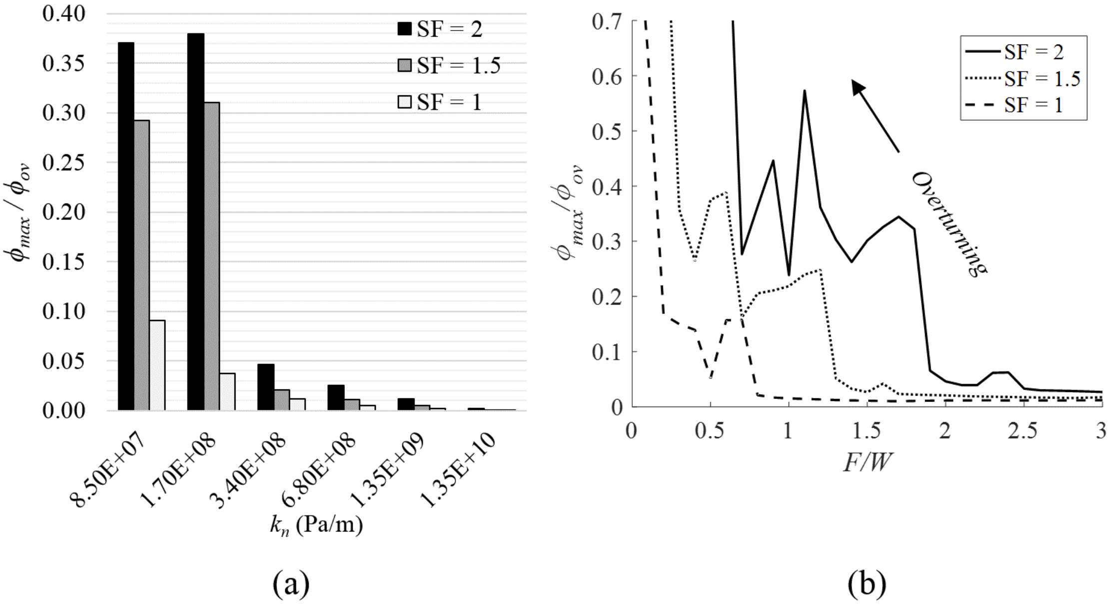

Fig. 7.16 Full time-history maximum response comparison for different earthquake scale factors (SF), and for (a) varying joint stiffness k_n and (b) varying overburden force F (normalized by the full weight of the wall W)

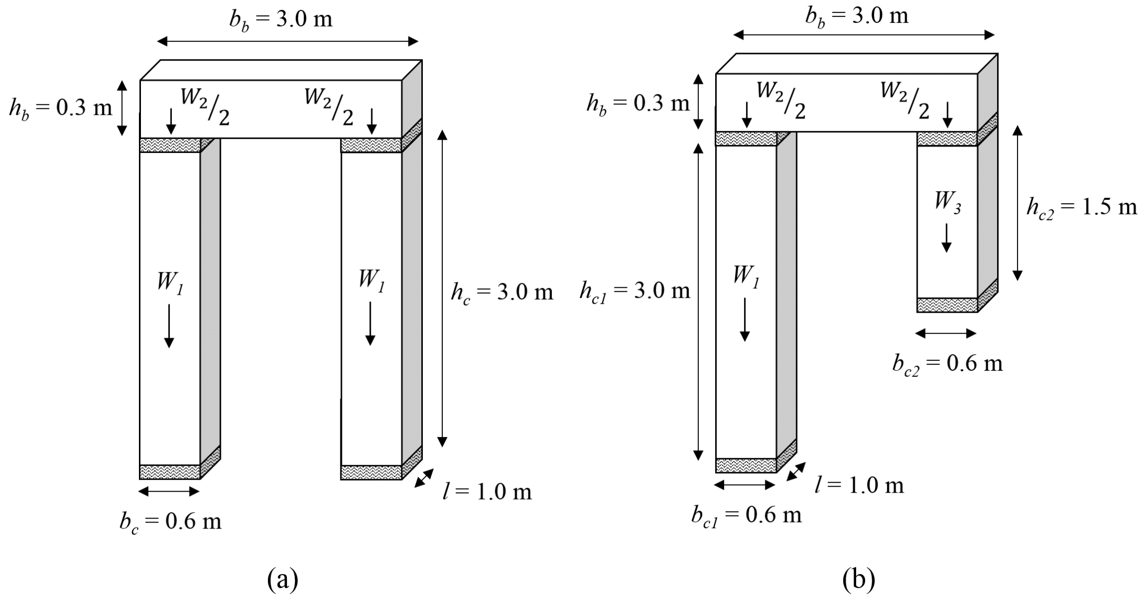

Fig. 7.17 Structural geometry and dimensions of the (a) symmetric rocking frame and (b) asymmetric rocking frame

In the case of the symmetric rocking frame (Fig. 7.19), a comparison of the predictions of the fully-flexible and semi-flexible interface models revealed a generally good correlation between the two for higher levels of interface stiffness ($k_n \geq 1.35$ GPa/m), while some scatter was observed in the results for the more flexible interface models. This scatter could be due in part to the fact that for lower levels of stiffness, the interfaces remain in the elastic zone for a larger range of rotations, and thus the difference between the fully-flexible and semi-flexible hinge locations for smaller rotations of the structure is not negligible. Consequently, when the fully-flexible model predicts small rotations of the structure, the semi-flexible model tends to yield a more conservative estimate of the response, thus resulting in larger rotation amplitudes as evidenced by the plots for k_n = 170 MPa/m and k_n = 680 MPa/m. Similar behaviour was also observed in the case of the two block mechanism, but is less obvious due to the large level of scaling applied to the ground motion, which resulted in collapse being predicted by both models after the first large pulse in the acceleration record.

Furthermore, a comparison of the fully-flexible, semi-flexible and rigid models for selected values of the interface stiffness (Fig. 7.20) demonstrated that once again the rigid model is the least conservative of the three - particularly in the case of interfaces with low stiffnesses.

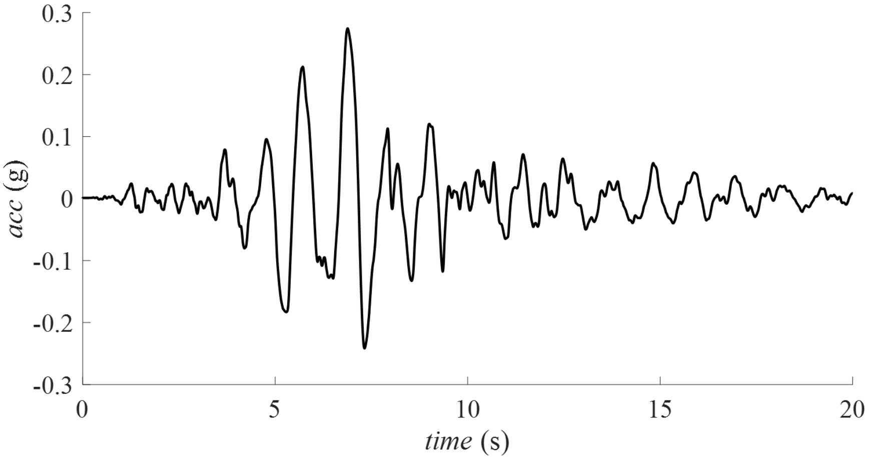

Fig. 7.18 Input ground motion (unscaled): 1989 Loma Prieta earthquake

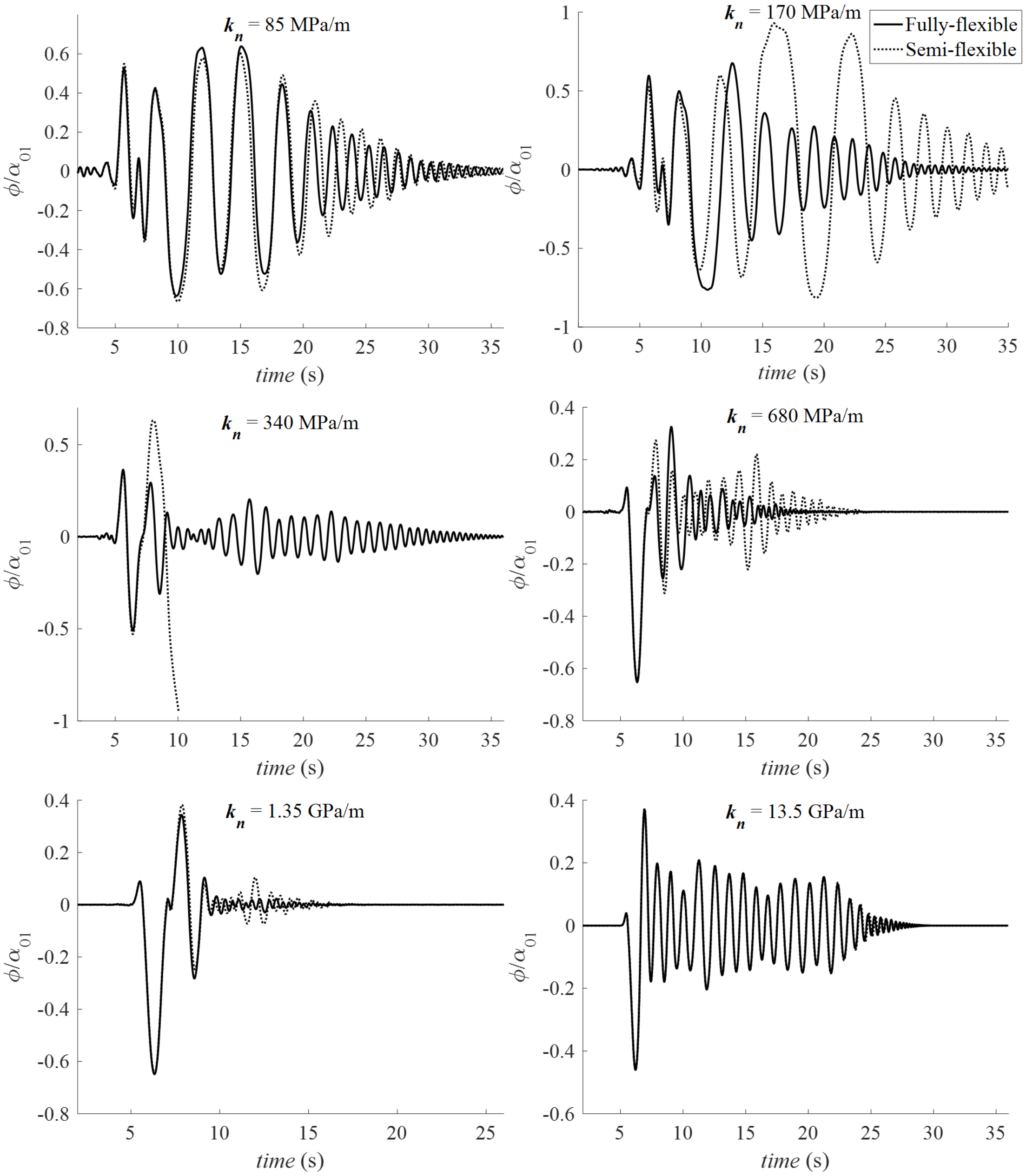

Fig. 7.19 Symmetric rocking frame: comparison of fully-flexible and semi-flexible interface models for varying values of interface stiffness k_n

In the case of the asymmetric rocking frame, a comparison of the predictions of the fully-flexible and semi-flexible interface models revealed similar trends to those observed for the symmetric rocking frame. The two models generally compared fairly well for higher interface stiffnesses, as well as larger rotations - as illustrated by the plot for k_n = 170 MPa/m, which, despite the low stiffness of the interface, resulted in identical responses being predicted by both models due to the relatively large

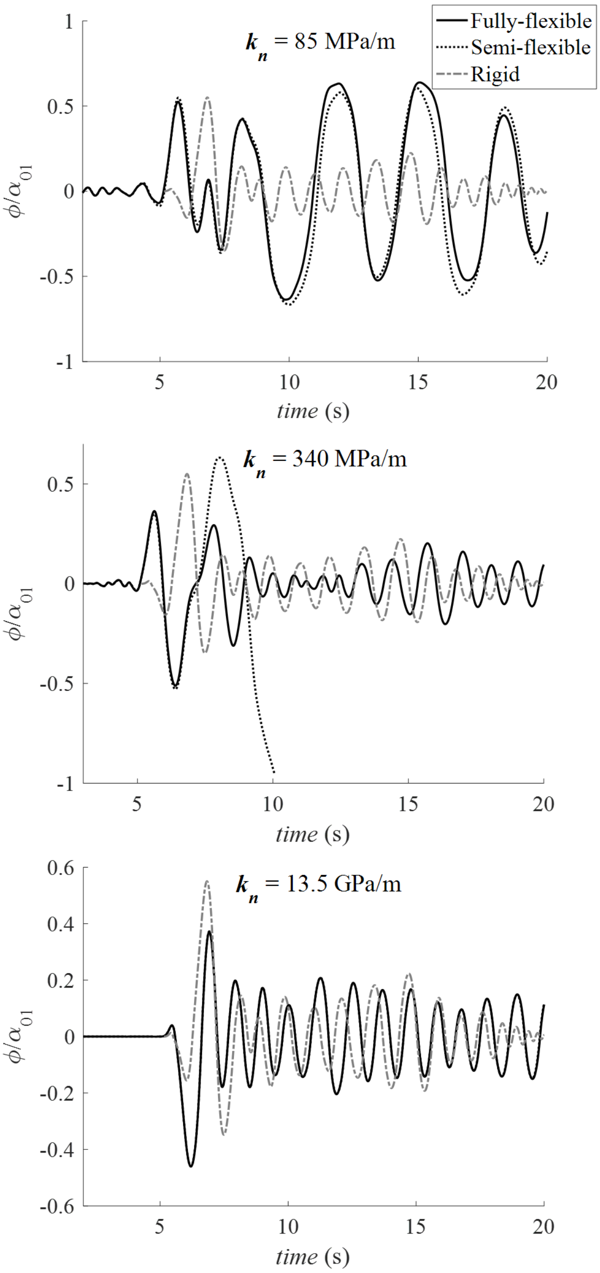

Fig. 7.20 Symmetric rocking frame: comparison of fully-flexible, semi-flexible and rigid interface models for selected values of interface stiffness k_n

rocking amplitudes experienced by the structure. Discrepancies between the predictions of the two models could also be partially attributed to the generally chaotic nature of the rocking response.

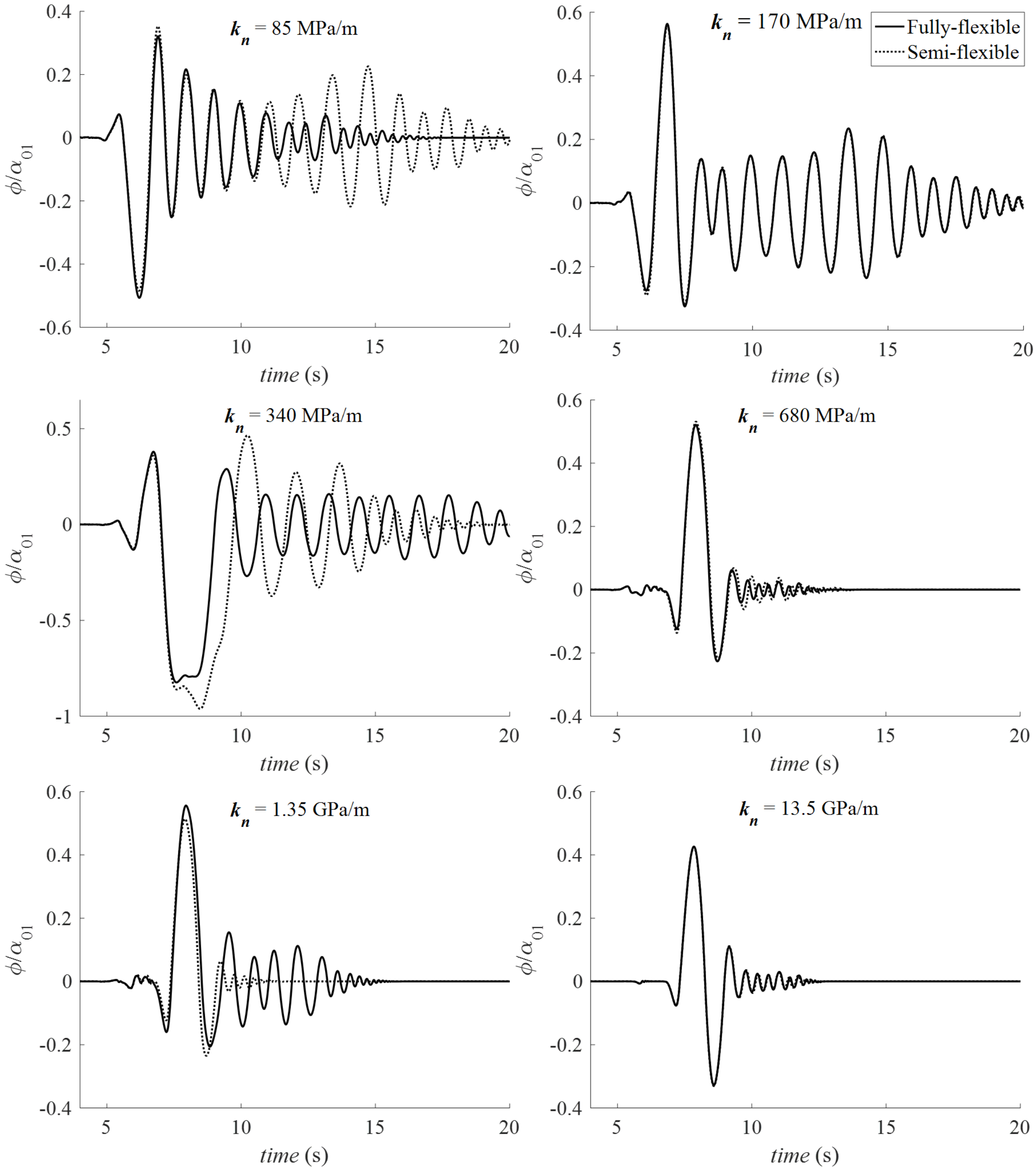

Fig. 7.21 Asymmetric rocking frame: comparison of fully-flexible and semi-flexible interface models for varying values of interface stiffness k_n

Finally, a comparison of the predictions of the fully-flexible, semi-flexible and rigid models (Fig. 7.22) once again highlighted the un-conservativeness of the rigid model, which tended to predict smaller rotations and generally damped out faster than its fully-flexible and semi-flexible counterparts.

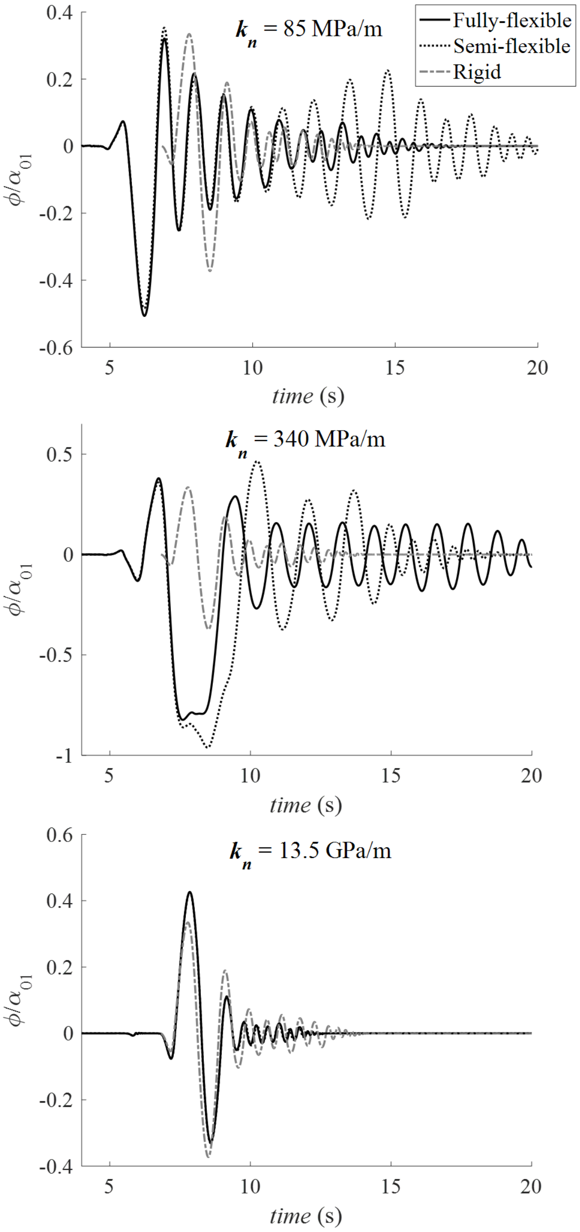

Fig. 7.22 Asymmetric rocking frame: comparison of fully-flexible, semi-flexible and rigid interface models for selected values of interface stiffness k_n

7.4.2 Validation of the models using DEM

In order to validate the equations of motion derived in Chapter 6 for practical use within the framework of the tool, the results of the previously-conducted time-history analyses were compared to the predictions obtained using discrete element modelling (DEM) in 3DEC.

3DEC models of both the symmetric and asymmetric frames were generated from the CAD models created in Rhino, based on the geometries and dimensions depicted in Fig. 7.17. Rigid blocks were used in the analysis, with a density ρ of $1800\,\mathrm{kg\,m^{-3}}$ being assumed for both structures. The joint normal stiffnesses k_n were the same as those used in the analytical models, while the shear stiffness k_s was set to $0.4k_n$ (Shawa et al., 2012). Furthermore, in order to prevent sliding failure, an artificially large friction angle of 80° was specified for all the joints.

As rigid blocks were being used in the analysis, each of the corresponding (horizontal) interfaces in 3DEC was made up of four vertical spring-dashpot elements - one in each corner. Consequently, rotation of the blocks would then occur about each of these corners, which is the same as the assumption of rigid interfaces. Thus to better capture the "shifting" of the rotation points, each of these interfaces needed to be further discretised to create additional contact points. In order to do this, the two columns of the frame were subdivided into n segments before export to 3DEC, resulting in (n+1) contact points at each of the interfaces. Once the geometry had been imported into the 3DEC environment, the columns were then joined back together so that they would behave as singular rigid bodies.

However, increasing the number of contacts tends to increase the solve time, thus in order to determine the optimal level of discretisation, a parametric study was conducted using as a starting point the asymmetric rocking frame. The number of segments that each of the columns of the frame were subdivided into was varied, and each of these discretised models was then subjected to the Loma Prieta ground motion record (Fig. 7.18), with a scale factor of 1.25 being applied to the ground motion (as was done in the analytical simulations). However, to minimise computational burden, the numerical analyses were only run for the first 20 seconds of the record, as this was found to be the most destructive. Furthermore, stiffness-proportional Rayleigh damping was used for the analyses in order to damp out the effect of unrealistic high-frequency vibrations (DeJong, 2009), with the corresponding damping constants β_R (which varied with the level of discretisation) being listed in Table 7.3. Note that mass damping (α_R) was set to zero for these analyses.

Table 7.3 Stiffness-proportional damping constants (β_R) specified for the different levels of interface discretisation

Discretisation	β_R
2	3.22×10^{-2}
10	1.45×10^{-2}
20	1.02×10^{-2}
80	5.14×10^{-3}

The response predicted by each of these models is presented in Fig. 7.23. From this plot it can be seen that the response of the structure tends to increase with an increase in discretisation, with the response for higher levels of discretisation (disc20 and disc80) being nearly identical. Thus disc20 was determined to be the optimal level of discretisation, as it provides reasonably accurate predictions

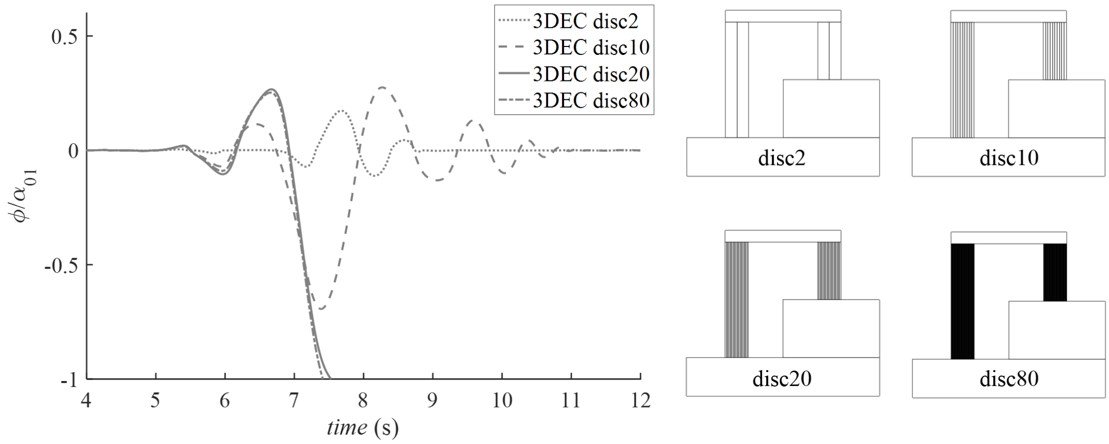

Fig. 7.23 Predicted response of the 3DEC models for different levels of interface discretisation

while minimising computational burden/solve time, as evidenced by the fact that simulation using the disc20 model took half as long as with the disc80 model.

Using this level of discretisation, the 3DEC model for the symmetric rocking frame was then run for the different values of interface stiffness, and the predicted responses for each value of k_n were compared to those obtained using the fully-flexible interface formulation of the analytical model (Fig. 7.24). As Fig. 7.24 illustrates, in general the two solutions compare fairly well for most considered values of k_n - as evidenced by the plot of k_n = 85 MPa/m, where the two solutions are almost identical for the first few cycles of motion. However, for k_n = 170 MPa/m and 340 MPa/m, the numerical model predicted collapse while the analytical model indicated a return to equilibrium - the differences in response of the two models could be attributed to factors such as the chaotic nature of the rocking response, as well as the sensitivity of both models to damping.

Similarly in the case of the asymmetric rocking frame (Fig. 7.25), a generally good correlation was observed between the two models for almost all considered values of interface stiffness k_n, with the exception of k_n = 340 MPa/m, where the numerical model predicted collapse while the analytical model predicted a return to equilibrium. However, up until the point of collapse, the two solutions also compare fairly well.

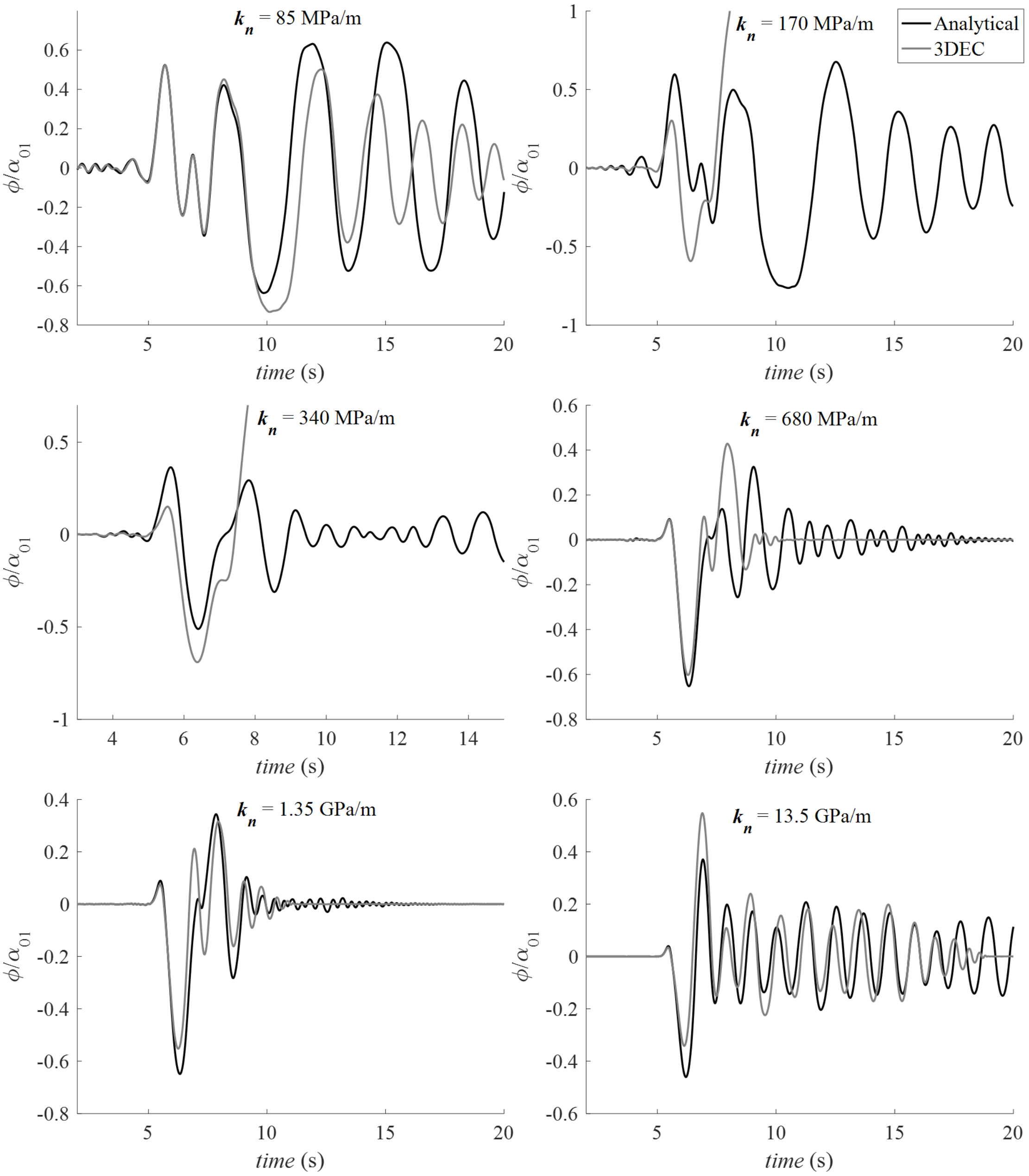

Fig. 7.24 Symmetric rocking frame: comparison of analytical (fully-flexible) and numerical (3DEC) predictions for varying values of interface stiffness k_n

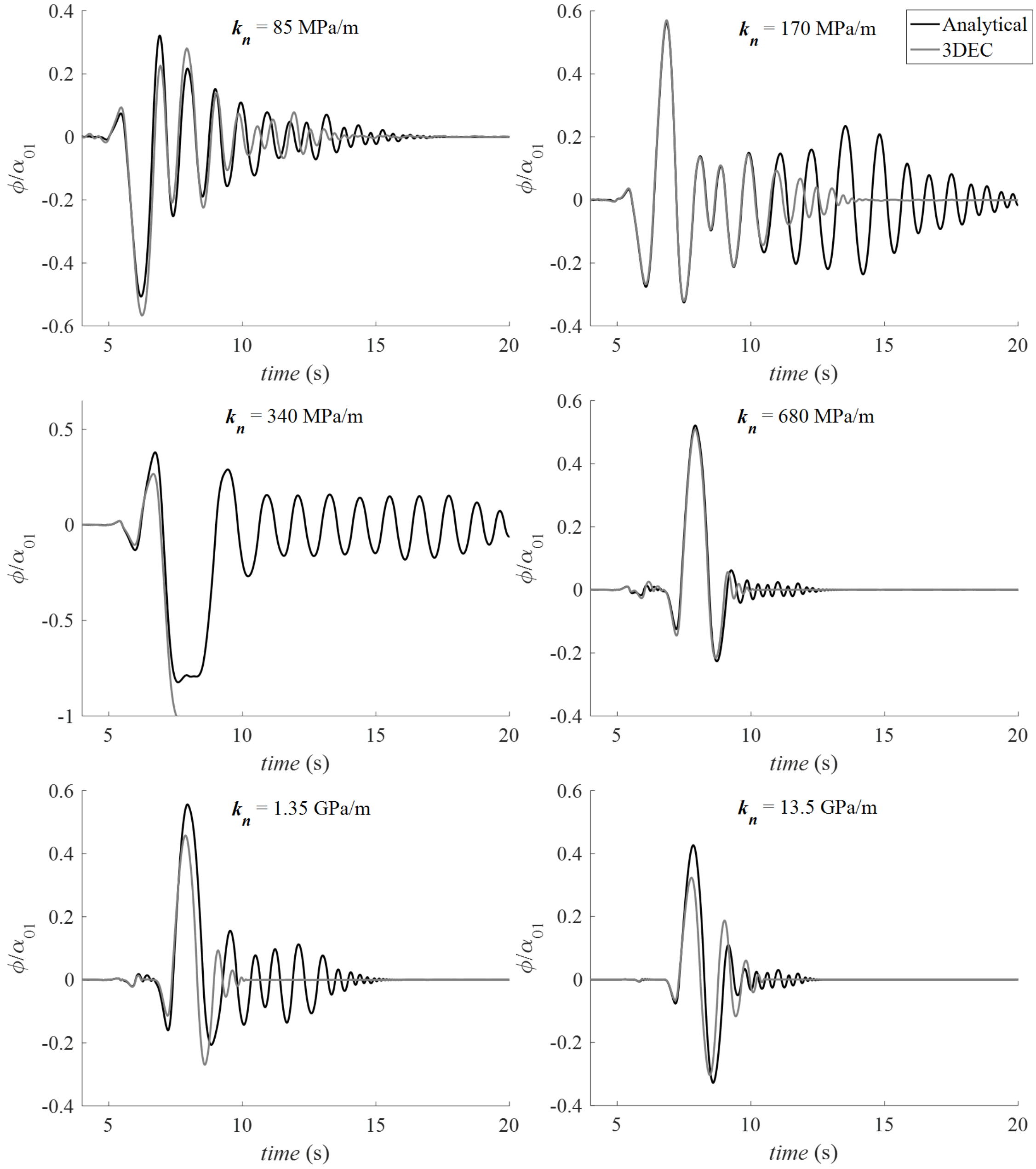

Fig. 7.25 Asymmetric rocking frame: comparison of analytical (fully-flexible) and numerical (3DEC) predictions for varying values of interface stiffness k_n

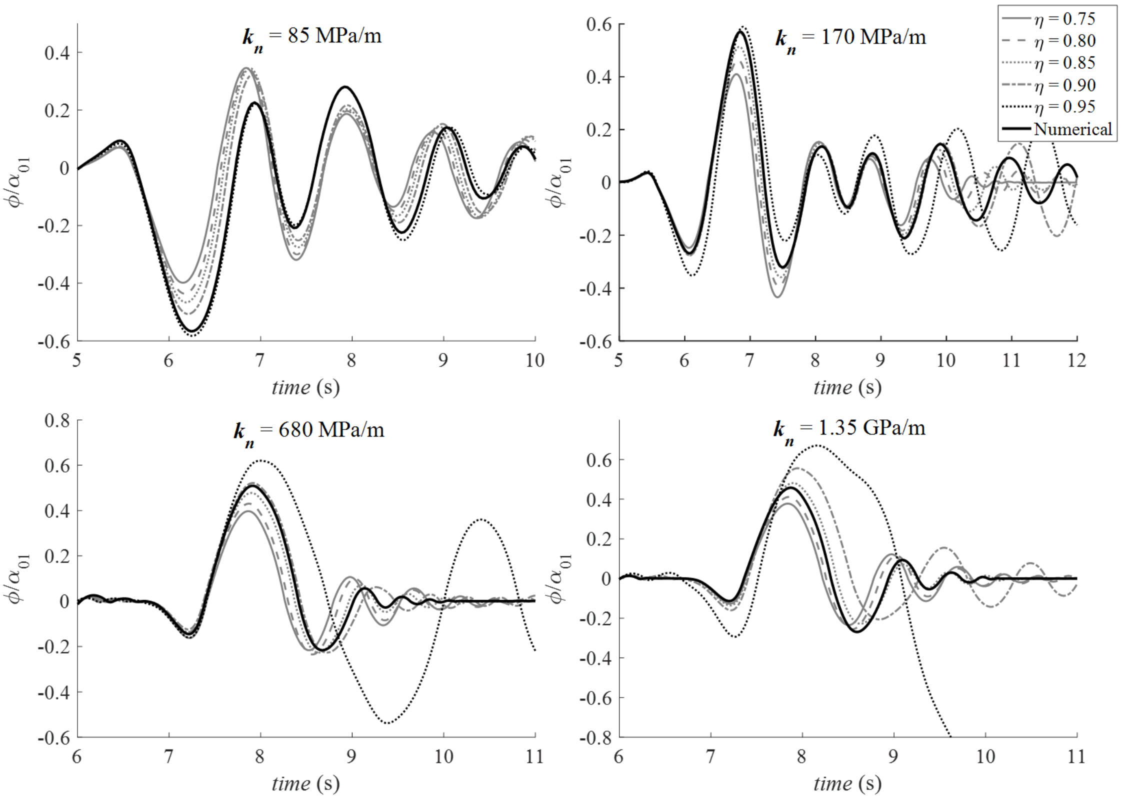

Fig. 7.26 Calibration of the coefficient of restitution of the asymmetric rocking frame

7.4.3 Calibration of the coefficient of restitution

In the case of the asymmetric rocking frame, the coefficient of restitution η cannot be easily determined analytically and instead needs to be calibrated based on the results of either experimental tests or numerical simulations. For this particular case study, η was thus calibrated against the results of the numerical simulations in 3DEC. In order to do this, upper and lower bounds for this parameter were first determined using the analytical formulation for η_{SF} for the symmetric rocking frame (Equation 6.72), but in this case considering two different frame geometries - the first with a column height corresponding to h_{c1} (i.e. the height of the first column of the asymmetric frame, Fig. 7.17b) and the second with a column height equal to h_{c2} (i.e. the height of the second column of the asymmetric frame, Fig. 7.17b). This resulted in upper and lower bounds on η of 0.95 and 0.75 respectively.

Analyses were then run using these two values of η, as well as three intermediate values of this parameter, for each of the different values of interface stiffness k_n. The results of these analyses were then compared to those obtained from the numerical simulations in 3DEC, as illustrated by Fig. 7.26. As Fig. 7.26 demonstrates, for lower values of the interface stiffness (k_n = 85 MPa/m), the response of the numerical model is best captured by the model using the highest value of the coefficient of restitution (η = 0.95). In the case of the intermediate stiffnesses (k_n = 170 and 680 MPa/m), the numerical response is best reproduced by the models with $\eta = 0.90$. Finally, in the case of higher values of $k_n (= 1.35$ GPa/m), $\eta = 0.85$ was observed to predict a response most similar to the 3DEC simulation. Thus $\eta = 0.90$ was specified as an average, as this was found to best capture the majority of the numerical results.

7.5 Broader applications of the new analytical models

In addition to modelling non-rigid interfaces between blocks, the new analytical models could also be used to account for damage to structures, as well as model the reduction in dynamic capacity of poorly built multi-leaf walls - which often lack proper transverse bonds between the external and internal leaves and consequently cease to behave as rigid rocking bodies, with failure instead occurring via the disaggregation of the wall section (de Felice, 2011). The numerically-obtained capacity curves for these structures (Fig. 2.6b) tend to display a significant reduction in both strength and displacement capacity (25% and 35% respectively) as compared to the purely rigid model (de Felice, 2011).

Thus in order to better capture the dynamic behaviour of these structures using analytical methods, an equivalent stiffness k_n could be defined, which takes into account wall section morphology, quality of masonry, as well as any pre-existing damage within the structure - calibrated based on the results of either experimental tests or numerical simulations.

7.6 Summary

The objective of this chapter was to evaluate the ability of the analytical models presented in Chapter 6 to model the dynamic response of masonry structures with non-rigid interfaces. The equations of motion derived for the different mechanisms were used for the generation of moment-rotation curves, as well as for the free-rocking response and full time-history analysis of a range of simple structural geometries. Parametric studies were also conducted to examine the influence of interface geometry, stiffness and crushing on the dynamic response of these structures. These investigations enabled the following conclusions to be drawn:

- Structures with rectangular interfaces are generally more resistant to overturning than their circular counterparts, while hollow structures are more resistant to collapse than solid structures.
- For a given structure, increasing the interface stiffness (for a fixed compressive strength) consistently increases the dynamic resistance, with the structure experiencing crushing faster for higher levels of stiffness. However, increasing the compressive strength (for a fixed stiffness) only increases the seismic resistance to a certain threshold - beyond which the behaviour of the interface remains entirely elastic and the structure does not experience crushing at all.
- In general, the semi-flexible interface models are capable of adequately capturing the dynamic response of their fully-flexible counterparts for both free-rocking as well as full time-histories

for all considered mechanisms. The predictions of these two models are also consistently more conservative than those of the rigid interface model. Further comparison between the semi-flexible and fully-flexible predictions revealed the semi-flexible model to be the more conservative of the two, although exceptions to these general trends can always be found due to the chaotic nature of the rocking response.

- The tendency of the rigid model to underestimate the response was reiterated through the case study of the Dharahara Tower - which also demonstrates a real-world application of the new flexible interface model. The purely rigid model predicted very small rotations of the tower, while the inclusion of a flexible interface (with finite compressive strength) resulted in overturning of the structure as was observed in reality, thus highlighting the importance of considering both interface stiffness as well as crushing effects.
- In the case of the cracked wall section (two block mechanism), an increase in overburden force was found to yield mixed results. While increasing the overburden load increases the effective stiffness of the system, it also causes material crushing. For larger loads, these crushing effects tend to counteract the beneficial influence of the force, resulting in a levelling off of the maximum rocking response of the wall, as well as a reduction in the overturning rotation of the structure.
- Validation of the new models for the more complex multiple block mechanisms was also carried out through a comparison with the results obtained using numerical modelling in 3DEC, and in general, a fairly good correlation was observed between the analytical and numerical predictions for both the symmetric and asymmetric rocking frames for all considered levels of interface stiffness.

In addition to modelling non-rigid interfaces, these new analytical models could also be applied to the analysis of damaged or poorly-built wall sections, through the definition of an equivalent stiffness which could be calibrated based on the results of either experimental or numerical campaigns.

Chapter 8

Application of the tool for seismic assessment

8.1 Introduction

The case studies used to illustrate potential applications of the tool thus far have comprised fairly simple/regular structural geometries, and have focussed for the most part on comparing the relative dynamic resilience of masonry collapse mechanisms (Chapter 5). Thus in order to demonstrate the tool's ability to analyse structures with complex geometries (such as those which have been reconstructed using point cloud data from a laser scanner), as well as its capacity for conducting seismic assessment using code-based methods, it was also used for the safety assessment of the Great House of the Casa Grande Ruins National Monument in Arizona, USA (Fig. 8.1).

Originally constructed to demonstrate box-like behaviour, decay and degradation of the Great House over the years - in the form of loss of the roof and floors, partial collapse of the exterior walls, as well as the development of vertical cracks and fissures at wall junctions - resulted in the structure being reduced to an assemblage of laterally unsupported walls with an increased vulnerability to overturning (Fattal, 1977).

This chapter conducts a seismic vulnerability analysis of these walls, in order to both identify the wall sections which are most susceptible to overturning, as well as evaluate the seismic capacity of these isolated wall elements. To do the former, the tool will be used to generate overturning plots in order to compare the different wall mechanisms and identify which one(s) are most vulnerable to collapse, while the latter will be accomplished through the application of code-based assessment methods. While the rigid model presented in Chapter 3 will be used to initially identify the most vulnerable mechanisms, more detailed analysis into these critical wall sections will then be conducted using the flexible interface model.

The seismic analysis is part of a broader inter-disciplinary research campaign which seeks to better understand the period building technology as well as the structure's current physical condition,

Fig. 8.1 Great House of the Casa Grande Ruins National Monument (USA) (photograph by N. Dixon, reproduced from Porter et al. (2018))

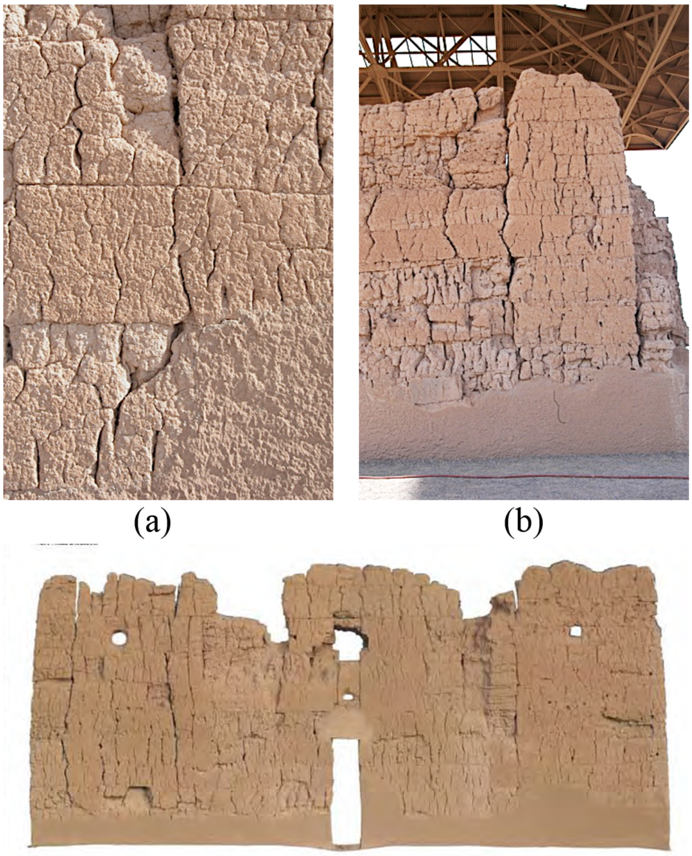

(a)

(b)

(c)

Fig. 8.2 East perimeter wall showing (a) horizontal coursing and (b) large vertical cracks; (c) west perimeter wall displaying similar vertical cracking behaviour (adapted from Porter et al. (2018))

in order to minimise future interventions and use them as efficiently as possible (Porter et al., 2018). This research was carried out in collaboration with Professor Douglas Porter at the University of Vermont, who also provided the point cloud data used for the reconstruction of the wall geometry in Rhino.

8.2 Background

Originally occupied between 1350-1450 AD (Porter et al., 2018), the Great House of the Casa Grande Ruins National Monument is the largest surviving prehistoric earthen building in the United States, and is the only surviving example of Classic Period Hohokam "Great House" architecture (Matero, 1999).

Rectangular in plan, the building has overall dimensions of 13 m $\times$ 18 m (Fattal, 1977), and walls ranging in height from 7.6 m (for the outer walls) to 9.1 m (for the inner walls) (Matero, 1999). These walls have an average thickness of 1.25 m, and were constructed using lenses of caliche, which were deposited onto the walls in horizontal courses of varying heights (Fig. 8.2a), with an average course thickness of 61 - 76 cm (Porter et al., 2018).

However, erosion of the walls over the years, coupled with the removal of wooden structural elements that supported floor and roof frame members, has resulted in reduction of the wall cross-sections by almost as much as 50% in some places (Porter et al., 2018). Moreover, previous earthquakes as well as damage due to animal activity led to the development of large vertical cracks and fissures in the walls (Fig. 8.2b & c), which effectively divided them into a series of tall and slender laterally-unsupported columns, with an increased vulnerability to overturning collapse (Matero, 1999; Porter et al., 2018). While early intervention measures in the 1890s to stabilise these vulnerable wall elements comprised wooden beams and iron tie-rods, more recent proposals recommend the use of an extensive system of wall cores as well as the reinstatement of original wooden structural elements (Porter et al., 2018). The purpose of this seismic analysis is to determine which walls, if any, are in need of these interventions.

8.3 Seismic analysis using the rigid rocking tool

In the first set of analyses, the rigid rocking tool is used to identify the most vulnerable walls in the structure. This is done through the use of overturning plots (to compare the relative vulnerability of the walls to sinusoidal pulses of varying frequency f_p and amplitude a_p), as well as through the employment of code-based methods (to determine the actual capacity of the walls with respect to the expected ground motions on site). The wall segments chosen for analysis are either isolated from corners or abutting walls (which could provide bracing) by large cracks or voids, or have suffered erosion at their bases which effectively reduces the wall section by 33-50%. It is also assumed that each of these wall elements act independently - that is, they are not sufficiently connected to each other.

In total, a seismic analysis of 7 different wall sections (comprising both exterior and interior walls) of the house was conducted, resulting in a total of 8 different mechanisms (as two mechanisms were considered for Wall 0), as illustrated by Figs. 8.3 and 8.4. Walls 0a, 2, 3, and 5 are full-height segments isolated by cracks and voids, while Walls 0b, 1, 4, and 6 have substantial section losses at their bases. The material properties adopted for the analysis of these walls can be found in Table 8.1.

Table 8.1 Material properties adopted for the caliche walls (Matero, 1999)

Density, ρ ($\mathrm{kg\,m^{-3}}$)	2240
Young's modulus, E (GPa)	6.89
Compressive strength, f_m (MPa)	1.00

Models of each of these walls were created in Rhino using point cloud data obtained from the laser scan of the site (Fig. 8.3). Capturing the exact geometry of these walls is essential to accurately model stability against overturning, particularly to capture the effects of potential existing lean of the walls and local loss of material (especially for Walls 1, 4, and 6). The point cloud data was then used to construct a mesh which in turn was used to generate a closed solid. Each wall was assumed to behave like single rocking block, with the axis of rotation being defined at the base of the wall section, while two-sided rocking was assumed in all cases. Table 8.2 lists the rocking parameters calculated by the script in Rhino for each of these different walls/mechanisms.

Table 8.2 Rocking parameters computed by the Rhinoscript for the different wall mechanisms

Mechanism	p_{eq} ($\mathrm{s^{-1}}$)	λ (rad)	η	R_0 (m)
Wall 0a (W0a)	1.60	0.14	0.97	2.84
Wall 0b (W0b)	3.36	0.54	0.62	0.62
Wall 1 (W1)	2.15	0.25	0.90	1.75
Wall 2 (W2)	1.60	0.23	0.92	2.88
Wall 3 (W3)	1.62	0.20	0.94	2.71
Wall 4 (W4)	2.67	0.34	0.83	1.04
Wall 5 (W5)	1.63	0.24	0.92	2.72
Wall 6 (W6)	2.26	0.21	0.94	1.46

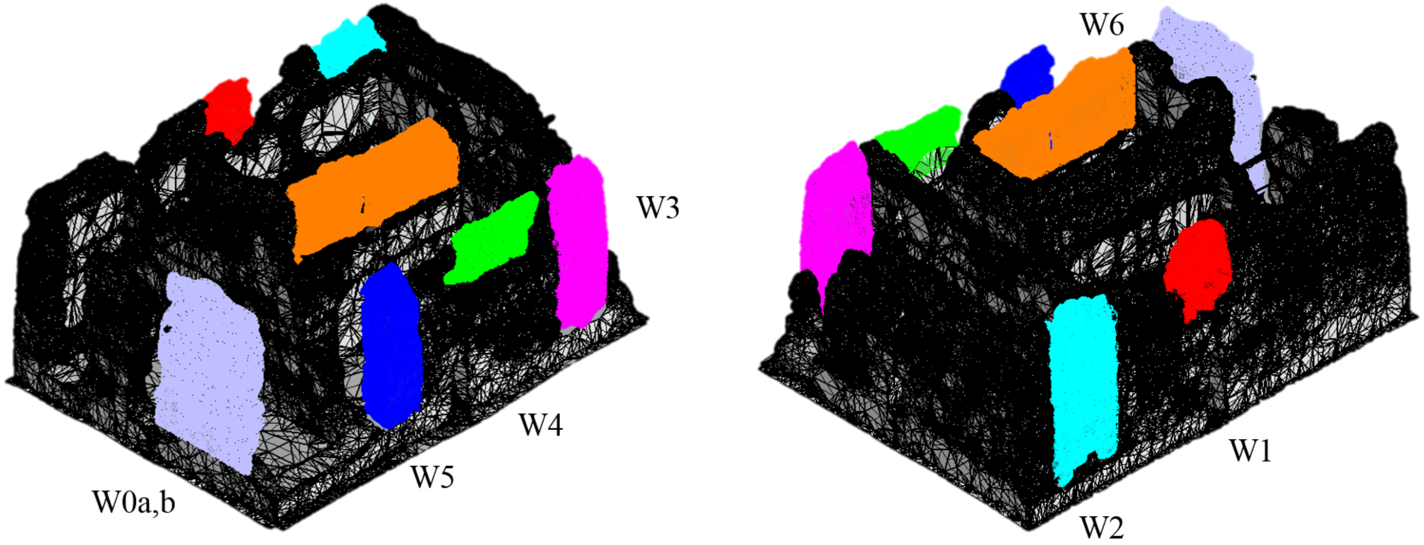

Fig. 8.3 Laser scan of the Great House of the Casa Grande Ruins National Monument (USA), with the different walls/mechanisms highlighted

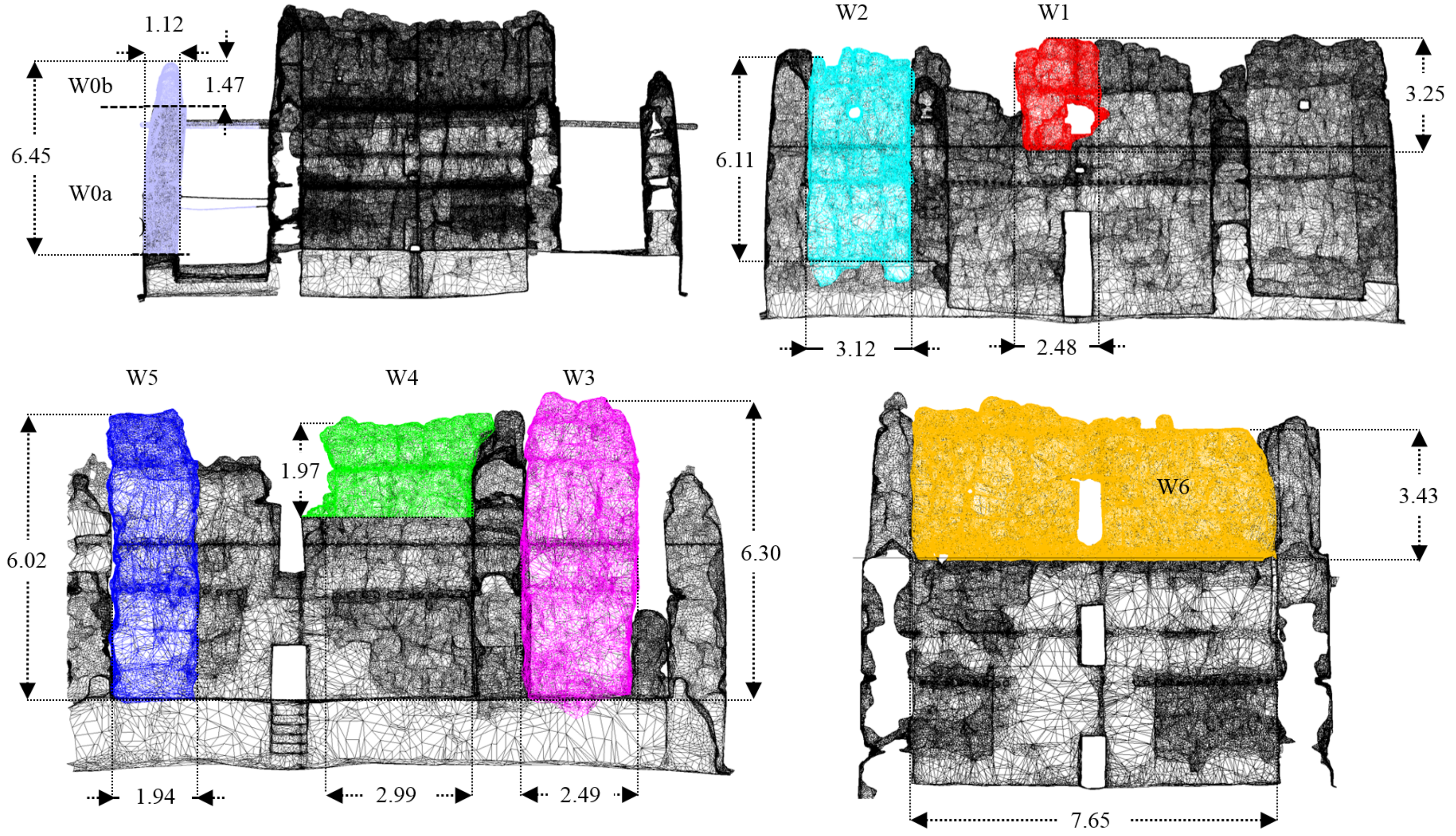

Fig. 8.4 Casa Grande Ruins National Monument (USA) - geometry of the considered mechanisms (all dimensions in m)

8.3.1 Evaluation of critical mechanisms

The rocking parameters computed by the tool were then used to generate the corresponding equations of motion, which were exported to MATLAB to be solved for the pulse response in order to generate overturning plots, as illustrated by Fig. 8.5. As a number of the mechanisms (namely W0b, W1, W4 and W6) take place above ground level, their overturning plots needed to be scaled to account for amplification of the ground motion, using the method outlined in Section 3.4.1. To do this, the natural frequency f_n, modal height h_e and height h at which each mechanism takes place were determined for each of these walls using Lord Rayleigh's principle, and are listed in Table 8.3 (alternatively, if desired, a FEM analysis could also be conducted to estimate the natural frequency). As multiple mechanisms were being compared, the tool automatically determined the critical mechanism for each pulse frequency. Moreover, to illustrate the importance of accounting for ground motion amplification when comparing the relative vulnerability of the different wall sections, both the unscaled (Fig. 8.5a) and scaled (Fig. 8.5b) overturning plots are presented here.

Table 8.3 Parameters used for scaling the overturning plots for the Casa Grande Ruins National Monument

Mechanism	f_n (Hz)	h_e (m)	h (m)
Wall 0b (W0b)	7.72	4.73	4.98
Wall 1 (W1)	6.22	4.66	3.11
Wall 4 (W4)	6.16	4.20	3.76
Wall 6 (W6)	2.50	6.01	4.77

From this comparison it was found that Wall 0a was most likely to overturn for lower pulse frequencies (< 0.6 Hz scaled and < 1.2 Hz unscaled), while Wall 6 was most vulnerable for pulses in the range of 0.6 – 3.0 Hz (scaled) and for pulse frequencies greater than 1.2 Hz (unscaled). This is because larger walls require a lower frequency pulse to overturn. For higher frequency pulses, the smaller walls are more vulnerable even if they are less slender. This was also the case for Wall 0b, which was found to be most susceptible to collapse for frequencies greater than 3.0 Hz - due in part to its relatively small scale, as well as the effect of accounting for ground motion amplification up the structure.

However, this method of analysis assumes that the interface between the walls and the ground is perfectly rigid, that is - infinitely stiff, with an infinite compressive strength, which is not the case in reality. In fact, the finite compressive strength of the material, coupled with the large scale of the walls, may well have resulted in some crushing of the masonry occurring at the base – thus potentially making the results presented here un-conservative. These assumptions will be addressed in Section 8.4.

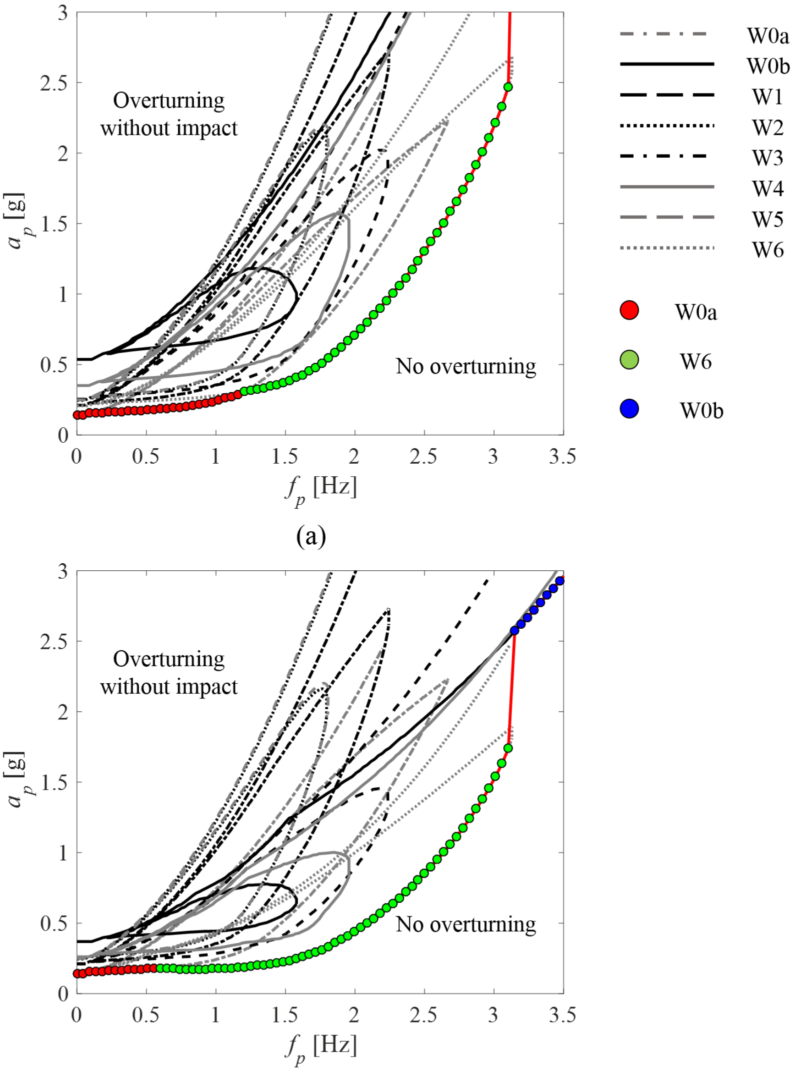

(a)

(b)

Fig. 8.5 Comparison of the overturning plots for the different walls: (a) without and (b) with amplification

8.3.2 Code-based seismic assessment

While the overturning plots provide a good picture of the relative vulnerability of each collapse mechanism, they do not provide a prediction of the maximum response expected for a specific site with a specific seismic hazard. In order to do this, the rocking response of each wall segment was also evaluated using the procedures found in ASCE 43-05 (2007) and the Italian Building Code (DMI, 2008), both of which use linear-elastic response spectra to predict the maximum rocking response of a structure. For the purpose of this assessment, the linear-elastic response spectrum was approximated using the shape of the design spectrum as specified by the International Building Code (International Code Council, 2009), with the parameters used for the definition of this spectrum being listed in Table 8.4.

Table 8.4 Seismic design parameters used for the definition of the response spectrum

Maximum Considered Earthquake (MCE) values:	S_s	0.25 g
	S_1	0.08 g
	T_L	6 s
For Site Class = B, response spectra defined by:	S_{DS}	0.167 g
	S_{D1}	0.053 g

Both code methods use an equivalent linear elastic oscillator to approximate the structure, and calculate an equivalent period in order to determine the spectral demand from the response spectrum. In order to calculate these equivalent periods, both methods require as input the slenderness of the structure α_0 (= λ for the simple single block mechanism), the radius of rotation R_0, and in the case of the ASCE 43-05 method, the rocking frequency parameter p_{eq} - all of which can be readily calculated by the tool and are already listed in Table 8.2 for each of the different walls/mechanisms. However, while the two methods are similar in their use of an approximate equivalent period to determine the spectral demand, their definition of this period is different. While ASCE 43-05 defines the equivalent period by equating the potential energy of the rocking structure to that of the deformed linear oscillator at maximum displacement, the Italian code approximates this period through the calculation of the secant period of the mechanism at 40% of the critical displacement - which in turn is defined as 40% of the collapse displacement of the centre of mass of the structure (DeJong, 2014; Shawa et al., 2012).

The two code methods also differ in their definition of the overturning rotation $\phi_{ov,c}$ - i.e. the rotation upon the exceedance of which the structure is predicted to overturn and collapse. While the Italian code sets the allowable rotation equal to 40% of the analytical (in this case rigid) overturning rotation ϕ_{ov}, the ASCE 43-05 method, due to its cryptic definition of the spectral acceleration capacity $S_{a,CAP}$ (and correspondingly the design spectral displacement $S_{d,CAP}$), specifies an allowable rotation that, depending on the aspect ratio of the structure, is approximately equal to 66% - 75% of the analytical overturning rotation (DeJong, 2014).

The predictions of both code methods are presented in terms of the variation of the peak ground acceleration (PGA) with the maximum rocking angle ϕ as illustrated by Fig. 8.6. Note that to enable comparison between the relative magnitudes of the rotations predicted by the two methods, in both plots ϕ is expressed as a fraction of the analytical overturning rotation ϕ_{ov}. In the case of the single rocking block mechanism with a rigid interface, this overturning rotation is equal to the slenderness α_0 of the wall under consideration, that is, $\phi_{ov} = \alpha_0$. The PGAs required to cause overturning of each of the walls can then be extracted directly from these plots, and are listed in Table 8.6 for both code methods. In the case of the Italian code, this is simply done by determining the PGA for $\phi_{ov,c}/\phi_{ov} = 0.4$ for each of the different walls, while in the case of the ASCE 43-05 procedure, the ratio of $\phi_{ov,c}/\phi_{ov}$ corresponding to the overturning displacement first needed to be determined and is listed in Table 8.5 for each of the different walls/mechanisms.

From Fig. 8.6 and Table 8.6 it can be seen that both the ASCE 43-05 method and the Italian code predict the same relative resilience of the different wall sections - namely that Walls 0a and 6 are most vulnerable to collapse, while Walls 0b, 2 and 5 are least vulnerable. However, a more detailed comparison of the predictions of the two methods reveals that the Italian code is generally more conservative than its ASCE 43-05 counterpart. This is further evidenced by a comparison of the predictions of the two methods for Wall 0a (Fig. 8.7) from which it can be seen that for nearly all considered levels of PGA, ASCE 43-05 consistently predicts smaller rotations of the structure than the Italian code. Such behaviour is likely because the Italian Code was more directly derived to deal with collapse mechanisms in ageing buildings, while ASCE 43-05 was not. However, given that the PGA of the site is 0.10g (International Code Council, 2009), it can be seen that rocking is unlikely to initiate (and thus overturning unlikely to occur) for any of the collapse mechanisms considered.

A qualitative comparison between the results of the overturning plots (Fig. 8.5) and those obtained from the two code-based procedures (Fig. 8.6) reveals a generally good agreement between the three sets of results in terms of the relative resilience of the collapse mechanisms. All three plots predict a greater resistance to collapse (larger PGAs required) for wall segments 2 and 5 while wall segments 0a and 6 are found to be most vulnerable to failure. The main exception is Wall 0b - while both code methods predict the largest resistance to overturning for this wall segment, the overturning plots indicate that it is most vulnerable to collapse for higher frequency pulses, due in part to accounting for the effects of ground motion amplification in the structure.

Wall 0b notwithstanding, the predictions of the code-based methods are generally more conservative than the overturning plots (especially in the higher frequency range), while for the lower frequency (longer period) pulses it can be seen that the code-based procedures actually tend to overestimate the dynamic resistance of the walls and are thus un-conservative.

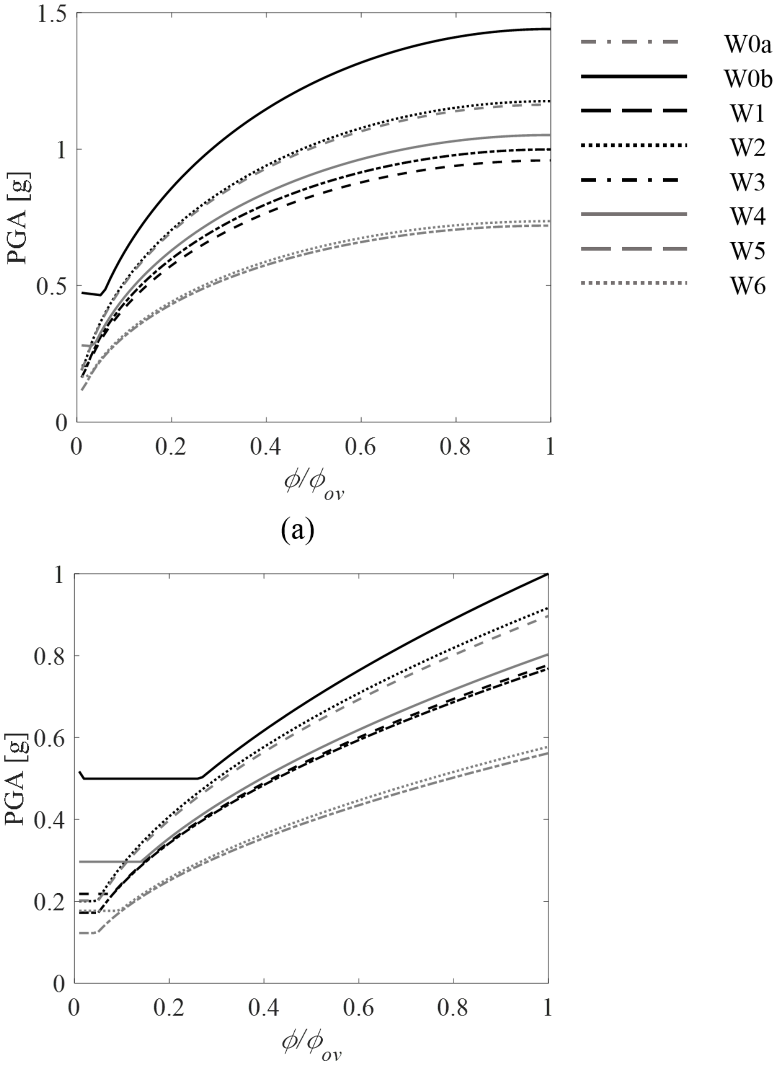

(a)

(b)

Fig. 8.6 Variation of the maximum rocking rotation ϕ (normalized by the analytical overturning rotation ϕ_{ov}) with PGA for the different wall sections, as derived by the (a) ASCE 43-05 procedure and (b) the Italian Building Code

8.4 Seismic analysis using the flexible interface model

In the second set of analyses, the critical mechanisms identified by the rigid rocking tool in Section 8.3 were analysed in more detail using the flexible interface model as developed in Chapter 6, in order to evaluate the influence of crushing on the seismic resilience of the walls. A code-based seismic assessment was also conducted using this model, in order to demonstrate how the new flexible interface formulations can be feasibly implemented within codes of practice.

Table 8.5 Rotation predicted by ASCE 43-05 to cause collapse ($\phi_{ov,c}$) normalized by the analytical overturning rotation (ϕ_{ov})

Mechanism	$\phi_{ov,c}/\phi_{ov}$
Wall 0a (W0a)	0.69
Wall 0b (W0b)	0.86
Wall 1 (W1)	0.64
Wall 2 (W2)	0.69
Wall 3 (W3)	0.71
Wall 4 (W4)	0.72
Wall 5 (W5)	0.71
Wall 6 (W6)	0.68

Table 8.6 PGAs predicted to cause overturning by the ASCE 43-05 and Italian Building Code methods

Mechanism	PGA [g]	
	ASCE 43-05	Italian Building Code
Wall 0a (W0a)	0.68	0.35
Wall 0b (W0b)	1.43	0.62
Wall 1 (W1)	0.89	0.49
Wall 2 (W2)	1.12	0.58
Wall 3 (W3)	0.96	0.48
Wall 4 (W4)	1.01	0.50
Wall 5 (W5)	1.11	0.56
Wall 6 (W6)	0.70	0.36

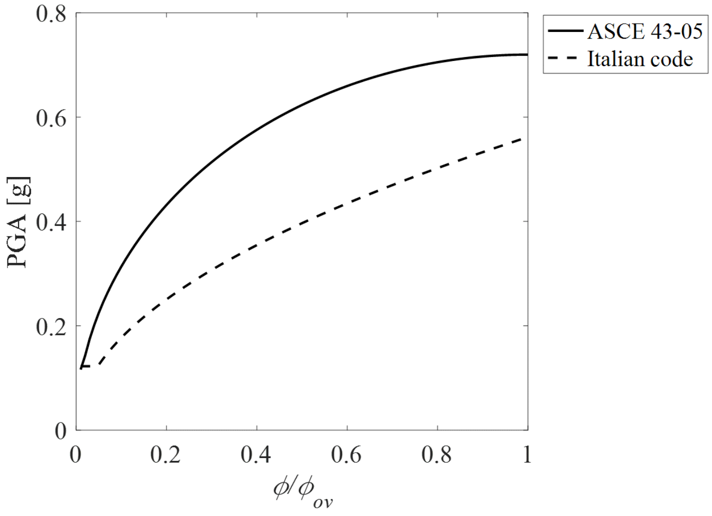

Fig. 8.7 Comparison of the variation of maximum rocking rotation ϕ with PGA for Wall 0a, as derived by ASCE 43-05 and the Italian Building Code

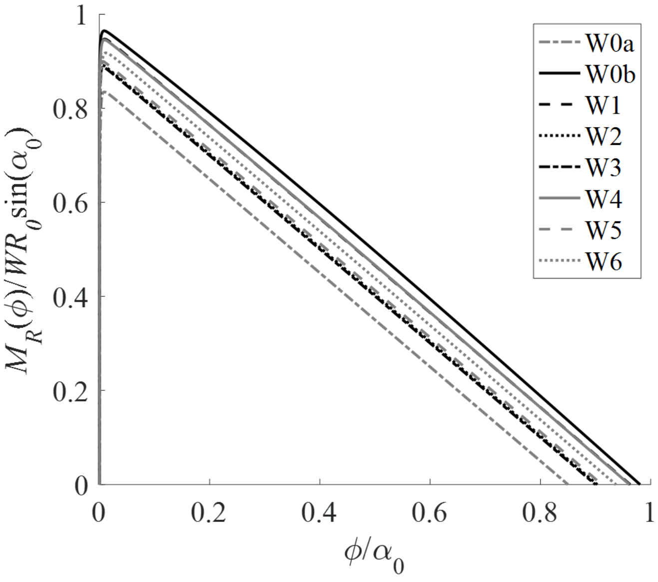

Fig. 8.8 Moment-rotation curves generated for the different wall sections

8.4.1 Evaluation of critical mechanisms

The effect of crushing on the dynamic resistance of the different wall sections was first evaluated by using the expressions derived for the shifting hinge location $a_f(\phi)$ in Chapter 6, in conjunction with Equation 7.1, to generate moment-rotation curves for the different walls/mechanisms. The interfaces for all the walls were approximated as solid rectangular cross-sections, characterised by a compressive strength f_m = 1.00 MPa (Table 8.1), while the stiffness of each interface was calculated by dividing the Young's modulus E of caliche (Table 8.1) by the average thickness of a single course of the material - determined to be 0.69 m - leading to an approximate stiffness k_n = 10.0 GPa/m.

The moment-rotation curves generated for each of the walls (normalized by the maximum rigid restoring moment $WR_0\sin(\alpha_0)$) can be found in Fig. 8.8. From this figure it can be seen that due to the high stiffness and low compressive strength of the caliche, all the wall segments experience crushing fairly rapidly, with Wall 0a exhibiting the greatest relative reduction in dynamic capacity (as compared to the rigid model). In fact, the full height wall segments (namely Walls 0a, 2, 3 and 5) generally exhibit a greater reduction in dynamic capacity - which is to be expected, as due to their larger scale, crushing effects are more likely to play a role in the reduction of their seismic resistance. Note that in this plot, the curves for Walls 2 and 3 are overlapping, as are the curves for Walls 1 and 4.

To further investigate the influence of crushing on reduction in dynamic capacity, a more detailed analysis was conducted into the response of the two most critical wall sections as identified by the tool in Section 8.3 - namely Walls 0a and 6. The response of these walls to pulse-type excitations was investigated by solving Equation 6.54 for pulses of varying frequency f_p and amplitude a_p, and the results of these analyses are presented in Fig. 8.9, with crosses ($\times$) being used to represent cases in

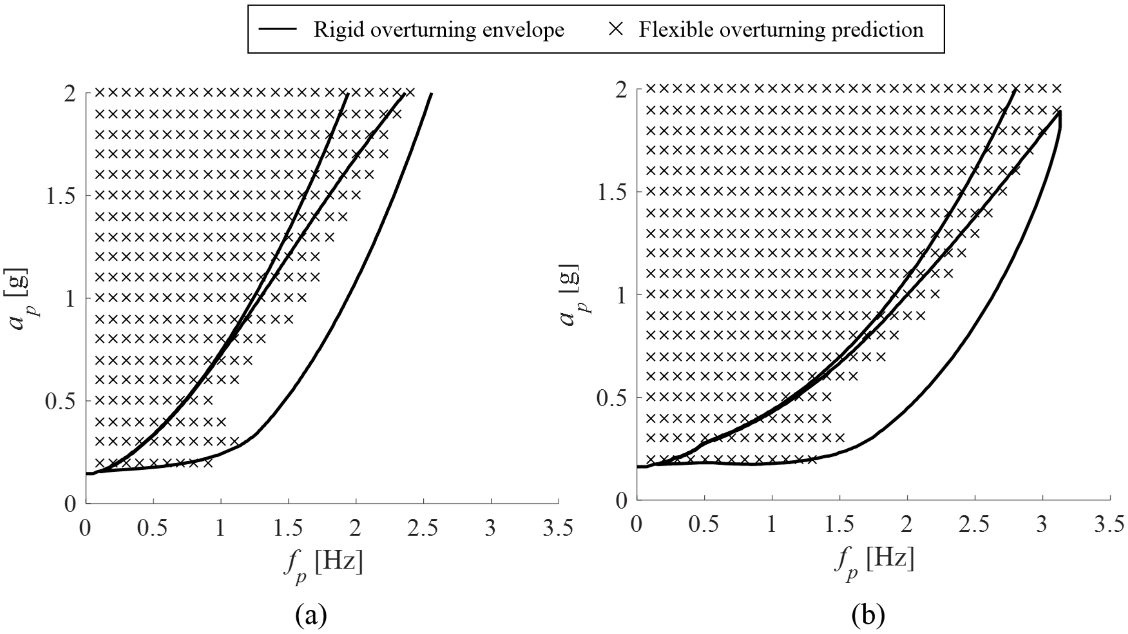

Fig. 8.9 Comparison of the rigid and flexible overturning spectra for: (a) Wall 0a and (b) Wall 6

which the walls were found to overturn and collapse. Furthermore, to facilitate comparison with the predictions of the rigid model, the overturning envelopes generated for the walls in Section 8.3 were also superimposed onto the overturning spectra in Fig. 8.9.

As Fig. 8.9 illustrates, for both wall sections, the two models compare fairly well for low-frequency pulses ($f_p \leq 1$ and 1.5 Hz for W0a and W6 respectively). However, for higher frequency pulses, the rigid model tends to underestimate the pulse amplitude required to cause overturning without impact, while over-estimating the pulse frequencies capable of causing collapse after a single impact. These discrepancies are particularly predominant in the case of Wall 0a, due in part to the greater reduction in dynamic capacity of this mechanism because of crushing effects at the interface.

In addition to single sinusoidal pulses, the performance of the two mechanisms when subjected to a full earthquake ground motion record was also compared - using in this case the ground motion recorded during the 1940 El Centro earthquake (Fig. 8.10a). As the mechanism for Wall 6 takes place at a height above ground level, amplification effects also needed to be accounted for, and this was done by calculating an appropriate scale factor for the ground motion, using the methodology outlined in Section 3.4.1. In addition to f_n, h_e and h, which had already been computed for the scaling of the overturning plots in Section 8.3 (Table 8.3), the spectral acceleration S_a at the natural period T_n of the wall also needed to be determined - as indicated by the red dot in Fig. 8.10b. Using Equation 3.48, the scale factor was then calculated, and was found to be 2.0 for this mechanism. Note that as the mechanism for Wall 0a takes places approximately at ground level, no scaling was applied to the ground motion for this mechanism.

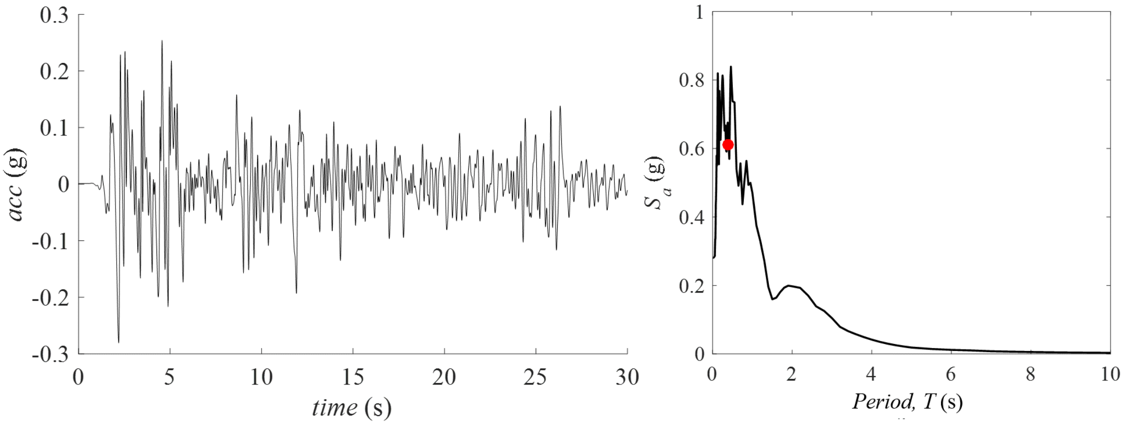

(a) (b)

Fig. 8.10 1940 El Centro earthquake: (a) input ground motion (unscaled) and (b) elastic acceleration response spectra (5% damping)

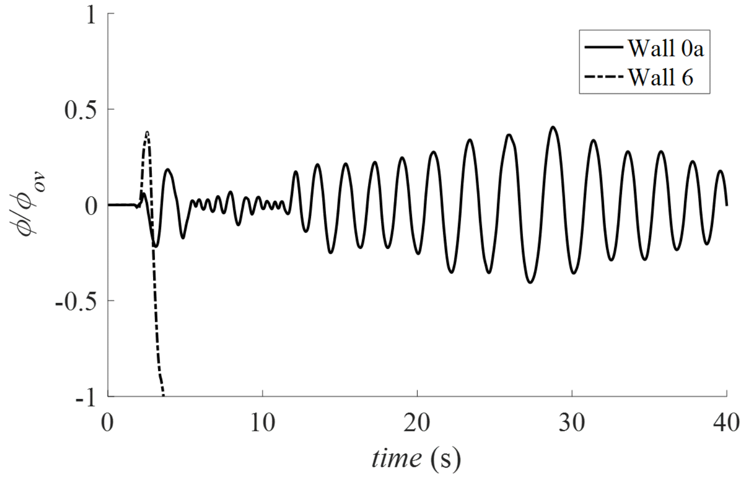

Fig. 8.11 Predicted response of Walls 0a and 6 to the 1940 El Centro ground motion

The response of the two walls upon being subjected to the appropriately-scaled ground motion can be found in Fig. 8.11. As the results of the time-history analyses indicate, due to the large level of scaling applied to the ground motion for Wall 6, this structure was found to collapse, while Wall 0a - despite undergoing relatively large rotations, was eventually observed to return to equilibrium. This also corresponds well with the results of the overturning spectra (Fig. 8.9), as for the range of pulse frequencies and amplitudes considered, Wall 6 was generally found to be more susceptible to collapse than Wall 0a.

8.4.2 Code-based seismic assessment

The new flexible interface model (with crushing effects included as in Section 8.4.1) was also implemented within code-based seismic assessment procedures - specifically the response spectra procedure outlined in ASCE 43-05 and the Italian Building Code, as well as the response-history analysis method prescribed by ASCE 43-05.

In the case of the response spectra procedure, the equivalent periods of the mechanisms are now determined using $R(\phi)$, $\alpha(\phi)$ and in the case of the ASCE 43-05 method, $p_{eq}(\phi)$ (as opposed to R_0, α_0 and p_{eq} as in the rigid case), which change magnitude based on the rotation ϕ of the structure (and consequently based on the shifting hinge location $a_f(\phi)$). The predictions of these code-based methods using the new interface model can be found in Fig. 8.12.

While the flexible interface model with a finite compressive strength (i.e. crushing effects) generally predicts a very similar relative dynamic resilience of the walls as its rigid counterpart, there is however, a marked reduction in the actual dynamic capacity of the different mechanisms - as illustrated by a comparison of the PGAs predicted to cause overturning by both models (Table 8.7, determined following the same procedure as in Section 8.3.2). From this comparison it can be seen that for all considered wall mechanisms, the flexible model with crushing effects consistently requires a smaller PGA for collapse to occur. Furthermore, the reduction in PGA is more significant in the case of the full-height wall segments (W0a, W2, W3 and W5) due to the greater effect of crushing at their bases. This observation is reiterated by comparing the rigid and flexible interface predictions for Walls 0a and 6 (i.e. the two critical wall segments) as derived by the Italian Building Code method. As Fig. 8.13 illustrates, while the PGAs predicted to cause the same rocking rotation by the flexible models are consistently lower than their rigid counterparts, the difference between the two is more pronounced in the case of Wall 0a (i.e. the full-height wall segment) than Wall 6.

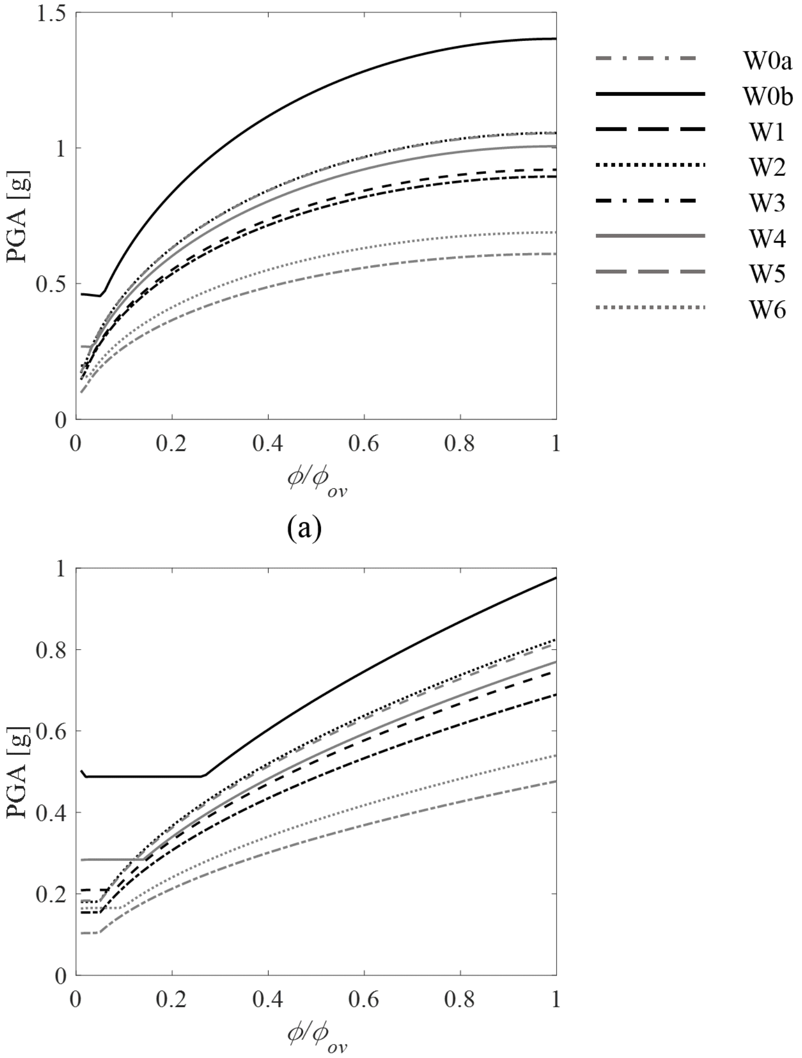

(a)

(b)

Fig. 8.12 Comparison of the maximum predicted rocking rotation ϕ (normalized by the overturning rotation ϕ_{ov}) with PGA for the flexible interface model with crushing effects, as derived by the (a) ASCE 43-05 procedure and (b) the Italian Building Code

Table 8.7 Comparison of the PGAs predicted to cause overturning by the code-based methods for the rigid and flexible (with crushing) interface models

Mechanism	PGA [g]			
	ASCE 43-05		Italian Building Code	
	Rigid	Flexible	Rigid	Flexible
Wall 0a (W0a)	0.68	0.58	0.35	0.30
Wall 0b (W0b)	1.43	1.39	0.62	0.60
Wall 1 (W1)	0.89	0.86	0.49	0.47
Wall 2 (W2)	1.12	1.00	0.58	0.52
Wall 3 (W3)	0.96	0.86	0.48	0.43
Wall 4 (W4)	1.01	0.97	0.50	0.48
Wall 5 (W5)	1.11	1.01	0.56	0.51
Wall 6 (W6)	0.70	0.65	0.36	0.34

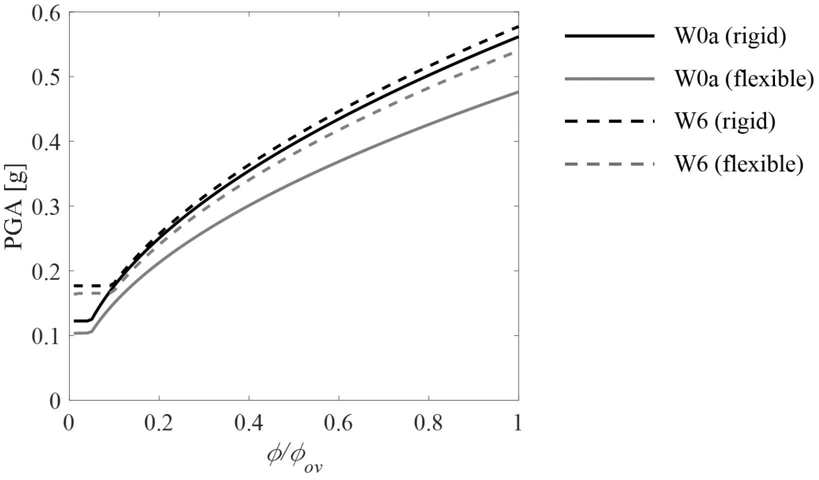

Fig. 8.13 Comparison of the rigid and flexible (with crushing) interface models, in terms of the variation of the maximum predicted rocking rotation ϕ (normalized by the overturning rotation ϕ_{ov}) with PGA, as derived by the Italian Building Code

The flexible interface model with crushing was also used to conduct a code-based response-history analysis, following the procedure outlined in ASCE 43-05. In order to do this, five earthquake ground motion records were selected from the PEER NGA database (PEER, 2014), and were scaled in order to match the target spectrum for the site. This target spectrum has the same shape as the design spectrum from Section 8.3, but is now scaled to 0.10g, in order to match the PGA of the site. The selected records had the smallest mean squared errors (MSE) of all the records in the database, as compared to the target spectrum, and are listed in Table 8.8, while their corresponding response spectra can be found in Fig. 8.14a. Note that the PGAs listed in Table 8.8 are those measured after

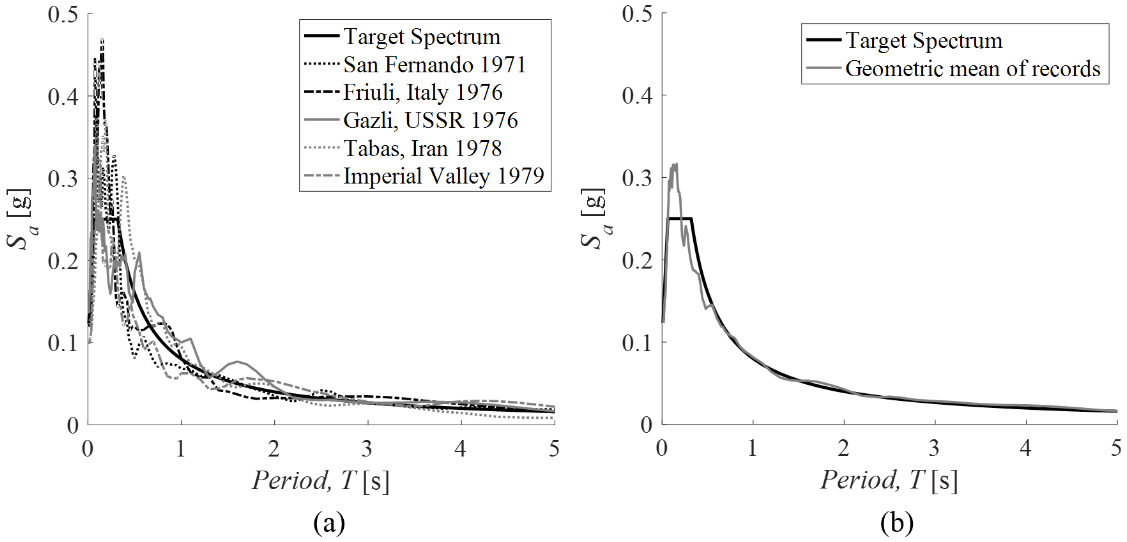

Fig. 8.14 Target spectrum for the site with: (a) the scaled response spectra of the selected earthquakes and (b) the geometric mean of the scaled earthquake records

the scaling of the ground motion records. Furthermore, the geometric mean of these five records is plotted in Fig. 8.14b, which compares reasonably well with the target spectrum of the site.

Table 8.8 Earthquake ground motion records selected for analysis from the PEER NGA database

Earthquake Event	NGA ID	Magnitude	MSE	Scale Factor	PGA [g]
San Fernando 1971	92	6.61	0.063	2.86	0.08
Friuli, Italy 1976	121	6.50	0.102	3.37	0.10
Gazli, USSR 1976	126	6.80	0.083	0.11	0.08
Tabas, Iran 1978	139	7.35	0.084	0.23	0.07
Imperial Valley 1979	172	6.53	0.084	0.50	0.07

The scaled ground motion records were then used to conduct a full time-history analysis of the two critical wall segments (Walls 0a and 6). Moreover in the case of Wall 6, Equation 3.48 was used to compute the additional scale factors required to account for amplification of ground motion up the structure, and these are listed in Table 8.9 for each of the different earthquake records.

However, this method of simply applying a scale factor to the entire ground motion to account for amplification effects is an approximation. In reality the structure would filter the motion, resulting in a change in frequency content between the base of the structure and the bottom of the mechanism. One method to better capture this change in frequency content would be to use a single-degree-of-freedom oscillator with a frequency corresponding to the natural frequency of the structure under consideration, to calculate the response at different heights along the structure. This response could then be used as input at the base of the mechanism. However, in order for this method to be effective, the natural frequency of the structure needs to be determined accurately. Thus for the purpose of this analysis, the ground motion was simply scaled up using Equation 3.48 and the change in frequency content ignored - as this is sensitive to the natural frequency of the structure, which is challenging to calculate accurately without a detailed finite element model.

Table 8.9 Scale factors computed by Equation 3.48 for Wall 6, for the selected ground motion records

Earthquake Event	Scale Factor
San Fernando 1971	1.4
Friuli, Italy 1976	1.1
Gazli, USSR 1976	1.6
Tabas, Iran 1978	1.8
Imperial Valley 1979	1.4

The "best-estimate" of the rocking demand using the response-history method is the average of the maximum predicted rocking response from all five simulations. The results of these analyses (normalised by the analytical overturning rotation ϕ_{ov}) are presented in Table 8.10 for the two walls, for different levels of scaling of the target spectrum. Furthermore, to facilitate comparison of the predictions of the time-history analyses with those obtained using the response spectra procedures, the results of those analyses are also listed in Table 8.10, along with the code-based allowable rotations for each of the different methods. Note that for the time-history method, the allowable rotation is determined by simply applying a safety factor of 2 to the analytical overturning rotation.

Table 8.10 Comparison of the predictions of the different code-based methods for the maximum rocking response of the critical wall segments

Method	Wall 0a : ϕ/ϕ_{ov}			$\phi_{ov,c}/\phi_{ov}$
	PGA = 0.10g	PGA = 0.20g	PGA = 0.30g	
ASCE 43-05 (response spectra)	0.010	0.060	0.130	0.689
Italian code (response spectra)	0.010	0.175	0.400	0.400
ASCE 43-05 (time-history)	0.014	0.058	0.173	0.500
Method	Wall 6 : ϕ/ϕ_{ov}			$\phi_{ov,c}/\phi_{ov}$
	PGA = 0.10g	PGA = 0.20g	PGA = 0.30g	
ASCE 43-05 (response spectra)	N/A	0.045	0.100	0.682
Italian code (response spectra)	N/A	0.140	0.310	0.400
ASCE 43-05 (time-history)	0.002	0.052	0.235	0.500

From this comparison it can be seen that for Wall 0a, the predictions of the time-history simulations compare reasonably well with those obtained using the ASCE 43-05 response spectra procedure for all considered levels of scaling of the PGA. The predicted rotations are also considerably smaller than the analytical overturning rotation (at most ϕ/ϕ_{ov} = 0.17) as well as the code-based allowable rotation (at most $\phi/\phi_{ov,c}$ = 0.35). The Italian code, on the other hand, yields far more conservative predictions, and in the case of the PGA of 0.30g even predicts overturning of the structure.

In the case of Wall 6, the time-history simulations consistently yield more conservative predictions than the ASCE 43-05 response spectra method. In the case of the PGA of 0.30g in particular, the response obtained using time-history analyses was considerably larger than the rotation predicted by the response spectra method. This is due to the effect of rocking amplification in the case of the Gazli, USSR ground motion record, which predicted a maximum rotation for the structure which was almost three times as high as the other records - thus skewing the average. However, these rotations are still smaller than the code-based allowable rotations, as well as the rotations predicted by the Italian code - with the exception of the PGA of 0.10g, where the Italian code predicted no response at all.

8.5 Summary

In this chapter, the computational tool was used to conduct a seismic vulnerability analysis of the Great House of the Casa Grande Ruins National Monument, USA. Through this analysis, the ability of the tool to integrate complicated geometry obtained from laser scan data with the dynamic analysis of rocking mechanisms was demonstrated. The capacity of the detailed wall geometries to resist overturning due to earthquake loading was quantified using both rocking dynamics theory as well as a variety of code-based methods, for both the rigid and flexible interface models, while the most vulnerable portions of the structure were also identified. The main findings from these investigations are summarised below:

- A comparison of the overturning plots generated for the structure using the rigid rocking tool indicated that Walls 0a and 6 are most vulnerable to collapse. These observations were corroborated by the results of the code-based methods, which also predicted the highest vulnerabilities for these two wall segments.

- In fact, a qualitative comparison between the results of the overturning plots and those obtained from the two code-based procedures revealed a generally good agreement between the three sets of results in terms of the relative resilience of the different collapse mechanisms. However, while the predictions of the code-based methods are generally more conservative than the overturning plots (especially in the higher frequency range), for the lower frequency (longer period) pulses it can be seen that the code-based procedures actually tend to overestimate the dynamic resistance of the walls and are thus un-conservative.

- The introduction of the flexible interface model with crushing effects generally reduces the dynamic resistance of the walls. In the case of the overturning plots, the introduction of a flexible interface with a finite compressive strength generally led to a reduction in the pulse amplitude required to cause overturning without impact, while also decreasing the range of pulse frequencies capable of causing single-impact overturning. Similarly in the case of the code-based response spectra methods, the flexible interface model generally decreased the PGA predicted to cause overturning of the walls - with this effect being more pronounced in the case of the larger-scale full height walls, due to the greater influence of crushing effects at their bases.

- A comparison of predictions of the ASCE 43-05 procedure and those of the Italian Building Code (Table 8.7) shows that, for both the rigid and flexible interface models, the procedure outlined in the Italian code is generally more conservative than its ASCE 43-05 counterpart. This is likely because the Italian Code is more directly derived to deal with collapse mechanisms in ageing buildings.
- Furthermore, a comparison of the predictions of the ASCE 43-05 response spectra and time-history methods also revealed a reasonably good correlation between both sets of results.
- Given that the PGA of the site is 0.10g, rocking is unlikely to initiate (for the rigid models), and thus overturning unlikely to occur (for both rigid and flexible models) for any of the collapse mechanisms considered. Thus using any of the analytical methods that are currently available, none of the walls are in danger of collapse as a result of overturning.

Chapter 9

Conclusions

9.1 Summary of findings

This research has two main objectives: (1) To develop a simple computational modelling tool to rapidly predict critical mechanisms and dynamic collapse of any user-defined structural geometry, and (2) to develop a new interface formulation to more realistically model the influence of interface stiffness and crushing (i.e. material damage) on the dynamic response of masonry structures - which can also be implemented within the framework of the tool.

Starting with a digital drawing of a user-defined structural geometry in Rhino (a typical CAD software), the tool calculates the equivalent rocking parameters defining a range of different collapse mechanisms, which are then exported to MATLAB where either rocking dynamics can be used to derive and solve the relevant equations of motion, or, depending on the purpose of the analysis, a code-based seismic assessment can be conducted instead. Furthermore, to better capture the dynamic behaviour of real-world structures, a new formulation is proposed to account for ground motion amplification effects. In the case of the flexible interfaces with a finite compressive strength (i.e. crushing effects), expressions are also derived to account for the inward-shift of the rocking rotation points, which in turn are used to re-derive the rocking equations of motion for the different mechanisms. The tool is then used for the seismic analysis of a number of case-studies, comprising masonry structures of varying scales and typologies. The main findings from these investigations are as follows:

- **Complex geometries and mechanisms**: The ability of the tool to model complex structural geometries was demonstrated through its application to the seismic analysis of a number of structures reconstructed using point cloud data from the laser scanner - including a temple and tower damaged during the 2015 Gorkha earthquake, as well as the walls of a historic earthen structure, while its capacity for modelling complex mechanisms as well as the beneficial influence of reinforcement was demonstrated through its application to the analysis of a typical Italian church.

- **Time-history analyses**: A comparison of the time-history predictions of the tool with the results of experimental shaking table tests revealed a generally good correlation between both sets of results - however, this correlation is influenced by the selection of appropriate mechanisms for analysis, which depend in turn upon user experience and engineering judgement. Similarly in the case of the monuments damaged during the 2015 Gorkha earthquake, a comparison of the predictions of the analytical model with the results of numerical simulations in 3DEC showed the tool to be capable of adequately reproducing two-dimensional collapse, but inherently limited when it came to capturing more complex three-dimensional rocking response.
- **Overturning plots**: In the case of seismic analyses involving multiple different structures and/or mechanisms, the overturning plots generated by the tool were found to be an effective means of comparing the relative dynamic resilience of different collapse mechanisms, with the tool's ability to identify the most vulnerable mechanisms for each pulse frequency also being demonstrated. These plots also enabled investigations to be conducted into the influence of slenderness and scale on the rocking stability of the structures. While slenderness was generally found to control the point at which rocking initiates (for the rigid interface model), as well as the minimum acceleration required for extremely long-period pulses to cause overturning, the magnitude of rotation, and consequently collapse, is dependent upon the scale of the structure, with smaller structures generally being more susceptible to collapse.
- **Ground motion amplification**: Ground motion amplification was found to play a significant role in the reduction of the dynamic capacity of collapse mechanisms which took place at a height above ground level. When applied to full time-history analyses, as in the case of the analysis of the two columns damaged during the 2015 Gorkha earthquake, accounting for amplification effects resulted in the predictions of the tool comparing fairly well with the field observations. Similarly, in the case of the seismic analysis of the Italian church, taking these effects into consideration through the scaling of the overturning plots was observed to generally reduce the minimum pulse amplitude required for overturning to occur, and in some cases even change the relative vulnerabilities of the different collapse mechanisms.
- **Interface flexibility and crushing**: Modelling interfaces as flexible (as opposed to rigid) tends to reduce the dynamic resistance of the structure due to the inward-shift of the rocking rotation points. However, the extent of this reduction in dynamic capacity depends on several factors, which can broadly be divided into properties of the interface - such as the interface geometry, stiffness and compressive strength, and properties of the structure - such as density, scale and overburden loads. In general, structures with rectangular interfaces are more resistant to overturning than their circular counterparts, while hollow structures are more resistant to collapse than solid structures. Furthermore, increasing the interface stiffness for a given structure consistently increases the seismic resistance, while increasing compressive strength only increases the dynamic capacity to a certain threshold - beyond which the behaviour of the

interface remains entirely elastic and the structure does not experience crushing at all. However, increasing the overburden force (in the case of the two block mechanism) yields mixed results - while an increase in overburden load leads to an increase in the effective stiffness of the system, it also causes crushing, which tends to counteract the beneficial influence of the force. The importance of considering crushing effects was further highlighted through the case-study of the tower damaged during the 2015 Gorkha earthquake - while the rigid interface model predicted very small rotations of the tower, the inclusion of a flexible interface with a finite compressive strength resulted in overturning of the structure as was observed in reality. Finally, a comparison of the predictions of the new models for the more complex multiple block mechanisms with the results obtained using discrete element modelling (DEM) in 3DEC, revealed a generally good correlation between both sets of results for all considered levels of interface stiffness - thus providing confidence in these new analytical formulations.

- **Semi-flexible interface model**: Proposed as a simplified alternative to the fully-flexible interface models, the semi-flexible interface models were found to be capable of adequately reproducing the dynamic response of the fully-flexible models for both free-rocking as well as full time-histories, for all considered mechanisms.

- **Comparison of rocking dynamics and code-based assessment procedures**: A generally good correlation was observed between the predictions of the overturning plots (obtained using rocking dynamics) and those of the code-based procedures, in terms of the relative resilience of the different collapse mechanisms. However, in the higher frequency range the code-based methods tend to yield more conservative predictions than the overturning plots, while in the lower frequency range they tend to over-estimate dynamic resistance and are thus un-conservative.

9.2 Scientific contributions

As the findings in Section 9.1 demonstrate, the two main objectives of the research have been met. Namely, (1) a computational modelling tool, capable rapidly comparing different mechanisms and modelling complex structural geometries was developed and (2) a new formulation to model the influence of interface stiffness and crushing was proposed. More specifically, the new contributions of this research include:

- **Derivation of rocking equations of motion for user-defined structural geometries**: The tool's implementation in Rhino enables the rocking equations of motion to be derived for any user-defined structural geometry, thus making the tool particularly useful for the analysis of structures with irregular geometries such as statues and temples, or walls which have suffered from substantial section losses due to decay and degradation.

- **Extension of the procedure to account for ground motion amplification effects**: This extension of Priestley's (1985) approach accounts for the effect of ground motion amplification in both the overturning plots as well as the full time-history analyses (through the calculation of an appropriate scale factor for the input ground motion), thereby making it possible to effectively represent the reduction in dynamic capacity of collapse mechanisms which take place at a significant height above ground level - albeit in an approximate manner.
- **Development of a methodology for rapid comparison and identification of vulnerable collapse mechanisms**: Through the use of overturning plots, the tool makes it possible to rapidly compare the relative dynamic resilience of different collapse mechanisms. Furthermore, the methodology developed in MATLAB also enables automatic detection of the most vulnerable mechanism for each pulse frequency.
- **Derivation of expressions for the inward-shift of rocking rotation points due to the presence of flexible interfaces, for different interface geometries**: This extension builds on the approach originally proposed by Costa (2012) for the single rocking block - which accounts for the inward-shift of the rocking rotation point due to the presence of a flexible interface with a finite compressive strength (i.e. crushing) - to derive similar expressions for more complex geometries such as hollow rectangular, solid circular and hollow circular interfaces - as are found in many real-world masonry structures.
- **Re-derivation of the rocking equations of motion to account for the influence of flexible interfaces**: Starting from Lagrange's equation, the rocking equation of motion is re-derived for the single, two and multiple block mechanisms in order to account for the presence of flexible interfaces with crushing effects. Comparison with the results of numerical (DEM) simulations and field observations provides confidence in these new analytical models.
- **Development of a semi-flexible interface model**: To reduce computational burden, an alternative to the flexible interface model is proposed, which captures the inward-shift of the rocking rotation points in a more simplified/approximate manner than its fully-flexible counterpart. This model is also used to re-derive the coefficient of restitution as well as the relationship between the relative rotations of the blocks, for the different mechanisms.

9.3 Practical applications

The tool has the potential to be extremely useful in European countries, which have an abundance of cultural heritage vulnerable to seismic action. Furthermore, the use of a CAD model of the structure as input - which most engineers will most-likely already have - eliminates the need to generate a new model for analysis, which can be labour-intensive and time-consuming. In fact, the tool requires the exact same input as the analyses that engineers are doing every day, but provides a much more appropriate result by accounting more directly for dynamic effects.

Furthermore, by making it open-source, easy to use and computationally-inexpensive, the tool could be especially useful to engineers in developing countries such as India, Nepal and Pakistan, which are highly seismic zones with limited funding for protection of built heritage and which consequently tend to suffer a disproportionately large number of casualties during earthquakes.

9.4 Future research

While the proof-of-concept of the computational tool has been demonstrated, significant new theoretical and computational developments are required before it can be disseminated for practical use. Specifically these include:

- **Development of a new software platform in Python**: At present, the equivalent rocking parameters extracted by the scripts in Rhino are written to a text file for export to MATLAB where they are then used to generate and solve the corresponding equation of motion for the mechanism. While such an approach serves its purpose, it is primitive and cumbersome when dealing with multiple and different mechanisms – especially in the case of parametric studies or when solving iteratively to determine critical mechanisms. Instead, Python (Python Software Foundation, 2016) could be used to interface directly with the CAD-software (initially with Rhino, with the future aim to generalise to other CAD platforms), while the reliance on MATLAB could also be eliminated. To achieve this, the scripts that are currently written in Rhino and MATLAB would need to be converted to equivalent Python scripts. In the case of the scripts in Rhino, this could be done by selective use of RhinoScriptSyntax in Python, while for the MATLAB scripts SciPy and NumPy (Jones et al., 2001; Van Der Walt et al., 2011) could be used instead.

- **Automatic generation of collapse mechanisms**: Thus far, the tool has been limited to user-defined collapse mechanisms, which is tedious, and requires special expertise and experience from the user. Thus to make to tool more useful in practice, it should automatically define different mechanisms, based on the presence of certain macro-elements within the structure, and determine the most vulnerable one(s). Specifically, this would require automatic detection of typical structural elements (such as vaults, walls etc.) in the CAD geometry, followed by an iterative (trial and error) process to determine critical mechanisms for the given structure. In the case of structural elements such as vaults, new equations of motion would also need to be derived to model their more complicated 3D collapse mechanisms. Once this procedure is completed, an extensive number of example structures (and example components of structures) could be modelled using the tool, and critical collapse mechanisms determined using this process. These results could then be used as a training set to optimise the automatic definition of important collapse mechanisms within a given geometry, to limit computational burden.

- **Integration of the tool with other computational analysis programs**: In order to enable practical application of the tool, it is important to more accurately account for dynamic amplification effects, which depends in turn upon the accurate determination of the natural frequencies of the structure. One way of doing this would be to link the tool with an open-source finite element analysis (FEA) package (e.g. OpenSees). While FEA is not efficient in modelling complex collapse states involving large displacements and loss of contact at element interfaces, it is very effective in solving eigenvalue problems. Thus, FEA could be used in the background to automatically determine the natural frequencies of the structure, and thus more accurately model collapse towards the top of the structure (i.e. towers, chimneys, upper floor walls).

- **Development of a new theoretical framework to realistically model accumulated damage**: At present, analytical expressions have been derived for the inward-shift of rotation points due to the presence of flexible interfaces and crushing (i.e. material damage). However, no methodology currently exists to account for the accumulation of damage during an earthquake. Thus there is a need to develop a new algorithm to solve the equations of motion to account for damage accumulation due to crushing effects in previous cycles of the motion. This could be done through the development of a new constitutive model to capture the non-linear behaviour of the interfaces, including the effects of cyclic loading.

- **Retrofit optimisation**: Retrofits such as tie bars have proven to be effective at increasing the resistance of masonry façades and walls to out-of-plane collapse. However, such retrofit measures can be quite expensive and tend to disturb the original fabric/aesthetics of the structure. At present, following the approach presented in Mauro et al. (2015), the tool models the restraining influence of the tie bars as a constant static force (Chapter 3). While this approach is a good approximation, it should be refined by replacing the constant force with a spring of constant stiffness instead – as presented in Casapulla et al. (2017) and Giresini and Sassu (2017). Using either of these approaches, the assessment algorithm could then be used to determine the optimal number and location of the tie bars, in order to minimise intervention and use them as effectively as possible.

- **Development of a new user-interface**: To make the tool accessible to practising engineers and academics, a user-interface needs to be developed. The idea here is that the user would open the 3D geometric model directly within a given CAD environment or independent application, and Python scripts would then be run to derive and solve the relevant equations of motion. The analysis results could then be output directly within the CAD environment or in the new independent interface. If multiple mechanisms are being compared, the tool could also highlight the critical mechanisms directly in the CAD file. The interface could also allow the user to select numerous options related to the analysis (interface typology, crushing, retrofits etc.), as well as input related material properties and seismicity parameters that can be used to access a catalogue of potential ground motions, or enable user-supplied ones. A user-interface to enable code-based assessment methods to be compared to analysis results could also be included.

References

Acikgoz, S. and DeJong, M. J. (2012). The interaction of elasticity and rocking in flexible structures allowed to uplift. *Earthquake Engineering & Structural Dynamics*, 41:2177–2194.

Aedes Software Snc (1997). AEDES Software.

Alexandris, A. P., Protopapa, E., and Psycharis, I. N. (2004). Collapse mechanisms of masonry buildings drived by the distinct element method. In *Proceedings of 13th World Conference on Earthquake Engineering*, Vancouver, B.C.

Allen, R. H. and Bielaks, J. (1986). On the dynamic response of rigid body assemblies. *Earthquake Engineering & Structural Dynamics*, 14:861–876.

Applied Technology Council (ATC) (1998). Evaluation of earthquake damaged concrete and masonry wall buildings. Basic procedures manual, FEMA 306. Technical report, Redwood City.

Applied Technology Council (ATC) (2000). Pre-standard and commentary for the seismic rehabilitation of buildings, FEMA 356. Technical report, Washington DC.

ASCE 43-05 (2007). Seismic Design Criteria for Structures, Systems, and Components in Nuclear Facilities. Technical report, American Society of Civil Engineers and Structural Engineering Institute.

Atkinson, R., Amadei, B., Saeb, S., and Sture, S. (1989). Response of masonry bed joints in direct shear. *Journal of Structural Engineering*, 115(9):2276–2296.

Augenti, N. and Parisi, F. (2010). Learning from Construction Failures due to the 2009 L ' Aquila, Italy, Earthquake. *Journal of Perfomance of Constructed Facilities*, 24(6):536–555.

Azevedo, J. and Sincraian, G. (2001). Modelling the Seismic Behaviour of Monumental Masonry Structures. In *Proceedings of the International Congress - ARCHI 2000*.

Azevedo, J., Sincraian, G., and Lemos, J. V. (2000). Seismic Behaviour of Blocky Masonry Structures. *Earthquake Spectra*.

Barton, N. (1976). The shear strength of rock and rock joints. *International Journal of Rock Mechanics and Mining Sciences and*, 13(9):255–279.

Betti, M. and Vignoli, A. (2008). Modelling and analysis of a Romanesque church under earthquake loading: Assessment of seismic resistance. *Engineering Structures*, 30(2):352–367.

Betti, M. and Vignoli, A. (2011). Numerical assessment of the static and seismic behaviour of the basilica of Santa Maria all'Impruneta (Italy). *Construction and Building Materials*, 25(12):4308–4324.

Bhagat, S., Buddika, H. A., Adhikari, R. K., Shrestha, A., Bajracharya, S., Joshi, R., Singh, J., Maharjan, R., and Wijeyewickrema, A. C. (2017). Damage to Cultural Heritage Structures and Buildings Due to the 2015 Nepal Gorkha Earthquake. *Journal of Earthquake Engineering*, pages 1–20.

Block, P., Ciblac, T., and Ochsendorf, J. (2006). Real-time limit analysis of vaulted masonry buildings. *Computers and Structures*, 84(29-30):1841–1852.

Bui, T. T. and Limam, A. (2012). Masonry Walls under Membrane or Bending Loading Cases : Experiments and Discrete Element Analysis. In Topping, B., editor, *Proceedings of the Eleventh International Conference on Computational Structures Technology*, page Paper 119, Stirlingshire, Scotland. Civil-Comp Press.

Campillo, M., Gariel, J. C., Aki, K., and Sánchez-Sesma, F. (1989). Destructive Strong Ground Motion in Mexico City: Source, Path and Site Effects During Great 1985 Michoacán Earthquake. *Bulletin of the Seismological Society of America*, 79(6):1718–1735.

Candeias, P. X., Costa, A. C., Mendes, N., Costa, A. A., and Lourenço, P. B. (2017). Experimental Assessment of the Out-of-Plane Performance of Masonry Buildings Through Shaking Table Tests. *International Journal of Architectural Heritage*, 11(1):31–58.

Capozucca, R. (2011). Shear Behaviour of Historic Masonry Made of Clay Bricks. *The Open Construction and Building Technology Journal*, 5(1):89–96.

Casapulla, C., Giresini, L., and Lourenço, P. B. (2017). Rocking and Kinematic Approaches for Rigid Block Analysis of Masonry Walls: State of the Art and Recent Developments. *Buildings*, 7(3):69.

Casarin, F. and Modena, C. (2008). Seismic Assessment of Complex Historical Buildings: Application to Reggio Emilia Cathedral, Italy. *International Journal of Architectural Heritage*, 2(3):304–327.

Castellazzi, G., Gentilini, C., and Nobile, L. (2013). Seismic Vulnerability Assessment of a Historical Church : Limit Analysis and Nonlinear Finite Element Analysis. *Advances in Civil Engineering*, 2013:12.

Clemente, P. (1998). Introduction to the dynamics of stone arches. *International Journal of Earthquake Engineering and Structural Dynamics*, 27:513–522.

Costa, A., Arêde, A., Costa, A. A., Ferreira, T. M., Gomes, A., and Varum, H. (2014). Experimental study of the out-of-plane behaviour of unreinforced sacco stone masonry walls : Comparative analysis of two different test setups. In *Proceedings of the 9th International Masonry Conference*, Guimaraes.

Costa, A. A. (2012). *Seismic Assessment of the Out-of-Plane Performance of Traditional Stone Masonry Walls*. PhD thesis, University of Porto.

Costa, A. A., Arêde, A., Penna, A., and Costa, A. (2013). Free rocking response of a regular stone masonry wall with equivalent block approach: experimental and analytical evaluation. *Earthquake Engineering & Structural Dynamics*, 42(15):2297–2319.

Cundall, P. A. (1988). Formulation of a three-dimensional distinct element model—Part I. A scheme to detect and represent contacts in a system composed of many polyhedral blocks. *International Journal of Rock Mechanics and Mining*, 25(3):107–116.

Dal Cin, A. and Russo, S. (2014). Influence of the annex on seismic behavior of historic churches. *Engineering Failure Analysis*, 45:300–313.

D'Ayala, D. (2005). Force and displacement based vulnerability assessment for traditional buildings. *Bulletin of Earthquake Engineering*, 3:235–265.

D'Ayala, D. and Speranza, E. (2002). An Integrated Procedure for the Assessment of Seismic Vulnerability of Historic Buildings. In *Proceedings of the 12th European Conference on Earthquake Engineering*, page Paper 561.

D'Ayala, D. and Speranza, E. (2003). Definition of Collapse Mechanisms and Seismic Vulnerability of Historic Masonry Buildings. *Earthquake Spectra*, 19(3):479–509.

de Felice, G. (2011). Out-of-Plane Seismic Capacity of Masonry Depending on Wall Section Morphology. *International Journal of Architectural Heritage*, 5(4-5):466–482.

de Felice, G., De Santis, S., Lourenço, P. B., and Mendes, N. (2017). Methods and Challenges for the Seismic Assessment of Historic Masonry Structures. *International Journal of Architectural Heritage*, 11(1):143–160.

de Felice, G. and Giannini, R. (2000). Assessment of Seismic Vulnerability To Out-of-Plane Collapse of Masonry Walls. In *Proceedings of the 12th World Conference on Earthquake Engineering*.

De Lorenzis, L., DeJong, M. J., and Ochsendorf, J. A. (2007). Failure of masonry arches under impulse base motion. *Earthquake Engineering & Structural Dynamics*, 36(14):2119–2136.

de Luca, A., Giordano, A., and Mele, E. (2004). A simplified procedure for assessing the seismic capacity of masonry arches. *Engineering Structures*, 26(13):1915–1929.

Decanini, L. D., Liberatore, D., Liberatore, L., and Sorrentino, L. (2012). Preliminary Report on the 2012, May 20, Emilia Earthquake. Technical report, Sapienza University of Rome.

DeJong, M. J. (2009). *Seismic Assessment Strategies for Masonry Structures*. Phd thesis, Massachusetts Institute of Technology.

DeJong, M. J. (2012a). Amplification of Rocking Due to Horizontal Ground Motion. *Earthquake Spectra*, 28(4):1405–1421.

DeJong, M. J. (2012b). Seismic response of stone masonry spires: Analytical modeling. *Engineering Structures*, 40:556–565.

DeJong, M. J. (2014). Rocking of Structures During Earthquakes: From Collapse of Masonry to Modern Design. *SECED Newsletter*, 25(3):1–8.

DeJong, M. J., De Lorenzis, L., Adams, S., and Ochsendorf, J. A. (2008). Rocking Stability of Masonry Arches in Seismic Regions. *Earthquake Spectra*, 24(4):847–865.

DeJong, M. J. and Dimitrakopoulos, E. G. (2012). Equivalent rocking systems: Fundamental rocking parameters. In *Proceedings of the 15th World Conference in Earthquake Engineering (WCEE)*, Lisbon, Portugal.

DeJong, M. J. and Dimitrakopoulos, E. G. (2014). Dynamically equivalent rocking structures. *Earthquake Engineering & Structural Dynamics*, 43(10):1543–1563.

DeJong, M. J., Giardina, G., Plunkett, W., and Ochsendorf, J. A. (2015). Seismic design of a stone vault. In *SECED 2015 Conference: Earthquake Risk and Engineering towards a Resilient World*, pages 1–10, Cambridge.

DeJong, M. J. and Ochsendorf, J. A. (2006). Analysis of vaulted masonry structures subjected to horizontal ground motion. In Lourenco, P., Roca, P., Modena, C., and Agrawal, S., editors, *Proceedings, Fifth International Conference on the Structural Analysis of Historical Constructions*, pages 973–980, New Delhi.

DeJong, M. J. and Vibert, C. (2012a). Seismic response of stone masonry spires: Computational and experimental modeling. *Engineering Structures*, 40:566–574.

DeJong, M. J. and Vibert, C. (2012b). Seismic response of stone masonry spires: Computational and experimental modeling. *Engineering Structures*, 40:566–574.

Dimitrakopoulos, E. G. and DeJong, M. J. (2012). Revisiting the rocking block: closed-form solutions and similarity laws. *Proceedings of the Royal Society A: Mathematical, Physical and Engineering Sciences*, 468(2144):2294–2318.

Dimitri, R., De Lorenzis, L., and Zavarise, G. (2011). Numerical study on the dynamic behavior of masonry columns and arches on buttresses with the discrete element method. *Engineering Structures*, 33(12):3172–3188.

DMI (2008). Decreto del Ministro delle Infrastrutture 14 gennaio 2008. Approvazione delle nuove norme tecniche per le costruzioni. Gazzetta Ufficiale della Repubblica Italiana n. 29, Supplemento Ordinario n. 30. Technical report.

Doherty, K., Griffith, M. C., Lam, N. T. K., and Wilson, J. L. (2002). Displacement-based seismic analysis for out-of-plane bending of unreinforced masonry walls. *Earthquake Engineering & Structural Dynamics*, 31(4):833–850.

Doherty, K., Rodolico, B., Lam, N. T. K., Wilson, J. L., and Griffith, M. C. (2000). The Modelling of Earthquake Induced Collapse of Unreinforced Masonry Walls Combining Force and Displacement Principals. In *Proceedings of the 12th World Conference on Earthquake Engineering*, pages 1–8.

Drei, A. and Oliveira, C. (2001). The seismic behaviour of the "Aqueduto da Amoreira” in Elvas using distinct element modelling. In Lourenço, P. B. and Roca, P., editors, *Proceedings, 3rd International Seminar on Historical Constructions*, pages 903–912, Guimaraes.

Drysdale, R., Vanderkeyl, R., and Hamid, A. (1979). Shear strength of brick masonry joints. In *Proceedings, 5th International Brick Masonry Conference*, pages 106–113, Washington DC.

EC (Eurocode) 8 (2004). Design of structures for earthquake resistance—Part 1: General rules, seismic actions and rules for buildings. Technical report, Brussels.

EEFIT (2005). The Kashmir, Pakistan Earthquake of 8 October 2005: A Field Report By EEFIT. Technical Report October.

ElGawady, M. A., Ma, Q. T., Butterworth, J. W., and Ingham, J. M. (2011). Effects of interface material on the performance of free rocking blocks. *Earthquake Engineering & Structural Dynamics*, 40:375–392.

EN 1998-1 (2004). Eurocode 8. Design of structures for earthquake resistance—Part 1: General rules, seismic actions and rules for buildings. Technical report, Brussels, Belgium.

Fattal, S. (1977). Structural Preservation of Historic Monuments at Casa Grande and Tumacacori. Technical report, National Bureau of Standards, Washington DC.

Ferreira, T. M., Costa, A. A., Vicente, R., and Varum, H. (2015). A simplified four-branch model for the analytical study of the out-of-plane performance of regular stone URM walls. *Engineering Structures*, 83:140–153.

Fiorentino, G., Forte, A., Pagano, E., Sabetta, F., Baggio, C., Lavorato, D., Nuti, C., and Santini, S. (2017). Damage patterns in the town of Amatrice after August 24th 2016 Central Italy earthquakes. *Bulletin of Earthquake Engineering*, pages 1–25.

Galetzka, J., Melgar, D., Genrich, J. F., Geng, J., Owen, S., Lindsey, E. O., Xu, X., Bock, Y., Avouac, J.-P., and Adhikari, L. B. (2015). Slip pulse and resonance of Kathmandu basin during the 2015 Gorkha earthquake Nepal. *Science*, 349(6252):1091–1095.

Gazetas, G., Garini, E., Berrill, J. B., and Apostolou, M. (2012). Sliding and overturning potential of Christchurch 2011 earthquake records. *Earthquake Engineering & Structural Dynamics*, 41:1921–1944.

Giresini, L., Fragiacomo, M., and Lourenço, P. B. (2015). Comparison between rocking analysis and kinematic analysis for the dynamic out-of-plane behavior of masonry walls. *Earthquake Engineering & Structural Dynamics*.

Giresini, L. and Sassu, M. (2017). Horizontally restrained rocking blocks: evaluation of the role of boundary conditions with static and dynamic approaches. *Bulletin of Earthquake Engineering*, 15(1):385–410.

Goda, K., Kiyota, T., Pokhrel, R. M., Chiaro, G., Katagiri, T., Sharma, K., and Wilkinson, S. (2015). The 2015 Gorkha Nepal earthquake: insights from earthquake damage survey. *Frontiers in Built Environment*, 1(8):1–15.

Graziotti, F., Tomassetti, U., Penna, A., and Magenes, G. (2016). Out-of-plane shaking table tests on URM single leaf and cavity walls. *Engineering Structures*, 125:455–470.

Griffith, M. C., Lam, N. T. K., Wilson, J. L., and Doherty, K. (2004). Experimental Investigation of Unreinforced Brick Masonry Walls in Flexure. *Journal of Structural Engineering*, 130(3):423–432.

Hart, R., Cundall, P. A., and Lemos, J. V. (1988). Formulation of a three-dimensional distinct element model—Part II. Mechanical calculations for motion and interaction of a system composed of many polyhedral blocks. *International Journal of Rock Mechanics and Mining Sciences & Geomechanics Abstracts*, 25(3):117–125.

Heyman, J. (1995). *The Stone Skeleton: Sturctural Engineering of Masonry Architecture*. Cambridge University Press, Cambridge.

Hough, S. E., Martin, S., Bilham, R., and Atkinson, G. M. (2002). The 26 January 2001 M 7.6 Bhuj, India, Earthquake: Observed and Predicted Ground Motions. *Bulletin of the Seismological Society of America*, 92(6):2061–2079.

Housner, G. W. (1963). The Behavior of Inverted Pendulum Structures during Earthquakes. *Bulletin of the Seismological Society of America*, 53(2):403–417.

International Code Council (2009). International Building Code. Technical report, ICC.

Itasca Consulting Group (2007a). 3DEC - 3 Dimensional Distinct Element Code.

Itasca Consulting Group (2007b). *3DEC 3-Dimensional Distinct Element Code, Version 4.10: Theory and Background*. ICG, Minneapolis, Minnesota.

Iwan, W. and Chen, X. (1994). Important near-field ground motion data from the Landers earthquake. In Duma, G., editor, *Proceedings, 10th European Conference on Earthquake Engineering*, Rotterdam.

Jones, E., Oliphant, E., Peterson, P., and Al, E. (2001). SciPy: Open Source Scientific Tools for Python.

Kaushik, H. B., Rai, D. C., and Jain, S. K. (2007). Stress-Strain Characteristics of Clay Brick Masonry under Uniaxial Compression. *Journal of Materials in Civil Engineering*, 19(9):728–739.

Koh, A.-S., Spanos, P. D., and Roesset, J. M. (1986). Harmonic rocking of rigid block on flexible foundation. *Journal of Engineering Mechanics*, 112(11):1165–1180.

Lagomarsino, S. (2015). Seismic assessment of rocking masonry structures. *Bulletin of Earthquake Engineering*, 13:97–128.

Lagomarsino, S. and Ottonelli, D. (2012). MB_PERPETUATE.

Lagomarsino, S., Penna, A., Galasco, A., and Cattari, S. (2013). TREMURI program: An equivalent frame model for the nonlinear seismic analysis of masonry buildings. *Engineering Structures*, 56:1787–1799.

Lemos, J. V. (1998). Discrete element modelling of the seismic behavior of stone masonry arches. In *Proceedings of the Fourth International Symposium on Computer Methods in Structural Masonry*, pages 220–227.

Lemos, J. V. (2007). Discrete Element Modeling of Masonry Structures. *International Journal of Architectural Heritage*, 1(2):190–213.

Lemos, J. V. and Campos Costa, A. (2017). Simulation of Shake Table Tests on Out-of-Plane Masonry Buildings. Part (V): Discrete Element Approach. *International Journal of Architectural Heritage*, 11(1):117–124.

Lipo, B. and de Felice, G. (2016). Smooth-rocking oscillator under natural accelerograms. In Papadrakakis, M., Papadopoulos, V., Stefanou, G., and Plevris, V., editors, *ECCOMAS Congress 2016: 7th European Congress on Computational Methods in Applied Sciences and Engineering*, number June, pages 5–10, Crete Island, Greece.

Lipo, B. and de Felice, G. (2017). Seismic resilience of masonry walls rocking on elastic foundation. In *Proceedings of the 16th World Conference in Earthquake Engineering (WCEE)*, Santiago, Chile.

Magenes, G. (2000). A method for pushover analysis in seismic assessment of masonry buildings. In *Proceedings of the 12th World Conference on Earthquake Engineering*, page Paper no. 1866.

Magenes, G. (2006). Masonry Building Design in Seismic Areas: Recent Experiences and Prospects from a European Standpoint. In *1st European Conference on Earthquake Engineering and Seismology*, Geneva, Switzerland.

Makris, N. and Konstantinidis, D. (2001). The rocking spectrum and the shortcomings of design guidelines. Technical report.

Makris, N. and Roussos, Y. (1998). Rocking response and overturning of equipment under horizontal pulse-type motions, Report No. PEER-98/05. Technical report, Pacific Earthquake Engineering Research Center, University of California, Berkeley.

Makris, N. and Vassiliou, M. F. (2013). Planar rocking response and stability analysis of an array of free-standing columns capped with a freely supported rigid beam. *Earthquake Engineering & Structural Dynamics*, 42(3):431–449.

Makris, N. and Zhang, J. (1999). Rocking Response and Overturning of Anchored Equipment under Seismic Excitations. Technical report, University of California, Berkeley.

Matero, F. (1999). Documentation and Assessment of Wall Conditions for the Casa Grande, Casa Grande Ruins National Monument, Arizona. Technical report, University of Pennsylvania.

Mauro, A., de Felice, G., and DeJong, M. J. (2015). The relative dynamic resilience of masonry collapse mechanisms. *Engineering Structures*, 85:182–194.

Mehrotra, A., Arêde, A., and DeJong, M. J. (2015). Discrete Element Modeling of a Post-Tensioned Masonry Arch. In Kruis, J., Tsompanakis, Y., and Topping, B., editors, *Proceedings of the 15th International Conference on Civil, Structural and Environmental Engineering Computing*, pages 1–16, Prague. Civil-Comp Press.

Mele, E., de Luca, A., and Giordano, A. (2003). Modelling and analysis of a basilica under earthquake loading. *Journal of Cultural Heritage*, 4:355–367.

Mendes, N., Costa, A. A., Lourenço, P. B., Bento, R., Felice, G. D., Gams, M., Griffith, M. C., Ingham, J. M., Lagomarsino, S., Lemos, J. V., Liberatore, D., Oliveira, D. V., Penna, A., Sorrentino, L., Modena, C., and Beyer, K. (2017). Methods and Approaches for Blind Test Predictions of Out-of-Plane Behavior of Masonry Walls : A Numerical Comparative Study. *International Journal of Architectural Heritage*, 11(1):59–71.

Menon, A., Shukla, S., Samson, S., Aravaind, N., Romão, X., and Paupério, E. (2017). Field observations on the performance of heritage structures in the Nepal 2015 earthquake. In *Proceedings of the 16th World Conference on Earthquake Engineering*, number June 2015, Santiago, Chile.

Mirabella-Roberti, G. and Calvetti, F. (1998). Distinct element analysis of stone arches. In Sinopoli, A., editor, *Arch Bridges*, pages 181–186. Rotterdam.

Mirabella-Roberti, G. and Spina, O. (2001). Discrete element analysis on the Sardinian' Nuaraghe. In Lourenço, P. B. and Roca, P., editors, *Proceedings, 3rd International Seminar on Historical Constructions*, pages 719–727, Guimaraes.

Mordant, C., Denoel, V., and Degee, H. (2015). Rocking behaviour of simple unreinforced load-bearing masonry walls including soundproofing rubber layers. In Papadrakakis, M., Papadopoulos, V., and Plevris, V., editors, *5th ECCOMAS Thematic Conference on Computational Methods in Structural Dynamics and Earthquake Engineering*, pages 759–771, Crete Island, Greece.

National Planning Commission (NPC) (2015). Nepal Earthquake 2015: Post Disaster Needs Assessment, Executive Summary. Technical report, Government of Nepal, Kathmandu.

NZS (2004). NZS 1170.5: 2004: Structural Design Actions: Part 5: Earthquake actions, New Zealand. Technical report, Standards New Zealand.

Oliveira, C., Lemos, J. V., and Sincraian, G. (2002). Modelling large displacements of structures damaged by earthquake motions. *European Earthquake Engineering*, 16(3):56–71.

Oppenheim, I. J. (1992). The masonry arch as a four-link mechanism under base motion. *Earthquake Engineering & Structural Dynamics*, 21:1005–1017.

Papantonopoulos, C., Psycharis, I. N., Papastamatiou, D. Y., Lemos, J. V., and Mouzakis, H. P. (2002). Numerical prediction of the earthquake response of classical columns using the distinct element method. *Earthquake Engineering and Structural Dynamics*, 31(9):1699–1717.

Papastamatiou, D. Y. and Psycharis, I. N. (1993). Seismic response of classical monuments-a numerical perspective developed at the Temple of Apollo in Bassae, Greece. *Terra Nova*, 5(6):591–601.

Parajuli, H. R., Kiyono, J., and Taniguchi, H. (2011). Structural Assessment of the Kathmandu World Heritage Buildings. In *Proceedings of the 31st Conference on Earthquake Engineering*.

Parajuli, R. R. and Kiyono, J. (2015). Ground Motion Characteristics of the 2015 Gorkha Earthquake, Survey of Damage to Stone Masonry Structures and Structural Field Tests. *Frontiers in Built Environment*, 1.

PCM-DPC MiBAC (2006). Model A-DC Scheda per il rilievo del danno ai beni culturali - Chiese.

PEER (2014). PEER Ground Motion Database.

Penna, A. and Galasco, A. (2013). A Macro-Element Model for the Nonlinear Analysis of Masonry Members Including Second Order Effects. In Papadrakakis, M., Papadopoulos, V., and Plevris, V., editors, *4th ECCOMAS Thematic Conference on Computational Methods in Structural Dynamics and Earthquake Engineering*, Kos Island, Greece.

Penna, A., Galasco, A., and Magenes, G. (2015). Macro-element modelling of earthquake-induced local failure modes in existing masonry building. In *SECED 2015 Conference: Earthquake Risk and Engineering towards a Resilient World*, Cambridge.

Penna, A., Lagomarsino, S., and Galasco, A. (2014). A nonlinear macroelement model for the seismic analysis of masonry buildings. *Earthquake Engineering and Structural Dynamics*, 43(2):159–179.

Porter, D., Mehrotra, A., DeJong, M. J., Bass, A., and Guebard, M. (2018). (under review). Material and Seismic Assessment of the Great House at Casa Grande Ruins National Monument, Arizona. *Journal of Architectural Engineering*.

Preti, M., Marini, A., Bolis, V., and Giuriani, E. (2013). Experimental response of a large-scale transverse arch subjected to horizontal cyclic loading. In *Proceedings of the 15th Italian Conference on Earthquake Engineering*, Padua.

Priestley, M. (1985). Seismic behaviour of unreinforced masonry walls. *Bulletin of the New Zealand Society for Earthquake Engineering*, 18(2):191–205.

Psycharis, I. N. (1990). Dynamic Behaviour of Rocking Two-Block Assemblies. *Earthquake Engineering & Structural Dynamics*, 19:555–575.

Psycharis, I. N. and Jennings, P. C. (1983). Rocking of slender rigid bodies allowed to uplift. *Earthquake Engineering & Structural Dynamics*, 11:57–76.

Psycharis, I. N., Lemos, J. V., Papastamatiou, D. Y., Zambas, C., and Papantonopoulos, C. (2003). Numerical study of the seismic behaviour of a part of the Parthenon Pronaos. *Earthquake Engineering & Structural Dynamics*, 32(13):2063–2084.

Python Software Foundation (2016). Python Language Reference.

Rai, D. C. and Dhanapal, S. (2013). Bricks and mortars in Lucknow monuments of c. 17-18 century. *Current Science*, 104(2):238–244.

Rai, D. C., Singhal, V., Raj S, B., and Sagar, S. L. (2016). Reconnaissance of the effects of the M7.8 Gorkha (Nepal) earthquake of April 25, 2015. *Geomatics, Natural Hazards and Risk*, 7(1):1–17.

Restrepo-Vélez, L. F. (2004). *Seismic Risk of Unreinforced Masonry Buildings*. PhD thesis, Rose School, University of Pavia.

Restrepo-Vélez, L. F., Magenes, G., and Griffith, M. C. (2014). Dry stone masonry walls in bending-Part I: Static tests. *International Journal of Architectural Heritage*, 8(1):1–28.

Robert McNeel & Associates (2014). Rhinoceros 5.

Roh, H. and Reinhorn, A. M. (2009). Analytical modeling of rocking elements. *Engineering Structures*, 31(5):1179–1189.

Sahlin, S. (1971). *Structural Masonry*. Prentice-Hall.

Shawa, O. A., de Felice, G., Mauro, A., and Sorrentino, L. (2012). Out-of-plane seismic behaviour of rocking masonry walls. *Earthquake Engineering & Structural Dynamics*, 41:949–968.

Sorrentino, L., Al Shawa, O., and Decanini, L. D. (2011). The relevance of energy damping in unreinforced masonry rocking mechanisms. Experimental and analytic investigations. *Bulletin of Earthquake Engineering*, 9(5):1617–1642.

Sorrentino, L., Kunnath, S., Monti, G., and Scalora, G. (2008a). Seismically induced one-sided rocking response of unreinforced masonry facades. *Engineering Structures*, 30(8):2140–2153.

Sorrentino, L., Liberatore, L., Decanini, L. D., and Liberatore, D. (2014). The performance of churches in the 2012 Emilia earthquakes. *Bulletin of Earthquake Engineering*, 12(5):2299–2331.

Sorrentino, L., Masiani, R., and Griffith, M. C. (2008b). The vertical spanning strip wall as a coupled rocking rigid body assembly. *Structural Engineering and Mechanics*, 29(4):433–453.

Spanos, P. D. and Koh, A.-S. (1984). Rocking of rigid bodies due to harmonic shaking. *Journal of Engineering Mechanics*, 110:1627–1642.

Spanos, P. D., Roussis, P. C., and Politis, N. P. (2001). Dynamic analysis of stacked rigid blocks. *Soil Dynamics and Earthquake Engineering*, 21(7):559–578.

STADATA (2012). 3Muri Program.

Stockl, S. and Hofmann, P. (1986). Tests on the shear bond behaviour in the bed-joints of masonry. *Masonry International*, pages 292–303.

Takai, N., Shigefuji, M., Rajaure, S., Bijukchhen, S., Ichiyanagi, M., Dhital, M. R., and Sasatani, T. (2016). Strong ground motion in the Kathmandu Valley during the 2015 Gorkha, Nepal, earthquake. *Earth, Planets and Space*, 68(10).

Tomazevic, M. (1978). The computer program POR. Report ZRMK. Technical report, Ljubljana.

Ungewitter, G. G. and Mohrmann, K. (1901). *Lehrbuch der gotischen Konstruktionen*. H. Tauchnitz, Leipzig.

Van Der Walt, S., Colbert, S. C., and Varoquaux, G. (2011). The NumPy array: A structure for efficient numerical computation. *Computing in Science and Engineering*, 13(2):22–30.

Zhang, P. and Makris, N. (2001). Rocking response of free-standing blocks under cycloidal pulses. *Journal of Engineering Mechanics*, 127:473–483.

Zhuge, Y. (2008). Distinct element modelling of unreinforced masonry wall under seismic loads with and without cable retrofitting. *Transactions of Tianjin University*, 14(S1):471–475.

Related publications by the author

Porter, D., Mehrotra, A., DeJong, M.J., Bass, A. and Guebard, M. (under review). Material and Seismic Assessment of the Great House at Casa Grande Ruins National Monument, Arizona. *Journal of Architectural Engineering*.

Mehrotra A. and DeJong M.J. (2018). The influence of interface geometry, stiffness and crushing on the dynamic response of masonry collapse mechanisms. *Earthquake Engineering & Structural Dynamics*, 47:2661-2681.

Mehrotra A. and DeJong M.J. (2018). A methodology to account for crushing effects during out-of-plane collapse of masonry. In *Proceedings of the 11th International Conference on Structural Analysis of Historical Constructions (SAHC 2018)*, Cusco, Peru.

Mehrotra A. and DeJong M.J. (2018). A CAD-interfaced dynamics-based tool for analysis of masonry collapse mechanisms. *Engineering Structures*, 172:833-849.

Mehrotra A. and DeJong M.J. (2017). The performance of slender monuments during the 2015 Gorkha earthquake. *Earthquake Spectra*, 33(S1):S321-S343.

Mehrotra A. and DeJong M.J. (2017). A modelling tool for dynamic analysis of masonry collapse mechanisms. In *Proceedings of the 16th World Conference on Earthquake Engineering (16WCEE)*, Santiago, Chile.

Mehrotra A. and DeJong M.J. (2016). Analysis of historical monuments damaged by the 2015 Nepal earthquake. In *Proceedings of the 10th International Conference on Structural Analysis of Historical Constructions (SAHC 2016)*, Leuven, Belgium.